Domain-Based Local Pair Natural Orbital Second-Order Møller-Plesset Perturbation Theory, and the Development of its Analytical Gradient

Dissertation
zur
Erlangung des Doktorgrades (Dr. rer. nat.)
der
Mathematisch-Naturwissenschaftlichen Fakultät
der
Rheinischen Friedrich-Wilhelms-Universität Bonn

vorgelegt von
Peter Pinski
aus
Kiew, Ukraine

Bonn, Januar 2020

Angefertigt mit Genehmigung der Mathematisch-Naturwissenschaftlichen Fakultät der Rheinischen Friedrich-Wilhelms-Universität Bonn

1. Gutachter: Prof. Dr. Frank Neese

2. Gutachter: Prof. Dr. Stefan Grimme

Tag der Promotion: 18. Juni 2020

Erscheinungsjahr: 2020

Abstract

Dynamic electron correlation methods are known to have a computational cost that scales with a high power of the system size: for example, $O(N^5)$ for second-order Møller-Plesset perturbation theory (MP2), and $O(N^7)$ for coupled cluster with single, double and perturbative triple excitations (CCSD(T)). Domain-based local pair natural orbital (DLPNO) methods reduce this scaling, while maintaining a modest prefactor, using several approximations: most critically by expanding the virtual space in truncated sets of pair natural orbitals (PNOs), which are combined with the domain approximation and orbital pair screening.

The first part of this work consists of the implementation of MP2 in the DLPNO framework, drawing closely upon the previously existing DLPNO-CCSD method. Several improvements were introduced in the process: (1) The transformation routine for one-external three-index integrals was replaced with a formally linear scaling algorithm, which treats sparsity relationships in a systematic framework. (2) A new domain selection criterion was introduced based on the differential overlap integral between occupied localised orbitals and redundant projected atomic orbitals. (3) An improved, more accurate procedure to screen orbital pairs was developed. DLPNO-MP2 was confirmed to reproduce energy differences computed with the canonical resolution of the identity (RI-)MP2 method to within chemical accuracy, and its performance was demonstrated in large-scale calculations. A simple unrestricted variant of DLPNO-MP2 was implemented for open-shell calculations.

The second and major part of this thesis is the development of the analytical gradient for the closed-shell DLPNO-MP2 method. Importantly, the exact derivative of the entire

energy was taken. Mathematical contributions to account for the relaxation of PNOs were described for the first time in the context of local correlation methods. Calculations of electric field gradients with exact and approximate derivatives emphasise the importance of the individual contributions. Additionally, a procedure was introduced to circumvent singularities in the coupled-perturbed localisation equations, which are caused by continuously degenerate localised orbitals.

Extensively testing the DLPNO-MP2 gradient in geometry optimisations showed that it reproduces covalent RI-MP2 bond lengths to well within 0.1 pm. Errors in interatomic distances between non-covalently interacting system parts do not exceed 1 % with default thresholds and 0.3 % with tight thresholds. The DLPNO-MP2 gradient becomes substantially more efficient than the RI-MP2 gradient beyond ca. 70 atoms, while a similar computational effort is incurred in smaller applications. Among the most demanding calculations demonstrated in this work were the geometry optimisation of a host-guest complex containing 205 atoms and more than 4000 basis functions, and a single-point gradient calculation for crambin with 644 atoms and over 12 000 basis functions. Spin-component scaling and double-hybrid density functionals are supported by the implementation.

List of publications

Published parts of this thesis

Parts of this thesis have appeared in the following publications:

1. P. Pinski, C. Riplinger, E. F. Valeev, F. Neese: "Sparse maps—A systematic infrastructure for reduced-scaling electronic structure methods. I. An efficient and simple linear scaling local MP2 method that uses an intermediate basis of pair natural orbitals", J. Chem. Phys. **143**, 034108 (2015).

   A prototype implementation of the "DLPNO-MP2" method for closed-shell systems with the linear scaling integral transformation routine, the numerical differential overlap integration, and a large part of the "Sparse Maps" infrastructure were provided by my co-authors. I created a technically improved implementation of "DLPNO-MP2", contributed important modifications to the "Sparse Maps" infrastructure (particularly the map extension), and introduced the new pair prescreening procedure. All calculations reported in the "numerical results" section of the publication were performed by me.

2. P. Pinski, F. Neese: "Communication: Exact analytical derivatives for the domain-based local pair natural orbital MP2 method (DLPNO-MP2)", J. Chem. Phys. **148**, 031101 (2018).

   I performed the work reported in the publication, and was advised by Frank Neese.

3. P. Pinski, F. Neese: "Analytical gradient for the domain-based local pair natural orbital second order Møller-Plesset perturbation theory method (DLPNO-MP2)", J. Chem. Phys. **150**, 164102 (2019).

   I performed the work reported in the publication, and was advised by Frank Neese.

Further publications

The publications listed below are not part of this thesis.

1. P. Pinski, G. Csányi: "Reactive Many-Body Expansion for a Protonated Water Cluster", J. Chem. Theory Comput. **10**, 68-75 (2014).

2. C. Riplinger, P. Pinski, U. Becker, E. F. Valeev, F. Neese: "Sparse maps—A systematic infrastructure for reduced-scaling electronic structure methods. II. Linear scaling domain based pair natural orbital coupled cluster theory", J. Chem. Phys. **144**, 024109 (2016).

3. F. Pavošević, P. Pinski, C. Riplinger, F. Neese, E. F. Valeev: "SparseMaps—A systematic infrastructure for reduced-scaling electronic structure methods. IV. Linear-scaling second-order explicitly correlated energy with pair natural orbitals", J. Chem. Phys. **144**, 144109 (2016).

4. F. Pavošević, C. Peng, P. Pinski, C. Riplinger, F. Neese, E. F. Valeev: "SparseMaps—A systematic infrastructure for reduced scaling electronic structure methods. V. Linear scaling explicitly correlated coupled-cluster method with pair natural orbitals", J. Chem. Phys. **146**, 174108 (2017).

5. M. Sparta, M. Retegan, P. Pinski, C. Riplinger, U. Becker, F. Neese: "Multilevel Approaches within the Local Pair Natural Orbital Framework", J. Chem. Theory Comput. **13**, 3198-3207 (2017).

Acknowledgement

First and foremost, I am grateful to Frank Neese for entrusting me with this research project, and providing me with crucial guidance in the process, while giving me a lot of freedom to pursue my own ideas. I also thank the members of the examination committee for taking their time to review this work.

During my time in Mülheim I benefited a lot from interacting with many bright and inspiring people, for which I would like to thank all past and present group members.

Christoph Riplinger was an instrumental person to work with on the DLPNO methodology and beyond. I thank our collaborators from Virginia Tech on sparsity and explicit correlation, Ed Valeev and Fabijan Pavošević; and Manuel Sparta and Marius Retegan for including me in the multilevel paper.

To Ute Becker I am obliged for parallelising the code, and for our lively discussions about bugs and other struggles of an orca. Simone Koßmann took care of me during the first months of my PhD. I thank Frank Wennmohs, for being a benevolent head of development, and the other members of the development and maintenance team Kantharuban "Kanthen" Sivalingam, Dimitrios Liakos and Dagmar Lenk.

I had useful discussions with Yang Guo—the second-order orbital localiser emerged as the re-write of a code of his; and with Róbert Izsák, Georgi Stoychev, Alexander Auer, Masaaki Saitow, Giovanni Bistoni and Dipayan Datta.

A special thanks goes to the many office mates I had over the duration of my PhD.

The Max Planck Society and Fonds der Chemischen Industrie funded this project.

Finally, I would like to thank my family and my close ones, who supported me during this time and accepted everything that I excused with writing this thesis.

Contents

Chapter 1

Introduction

To understand and predict the behaviour of the electrons in a chemical system, it is necessary to solve the many-electron Schrödinger equation to a high degree of accuracy. While a precise solution can be achieved formally through full configuration interaction (CI) in a (near-)complete basis set, the associated computational cost rises exponentially with the size of the system, allowing its usage only for a small number of electrons. Meaningful results for particular problems can be obtained with approximate wave function methods, which recover a sufficiently large part of the electron correlation energy.[1, 2]

From a conceptual viewpoint, it is useful to distinguish between dynamic and static contributions to the correlation energy. If a single Slater determinant dominates the full CI expansion of the exact wave function, the correlation energy is regarded as being of dynamic nature. For such problems, truncated coupled cluster schemes provide a systematically improvable hierarchy of methods to obtain accurate electronic energies. Other types of dynamic correlation methods include Møller-Plesset perturbation theory, albeit the energy may diverge at higher orders of the expansion; and truncated configuration interaction, which is, however, not size consistent and not size extensive. The computational cost of these methods typically increases polynomially as a higher power of the system size, e.g. $O\left(N^5\right)$ for second-order Møller-Plesset perturbation theory (MP2), $O\left(N^6\right)$ for coupled cluster with single and double excitations (CCSD), and $O\left(N^7\right)$ for the perturbative triple excitations correction in the CCSD(T) method.

Whenever a single Slater determinant cannot represent a wave function that is at least qualitatively correct, it becomes necessary to employ static correlation approaches such as the complete active space self-consistent field method (CASSCF). As the active space is limited to include only the few most important orbitals, a large part of the dynamic correlation energy needs to be recovered using multi-reference counterparts of single-reference methods such as Møller-Plesset perturbation theory, truncated configuration interaction or coupled cluster.

The steep scaling of the computational expense for dynamic correlation methods places firm upper boundaries upon the size of the problems that can be investigated. Implementations which perform such calculations on supercomputing facilities, instead of personal computers or small-scale clusters, are able to push these limits only to a limited degree.[3–6] Over the past decades this has created a desire for approximate methods, which exploit the locality of dynamic correlation to reduce the computational cost for larger systems.

Local correlation methods were introduced in the 1980s by Pulay and Saebø.[7–11] After performing a localisation of the occupied orbitals, individual domains were determined for each of them. The virtual space in those methods was spanned in a basis of projected atomic orbitals (PAOs). Despite their unfortunate property of being linearly dependent, PAOs circumvent the requirement for a localisation of the virtual molecular orbitals, which remains a substantial technical challenge despite recent progress.[12–14] Excitations were included from occupied MOs only to those PAOs that are members of the respective domains. Several further important ideas were contained in those early contributions, such as merging of domains for orbital pairs, the approximate treatment of weak pairs,[10] or the Hylleraas functional formulation of MP2 in a local, non-orthogonal basis.[9] The approximations were designed to recover the canonical counterpart of the respective methods in the absence of truncation, and ca. 96 % to 99 % of the canonical total correlation energy were reproduced with truncations in place.

Domain-based local correlation methods were refined subsequently by Werner, Schütz and their co-workers, who created production quality implementations of MP2[15] and

coupled cluster.[16–18] These were combined to great benefit[19, 20] with the resolution of the identity technique for the two-electron integrals,[21, 22] which is also called density fitting by some authors. By truncating auxiliary functions to fitting domains, exploiting locality in the transformation routine, employing multipole screening of orbital pairs, and in the case of coupled cluster also introducing a refined hierarchy of pair approximations, it was demonstrated that formally linear scaling local correlation algorithms can be developed.[19]

Even though ca. 98 % of the canonical correlation energy are reproduced with domains of up to four atoms per occupied orbital,[23] PAO-based truncation is not sufficient to achieve a satisfactory compromise between accuracy and efficiency. The total dynamic correlation energy of a mid-sized molecule is typically in the order of magnitude of $10\,\mathrm{MJ\,mol^{-1}}$. Errors in electronic energy differences, for example reaction energies, become relevant in a range of $1\,\mathrm{kJ\,mol^{-1}}$ or above. While it would be necessary to reproduce 99.99 % of the correlation energy to attain this degree of accuracy, in practice there is some extent of error cancellation. In our experience, around 99.9 % of the canonical correlation energy should be reproduced. This observation is in agreement with benchmark calculations.[24–26] PAOs from around 30 atoms need to be selected for each orbital pair, which makes such calculations very costly to perform.

While the domain approximation primarily relies on the spatial locality of the functions involved, approaches based on pair natural orbitals (PNOs) use information about the electron correlation itself to truncate the wave function more effectively. First proposed by Edmiston and Krauss as "pseudonatural orbitals",[27, 28] PNO-based electron correlation methods were implemented in the 1970s by Meyer[29, 30] and by Ahlrichs and co-workers,[31, 32] and used to perform calculations for molecules containing a few atoms. Even though Pulay still employed a variant of PNOs to accelerate calculations in his earliest work on local correlation,[7] the idea subsequently fell out of favour, probably because of the high computational and storage effort associated with the transformed four-index integrals in PNO basis. In the context of local correlation, Neese and co-workers resurrected the concept of pair natural orbitals in 2009, creating implementations of CEPA

(coupled electron pair approximation) and CCSD that could be used for systems with 100 atoms.[33, 34] The PNOs were constructed as the eigenvectors of the virtual part of the unrelaxed semicanonical MP2 density for each pair of localised occupied orbitals. Efficient routines for the calculation and handling of two-electron integrals in PNO basis were developed using a local RI approximation, which truncates auxiliary functions to fitting domains for orbital pairs. To reduce the computational cost further, weak pairs were treated at an approximate MP2 level. This first generation of local correlation methods in the ORCA quantum chemistry software[35, 36] is referred to as the local pair natural orbital (LPNO) approach.

Expanding the PNOs in a basis of canonical virtual MOs leads to some fifth-power scaling steps in the LPNO approach. In the domain-based local pair natural orbital coupled cluster method (DLPNO-CCSD(T)) by Riplinger and Neese,[37, 38] the pair natural orbital approach was therefore combined with the domain approximation, using projected atomic orbitals instead of virtual MOs as a basis to expand the PNOs. The majority of computationally significant steps in that method featured a formally linear scaling with system size, permitting calculations to be performed for systems containing many hundred atoms.

An alternative virtual basis for local correlation are orbital-specific virtuals (OSVs), which effectively correspond to PNOs of diagonal pairs (where double excitations originate from the same occupied spatial orbital).[39] The scheme was explored in the context of MP2[40] and coupled cluster.[41, 42] Krause and Werner compared PAOs, OSVs and PNOs as different bases to expand the virtual space, concluding that PNOs are the most compact representation to achieve a specific target accuracy.

The first part of this thesis in Chapter 2 describes the development and implementation of a local MP2 method named DLPNO-MP2, which was published by us in ref. [43]. It is closely related to the DLPNO-CCSD method,[37] but addresses several further aspects. In the original formulation of DLPNO-CCSD, the transformation of the one-external three-centre RI integrals became a bottleneck in large-scale calculations. The DLPNO-MP2 method incorporates an improved integral transformation routine, with

an associated computational cost that scales linearly with system size. To simplify the bookkeeping associated with sparse quantities that occur as a result of truncations in local correlation methods, the sparse map formalism is introduced and discussed. It is applied in the context of the linear scaling integral transformation, but can also be used in a broader context. A new scheme was introduced for domain construction, which uses a differential overlap criterion and thereby incorporates information about both the occupied and the virtual space. Finally, as part of this work it was recognised that the dipole-based prescreening procedure in the first implementation of DLPNO-CCSD was not sufficiently accurate, leading to the development of an improved method. In addition to the closed-shell DLPNO-MP2 method, the chapter describes a simple unrestricted implementation for open-shell calculations.

Subsequently, several other developments within the DLPNO framework were made, including: an improved implementation of DLPNO-CCSD(T), which incorporates the sparse maps framework and the linear scaling transformation routine for the one-external integrals;[44, 45] an open-shell version of the coupled cluster implementation, which is consistent with the closed-shell variant;[46] a multilevel scheme permitting treatment of different system parts at different accuracy levels;[47] explicitly correlated local MP2 and CCSD methods;[48, 49] local variants of n-electron valence state perturbation theory (NEVPT2)[50] and multi-reference coupled cluster;[51, 52] a local energy decomposition scheme for the analysis of molecular interactions;[53] and techniques for excited states.[54]

While our work on DLPNO-MP2 was in progress, a similar local MP2 method was published by Werner and co-workers.[55] The latter work is also based on domains and PNOs, albeit with OSVs in an intermediate step, and results in a linear scaling implementation. Related PNO-based developments by Werner and co-workers include linear scaling coupled cluster,[56, 57] explicitly correlated versions of local MP2 and CCSD,[58, 59] complete active space perturbation theory (CASPT2)[60] and spin-restricted open-shell MP2.[61]

Local correlation methods based on pair natural orbitals were also developed by Hättig and co-workers. Particularly relevant in the context of this work is their cubically scaling

PNO-MP2 implementation, which spans the pair natural orbitals in a basis of OSVs.[62] Other developments include PNO-based explicitly correlated coupled cluster,[63, 64] and methods for excited states.[65, 66]

Aside from the aforementioned methods, a number of other concepts have been explored in the development of local correlation methods. Ayala and Scuseria, and later Ochsenfeld and co-workers, developed reduced scaling implementations of MP2 through combining the Laplace transformation technique with integral screening.[67–69] Also, the AO-based coupled cluster method by Scuseria and Ayala,[70] and the triatomics in molecules approach by Head-Gordon and co-workers[71–73] need to be mentioned in this context.

Fragmentation methods take a different approach to exploit the locality of electron correlation: the correlation energy is broken down into contributions by fragments, which are calculated entirely independently. Examples include the cluster-in-molecule method (CIM),[74–76] the incremental method[77–79] and the divide-expand-consolidate (DEC) scheme.[80–82] An advantage of fragmentation methods is that they are easier to parallelise than "direct" local correlation methods; a disadvantage is that the subsystems need to be particularly large. As was shown by Guo and co-workers, a cluster-in-molecules scheme based on RI-MP2 is competitive with DLPNO-MP2, but CIM calculations based on CCSD(T) become unfeasible for realistic examples. However, a CIM scheme could be constructed successfully by fragmenting the DLPNO-CCSD(T) energy.[83] The latter approach is somewhat related to the developments by Kállay, Rolik, Nagy and their co-workers, who combine the cluster-in-molecules scheme with local natural orbitals and other approximations.[84–87]

Many interesting quantities are accessible in quantum chemistry via energy derivatives. For example, the gradient and the Hessian are needed to determine equilibrium geometries or vibrational frequencies, respectively; electrostatic derivatives provide access to electrostatic multipole moments and polarisabilities, and magnetic derivatives to nuclear magnetic resonance shifts or hyperfine coupling constants. Mixed derivatives with respect to nuclear coordinates and external fields are needed for properties such as

infrared absorption or Raman intensities.[88]

The development of derivatives for local correlation methods is affected by two obstacles. Firstly, methods such as Møller-Plesset perturbation theory or coupled cluster are non-variational. This interdependency between the wave function parameters needs to be considered explicitly; in contrast to fully variational methods, the Hellmann-Feynman theorem cannot be used to calculate molecular properties. Secondly, local approximations for the energy tend to make the derivatives more complex. Compared with the multitude of local correlation schemes that have been proposed to calculate energies with MP2, coupled cluster and related methods, the development of analytical derivatives has been attempted less often.

Notably, Werner, Schütz and their co-workers developed analytical gradients for several PAO-based local correlation methods. Of particular relevance for the present work is their implementation of the local MP2 gradient.[89–91] Moreover, the gradient was developed for local variants of the excited state methods second-order approximate coupled cluster (CC2)[92, 93] and algebraic diagrammatic construction (ADC(2)).[94] Beyond MP2 as a ground state method, the gradient was explored for local quadratic configuration interaction with singles and doubles (QCISD).[95] Second-order magnetic properties have been implemented for PAO-based local MP2.[96–98]

Ochsenfeld and co-workers implemented the analytical gradient and NMR shieldings for their Laplace transform-based reduced scaling MP2 schemes.[99–101] Among fragmentation methods, analytical gradients were developed for the MP2 implementation in the divide-expand-consolidate framework,[102, 103] and most recently for the cluster-in-molecules MP2 scheme.[104] Electrostatic properties have been examined within the incremental scheme.[105, 106]

First-order properties can be calculated with DLPNO-CCSD in its closed-shell and open-shell variants using the orbital-unrelaxed density matrix.[107, 108] McAlexander and Crawford explored optical response properties by simulating the behaviour of coupled cluster with several truncation schemes including PNOs.[109]

As the major part of this thesis, the analytical gradient has been developed and im-

plemented for the closed-shell DLPNO-MP2 method. It is described in Chapter 3, which is based on our publications in ref. [110] and [111]. The accuracy of the gradient has been examined in an extensive set of benchmark calculations, and the performance is demonstrated with large-scale calculations. An important goal was to obtain the exact gradient of the DLPNO-MP2 energy, without omitting any contributions or introducing further approximations beyond those taken for the energy itself. The relevance of this approach is shown through calculations of the electric field gradient at atomic nuclei. Since well-converged localised orbitals are needed to calculate the gradient accurately, section 3.2.4 describes the implementation of a second-order method for orbital localisation. In addition, a method was introduced to eliminate singularities in the gradient caused by continuously degenerate localised orbitals.

Concurrently with our work, an approximate analytical gradient for PNO-MP2 was developed by Frank and Hättig.[112] Limitations in the latter work include the omission of PNO and OSV relaxation. To the best of our knowledge, our publications describing the DLPNO-MP2 gradient are the first account of an exact analytical gradient for any PNO-based method. Very recently, Yang and co-workers have reported the implementation of the analytical gradient for an OSV-based MP2 method.[113] While some of the algebraic details of their derivation differ from this work, it incorporates the relaxation of OSVs in a similar way.

In many cases, dispersion-corrected density functional theory (DFT) provides a superior accuracy to MP2 at a fraction of the cost.[114, 115] Empirical schemes building upon MP2 were developed such as spin-component scaled variants of MP2 (SCS-MP2),[116–118] or double-hybrid density functionals (DHDFs).[119, 120] Indeed, double-hybrids were shown to be consistently more accurate than lower DFT rungs for the energetics of main-group systems.[114, 121] They were also found to provide accurate results for molecular geometries,[122, 123] vibrational frequencies,[124] dipole moments[125] and nuclear magnetic resonance shifts.[126] Even though there exist exceptions such as hydrogen bonding, for which the vast majority of density functionals provide a worse description than MP2,[127] for the majority of applications double-hybrids are likely going to be the more

useful alternative. The implementation of DLPNO-MP2 and of its closed-shell gradient support spin-component scaling and double-hybrid density functionals, and some initial results for geometry optimisations with DHDFs are provided.

Chapter 2

Linear scaling second-order Møller-Plesset perturbation theory with pair natural orbitals

2.1 Theory

2.1.1 Orbital-invariant Møller-Plesset perturbation theory

Second-order Møller-Plesset perturbation theory is among the simplest methods to approximate the correlation energy, which is missing in the Hartree-Fock approach, and therefore it is explained in many general textbooks on quantum chemistry.[2, 128] This work is concerned primarily with the restricted closed-shell Hartree-Fock (RHF) formulation. The Hartree-Fock energy in terms of occupied spatial molecular orbitals i, j is given by the following expression:

$$E_{\mathrm{RHF}} = V_{\mathrm{NN}} + 2\sum_{i} h_{ii} + \sum_{ij} \left[2\,(ii|jj) - (ij|ij)\right], \tag{2.1}$$

V_{NN} is the repulsion energy between the nuclei, h_{pq} are matrix elements of the one-electron integrals in molecular orbital basis, and $(pq|rs)$ represent the two-electron repulsion in-

tegrals between real orbitals:

$$(pq|rs) = \int\int \frac{p(\mathbf{r}_1)q(\mathbf{r}_1)r(\mathbf{r}_2)s(\mathbf{r}_2)}{|\mathbf{r}_1 - \mathbf{r}_2|} d\mathbf{r}_1 d\mathbf{r}_2 \tag{2.2}$$

The ground state Slater determinant Φ_0, with the orbitals chosen to minimise the expectation value of the Hamiltonian $\langle\Phi_0|\hat{H}|\Phi_0\rangle$, is an eigenfunction of the Fock operator $\hat{F}$:

$$\begin{aligned} \hat{F} &= \sum_{pq} F_{pq}\hat{E}_{pq} \\ F_{pq} &= h_{pq} + \sum_{i} \left[2\,(ii|pq) - (ip|iq)\right] \end{aligned} \tag{2.3}$$

In this expression for closed-shell restricted orbitals, $\hat{E}_{pq}$ is the spin-adapted replacement operator $\hat{a}^\dagger_{p\alpha}\hat{a}_{q\alpha} + \hat{a}^\dagger_{p\beta}\hat{a}_{q\beta}$. Self-consistent field (SCF) programs usually produce canonical orbitals, which make the Fock matrix diagonal:

$$F_{pq} = \varepsilon_p \delta_{pq} \tag{2.4}$$

As the Slater determinant is invariant to unitary transformations among the orbitals that it is constructed from, other choices such as localised orbitals are equally valid solutions to the Hartree-Fock problem. Only the Fock matrix elements between occupied orbitals i and virtual orbitals a need to vanish,

$$F_{ia} = 0, \tag{2.5}$$

which is equivalent with the Brillouin theorem.

Møller-Plesset theory regards the Fock operator as describing an unperturbed system, and treats the difference between the actual Hamiltonian and the Fock operator as a perturbation,

$$\begin{aligned} &\left(\hat{H}^{(0)} + \hat{V}\right)\left(\Phi_0 + \Psi^{(1)} + \Psi^{(2)} + \dots\right) \\ &\qquad = \left(E^{(0)} + E^{(1)} + E^{(2)} + \dots\right)\left(\Phi_0 + \Psi^{(1)} + \Psi^{(2)} + \dots\right), \end{aligned} \tag{2.6}$$

where $\hat{H}^{(0)} = \hat{F}$ and $\hat{V} = \hat{H} - \hat{F}$. The energy contributions of different order are given by Rayleigh-Schrödinger perturbation theory:

$$\begin{aligned} E^{(0)} &= \langle \Phi_0 | \hat{H}^{(0)} | \Phi_0 \rangle \\ E^{(1)} &= \langle \Phi_0 | \hat{V} | \Phi_0 \rangle \\ E^{(2)} &= \langle \Phi_0 | \hat{V} | \Psi^{(1)} \rangle \\ &\vdots \end{aligned} \tag{2.7}$$

In these expressions the wave function is subject to intermediate normalisation, so that $\langle \Phi_0 | \Psi^{(m)} \rangle = 0$ for $m > 0$. The normalisation factor $1/\sqrt{N!}$ of an N-electron Slater determinant ensures that it satisfies $\langle \Phi_n | \Phi_n \rangle = 1$ by construction.

Provided that the orbitals are canonical, excited determinants $\Phi_{n>0}$ are eigenfunctions of the operator $\hat{F}$ with eigenvalues $E_n^{(0)}$, each of which is a sum of the respective spin orbital energies. This results in the following expression for the first-order perturbed wave function:

$$|\Psi^{(1)}\rangle = -\sum_{n>0} |\Phi_n\rangle \frac{\langle \Phi_n | \hat{V} | \Phi_0 \rangle}{E_n - E_0} \tag{2.8}$$

The zeroth-order energy is simply the sum of the energies of the restricted canonical orbitals,

$$E^{(0)} = \sum_i 2\varepsilon_i, \tag{2.9}$$

while the Hartree-Fock energy equals the total energy at first order:

$$E^{(0)} + E^{(1)} = E_{\mathrm{RHF}} \tag{2.10}$$

Finally, the second-order term is the well-known MP2 correlation energy for canonical orbitals:

$$E^{(2)} = -\sum_{ijab} \frac{(ia|jb)\left[2\,(ia|jb) - (ib|ja)\right]}{\varepsilon_a + \varepsilon_b - \varepsilon_i - \varepsilon_j} \tag{2.11}$$

If the orbitals are not canonical, the situation becomes more complicated. Since the Fock matrix $\mathbf{F}$ is not diagonal, the excited determinants $\Phi_{n>0}$ obtained by replacing any occupied orbitals with virtual ones are in general no eigenfunctions of $\hat{F}$. As a

consequence, Eqs. (2.8) and (2.11) cannot be used in conjunction with an arbitrary orbital basis.

Møller-Plesset perturbation theory can be reformulated in a more general form using the Hylleraas functional:[129]

$$E_2\left[\Psi\right] = 2\,\mathrm{Re}\left\langle \Psi \middle| \hat{V} - E^{(1)} \middle| \Phi_0 \right\rangle + \left\langle \Psi \middle| \hat{H}^{(0)} - E^{(0)} \middle| \Psi \right\rangle \tag{2.12}$$

Since the Hylleraas functional has been discussed in the literature,[2, 130] only its most relevant properties in the context of this work will be mentioned here. Evaluating E_2 with a function $\Psi = \Psi^{(1)} + \chi$ yields the second-order perturbed energy together with an additional term:

$$E_2\left[\Psi_n^{(1)} + \chi\right] = E^{(2)} + \left\langle \chi \middle| \hat{H}^{(0)} - E^{(0)} \middle| \chi \right\rangle \tag{2.13}$$

Crucially, the second term is positive with an arbitrary χ, and it only becomes zero if χ is proportional to the ground state determinant Φ_0, or in the trivial case $\chi = 0$.

This establishes a variational principle, permitting $\Psi^{(1)}$ and $E^{(2)}$ to be found in an arbitrary basis by minimising the value of the Hylleraas functional,

$$E_2\left[\Psi\right] \geq E^{(2)}, \tag{2.14}$$

yielding the actual value $E^{(2)}$ if and only if $\Psi = \Psi^{(1)}$ (provided that Ψ is orthogonal to Φ_0).

The first-order perturbed wave function will be parameterised in this work through doubly excited singlet configuration state functions, following the generator state formalism:[131]

$$\Psi^{(1)} = \sum_{i \geq j} \sum_{ab} T_{ab}^{ij} \Psi_{ij}^{ab} \quad \text{with} \quad \Psi_{ij}^{ab} = \frac{1}{1+\delta_{ij}} \hat{E}_{ai} \hat{E}_{bj} \Phi_0 \tag{2.15}$$

In addition, amplitudes with interchanged indices i, j are defined as

$$T_{ab}^{ji} = T_{ba}^{ij}. \tag{2.16}$$

As the set of functions Ψ_{ij}^{ab} is not orthogonal, it is advantageous to construct a dual basis $\tilde{\Psi}_{ij}^{ab}$, which forms a biorthogonal system together with Ψ_{ab}^{ij}. These contravariant configuration state functions have associated amplitudes $\tilde{T}_{ab}^{ij}$:

$$\tilde{T}_{ab}^{ij} = \frac{1}{1+\delta_{ij}} \left(4T_{ab}^{ij} - 2T_{ba}^{ij}\right) \tag{2.17}$$

A modification is made for the development of local correlation methods. Instead of exciting the electrons into a common set of virtual orbitals a, b, the virtual functions a_{ij}, b_{ij} are made specific to each occupied orbital pair i, j:

$$\Psi^{(1)} = \sum_{i \geq j} \sum_{a_{ij} b_{ij}} T_{a_{ij} b_{ij}}^{ij} \Psi_{ij}^{a_{ij} b_{ij}} \tag{2.18}$$

Pulay and Saebø provided an expression for the Hylleraas functional,[9] which is reproduced below in a form that is equivalent to their original work:

$$E_2 = \sum_{i \geq j} \sum_{a_{ij} b_{ij}} \left[2 \left(i a_{ij} | j b_{ij}\right) \tilde{T}_{a_{ij} b_{ij}}^{ij} + F_{a_{ij} b_{ij}} D_{a_{ij} b_{ij}}^{ij}\right] - \sum_{ij} F_{ij} D_{ij} \tag{2.19}$$

The equation contains the virtual orbital-unrelaxed pair-specific difference density contributions $D_{a_{ij} b_{ij}}^{ij}$,

$$D_{a_{ij} b_{ij}}^{ij} = \sum_{\tilde{c}_{ij} \tilde{d}_{ij}} \left[T_{a_{ij} c_{ij}}^{ij} S_{c_{ij} d_{ij}} \tilde{T}_{b_{ij} d_{ij}}^{ij} + T_{c_{ij} a_{ij}}^{ij} S_{c_{ij} d_{ij}} \tilde{T}_{d_{ij} b_{ij}}^{ij}\right], \tag{2.20}$$

and the occupied orbital-unrelaxed difference density contributions D_{ij} ,

$$D_{ij} = \sum_{k} (1 + \delta_{ik}) \sum_{a_{jk} b_{jk}} \sum_{c_{ki} d_{ki}} T_{a_{jk} b_{jk}}^{jk} S_{b_{jk} c_{ki}} \tilde{T}_{c_{ki} d_{ki}}^{ki} S_{d_{ki} a_{jk}}. \tag{2.21}$$

In order to calculate the MP2 energy via the Hylleraas functional, its minimum with respect to the amplitudes $\mathbf{T}^{ij}$ needs to be found. This results in a set of linear equations,

$$R_{a_{ij} b_{ij}}^{ij} = 0, \tag{2.22}$$

with the residual

$$R^{ij}_{a_{ij}b_{ij}} = (ia_{ij}|jb_{ij}) + \sum_{c_{ij}d_{ij}} F_{a_{ij}c_{ij}} T^{ij}_{c_{ij}d_{ij}} S_{d_{ij}b_{ij}} + \sum_{c_{ij}d_{ij}} S_{a_{ij}c_{ij}} T^{ij}_{c_{ij}d_{ij}} F_{d_{ij}b_{ij}} - \sum_{k} \left[F_{ik} \sum_{c_{kj}d_{kj}} S_{a_{ij}c_{kj}} T^{kj}_{c_{kj}d_{kj}} S_{d_{kj}b_{ij}} + F_{kj} \sum_{c_{ik}d_{ik}} S_{a_{ij}c_{ik}} T^{ik}_{c_{ik}d_{ik}} S_{d_{ik}b_{ij}} \right] . \quad (2.23)$$

Substituting the residual expression into the Hylleraas functional Eq. (2.19) leads to the equation

$$E_2 = \sum_{i \geq j} \sum_{a_{ij}b_{ij}} \left[(ia_{ij}|jb_{ij}) + R^{ij}_{a_{ij}b_{ij}} \right] \tilde{T}^{ij}_{a_{ij}b_{ij}}, \quad (2.24)$$

which simplifies accordingly for $E^{(2)}$ once $\mathbf{R}^{ij} = 0$ has been established.

2.1.2 Local MP2 in a basis of projected atomic orbitals

In their seminal contributions, Pulay and Saebø showed that a local MP2 method (LMP2) can be formulated using domains of projected atomic orbitals.[7, 9] The LMP2 method was greatly refined by Werner, Schütz and co-workers.[15] By combining the RI approximation for the two-electron integrals with local fitting, and introducing prescreening techniques, they created an efficient, linear scaling implementation.[19]

Redundant projected atomic orbitals (PAOs) are obtained as a projection of atomic basis functions μ onto the space of virtual orbitals:

$$|\tilde{\mu}'\rangle = N_{\tilde{\mu}'} \left[1 - \sum_{i} |i\rangle \langle i| \right] |\mu\rangle \quad (2.25)$$

In the space spanned by the atomic basis functions, $\sum_p |p\rangle \langle p|$ is the identity operator if p is a summation over all orbitals. Since the total number of PAOs is identical with the number of basis functions, but the space spanned is that of the virtual orbitals, the full set of PAOs is always linearly dependent. While unnormalised PAOs ($N_{\tilde{\mu}'} = 1$) are a common choice in the literature, for practical purposes we prefer to use a factor $N_{\tilde{\mu}'}$ that normalises the PAOs to one, $\langle \tilde{\mu}' | \tilde{\mu}' \rangle = 1$.

Numerous methods exist to obtain a local representation of occupied orbitals.[132–

135] Localising virtual orbitals, on the other hand, represents a substantial technical challenge, despite some recent progress.[12–14] PAOs have a local spatial extent, because the one-particle density matrix decays exponentially with the distance in extended systems with a band gap (Kohn's conjecture[136, 137]). Deriving from atomic basis functions, PAOs are formally associated with specific atoms. Each occupied orbital i is assigned a subset of PAOs $\tilde{\mu}'$ referred to as the domain $\{i\}$. Different domain construction schemes exist in the Literature, e.g. Boughton-Pulay domains,[23] which have been extended by Werner and co-workers with criteria based on bonding and interatomic distances.[138] The preceding implementation of DLPNO-CCSD employed criteria based on Mulliken populations and basis function coefficients of the PAOs.[37] Tew has recently published the principal domain scheme, which requires the computation of semicanonical MP2 densities.[139]

In this work we use the differential overlap (DOI) between occupied orbitals and PAOs:

$$\mathrm{DOI}_{i\tilde{\mu}'} = \sqrt{\int i^2(\mathbf{r})\tilde{\mu}'^2(\mathbf{r})d\mathbf{r}} \tag{2.26}$$

PAOs $\tilde{\mu}'$ are part of the domain of orbital i if the differential overlap $\mathrm{DOI}_{i\tilde{\mu}'}$ exceeds a predefined threshold T_{CutDO}. Moreover, if at least one PAO centred on a specific atom is member of a domain $\{i\}$, then all PAOs associated with the atom are included in the domain, even if the corresponding differential overlap integrals are below the threshold. An advantage of the differential overlap criterion is that it explicitly probes the interaction between the MOs and the virtual functions, unlike other criteria that only consider the extent of the MOs explicitly, and take the locality of the PAOs for granted.

Pair domains are defined for orbital pairs ij as the union of the respective orbital domains: $\{ij\} = \{i\} \cup \{j\}$. In a first step, the linearly dependent set of $\{ij\}$ member functions is transformed to a reduced set of linearly independent pair-specific functions, the non-redundant PAOs $\tilde{\mu}_{ij}$. To simplify the energy calculation, an orthogonal transformation is determined in a second step such that the non-redundant PAOs make the Fock matrix diagonal, $F_{\tilde{\mu}_{ij}\tilde{\nu}_{ij}} \rightarrow \varepsilon_{\tilde{\mu}_{ij}}\delta_{\tilde{\mu}_{ij}\tilde{\nu}_{ij}}$. In such a basis of pseudo-canonical non-redundant

PAOs with energies $\varepsilon_{\tilde{\mu}_{ij}}$, the residual equation (2.23) becomes:

$$R^{ij}_{\tilde{\mu}\tilde{\nu}} = (i\tilde{\mu}|j\tilde{\nu}) + \left[\varepsilon_{\tilde{\mu}} + \varepsilon_{\tilde{\nu}} - F_{ii} - F_{jj}\right] T^{ij}_{\tilde{\mu}\tilde{\nu}} - \sum_{k\neq i} F_{ik} \sum_{\tilde{\eta}\tilde{\lambda}} S_{\tilde{\mu}\tilde{\eta}} T^{kj}_{\tilde{\eta}\tilde{\lambda}} S_{\tilde{\lambda}\tilde{\nu}} - \sum_{k\neq j} F_{kj} \sum_{\tilde{\eta}\tilde{\lambda}} S_{\tilde{\mu}\tilde{\eta}} T^{ik}_{\tilde{\eta}\tilde{\lambda}} S_{\tilde{\lambda}\tilde{\nu}} \quad (2.27)$$

For simplicity, the subscripts ij have been dropped. Non-redundant PAOs belonging to the same orbital pair are orthogonal, $S_{\tilde{\mu}_{ij}\tilde{\nu}_{ij}} = \delta_{\tilde{\mu}_{ij}\tilde{\nu}_{ij}}$, but among functions belonging to different pairs there is generally a non-vanishing overlap, which leads to the sum over k in Eq. (2.27).

A local RI approximation is employed in DLPNO-MP2. The two-electron integrals are factorised with an auxiliary basis set as:

$$(i\tilde{\mu}|j\tilde{\nu}) = \sum_{KL} (i\tilde{\mu}|K) \left(\mathbf{V}^{-1}\right)_{KL} (L|j\tilde{\nu}) \quad (2.28)$$

As an additional approximation, the sum over auxiliary functions K, L is restricted to the respective fitting domain: $K, L \in \{ij\}_{\mathrm{RI}}$. In DLPNO-MP2, a fitting domain $\{i\}_{\mathrm{RI}}$ includes auxiliary functions from all atoms that have a Mulliken population for orbital i above a threshold T_{CutMKN}. Fitting pair domains are constructed as unions of the respective domains for individual orbitals: $\{ij\}_{\mathrm{RI}} = \{i\}_{\mathrm{RI}} \cup \{j\}_{\mathrm{RI}}$.

2.1.3 Local MP2 in a basis of pair natural orbitals

While 98 % of the total correlation energy can typically be reproduced with PAOs from as few as four to six atoms per localised orbital,[23] domains containing ca. 20-30 atoms are usually needed to recover 99.9 %. With a triple-zeta basis set, this corresponds to around 1000 PAOs. Compared with the simpler energy equation for canonical MP2, evaluating Eq. (2.27) leads to a too high cost. This expense can be reduced considerably using pair natural orbitals (PNOs), as has also been proposed by Werner and co-workers while this work was underway.[55]

By neglecting off-diagonal Fock matrix elements $F_{i\neq j}$ in Eq. (2.27), approximate am-

plitudes $\breve{T}^{ij}_{\tilde{\mu}\tilde{\nu}}$ can be evaluated through a straightforward analytic expression:

$$\breve{T}^{ij}_{\tilde{\mu}\tilde{\nu}} = -\frac{(i\tilde{\mu}|j\tilde{\nu})}{\varepsilon_{\tilde{\mu}} + \varepsilon_{\tilde{\nu}} - F_{ii} - F_{jj}} \tag{2.29}$$

This is referred to as the semicanonical approximation: the pseudo-canonical, non-redundant PAOs diagonalise the Fock matrix, while the Fock matrix projection onto the localised occupied orbitals is generally non-diagonal. However, the off-diagonal elements are typically at least an order of magnitude smaller than those on the diagonal. These amplitudes are used to construct the semicanonical virtual pair density $\breve{\mathbf{D}}^{ij}$:

$$\breve{\mathbf{D}}^{ij} = \breve{\mathbf{T}}^{ij\dagger}\tilde{\breve{\mathbf{T}}}^{ij} + \breve{\mathbf{T}}^{ij}\tilde{\breve{\mathbf{T}}}^{ij\dagger} \tag{2.30}$$

Diagonalisation of this pair density yields approximate PNOs $\bar{d}^{ij}_{\tilde{\mu}\tilde{a}_{ij}}$:

$$\breve{\mathbf{D}}^{ij}\bar{\mathbf{d}}^{ij} = n_{\tilde{a}_{ij}}\bar{\mathbf{d}}^{ij} \tag{2.31}$$

If only those pair natural orbitals with an associated eigenvalue exceeding a truncation threshold are retained, $n_{\tilde{a}_{ij}} > T_{\mathrm{CutPNO}}$, this leads to a rapidly converging expansion of the virtual space for each orbital pair.[33] In this truncated basis, the residual equation (2.27) becomes:

$$\begin{aligned} R^{ij}_{\tilde{a}\tilde{b}} = \left(i\tilde{a}\middle|j\tilde{b}\right) + \left[\varepsilon_{\tilde{a}} + \varepsilon_{\tilde{b}} - F_{ii} - F_{jj}\right] T^{ij}_{\tilde{a}\tilde{b}} \\ - \sum_{k\neq i} F_{ik} \sum_{\tilde{c}\tilde{d}} S_{\tilde{a}\tilde{c}} T^{kj}_{\tilde{c}\tilde{d}} S_{\bar{d}\tilde{b}} - \sum_{k\neq j} F_{kj} \sum_{\tilde{c}\tilde{d}} S_{\tilde{a}\tilde{c}} T^{ik}_{\tilde{c}\tilde{d}} S_{\bar{d}\tilde{b}} \end{aligned} \tag{2.32}$$

With the converged amplitudes, the energy of the Hylleraas functional in PNO basis is given by a simple expression:

$$E_{\text{DLPNO-MP2}} = \sum_{i\geq j}\sum_{\tilde{a}\tilde{b}} \left(i\tilde{a}\middle|j\tilde{b}\right) \tilde{T}^{ij}_{\tilde{a}\tilde{b}} \tag{2.33}$$

In analogy to previous work,[33] the correlation energy contains a correction ΔE_{PNO}

for PNO truncation. It is determined as the energy change that results from a direct projection of the semicanonical amplitudes to the truncated pair natural orbital basis:

$$\Delta E_{\mathrm{PNO}} = \sum_{i \geq j} \left[\sum_{\tilde{\mu}\tilde{\nu}} (i\tilde{\mu}|j\tilde{\nu})\, \tilde{\tilde{T}}^{ij}_{\tilde{\mu}\tilde{\nu}} - \sum_{\tilde{a}\tilde{b}} \left(i\tilde{a} \middle| j\tilde{b} \right) \tilde{\tilde{T}}^{ij}_{\tilde{a}\tilde{b}} \right] \tag{2.34}$$

The largest part of the computational effort to solve Eq. (2.32) is expended upon the sum over k. Therefore, it is beneficial to skip small contributions if the magnitude of the occupied Fock matrix elements, $|F_{ik}|$ or $|F_{kj}|$, is below a cutoff F_{Cut}, as was done in ref. [15]. Even though the cost to evaluate the residual equation (2.32) would become formally linear scaling in the asymptotic limit if orbital pairs are prescreened, additionally skipping terms with small Fock matrix elements can lead to an earlier onset of linear scaling. An attempt to reduce the computational effort for the summation term with a second, more aggressively truncated set of PNOs did not lead to satisfactory results.

2.1.4 Prescreening of orbital pairs

As the total number of orbital pairs grows quadratically with system size, an overall linear scaling of the method can only be achieved if the number of pairs that make a relevant contribution to the energy is proportional to the size of the system. The first published implementation of DLPNO-CCSD included a quadratically scaling prescreening procedure with a very small prefactor of the computational cost function, which eliminates a large number of electron pairs before entering expensive integral generation routines.[37]

Energies of pairs were estimated using the following equation:

$$\varepsilon_{ij}^{\mathrm{OSV-DIP}} = -\frac{8}{|\mathbf{R}^{ij}|^6} \sum_{\tilde{a}_i \tilde{b}_j} \frac{\left[\langle i|\mathbf{r}|\tilde{a}_i\rangle \, \langle j|\mathbf{r}|\tilde{b}_j\rangle \right]^2}{\varepsilon_{\tilde{a}_i} + \varepsilon_{\tilde{b}_j} - F_{ii} - F_{jj}} \tag{2.35}$$

$$\mathbf{R}^{ij} = \langle i|\mathbf{r}|i\rangle - \langle j|\mathbf{r}|j\rangle \tag{2.36}$$

It was assumed that the semicanonical approximation is sufficiently accurate for screening purposes. For each orbital i, a truncated virtual space was spanned using pseudo-

canonical orbital-specific virtuals $\tilde{a}_i$ (OSVs) with energies $\varepsilon_{\tilde{a}_i}$. The concept of OSVs had been introduced previously by Chan and co-workers.[39] Integrals $\left(i\tilde{b}_j\middle|j\tilde{a}_i\right)$ were ignored based on the assumption that the truncated OSVs are located near their associated orbitals, and therefore the overlap with other distant occupied orbitals may be ignored. Most crucially, the two-electron integrals $\left(i\tilde{a}_i\middle|j\tilde{b}_j\right)$ were approximated using dipole integrals, which permitted a very fast evaluation of the expression. $\mathbf{R}^{ij}$ represents the distance vector between the centres of orbitals i and j. Orbital pairs were discarded if their estimated energy was below a specified theshold, commonly set to $1\,\mu E_\mathrm{h}$, and a contribution $\varepsilon_{ij}^{\mathrm{OSV-DIP}}$ was added for each omitted pair. Multipole-based approximations for prescreening purposes had already been discussed in earlier work by Werner and co-workers.[140]

We have observed, however, that Eq. (2.35) sometimes considerably underestimates the actual local MP2 energy even of the most distant orbital pairs. This may lead to neglect of pairs that ought to be treated at MP2 level. Therefore, Eq. (2.35) is replaced with a a more complete expression,

$$\varepsilon_{ij}^{\mathrm{DIP}} = -4 \sum_{\tilde{\mu}_i \tilde{\nu}_j} \frac{\left(M_{\tilde{\mu}_i \tilde{\nu}_j}^{ij}\right)^2}{\varepsilon_{\tilde{\mu}_i} + \varepsilon_{\tilde{\nu}_j} - F_{ii} - F_{jj}}, \tag{2.37}$$

where $M_{\tilde{\mu}_i \tilde{\nu}_j}^{ij}$ is the proper dipole approximation for the electrostatic interaction between the charge distributions $|i\tilde{\mu}_i\rangle$ and $|j\tilde{\nu}_j\rangle$:

$$M_{\tilde{\mu}\tilde{\nu}}^{ij} = \frac{\mathbf{r}^{i\tilde{\mu}}\mathbf{r}^{j\tilde{\nu}}}{\left|\mathbf{R}^{ij}\right|^3} - 3\frac{\left(\mathbf{r}^{i\tilde{\mu}}\mathbf{R}^{ij}\right)\left(\mathbf{r}^{j\tilde{\nu}}\mathbf{R}^{ij}\right)}{\left|\mathbf{R}^{ij}\right|^5} \quad \text{with} \quad \mathbf{r}^{i\tilde{\mu}} = \langle i|\mathbf{r}|\tilde{\mu}\rangle \tag{2.38}$$

For simplicity, the orbital subscripts of the virtual functions have been dropped. $\mathbf{r}^{i\tilde{\mu}}$ is a shorthand notation for the corresponding dipole integrals. Since the overlap of the occupied functions $|i\rangle$ and the virtual functions $|\tilde{\mu}_i\rangle$ is zero, the product $|i\tilde{\mu}_i\rangle$ does not have a net charge, and the dipole moment is, in general, the lowest non-vanishing multipole moment.

Instead of OSVs, Eq. (2.37) uses non-redundant pseudo-canonical PAOs $\tilde{\mu}$ to span the

virtual space. The necessary domains $\{i\}$ for prescreening may be smaller than those for the subsequent local MP2 calculations, and are constructed using a threshold T_{CutDOPre}. Circumventing the construction of OSVs, which are generated as PNOs for pairs $i = j$, is more efficient in this context.

As will be shown in Section 2.3.2, Eq. (2.37) converges correctly for the most distant pairs, but the energy of many pairs around 1 μE_{h} is still underestimated considerably. For orbitals that are not very far away from each other, the dipole approximation may not be sufficient to estimate pair energies: first, higher multipole moments become significant and second, the assumption of non-overlapping charge distributions may break down.

It is a viable option to incorporate higher moments into pair prescreening.[140, 141] We have, however, implemented the following refined procedure that uses only dipole integrals:

1. Pairs of occupied orbitals should only be screened out if the spatial distributions of their probability densities are almost non-overlapping. The first criterion is based on the differential overlap of the orbitals DOI_{ij}:

$$\mathrm{DOI}_{ij} = \sqrt{\int i^2(\mathbf{r}) j^2(\mathbf{r}) d\mathbf{r}} \tag{2.39}$$

   Pairs are not excluded from the subsequent MP2 calculation unless DOI_{ij} is below the threshold T_{CutDOij}. Section 2.3.2 demonstrates that the dipole estimate of the energy $\varepsilon_{ij}^{\mathrm{DIP}}$ becomes increasingly reliable for pairs with a small differential overlap of the localised MOs.

2. The dipole approximation may underestimate a pair energy because of an accidental orthogonality of the dipole moments. Therefore, we compute an upper bound to the interaction energy by assuming collinear orientation, which maximises the interaction energy as a function of the angle:

$$\varepsilon_{ij}^{\mathrm{COL}} = -\frac{16}{|\mathbf{R}^{ij}|^6} \sum_{\tilde{\mu}\tilde{\nu}} \frac{|\langle i|\mathbf{r}|\tilde{\mu}\rangle|^2 \, |\langle j|\mathbf{r}|\tilde{\nu}\rangle|^2}{\varepsilon_{\tilde{\mu}} + \varepsilon_{\tilde{\nu}} - F_{ii} - F_{jj}} \tag{2.40}$$

In order to screen a pair out, this upper boundary estimate needs to be below the threshold T_{CutPre}.

3. If both criteria $\mathrm{DOI}_{ij} < T_{\mathrm{CutDOij}}$ and $\left|\varepsilon_{ij}^{\mathrm{COL}}\right| < T_{\mathrm{CutPre}}$ are fulfilled simultaneously, the pair does not become subject to a more accurate treatment at the MP2 level. Instead, its energy is estimated using $\varepsilon_{ij}^{\mathrm{DIP}}$ as defined in Eq. (2.37).

2.1.5 Sparse maps

2.1.5.1 Sparsity relationships

All reduced scaling algorithms take advantage of sparsity in some way; specifically, this may mean avoiding storage of matrix elements below a given tolerance, or skipping terms in computations that are deemed to make a negligible contribution to the result. Computer code that exploits sparsity tends to be more complex, and therefore also more error prone and difficult to maintain. In order to simplify both the discussion and the implementation of such sparsity relationships, this section formalises concepts and provides a well-defined framework for discussion.

The first type of sparsity that we define is *additive sparsity*, which arises when a function is expanded as a linear combination of other functions, e.g. an MO $|i\rangle$ that is expressed in a basis of atomic orbitals $|\mu\rangle$:

$$|i\rangle = \sum_{\mu} c_{\mu i} \, |\mu\rangle \tag{2.41}$$

A sparse matrix $\mathbf{c}$ will have a non-negligible number of elements with a magnitude below a given tolerance threshold ε. For example, if $|i\rangle$ represents a localised molecular orbital, then the basis set coefficients will take smaller values in its tails. Indices $|c_{\mu i}| > \varepsilon$ exceeding the tolerance threshold are collected in a sparse map $\mathbf{L}\,(i \to \mu)$ generated by the matrix $\mathbf{c}$. The sparse map is a set of lists,

$$\mathbf{L}\,(i \to \mu) = \{\, L\,(i_1 \to \mu)\,, L\,(i_2 \to \mu)\,, \dots \}\,, \tag{2.42}$$

with each list representing the sparsity relationship between a given function $|i\rangle$ and the indices of its non-vanishing basis set coefficients:

$$L\left(i \rightarrow \mu\right) = \left\{ \mu_n : \mid c_{\mu_n i}| > \varepsilon \right\} \tag{2.43}$$

In this regard, a map that encodes additive sparsity is related to the compressed sparse row or compressed column format.[142]

The second type of sparsity that we define is *multiplicative sparsity*, which may exist between functions f and g occurring in products $f \cdot g$. This can be demonstrated for the Coulomb integrals $\mathbf{J}$ and exchange integrals $\mathbf{K}$:

$$J_{\mu\nu} = \sum_{\eta\lambda} P_{\eta\lambda} \left(\mu\nu|\eta\lambda\right) \tag{2.44}$$

$$K_{\mu\eta} = \sum_{\nu\lambda} P_{\nu\lambda} \left(\mu\nu|\eta\lambda\right) \tag{2.45}$$

Multiplicative sparsity is generated by the products of the local functions $\mu(\mathbf{r})\nu(\mathbf{r})$ and $\eta(\mathbf{r})\lambda(\mathbf{r})$, that decline rapidly with the distance of the respective atomic centres. The asymptotically exponential decay of the density matrix $\mathbf{P}$ with distance also generates a sparsity relationship, which would make construction of the exchange matrix linear scaling in principle (although this is not reached in actual implementations).[143] Efficient schemes for exchange evaluation make use of such sparsity relationships, for example the LinK[144] and COSX[145] algorithms.

Two-electron integrals in atomic orbital basis $(\mu\nu|\eta\lambda)$ are commonly screened using the Schwarz criterion,[146] which in itself reduces the number of integrals from $O(N^4)$ to $O(N^2)$:

$$|(\mu\nu|\eta\lambda)| \leq \sqrt{(\mu\nu|\mu\nu)\,(\eta\lambda|\eta\lambda)} \tag{2.46}$$

More elaborate screening techniques have also been discussed. Gill and co-workers investigated additional criteria based on Hölder's inequality with a different partitioning of the two-electron integrals.[147] The multipole-based QQR criterion was suggested by Ochsenfeld and co-workers.[148, 149]

The number of all possible target RI integrals $(i\tilde{\mu}'|K)$ scales as $O(N^3)$ with system size, and the required number of operations to perform a transformation from the initial AO basis integrals $(\mu\nu|K)$ grows as $O(N^4)$. In order to construct an algorithm that scales linearly, it is clearly necessary to reduce both the number of integrals and the number of operations needed to $O(N)$. The Schwarz inequality is not suited to screen the required set of transformed integrals $(i\tilde{\mu}'|K)$, as it requires the computation of $(i\tilde{\mu}'|i\tilde{\mu}')$. However, a sparsity relationship between the localised MOs i and the redundant PAOs $\tilde{\mu}'$ is generated by the differential overlap $\mathrm{DOI}_{i\tilde{\mu}'}$, which has been defined in Eq. (2.26) to determine domains. The differential overlap determines if the two functions have got sufficiently large values in a joint region of space. Moreover, ref. [43] shows numerically that the DOI approximates the equivalent Schwarz prescreening integral, usually underestimating the latter by up to an order of magnitude:

$$\sqrt{\int i^2(\mathbf{r})\tilde{\mu}'^2(\mathbf{r})d\mathbf{r}} \approx \sqrt{(i\tilde{\mu}'|i\tilde{\mu}')} \tag{2.47}$$

The DOI criterion $\mathrm{DOI}_{i\tilde{\mu}'} > \varepsilon$ therefore generates a sparse map $\mathbf{L}\,(i \to \tilde{\mu}')$. Unlike the Schwarz integrals, however, the DOI can be calculated in a linear scaling prodecure by numerical integration on a grid, as shown in ref. [43].

2.1.5.2 Operations on sparse maps

In order to construct algorithms using sparse maps, it is necessary to define general operations that can be performed using maps:

- *Inversion* of a sparse map $\mathbf{L}\,(f \to g)$ creates a map $\mathbf{L}\,(g \to f) = \mathbf{L}^{-1}\,(f \to g)$. The inverted sparse list $L\,(g_i \to f)$ contains element f_k if and only if the original sparse list $L\,(f_k \to g)$ contains g_i:

$$\begin{aligned} \mathbf{L}\,(g \to f) &= \mathbf{L}^{-1}\,(f \to g) \\ L\,(g_i \to f) &= \{\, f_k : g_i \in L\,(f_k \to g)\,\} \end{aligned} \tag{2.48}$$

- A *union* can be made, firstly, between two different sparse maps that address the

same function space. Secondly, a union can be made between sparse lists that are part of the same map. In the latter case, elements are included in the united list if they are in any of the original lists:

$$L\left(f_i \to g\right) \cup L\left(f_j \to g\right) = \left\{\, g_k : g_k \in L\left(f_i \to g\right) \vee g_k \in L\left(f_j \to g\right) \right\} \tag{2.49}$$

- An *intersection* is defined analogously to the union. Only elements that are members of both lists in question are retained:

$$L\left(f_i \to g\right) \cap L\left(f_j \to g\right) = \left\{\, g_k : g_k \in L\left(f_i \to g\right) \wedge g_k \in L\left(f_j \to g\right) \right\} \tag{2.50}$$

- *Chaining* two maps $\mathbf{L}\left(f \to g\right)$ and $\mathbf{L}\left(g \to h\right)$ creates a third map $\mathbf{L}\left(f \to h\right)$. In the chained map $\mathbf{L}\left(f \to h\right)$, a given element h_l is included if and only if there is a g_k in the sparse list $L\left(f_i \to g\right)$ which in turn connects to h_l in the list $L\left(g_k \to h\right)$:

$$\begin{aligned} \mathbf{L}\left(f \to h\right) &= \mathbf{L}\left(f \to g\right) \circ \mathbf{L}\left(g \to h\right) \\ L\left(f_i \to h\right) &= \left\{\, h_l : \exists g_k \colon g_k \in L\left(f_i \to g\right) \wedge h_l \in L\left(g_k \to h\right) \right\} \end{aligned} \tag{2.51}$$

Further operations will be needed that are specific to basis functions, shells or atoms:

- *Contraction.* When constructing maps for functions that can be assigned to particular atoms, for example for basis functions or PAOs, it is often desirable to include all functions for contributing atoms. The differential overlap criterion $\mathrm{DOI}_{i\tilde{\mu}'}$ alone likely generates a map $\mathbf{L}\left(i \to \tilde{\mu}'\right)$ that includes a subset of PAOs from each atom in each list. On the other hand, domains in DLPNO-MP2 contain all PAOs from atom A if the differential overlap criterion is exceeded for at least one of its functions. Formally, such a contraction can be made using the following chain of maps, with $L\left(A \to \tilde{\mu}'\right)$ representing the list of PAOs for a given atom:

$$\mathbf{L}\left(i \to \tilde{\mu}'_{\mathrm{A}}\right) = \mathbf{L}\left(i \to \tilde{\mu}'\right) \circ \mathbf{L}^{-1}\left(A \to \tilde{\mu}'\right) \circ \mathbf{L}\left(A \to \tilde{\mu}'\right) \tag{2.52}$$

The functions g in the map $\mathbf{L}(f \rightarrow g_{\mathrm{A}})$ are said to be contracted to atoms. Likewise, one can define a contraction to shells, $\mathbf{L}(f \rightarrow g_{\mathrm{S}})$, which includes all member functions g of a shell if at least one function from the same shell is contained in the original map $\mathbf{L}(f \rightarrow g)$.

- An *expansion* is similar to a contraction, meaning that all functions f belonging to atom A are assigned an identical mapping to functions g:

$$\mathbf{L}(f_{\mathrm{A}} \rightarrow g) = \mathbf{L}^{-1}(A \rightarrow f) \circ \mathbf{L}(A \rightarrow f) \circ \mathbf{L}(f \rightarrow g) \tag{2.53}$$

  As above, $L(A \rightarrow f)$ is a list of functions f for atom A. In a map $\mathbf{L}(f_{\mathrm{A}} \rightarrow g)$ expanded to atoms, each sparse list is the union of the original lists $L(f \rightarrow g)$ for functions f belonging to the same atom. Similarly, a map $\mathbf{L}(f_{\mathrm{S}} \rightarrow g)$ expanded to shells combines lists belonging to functions of the same shell.

  Contractions and expansions can be combined: in the sparse map $\mathbf{L}(f_{\mathrm{A}} \rightarrow g_{\mathrm{A}})$, all functions f belonging to the same atom are expanded to have identical sparse lists, and each list is contracted to include all functions g from a given atom.

2.1.6 Linear scaling RI integral transformation

In order to compute the RI-MP2 energy, it is necessary to calculate the RI integrals $(ia|K)$. Naturally, the number of such integrals scales as $O(N^3)$ with the system size, and the transformation from the basis function integrals $(\mu\nu|K)$ requires a computational effort scaling as $O(N^4)$. The simplest approach to generate the integrals $(i\tilde{\mu}'|K)$ for the DLPNO-MP2 method is to pre-calculate integrals for all combinations of MOs i, PAOs $\tilde{\mu}'$ and auxiliary functions K in the beginning, and to access each subset of integrals that is needed for any particular orbital pair during the calculation. As for RI-MP2, however, the storage effort and the number of instructions scale as $O(N^3)$ and $O(N^4)$ with system size, respectively. It is necessary to introduce a modified procedure achieving an overall linear scaling of the method, as the transformation can become a bottleneck for calculations with hundreds of atoms.

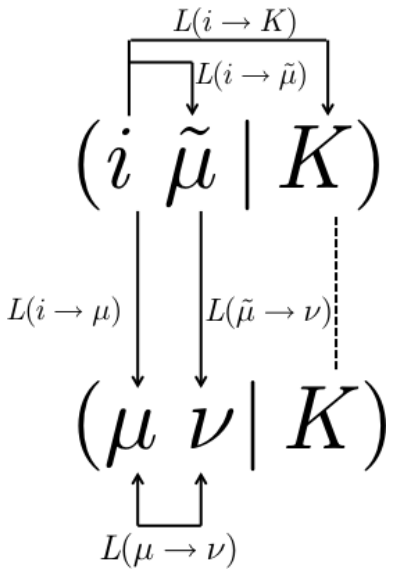

Figure 2.1: Illustration of the sparsity relationships for the transformation of the three-index integrals.

The RI integrals are given by the equation

$$(i\tilde{\mu}'|K) = \sum_{\nu\eta} c_{\nu i} \tilde{P}_{\eta\tilde{\mu}'} \, (\nu\eta|K) \, , \tag{2.54}$$

and the first step in the transformation is to generate integrals $(\nu\eta|K)$ for each auxiliary function K at a time (or, in practice, for entire shells of auxiliary functions at once). One index is transformed to the occupied localised MO basis first, $(\nu\eta|K) \to (i\eta|K)$, and the other index is transformed to the redundant PAO basis second, $(i\eta|K) \to (i\tilde{\mu}'|K)$. These transformation steps are usually implemented as matrix multiplications, for which highly optimised computational routines are available. With the number of auxiliary functions growing linearly in system size, it is necessary to ensure that the number of integrals and the number of operations per auxiliary function remains constant in the asymptotic limit. We refer to this relatively straightforward, but important principle as the linked index rule.

Figure 2.1 illustrates the sparse maps that are relevant in the context of the integral transformation. Between the MOs and the atomic basis functions there is an additive sparsity relation $\mathbf{L}\,(i \to \mu)$, which can be generated through the coefficient matrices of the localised MOs. Analogously, there is an additive sparsity relation between the redundant PAOs $\tilde{\mu}'$ and the basis functions ν, $\mathbf{L}\,(\tilde{\mu}' \to \nu)$, encoded through the PAO coefficient matrix $\tilde{P}_{\nu\tilde{\mu}'}$. Both maps are contracted to atoms, and the PAOs are expanded in addition,

expressed as $\mathbf{L}\,(i \to \mu_{\mathrm{A}})$ and $\mathbf{L}\,(\tilde{\mu}'_{\mathrm{A}} \to \nu_{\mathrm{A}})$.

The multiplicative sparse maps $\mathbf{L}\,(i \to \tilde{\mu}')$ are generated by the differential overlap integrals $\mathrm{DOI}_{i\tilde{\mu}'}$, and in addition the PAOs are contracted to atoms, $\mathbf{L}\,(i \to \tilde{\mu}'_{\mathrm{A}})$. Fitting domains of auxiliary functions $\{i\}_{\mathrm{RI}}$ are determined using the Mulliken populations of each orbital i. Hence, the Mulliken populations of the orbitals generate a sparsity relationship $\mathbf{L}\,(i \to K_{\mathrm{A}})$. The auxiliary functions are contracted to atoms by construction.

If suitable linked index relationships have been established that connect K to the atomic basis functions μ and ν, truncating the map $\mathbf{L}\,(\mu \to \nu)$ is not necessary to achieve linear scaling. It can, however, reduce the computational prefactor by eliminating integrals $(\mu\nu|K)$ that are close to zero. The first implementation of DLPNO-MP2 as published in ref. [43] did not truncate the sparse map $\mathbf{L}\,(\mu \to \nu)$. However, a subsequently improved version of the code exploits this sparsity relationship through Schwarz prescreening. As a multiplicative relation it could also be generated by a differential overlap criterion $\mathrm{DOI}_{\mu\nu}$, but in this case it is not necessary to replace the well-established and efficient Schwarz screening.

Clearly, the sparse lists $L\,(i \to \tilde{\mu}')$ and $L\,(i \to K)$, which are identical with the respective domains $\{i\}$ and $\{i\}_{\mathrm{RI}}$, do not represent the complete set of three-index integrals that are needed for a given orbital i: integrals $(i\tilde{\nu}'|j\tilde{\mu}')$ would be neglected for pair domains $\{ij\}$ if $\tilde{\nu}'$ is a member of $\{j\}$, but not of $\{i\}$. The same problem would also apply to the auxiliary functions. On the other hand, it may be assumed that such integrals indeed become negligible if the PAOs in the respective domains $\{i\}$ and $\{j\}$ are sufficiently far apart. One could generate maps $\mathbf{L}_2\,(i \to \tilde{\mu}')$ using a secondary threshold T_{CutDO2}, which is substantially tighter than domain threshold T_{CutDO}: $T_{\mathrm{CutDO2}} < T_{\mathrm{CutDO}}$. This would establish a linked index relationship, which exploits multiplicative sparsity by neglecting only sufficiently small integrals with little impact on the overall accuracy. Indeed, this reasoning was the original motivation behind introducing the differential overlap into the sparse map infrastructure. In practice, this concept was not successful: every cutoff T_{CutDO2} that neglected any RI integrals used in the subsequent DLPNO-MP2 calculation led to entirely uncontrollable errors in the energy. This does not rule out that a very tight

threshold could in principle be used successfully in very large systems, but calculations under realistic circumstances can only be performed if *all* integrals are calculated.

A *map extension* needs to be performed to obtain maps that encode all required integrals:

$$L_{\text{ext}}\left(i \to \tilde{\mu}'\right) = L\left(i \to j\right) \circ \mathbf{L}\left(j \to \tilde{\mu}'\right) \tag{2.55}$$

$$L_{\text{ext}}\left(i \to K\right) = L\left(i \to j\right) \circ \mathbf{L}\left(j \to K\right) \tag{2.56}$$

In the equations (2.55) and (2.56), $\mathbf{L}\left(i \to j\right)$ represents the orbital pairs that remain after prescreening. Therefore, the extended map $L_{\text{ext}}\left(i \to \tilde{\mu}'\right)$ contains the unions of the domain $\{i\}$ with domains $\{j\}$ for all remaining orbital pairings $L\left(i \to j\right)$ of i.

Without screening of orbital pairs, each list $L_{\text{ext}}\left(i \to \tilde{\mu}'\right)$ would simply contain the complete set of redundant PAOs $\tilde{\mu}'$ in the system, and $L_{\text{ext}}\left(i \to K\right)$ the complete set of auxiliary functions. Only those PAOs or auxiliary functions that are not connected to any orbitals in the system would be excluded. The latter sometimes occurs if the system contains ghost atoms, for example in counterpoise-corrected calculations.

DLPNO-MP2 calculations are performed with pair prescreening, so that each orbital i is only paired with other sufficiently close localised orbitals j. Since the extended lists $L_{\text{ext}}\left(i \to \tilde{\mu}'\right)$ and $L_{\text{ext}}\left(i \to K\right)$ represent an asymptotically constant number of indices $\tilde{\mu}'$ and K, the total number of integrals becomes proportional to the number of orbitals i, thus scaling linearly with system size.

The integral transformation according to Eq. (2.54) is performed via matrix multiplications, and it is driven by auxiliary functions. For each function K, the complete blocks of MOs and PAOs are given by the following maps:

$$\mathbf{L}\left(K \to i\right) = \mathbf{L}_{\text{ext}}^{-1}\left(i \to K_{\text{A}}\right) \tag{2.57}$$

$$\mathbf{L}\left(K \to \tilde{\mu}'\right) = \mathbf{L}_{\text{ext}}^{-1}\left(i \to K_{\text{A}}\right) \circ \mathbf{L}_{\text{ext}}\left(i \to \tilde{\mu}'_{\text{A}}\right) \tag{2.58}$$

Because of the chaining in Eq. (2.58), the map $\mathbf{L}\left(K \to \tilde{\mu}'\right)$ may contain some combinations of auxiliary functions and PAOs that are not needed in the actual integrals, but

this does not change the scaling.

The additive sparsity relationship between localised MOs or PAOs and the respective basis functions permits some basis function coefficients to be truncated. For each auxiliary function K, there is one block of AOs μ that are transformed to MO basis, and one different block of AOs ν that are transformed to redundant PAOs. These blocks are determined by the following chained map:

$$\mathbf{L}\left(K \to \mu^{\mathrm{MO}}\right) = \mathbf{L}_{\mathrm{ext}}^{-1}\left(i \to K_{\mathrm{A}}\right) \circ \mathbf{L}\left(i \to \mu_{\mathrm{A}}\right) \tag{2.59}$$

$$\mathbf{L}\left(K \to \nu^{\mathrm{PAO}}\right) = \mathbf{L}_{\mathrm{ext}}^{-1}\left(i \to K_{\mathrm{A}}\right) \circ \mathbf{L}_{\mathrm{ext}}\left(i \to \tilde{\mu}'_{\mathrm{A}}\right) \circ \mathbf{L}\left(\tilde{\mu}'_{\mathrm{A}} \to \nu_{\mathrm{A}}\right) \tag{2.60}$$

The "MO" and "PAO" superscripts have been introduced to distinguish between the respective spaces that the AOs span. A threshold T_{CutC} is used to truncate basis set coefficients with $|c_{\mu i}| < T_{\mathrm{CutC}}$ for MOs or $|\tilde{P}_{\nu\tilde{\mu}'}| < T_{\mathrm{CutC}}$ for PAOs.

Eqs. (2.59) and (2.60) yield superblocks of atomic orbitals that are much larger than the individual lists $L\left(i \to \mu_{\mathrm{A}}\right)$ or $L\left(\tilde{\mu}'_{\mathrm{A}} \to \nu_{\mathrm{A}}\right)$. This raises the question if it would not be preferable to sacrifice large matrix multiplications in favour of retaining smaller AO blocks, which would result in fewer arithmetic operations and a substantially reduced number of integrals $(\mu\nu|K)$ that need to be computed. However, Section 2.3.3 will show that basis function coefficients need to be truncated very conservatively, which justifies using these very large maps.

2.2 Implementation

The DLPNO-MP2 method was implemented as part of the ORCA quantum chemistry package.[35, 36] An outline of the computational steps in a DLPNO-MP2 calculation is provided by the scheme in Algorithm 1. The first step is a localisation of the occupied orbitals. In this work we performed all calculations with Foster-Boys orbitals,[132, 133] however, any type of suitable localised orbitals can be used in principle. As pointed out by Bistoni and co-workers, in practice it is necessary to use different PNO truncation thresholds for pairs of valence orbitals and for pairs of core orbitals.[150] We elaborate

Algorithm 1 Pseudocode to illustrate the DLPNO-MP2 algorithm. All truncation thresholds are printed on the right side of the listing.

Localise the molecular orbitals
Determine the projected atomic orbitals
Calculate the integrals $\mathrm{DOI}_{i\tilde{\mu}'}$, DOI_{ij}
Generate map $\mathbf{L}\left(i \to \tilde{\mu}'_{\mathrm{A}}\right)$ for prescreening ▷ T_{CutDOPre}
Perform the prescreening giving pair list (ij), estimate energy ΔE_{Pre} of screened out pairs ▷ T_{CutDOij}, T_{CutPre}
Calculate map $\mathbf{L}\left(i \to \mu_{\mathrm{A}}\right)$ ▷ T_{CutC}
Calculate map $\mathbf{L}\left(\tilde{\mu}' \to \nu_{\mathrm{A}}\right)$ ▷ T_{CutC}
Calculate map $\mathbf{L}\left(i \to \tilde{\mu}'_{\mathrm{A}}\right)$ ▷ T_{CutDO}
Calculate map $\mathbf{L}\left(i \to K_{\mathrm{A}}\right)$ ▷ T_{CutMKN}
Construct extended maps using screened pair list (ij)
Perform linear scaling integral transformation $(i\tilde{\mu}'|K)$
for all pairs (ij) **do**
    Construct pair domains from non-extended maps
    Construct local exchange operator $(i\tilde{\mu}|j\tilde{\nu})$
    Construct semicanonical amplitudes $\breve{T}^{ij}_{\tilde{\mu}\tilde{\nu}}$
    Construct semicanonical pair density $\breve{\mathbf{D}}^{ij} := \breve{\mathbf{T}}^{ij\dagger}\tilde{\breve{\mathbf{T}}}^{ij} + \breve{\mathbf{T}}^{ij}\tilde{\breve{\mathbf{T}}}^{ij\dagger}$
    Diagonalise pair density to obtain PNOs $\tilde{a}_{ij}$ ▷ T_{CutPNO}
    Transform $(i\tilde{\mu}|j\tilde{\nu}) \to \left(i\tilde{a}\middle|j\tilde{b}\right), \breve{T}^{ij}_{\tilde{\mu}\tilde{\nu}} \to \breve{T}^{ij}_{\tilde{a}\tilde{b}}$ and store on disk
    Estimate PNO energy error ΔE_{PNO}
end for
repeat
    for all pairs (ij) **do**
        Residual $R^{ij}_{\tilde{a}\tilde{b}} := \left(i\tilde{a}\middle|j\tilde{b}\right) + \left(\varepsilon_{\tilde{a}} + \varepsilon_{\tilde{b}} - F_{ii} - F_{jj}\right) T^{ij}_{\tilde{a}\tilde{b}}$ (in PNO basis)
        for all $k \in L\left(j \to k\right)$ **do**
            if $k \neq j$ and $|F_{ik}| \geq F_{\mathrm{Cut}}$ **then** ▷ F_{Cut}
                $\mathbf{R}^{ij} := \mathbf{R}^{ij} - F_{ik}\mathbf{S}^{ij,kj}\mathbf{T}^{kj}\mathbf{S}^{kj,ij}$
            end if
        end for
        for all $k \in L\left(i \to k\right)$ **do**
            if $k \neq i$ and $|F_{kj}| \geq F_{\mathrm{Cut}}$ **then** ▷ F_{Cut}
                $\mathbf{R}^{ij} := \mathbf{R}^{ij} - F_{kj}\mathbf{S}^{ij,ik}\mathbf{T}^{ik}\mathbf{S}^{ik,ij}$
            end if
        end for
    end for
    DIIS extrapolation of the amplitudes $T^{ij}_{\tilde{a}\tilde{b}}$ and residuals $R^{ij}_{\tilde{a}\tilde{b}}$
    Amplitude update: $T^{ij}_{\tilde{a}\tilde{b}} \to T^{ij}_{\tilde{a}\tilde{b}} - R^{ij}_{\tilde{a}\tilde{b}} / \left(\varepsilon_{\tilde{a}} + \varepsilon_{\tilde{b}} - F_{ii} - F_{jj}\right)$
    $E_{\mathrm{DLPNO-MP2}} := 0$
    for all pairs (ij) **do**
        $E_{\mathrm{DLPNO-MP2}} := E_{\mathrm{DLPNO-MP2}} + \sum_{\tilde{a}\tilde{b}} \left(i\tilde{a}\middle|j\tilde{b}\right) T^{ij}_{\tilde{a}\tilde{b}}$
    end for
until $E_{\mathrm{DLPNO-MP2}}$ converged and $\mathbf{R}^{ij} \approx 0$
Calculate total correlation energy $E_{\mathrm{C}} := E_{\mathrm{DLPNO-MP2}} + \Delta E_{\mathrm{PNO}} + \Delta E_{\mathrm{Pre}}$

upon this in Section 2.3.1.2. In order to retain a distinction between core and valence orbitals, the respective subsets of canonical orbitals are localised separately. If all electrons are correlated, localisations are therefore performed once for the core and once for the valence orbitals, whereas only the valence orbitals need to be localised for a frozen-core calculation.

Several matrices are calculated in a full basis of the entire system: for example, the Fock matrix $F_{\tilde{\mu}'\tilde{\nu}'}$ and the overlap matrix $S_{\tilde{\mu}'\tilde{\nu}'}$ are calculated once for all redundant PAOs, leading to a (N^3) computational and $O(N^2)$ storage requirement. The largest of these is usually the RI metric V_{PQ}, containing the Coulomb repulsion integrals between two auxiliary functions. It is beneficial to store the matrix on disk rather than in memory during those parts of the DLPNO-MP2 calculation that do not require it.

Following the construction of the maps and the orbital pair prescreening, the three-centre electron repulsion integrals are calculated in the integral transformation routine as outlined in Algorithm 2. The necessary space to store all integrals $(i\tilde{\mu}'|K)$ for a large system may be substantially larger than the available amount of memory, thus necessitating storage on disk. ORCA provides a data structure named "matrix container" to store higher-order tensors as sets of matrices. The first step of the integral transformation produces a matrix of integrals $(i\tilde{\mu}'|K)$ for each auxiliary function K, which is labelled $I^K_{i\tilde{\mu}'}$. Consequently, integrals are read most efficiently from disk if they share the same K. On the other hand, the DLPNO-MP2 calculation usually requires access to integrals for a specific orbital i at a time, so that it is preferable to arrange the data in the matrix container in terms of separate matrices $I^i_{K\tilde{\mu}'}$ for each given occupied orbital i. The sorting step $I^K_{i\tilde{\mu}'} \rightarrow I^i_{K\tilde{\mu}'}$ is an I/O-intensive and significant part of the overall computational expense for the integral transformation, but it is necessary to ensure efficient data access in the subsequent calculation.

After the calculation of the semicanonical amplitudes and the PNO construction, three further matrix containers are retained on disk: the transformation matrices $d^{ij}_{\tilde{\mu}'\tilde{a}}$ from redundant PAOs of each domain $\{ij\}$ to the respective PNOs, the transformed integrals $\left(i\tilde{a}\middle|j\tilde{b}\right)$, and a guess for the amplitudes $T^{ij}_{\tilde{a}\tilde{b}}$.

Algorithm 2 Pseudocode illustrating the implementation of the asymptotically linear scaling integral transformation routine.

for all auxiliary basis function shells K_S **do**
  for all basis function shells μ_S in $L\left(K_\mathrm{S} \to \mu_\mathrm{S}\right)$ **do** ▷ Primitive integrals
    for all basis function shells ν_S in $L\left(K_\mathrm{S} \to \nu_\mathrm{S}\right)$ **do**
      Compute integrals $(\mu\nu|K)$
    end for
  end for
  for all MOs $i \in L\left(K \to i\right)$ **do** ▷ Actual transformation
    for all $\nu \in L\left(K \to \nu\right)$ **do**
      $(i\nu|K) := 0$
      for all $\mu \in L\left(K \to \mu\right)$ **do**
        $(i\nu|K) := (i\nu|K) + c_{\mu i}\,(\mu\nu|K)$
      end for
    end for
  end for
  for all MOs $\tilde{\mu}' \in L\left(K \to \tilde{\mu}'\right)$ **do**
    for all MOs $i \in L\left(K \to i\right)$ **do**
      $(i\tilde{\mu}'|K) := 0$
      for all $\nu \in L\left(K \to \nu\right)$ **do**
        $(i\tilde{\mu}'|K) := (i\tilde{\mu}'|K) + \tilde{P}_{\nu\tilde{\mu}'}\,(i\nu|K)$
      end for
    end for
  end for
  Store $(i\tilde{\mu}'|K)$ on disk
end for
Sort integrals: leading index K to leading index i

In order to calculate the PNO residual in Eq. (2.32), overlap matrices such as $S_{\tilde{a}_{ij}\tilde{b}_{ik}}$ need to be generated. This is most efficiently achieved in memory during each iteration with the following steps:

1. For a given pair ij, identify all k such that either pair ik has not been screened out and F_{kj} is above the threshold, or kj has not been screened out and F_{ik} is above the threshold:

$$L\left(ij \to k\right) = \left\{\, k : k \in L\left(i \to k\right) \wedge |F_{kj}| > F_\mathrm{Cut} \,\right\} \cup \left\{\, k : k \in L\left(j \to k\right) \wedge |F_{ik}| > F_\mathrm{Cut} \,\right\} \quad (2.61)$$

2. Extract the *rectangular* matrix $S_{\tilde{\mu}'\tilde{\nu}'}$. The column indices $\tilde{\nu}'$ are members of the union of the respective domains $\{ik\}$ and $\{kj\}$, while the row indices $\tilde{\mu}'$ are members

of domain $\{ij\}$ only:

$$\tilde{\mu}' \in \{ij\} \tag{2.62}$$

$$\tilde{\nu}' \in \bigcup_{k \in L(ij \to k)} [\{ik\} \cup \{kj\}] \tag{2.63}$$

3. Transform the row indices of the matrix to the PNO basis of pair ij, $S_{\tilde{\mu}'\tilde{\nu}'} \to S_{\tilde{a}_{ij}\tilde{\nu}'}$.

4. For each pair ik (or kj), transform the appropriate columns of the matrix to the respective PNO basis, e.g. $S_{\tilde{a}_{ij}\tilde{\nu}'} \to S_{\tilde{a}_{ij}\tilde{b}_{ik}}$.

The residual equation in PNO basis, Eq. (2.32), is solved using an iterative algorithm that is based on the Jacobi method. If the amplitudes $T^{ij}_{\tilde{a}\tilde{b}}$ are mapped onto a one-dimensional vector, then the coefficient matrix of the associated linear equation system has $[\varepsilon_{\tilde{a}} + \varepsilon_{\tilde{b}} - F_{ii} - F_{jj}]$ as its diagonal entries. Accordingly, with $T^{ij[n]}_{\tilde{a}\tilde{b}}$ and $R^{ij[n]}_{\tilde{a}\tilde{b}}$ as the respective amplitudes and residuals in the n-th iteration, the amplitude update with the Jacobi algorithm is given by:

$$T^{ij[n+1]}_{\tilde{a}\tilde{b}} = T^{ij[n]}_{\tilde{a}\tilde{b}} - \frac{R^{ij[n]}_{\tilde{a}\tilde{b}}}{\varepsilon_{\tilde{a}} + \varepsilon_{\tilde{b}} - F_{ii} - F_{jj}} \tag{2.64}$$

With the Jacobi method alone, the iterative algorithm often performs poorly. A drastic improvement is achieved through incorporating convergence acceleration by direct inversion in the iterative subspace (DIIS).[151] In each iteration n, improved amplitudes $\mathbf{T}^{ij[n]\text{DIIS}}$ and associated residuals $\mathbf{R}^{ij[n]\text{DIIS}}$ are obtained by DIIS extrapolation. The update in Eq. (2.64) is then performed using $\mathbf{T}^{ij[n]\text{DIIS}}$ and $\mathbf{R}^{ij[n]\text{DIIS}}$ rather than $\mathbf{T}^{ij[n]}$ and $\mathbf{R}^{ij[n]}$.

With the DIIS-enhanced Jacobi algorithm, convergence is usually achieved within a modest number of iterations; divergence was only observed for systems with a near-linearly dependent atomic basis set in practice. Level shifting and damping can be used in addition. An algorithm based on the Jacobi method is likely suitable to solve the residual equations, because the off-diagonal Fock matrix elements F_{ij} are usually substantially smaller than the diagonal ones in a localised orbital basis.

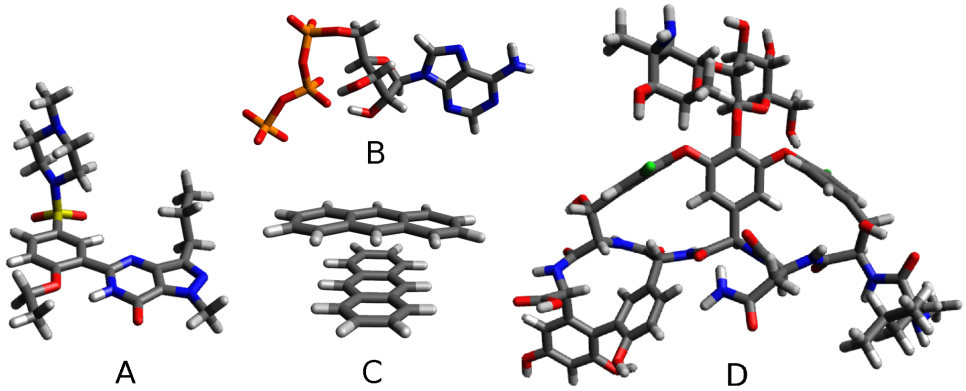

Figure 2.2: Systems used to investigate the DLPNO-MP2 thresholds. (A) Sildenafil (B) ATP^{4-} (C) Anthracene dimer (D) Vancomycin

2.3 Results

2.3.1 Selection of truncation thresholds

2.3.1.1 Computational approach

Correlation energies are typically in a range of several Hartree for mid-sized molecules to tens of Hartree for systems containing hundreds of atoms. Achieving an accuracy of $1\,\mathrm{kJ\,mol^{-1}}$ for a system with a correlation energy of $10\,\mathrm{MJ\,mol^{-1}}$ would require the ability to reproduce ca. 99.99 % of the total correlation energy. On the other hand, quantum chemical methods tend to rely on error cancellation in energy differences, and the absolute error in the total energy calculated with any approximate size-extensive method is expected to increase linearly with system size. Therefore, our aim is to define thresholds for DLPNO-MP2 so that 99.9 % of the total RI-MP2 correlation energy is reproduced. Subsequent benchmark calculations will demonstrate that this is an adequate default accuracy target. In this section, the approximations are investigated one threshold at a time. All calculations were performed with the Foster-Boys localisation method[132, 133] and with frozen core settings.

2.3.1.2 Truncated pair natural orbitals

The pair natural orbital truncation threshold T_{CutPNO} is examined using three systems: sildenafil; a weakly bonded anthracene dimer; and the adenosine triphosphate anion

		Basis functions		Auxiliary functions	
System	Atoms	def2-TZVP	def2-TZVPD	def2-TZVP/C	aug-cc-pVTZ/C
Sildenafil	63	1209	1512	2995	4919
ATP^{4-}	43		1312	2647	3961
Anthr. dimer	48	988	1216	2428	3888
Vancomycin	176	3593		8875	

Table 2.1: Numbers of atoms and basis functions in the investigated systems that are depicted in Figure 2.2.

(ATP^{4-}) in gas phase (Figure 2.2). These three systems are on the one hand large enough to examine the truncations, which may not become effective to the same extent in smaller molecules, but on the other hand they are small enough to perform these calculations without excessive computational cost. The numbers of atoms and basis functions are shown in Table 2.1. In order to isolate the effect of PNO truncation, all other thresholds were set to zero in the calculations.

Figure 2.3 shows the percentage of the total RI-MP2 correlation energy reproduced using a given threshold. The accuracy is increased substantially by the PNO energy correction ΔE_{PNO}, particularly for the more aggressive thresholds. Results with the diffuse def2-TZVPD basis are very similar to those with the def2-TZVP set. In order to recover 99.9 % of the correlation energy, a threshold of $T_{\mathrm{CutPNO}} = 1 \times 10^{-8}$ is chosen as the default value. Evidently, this is lower than the cutoff used in DLPNO-CCSD, for which 3.33×10^{-7} is recommended as the default value and 1.0×10^{-7} as a threshold for tight convergence.[24, 33, 37] Apparently, a larger number of PNOs is needed to achieve a comparable accuracy with DLPNO-MP2.

Bistoni and co-workers pointed out that the default PNO truncation threshold used in the DLPNO-CCSD method is not sufficient for core orbital pairs:[150] as the denominator is often much larger than with valence orbitals, the semicanonical amplitudes tend to be much smaller, and thus a lower PNO truncation threshold is needed to recover a comparable fraction of the correlation energy. They suggested scaling the threshold T_{CutPNO}, which was determined for valence correlation, by a factor of 0.01 for core and core-valence correlation pairs.

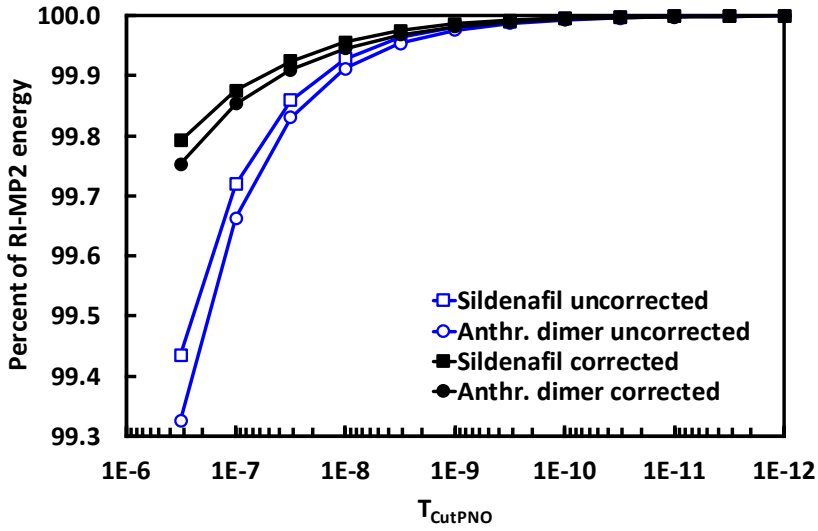

(a) Results calculated with the def2-TZVP basis and def2-TZVP/C for correlation fitting.

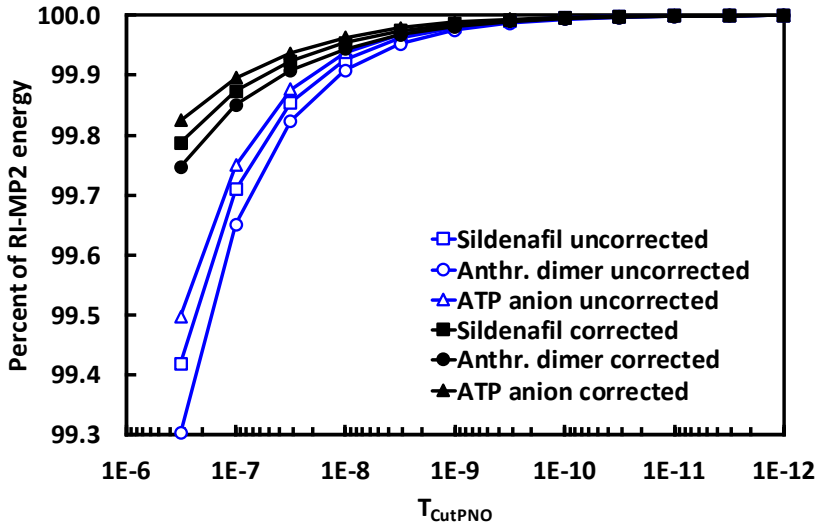

(b) Results calculated with the def2-TZVPD basis and aug-cc-pVTZ/C for correlation fitting.

Figure 2.3: Percentage of the total RI-MP2 correlation energy recovered with a given T_{CutPNO}. All other truncation thresholds are zero. The "corrected" results include the energy correction ΔE_{PNO}.

We found that the solution to scale the PNO threshold is also appropriate for DLPNO-MP2. Therefore, the threshold T_{CutPNO} is used for valence orbital pairs and $T_{\mathrm{CutPNO(Core)}}$ for pairs with one or two core orbitals. It is set to $T_{\mathrm{CutPNO(Core)}} = 0.01 \times T_{\mathrm{CutPNO}}$ by default. Note that this does not affect our calculations reported in this section and in ref. [43], as they were performed with frozen core settings.

2.3.1.3 Truncated domains of auxiliary functions

Fitting domains are determined using the Mulliken populations of individual orbitals. Figure 2.4 shows the convergence of the correlation energy with respect to RI-MP2 using different values of the T_{CutMKN} threshold. In these calculations, the pair natural orbitals were truncated using the previously determined threshold $T_{\mathrm{CutPNO}} = 10^{-8}$, whereas all remaining threshold were left at zero.

At a value of $T_{\mathrm{CutMKN}} = 10^{-3}$, as used in previous work,[33, 37] the energies are almost converged. Relative to results with fitting domains that encompass the entire system, the error is below 0.005 %, and thereby within the accuracy target by more than an order of magnitude. With the diffuse basis set def2-TZVPD, the fitting domains are considerably larger than with def2-TZVP. On the other hand, this larger size appears to be necessary to recover a comparable fraction of the canonical correlation energy.

Comparing DLPNO-MP2 results for def2-TZVPD in combination with different auxiliary sets, the errors relative to the respective RI-MP2 energies are about twice as large with def2-TZVP/C as with aug-cc-pVTZ/C. The fitting domains contain identical atoms in both cases, so it is possible that the more numerous and diffuse functions of aug-cc-pVTZ/C result in a more accurate fit with a given domain size.

2.3.1.4 Truncated domains of projected atomic orbitals

Calculations to determine the newly introduced domain threshold T_{CutDO} were performed in the presence of the already established cutoffs $T_{\mathrm{CutPNO}} = 10^{-8}$ for the PNOs and $T_{\mathrm{CutMKN}} = 10^{-3}$ for the fitting domains. We choose a default threshold of $T_{\mathrm{CutDO}} = 10^{-2}$, which reproduces ca. 99.9 % of the RI-MP2 energy (Figure 2.5).

With the basis set def2-TZVPD, the domains using the same differential overlap cutoff are somewhat larger than with def2-TZVP. Nevertheless, the error relative to RI-MP2 increases with the diffuse basis set; this indicates that larger domains are needed to reproduce a given accuracy target if a basis set contains very diffuse functions.

(a) Basis sets:
def2-TZVP
def2-TZVP/C

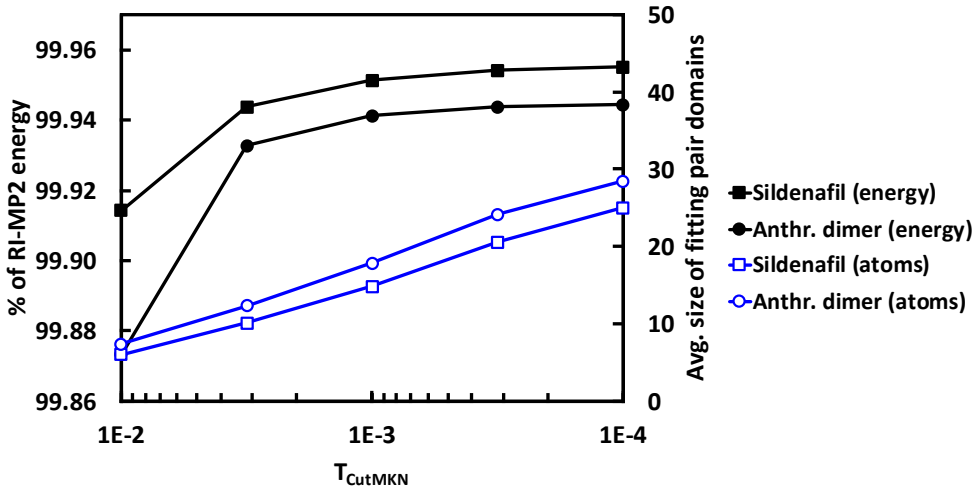

(b) Basis sets:
def2-TZVPD
def2-TZVP/C

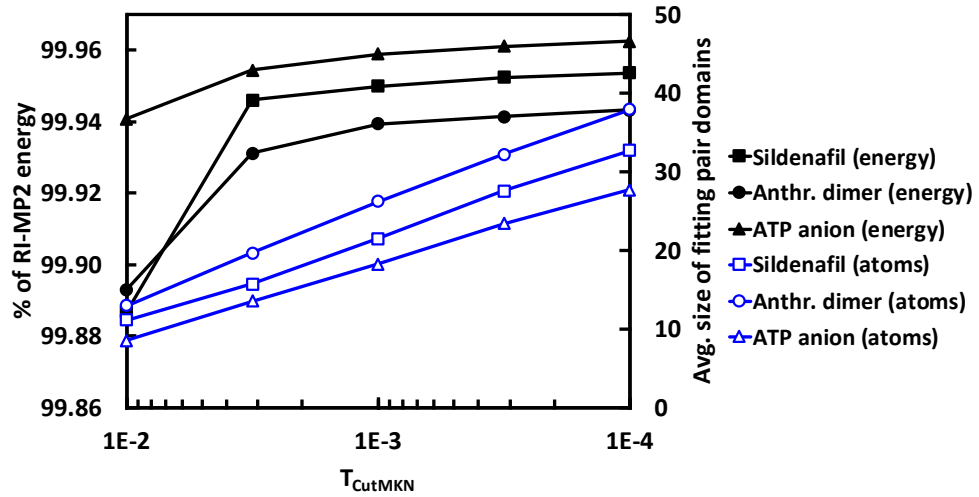

(c) Basis sets:
def2-TZVPD
aug-cc-pVTZ/C

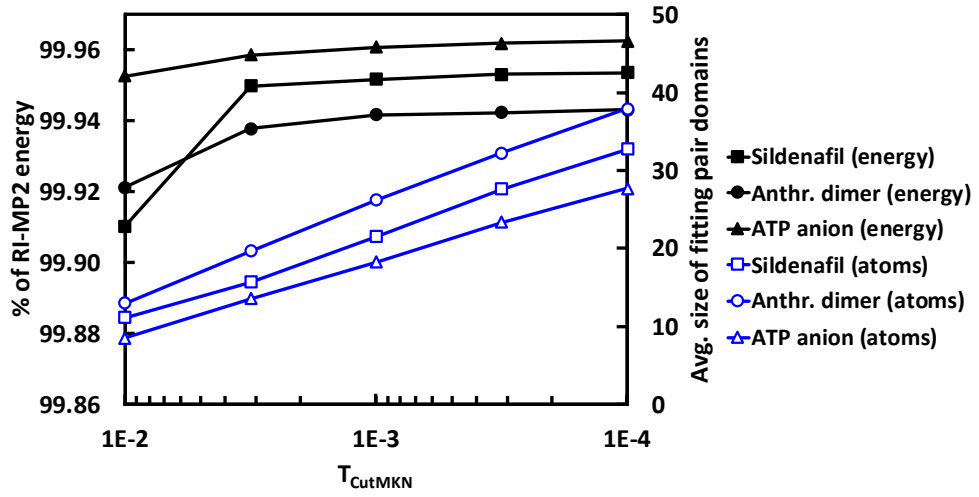

Figure 2.4: Percentage of the total RI-MP2 correlation energy recovered with a given T_{CutMKN}. In the asymptotic limit, the remaining error is due to the PNO truncation with $T_{\mathrm{CutPNO}} = 10^{-8}$. The blue lines associated with the right axis show the average number of atoms in the fitting pair domains.

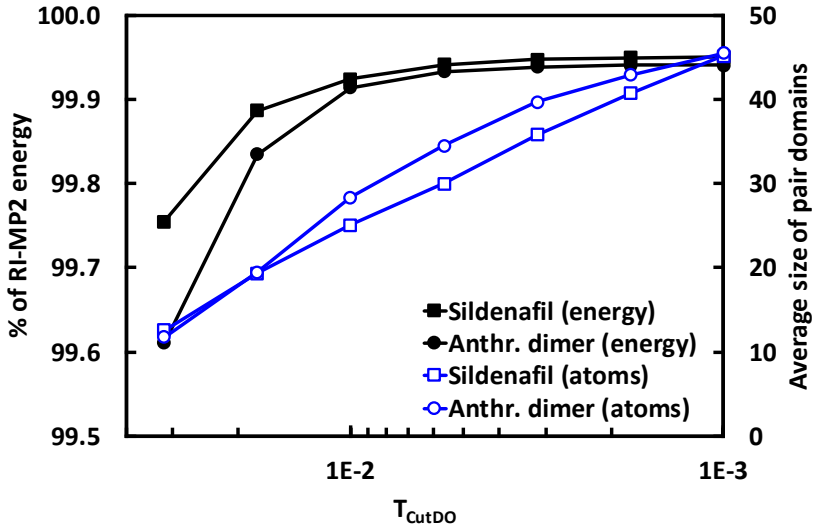

(a) Results calculated with the def2-TZVP basis and def2-TZVP/C for correlation fitting.

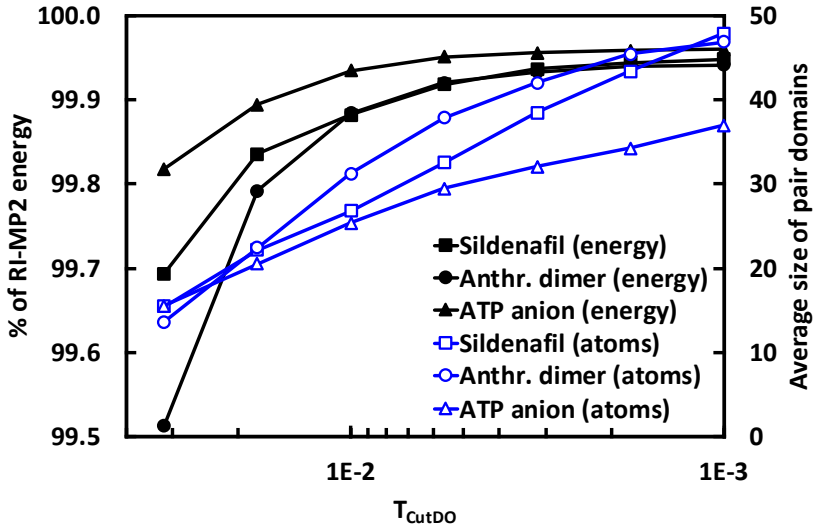

(b) Results calculated with the def2-TZVPD basis and aug-cc-pVTZ/C for correlation fitting.

Figure 2.5: Fraction of the total RI-MP2 correlation energy recovered with a given domain threshold T_{CutDO}. In the asymptotic limit, the remaining error is accounted for by the PNO and fitting domain truncations. The blue lines associated with the right axis show the average number of atoms for the pair domains.

2.3.1.5 Fock matrix truncation

The cutoff F_{Cut} for internal Fock matrix elements was determined using calculations for vancomycin (depicted in Figure 2.2) with the def2-TZVP basis. This molecule is sufficiently large to examine truncation errors that would be less apparent in smaller systems.

Figure 2.6 shows the error in the total correlation energy. T_{CutPNO}, T_{CutDO} and

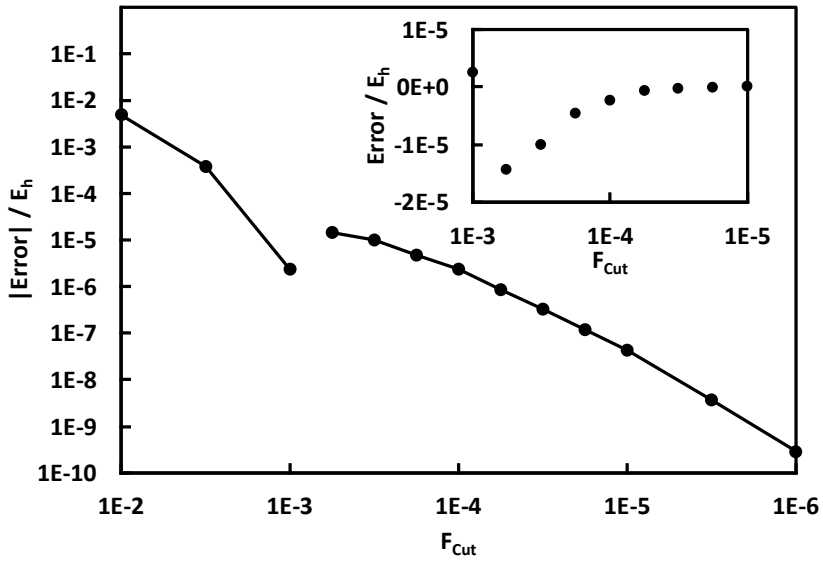

Figure 2.6: Magnitude of the error in the correlation energy caused by Fock matrix truncation with a given F_{Cut} for vancomycin in def2-TZVP basis. Inset: the signed error in a selected range. Below a cutoff of $10^{-3}\,E_{\mathrm{h}}$, the error changes its sign. The total correlation energy is $-18.3\,E_{\mathrm{h}}$. Default values are used for T_{CutPNO}, T_{CutMKN} and T_{CutDO}.

T_{CutMKN} were set to their previously determined default values, but no further truncations were involved. Since the error is relatively sensitive with respect to larger thresholds, a conservative cutoff $F_{\mathrm{Cut}} = 1 \times 10^{-5}\,E_{\mathrm{h}}$ is chosen, resulting in an insignificant error well below $1\,\mu E_{\mathrm{h}}$. This finding agrees with the results of Schütz and Werner.[15] If pair prescreening is enabled, which will be discussed later, 66 % of terms are dropped with this threshold.

2.3.1.6 Definition of default accuracy settings

While the default cutoffs have been selected to provide a reasonable compromise between accuracy and efficiency, in some cases it may be desirable to perform calculations that reproduce RI-MP2 even more closely, for example when investigating weak interactions. In analogy with previous work on DLPNO-CCSD(T),[24] we define LoosePNO, NormalPNO and TightPNO settings as represented in Table 2.2.

The two approximations with the largest impact on the accuracy are the pair natural orbital and domain truncations. For each accuracy setting, T_{CutPNO} is scaled up or down by a factor of 10, and T_{CutDO} by a factor of 2. Errors resulting from any of the other

Threshold	LoosePNO	NormalPNO	TightPNO
T_{CutPNO}	1×10^{-7}	1×10^{-8}	1×10^{-9}
T_{CutDO}	2×10^{-2}	1×10^{-2}	5×10^{-3}
T_{CutMKN}		1×10^{-3}	
F_{Cut}		1×10^{-5}	
T_{CutPre}		1×10^{-6}	
T_{CutDOij}		1×10^{-5}	
T_{CutDOPre}		3×10^{-2}	
T_{CutC}		1×10^{-3}	

Table 2.2: Truncation thresholds in the DLPNO-MP2 method.

approximations are at least an order of magnitude smaller, and therefore the remaining thresholds are left unchanged. While NormalPNO is meant to reproduce around 99.9 % of the RI-MP2 correlation energy, TightPNO settings would typically yield an accuracy of $> 99.95\,\%$. LoosePNO settings are expected to reproduce only ca. 99.7 % of the reference value.

2.3.2 Pair prescreening

An improved procedure for pair prescreening of orbital pairs was introduced in Section 2.1.4. As shown in Figure 2.7 for vancomycin, the new dipole energy expression yields a reasonably good estimate for the semicanonical pair energy of very distant pairs. Nonetheless, the semicanonical energies of many pairs around $1\,\mu E_{\mathrm{h}}$ are underestimated by a considerable margin. As opposed to that, the collinear modification of the dipole approximation overestimates the semicanonical pair energies, and it can be used as a reliable upper bound for the pair energy.

Figure 2.8 contains a plot of the relative error in the dipole energies, $\left(\varepsilon_{ij}^{\mathrm{DIP}} - \varepsilon_{ij}^{\mathrm{SC}}\right)/\varepsilon_{ij}^{\mathrm{SC}}$, against the differential overlap of the MOs, DOI_{ij}. It shows that the error of the dipole approximation is consistently below 40 % for all pairs with a differential overlap below 10^{-5}. In order to arrive at a reliable and accurate procedure, pairs are only screened out if their collinear dipole energy is below $T_{\mathrm{CutPre}} = 1\,\mu E_{\mathrm{h}}$, and at the same time the differential overlap of the occupied MOs T_{CutDOij} is below $T_{\mathrm{CutDOij}} = 1 \times 10^{-5}$. The energy contribution of the screened-out pairs, however, is calculated with the actual

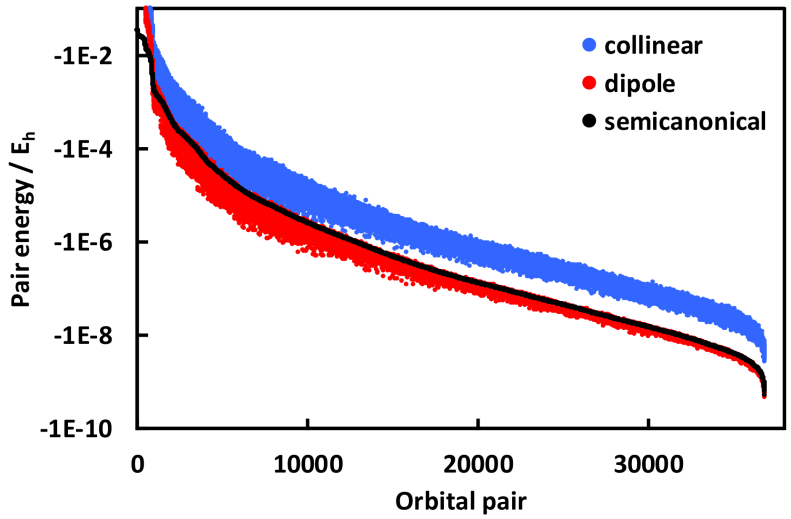

Figure 2.7: Pair energies for vancomycin in def2-TZVP basis. The black dots show the semicanonical energy of a pair with $T_{\mathrm{CutDO}} = 1 \times 10^{-2}$. Proper dipole and collinear dipole energies of the respective pairs are shown by the red and blue dots, and have been calculated with $T_{\mathrm{CutDOPre}} = 3 \times 10^{-2}$. All pairs are ordered by their semicanonical energy.

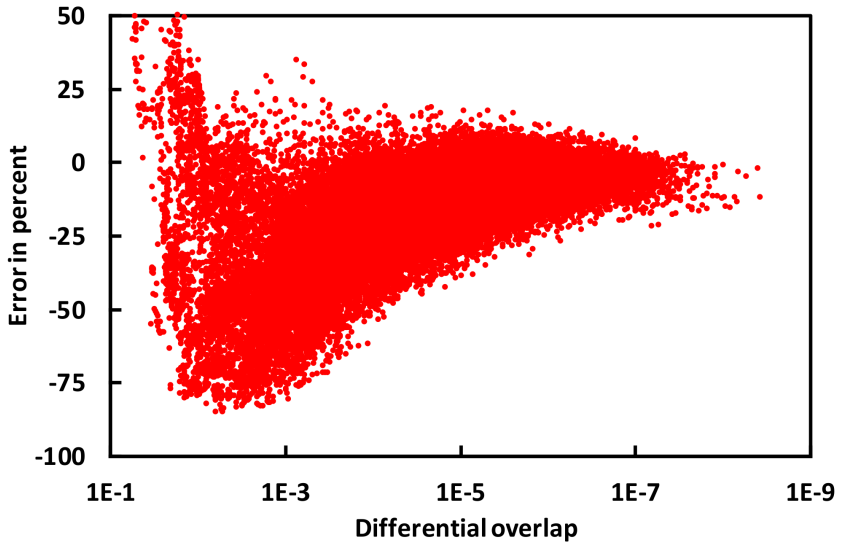

Figure 2.8: Error in the dipole pair energy relative to the respective semicanonical energy of pair ij plotted against the differential overlap of the orbitals, DOI_{ij}. The data was calculated for vancomycin in def2-TZVP basis.

dipole approximation. A reduced differential overlap threshold of $T_{\mathrm{CutDOPre}} = 3 \times 10^{-2}$ was found to be sufficient to construct domains of PAOs in the dipole expressions.

For vancomycin in def2-TZVP basis, this conservative procedure removes 16 266 out of 36 856 orbital pairs from the remaining local MP2 calculation. The contribution of these pairs accounts for 0.0033 % of the correlation energy; an error of only 0.0003 % in

the total correlation energy remains after adding the dipole correction.

On the other hand, the old prescreening procedure as used in the first implementation of DLPNO-CCSD removed 25 460 pairs accounting for 0.032 % of the correlation energy. An error of 0.011 % remained in the total correlation energy after adding the energy correction, which is less accurate than the new treatment by more than an order of magnitude. With the deprecated prescreening procedure, the error was almost in a comparable range as the deviations introduced by the PNO and domain approximations, especially in combination with tight thresholds.

2.3.3 Truncating atomic orbital coefficients in the RI integral transformation

This section provides a detailed analysis of atomic orbital coefficient truncation in the RI integral transformation. We first consider individual truncation for each MO and PAO. This implies that a set of basis coefficients will be retained according to the map $\mathbf{L}\left(i \to \mu_\mathrm{A}\right)$ for each MO i. Similarly, one individual set of coefficients will be used for all PAOs centred on the same atom according to the map $\mathbf{L}\left(\tilde{\mu}'_\mathrm{A} \to \nu_\mathrm{A}\right)$. While this does not correspond to the procedure in the integral transformation routine, which uses superblocks of AO coefficients as described previously, it is a more straightforward approach for an error analysis. In addition, this approach is more similar to the integral transformation routine reported by Werner and co-workers,[55] albeit they use a different criterion to select basis set coefficients, and perform a fitting of the truncated MOs and PAOs to reduce errors.

Table 2.3 shows the total correlation energy of vancomycin with different choices of T_CutC. The error incurred from MO coefficient truncation (Table 2.3a) is controllable and well within the 99.9 % accuracy target with a cutoff $T_\mathrm{CutC} = 10^{-2}$, leading to maps $\mathbf{L}\left(i \to \mu_\mathrm{A}\right)$ containing basis functions from 35 atoms on average. Interestingly, the error is reduced by an order of magnitude with prescreening of orbital pairs.

By contrast, truncating PAOs (Table 2.3b) leads to excessive errors unless a very conservative threshold is used. Even with $T_\mathrm{CutC} = 10^{-3}$, which includes AO coefficients

	Correlation energy / E_h		
T_CutC	no pair prescreening	with pair prescreening	Atoms
10^{-2}	−18.314 052 905 770	−18.311 105 040 428	35.1
10^{-3}	−18.311 730 112 266	−18.311 293 162 660	92.3
10^{-4}	−18.311 549 912 531	−18.311 266 679 686	148.1
10^{-5}	−18.311 548 215 432	−18.311 266 604 688	171.2
0	−18.311 548 208 086	−18.311 266 604 344	176.0

(a) Atomic basis functions are truncated individually for each MO using the maps in $\mathbf{L}\,(i \to \mu_A)$.

	Correlation energy / E_h		
T_CutC	no pair prescreening	with pair prescreening	Atoms
10^{-2}	−11 467.257 109 350 041	−10 852.520 210 865 197	73.7
10^{-2}	−18.472 749 534 494	−18.355 932 985 249	135.4
10^{-4}	−18.311 571 831 156	−18.311 267 088 375	168.4
10^{-5}	−18.311 548 218 125	−18.311 266 604 344	175.7
0	−18.311 548 208 086	−18.311 266 604 344	176.0

(b) Atomic basis functions are truncated individually for PAOs using the maps in $\mathbf{L}\,(\tilde{\mu}'_A \to \nu_A)$.

Table 2.3: DLPNO-MP2 correlation energy of vancomycin (def2-TZVP) with different values of the atomic orbital cutuff T_CutC, with or without prescreening of orbital pairs.

from 135 atoms for each PAO on average, the error in the total correlation energy is 0.2 % or 0.9 % with and without prescreening, respectively. This behaviour is likely a result of linear dependencies in the PAO space, as will be demonstrated next.

Since the dimension of the space spanned by the redundant PAOs in each domain is not known *a priori*, the first step in the transformation to non-redundant PAOs is to determine the rank of the overlap matrix of PAOs, $S_{\tilde{\mu}'\tilde{\nu}'}$, with $\tilde{\mu}', \tilde{\nu}' \in \{ij\}$. This is accomplished by diagonalising the overlap matrix and discarding eigenvectors with associated eigenvalues below a threshold with the default value $S_\mathrm{Cut} = 10^{-8}$. A tighter value for this threshold leads to a more complete recovery of the external space, but also to larger coefficients in some of the non-redundant PAO vectors.

As the transformation matrix between redundant and non-redundant PAOs is determined using overlap integrals without truncation, neglecting even minimal contributions of atomic basis functions to the integrals $(i\tilde{\mu}'|K)$ can lead to large errors. Table 2.4 shows errors in the total energy calculated with different overlap cutoffs S_Cut. Basis set coeffi-

	Correlation energy error / E_h	
S_Cut	no pair prescreening	with pair prescreening
10^{-6}	-0.044	-0.019
10^{-7}	-0.156	-0.043
10^{-8}	-0.161	-0.045
10^{-9}	-0.161	-0.045

Table 2.4: Error in the total correlation energy of vancomycin (def2-TZVP) caused by AO coefficient truncation, calculated with different overlap cutoffs S_Cut. Basis functions were truncated for PAOs individually with a cutoff $T_\mathrm{CutC} = 10^{-3}$.

cients of PAOs are truncated using the threshold $T_\mathrm{CutC} = 10^{-3}$ in each case. Reducing S_Cut increases the errors, as the non-redundant eigenvectors of $S_{\tilde{\mu}'\tilde{\nu}'}$ are multiplied with the inverse square root of the associated eigenvalues, resulting in larger coefficients for some of the vectors. On the other hand, if basis functions are truncated for MOs but not for PAOs, then the results are only marginally affected by S_Cut.

While Werner and co-workers did not provide an analysis of errors resulting from AO coefficient truncation for their PNO-LMP2 implementation, they also found that large AO blocks are required. Indeed, they chose to disable PAO truncation by default, thus making their method formally quadratically scaling.

In contrast to the previous analysis, the integral transformation implemented in the DLPNO-MP2 method performs basis set truncation to produce entire superblocks of AOs. When calculating the RI integrals $(i\tilde{\mu}'|K)$ for a specific function K, the common AO block for all MOs is defined through the map $L_\mathrm{ext}\,(K \to i) \subset \mathbf{L}\,(i \to \nu_\mathrm{A})$, where the map from auxiliary functions to MOs is obtained by inverting the extended map from MOs to auxiliary functions, $\mathbf{L}_\mathrm{ext}\,(K \to i) = \mathbf{L}_\mathrm{ext}^{-1}\,(i \to K_\mathrm{A})$. An even larger block of AOs is obtained for PAOs, specified by the map $L_\mathrm{ext}\,(K \to i) \subset \mathbf{L}_\mathrm{ext}\,(i \to \tilde{\mu}'_\mathrm{A}) \subset \mathbf{L}\,(\tilde{\mu}'_\mathrm{A} \to \nu_\mathrm{A})$. While this approach was introduced for computational convenience, it also ensures accurate results, as will be illustrated below.

In vancomycin, the maps from auxiliary functions K to PAOs $\tilde{\mu}$' are so extensive that each sparse list contains all PAOs in the entire molecule. Therefore, the corresponding AO blocks contain all basis functions in the molecule (unless an inappropriately loose threshold T_CutC is chosen that excludes all basis functions on an atom from all PAOs).

T_{CutC}	Energy / E_h	AOs
10^{-1}	−47.642 453 703 426	2844
10^{-2}	−18.315 396 006 719	3386
10^{-3}	−18.311 266 715 618	3579
10^{-4}	−18.311 266 604 344	3593
0	−18.311 266 604 344	3593

Table 2.5: Correlation energy of vancomycin (def2-TZVP) with different thresholds T_{CutC}. The MOs are truncated to AO superblocks given by $\mathbf{L}_{\mathrm{ext}}\,(K \to i) \subset \mathbf{L}\,(i \to \nu_\mathrm{A})$. Numbers of AOs per block (rightmost column) are averaged over shells of auxiliary functions.

	MOs truncated		PAOs truncated	
T_{CutC}	Energy / E_h	AOs	Energy / E_h	AOs
10^{-1}	−49.987 054 208 335	1178	−39.901 165 401 502	3012
10^{-2}	−39.901 353 476 710	2159	−39.901 165 401 501	3988
10^{-3}	−39.901 165 442 252	2779	−39.901 165 401 501	4578
0	−39.901 165 401 501	8787	−39.901 165 401 501	8787

Table 2.6: Correlation energy of a linear $\mathrm{H}-(\mathrm{CH_2CHCl})_{75}-\mathrm{H}$ chain (def2-TZVP) with different T_{CutC}. Either the MOs or the PAOs were truncated to superblocks of basis functions. The number of AOs per block was averaged over shells of auxiliary functions.

The size of the AO coefficient block for the MOs can still be influenced by choosing a different T_{CutC}, as shown in Table 2.5. While the accuracy target for DLPNO-MP2 can be met with the cutoff value 10^{-2}, we make the more conservative choice $T_{\mathrm{CutC}} = 10^{-3}$ for both MOs and PAOs, which yields an error below the Microhartree range. This may be considered a safer choice: the size of the AO blocks depends not only on T_{CutC}, but also on the size of the $\mathbf{L}_{\mathrm{ext}}\,(i \to K_\mathrm{A})$ maps (determined by T_{CutMKN}), and in the case of PAOs also the $\mathbf{L}_{\mathrm{ext}}\,(i \to \tilde{\mu}'_\mathrm{A})$ maps (determined by T_{CutDO}). Most crucially, via the map extension both sets of maps depend strongly on the screened orbital pair list.

In the calculations with vancomycin, superblocks of basis functions for PAOs spanned the entire molecule. No substantial impact of PAO truncation is to be expected for three-dimensional molecules containing about 200 atoms. Further calculations were performed for a linear $\mathrm{H}-(\mathrm{CH_2CHCl})_{75}-\mathrm{H}$ chain using the def2-TZVP basis. Table 2.6 shows that the error in the energy is entirely negligible with a threshold of 10^{-3}, while 48 % of the basis functions are dropped for the PAOs in the integral transformation, and 68 % for the MOs. Further gains for very large systems could possibly be made with more ambitious

tuning of T_{CutC}, however, uncontrollable errors can be caused by too aggressive truncation of PAOs, as shown above.

As these results emphasise that the long tails of PAOs need to be taken into account, one cannot help but wonder whether a more compact and linearly independent alternative to PAOs could be found. In this context, the discussion by Jørgensen and co-workers on the localisability of virtual molecular orbitals is of relevance.[12–14]

Instead of truncating MOs and PAOs only in the RI integral transformation, one could consider using truncated MOs and PAOs throughout the entire DLPNO-MP2 calculation. As the transformation between redundant and non-redundant PAOs would be determined using the already truncated PAOs, the aforementioned difficulties could in principle be overcome. However, truncated PAOs are not an exact representation of the virtual space, as they are not strictly orthogonal to the occupied orbitals. When testing such a procedure, the domain-specific Fock matrix in non-redundant PAO basis sometimes had eigenvalues below the LUMO energy of the system; this contamination with occupied space components can be interpreted as a violation of the Pauli principle. One could attempt to refit PAOs under the constraint that they remain strictly orthogonal to the occupied MOs, and use those PAOs throughout the entire calculation. However, we found that the simpler approach to use superblocks of atoms orbitals with a truncation threshold of $T_{\mathrm{CutC}} = 10^{-3}$ is satisfactory.

These results emphasise that even small errors in the RI integrals can lead to large overall errors. Under practical circumstances, it is not possible to discard integrals $(i\tilde{\mu}'|K)$ if the specific combination of i and $\tilde{\mu}'$ appears in any pair domain. Therefore, using the extended maps $\mathbf{L}_{\mathrm{ext}}\,(i \to \tilde{\mu}')$ and $\mathbf{L}_{\mathrm{ext}}\,(i \to K)$ in the integral transformation is mandatory to ensure that all required integrals are computed.

2.3.4 Benchmark calculations

Four benchmark sets were employed in order to investigate the accuracy of the DLPNO-MP2 method for energy differences: the test set for chemical reaction energies by Friedrich and Hänchen,[152] conformational energies of melatonin[153] and 1,4-butanediol,[154] as

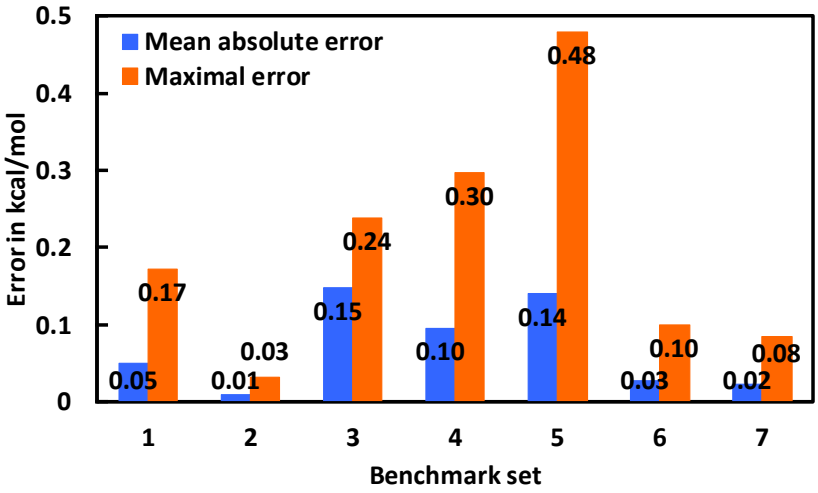

Figure 2.9: Mean absolute and maximum absolute errors in the benchmark sets:
(1) Reaction set by Friedrich and Hänchen (def2-TZVP)
(2) Conformers of 1,4-butanediol (def2-TZVP)
(3) Conformers of melatonin (def2-TZVP)
(4) S66 set without counterpoise correction (def2-TZVP)
(5) S66 set without counterpoise correction (def2-TZVPD)
(6) S66 set with counterpoise correction (def2-TZVP)
(7) S66 set with counterpoise correction (def2-TZVPD)

well as the S66 set.[155] The same four sets had been used previously to investigate the accuracy of DLPNO-CCSD(T).[24] Reference energies were computed with the RI-MP2 method. All DLPNO-MP2 calculations were performed with NormalPNO settings and, unless noted otherwise, using the def2-TZVP basis set. A graphical summary of the results is provided in Figure 2.9.

2.3.4.1 Chemical reactions

The performance of DLPNO-MP2 for chemical reaction energies was investigated using the test set by Friedrich and Hänchen, which contains 51 reactions of organic molecules (Figure 2.10). On average, reaction energies calculated with DLPNO-MP2 deviate by $0.05\,\mathrm{kcal\,mol^{-1}}$ from RI-MP2, with a largest error of $0.17\,\mathrm{kcal\,mol^{-1}}$.

To put these errors into context, the mean absolute deviation of MP2-F12/B reaction energies from CCSD(T)(F12*) results were reported as $11.6\,\mathrm{kJ\,mol^{-1}}$ ($2.8\,\mathrm{kcal\,mol^{-1}}$), with a largest error of $-56.2\,\mathrm{kJ\,mol^{-1}}$ ($-13\,\mathrm{kcal\,mol^{-1}}$).[152] The two explicitly correlated methods are approximations to the respective complete basis set limits of MP2 and

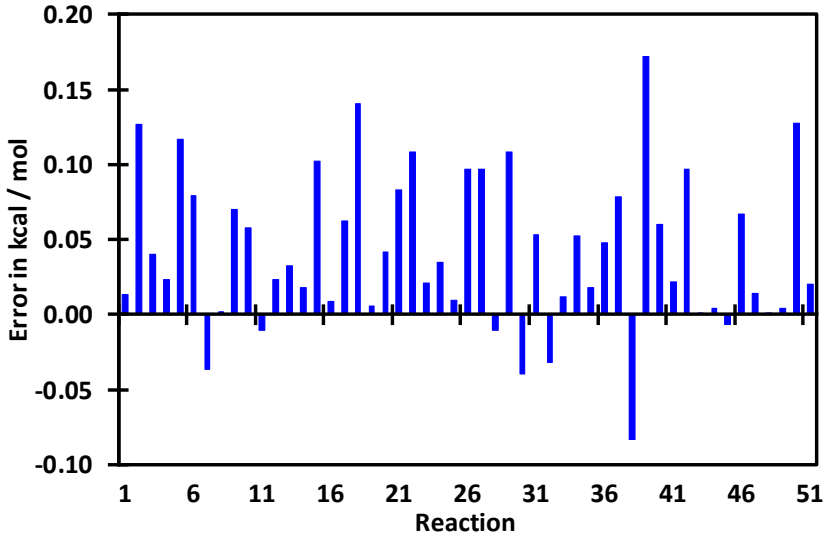

Figure 2.10: Errors in reaction energies for the test set by Friedrich and Hänchen.

CCSD(T), which shows that the deviations introduced by the approximations in DLPNO-MP2 are almost two order of magnitude below the estimated intrinsic error of the MP2 method. Sufficiently small molecules to perform canonical coupled cluster calculations were chosen for this test set. Therefore, it would be necessary to investigate reactions of larger molecules to draw more general conclusions about the limiting behaviour of the local approximations.

The direction of the reactions in the test set has been specified such that the electronic contribution to the reaction energy is negative. With a few exceptions, the MP2 reaction energies are also negative. In most cases, DLPNO-MP2 slightly overestimates the reaction energy.

2.3.4.2 Conformational energies

Relative energies of conformers were investigated for different geometries of 1,4-butanediol and of melatonin. The energy differences were determined with respect to the energetically lowest conformer, which is predicted correctly by both RI-MP2 and DLPNO-MP2.

RI-MP2 conformational energies of 1,4-butanediol are reproduced by DLPNO-MP2 with high accuracy (Figure 2.11), incurring a mean absolute error of 0.01 kcal mol^{-1} and a largest error of 0.03 kcal mol^{-1}. Such a good agreement is likely achieved because of the small molecular size (16 atoms), so that the local approximations do not become fully

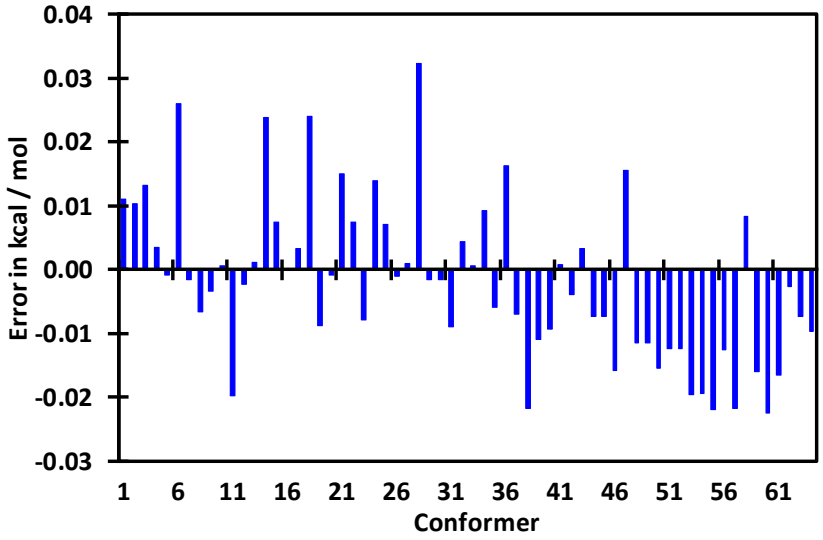

Figure 2.11: Errors in relative conformational energies of 1,4-butanediol.

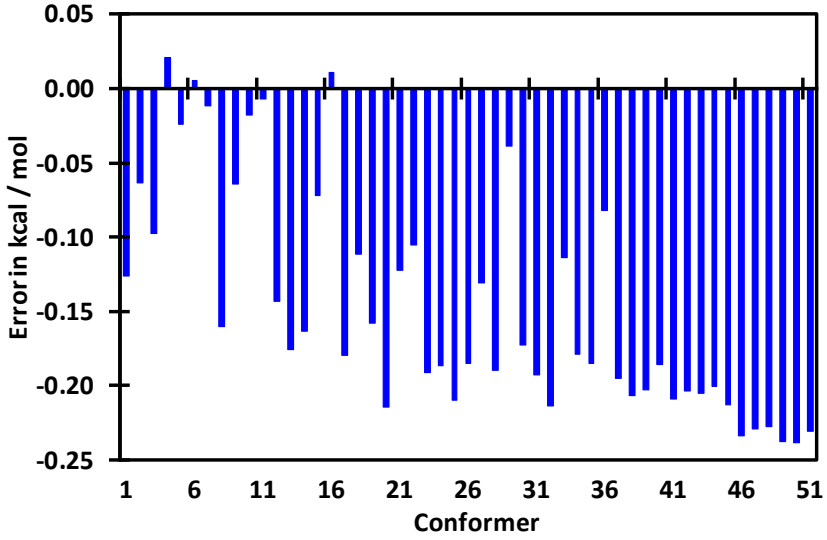

Figure 2.12: Errors in relative conformational energies of melatonin.

effective.

The errors in the relative energies of melatonin conformers with 33 atoms are significantly larger (Figure 2.12), with a mean absolute error of 0.15 kcal mol^{-1} and a maximal error of 0.24 kcal mol^{-1}. In most cases, the energy difference between the lowest and the higher lying conformers is underestimated.

The estimate of the intrinsic root mean square error of the MP2 method for the melatonin conformer energies is 0.91 kcal mol^{-1} (and 0.47 kcal mol^{-1} for the 12 lowest-lying conformers).[153] This exceeds the additional error introduced in DLPNO-MP2. However, TightPNO thresholds may be preferable for accurate calculations.

2.3.4.3 Noncovalent interactions

The S66 set contains geometries of non-covalently bonded molecule dimers with different types of interactions. Firstly, interaction energies in dimers were calculated without counterpoise correction as $E(\mathrm{AB}) - E(\mathrm{A}) - E(\mathrm{B})$, where $E(\mathrm{AB})$ is the energy of the dimer, and $E(\mathrm{A})$ and $E(\mathrm{B})$ are the respective energies of the monomer fragments. Second, counterpoise corrected energies were calculated as $E(\mathrm{AB}) - E(\mathrm{A}^*) - E(\mathrm{B}^*)$, with $E(\mathrm{A}^*)$ and $E(\mathrm{B}^*)$ as the respective energies of the monomers in the dimer basis set. Geometry relaxation is not accounted for in the definition of S66. The calculations were performed using the def2-TZVP set with def2-TZVP/C, and in addition also using the def2-TZVPD set in combination with the aug-cc-pVTZ/C auxiliary basis. Results are presented in Figure 2.13.

A maximum deviation of $0.30\,\mathrm{kcal\,mol^{-1}}$ between DLPNO-MP2 and RI-MP2 is obtained for dimer interaction energies using the def2-TZVP basis without counterpoise correction (Figure 2.13a). With the def2-TZVPD basis, the maximum error increases to $0.48\,\mathrm{kcal\,mol^{-1}}$. The mean absolute errors are $0.10\,\mathrm{kcal\,mol^{-1}}$ with the def2-TZVP set and $0.14\,\mathrm{kcal\,mol^{-1}}$ with def2-TZVPD. However, averaging over the entire set is not necessarily meaningful, as the systems in S66 span a very broad range of sizes: for the smallest dimer in the test set, $(H_2O)_2$, DLPNO-MP2 reproduces more than 99.99 % of the total RI-MP2 correlation energy with the default truncation thresholds. As the error relative to the total RI-MP2 correlation energy increases by an order of magnitude for larger systems, the largest errors are most relevant to assess the performance of the method. The results on threshold investigation in Section 2.3.1 suggest that the domain approximation is primarily responsible for the larger errors with the diffuse basis set.

DLPNO-MP2 predicts weaker bonding strengths of the monomers than RI-MP2 in most cases. The error of the MP2 method itself in the basis set limit has been reported as $0.45\,\mathrm{kcal\,mol^{-1}}$ (mean unsigned error) or $0.69\,\mathrm{kcal\,mol^{-1}}$ (root mean square error) for the S66 set.[155] While this means that even the largest deviations incurred from the local approximations are within the accuracy margins of the MP2 method, it may be advisable to use tighter thresholds when high precision is required.

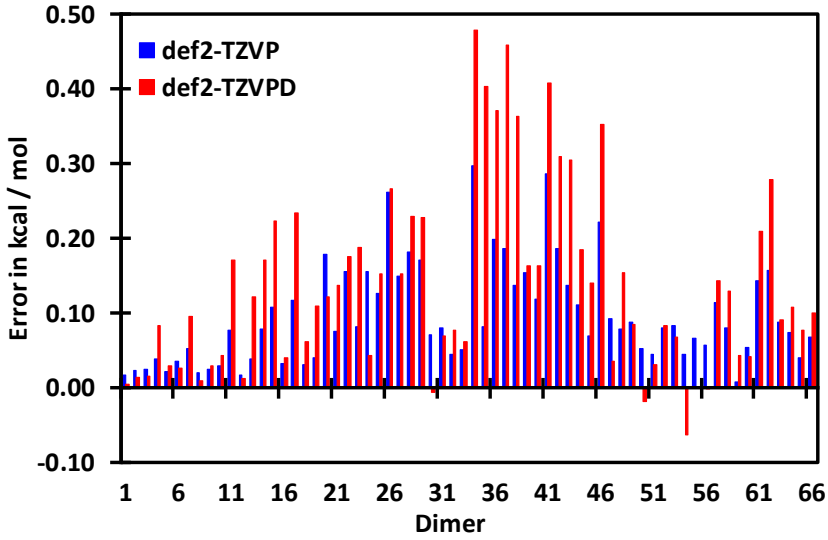

(a) Deviations of DLPNO-MP2 dimerisation energies from RI-MP2, each calculated without counterpoise corrections.

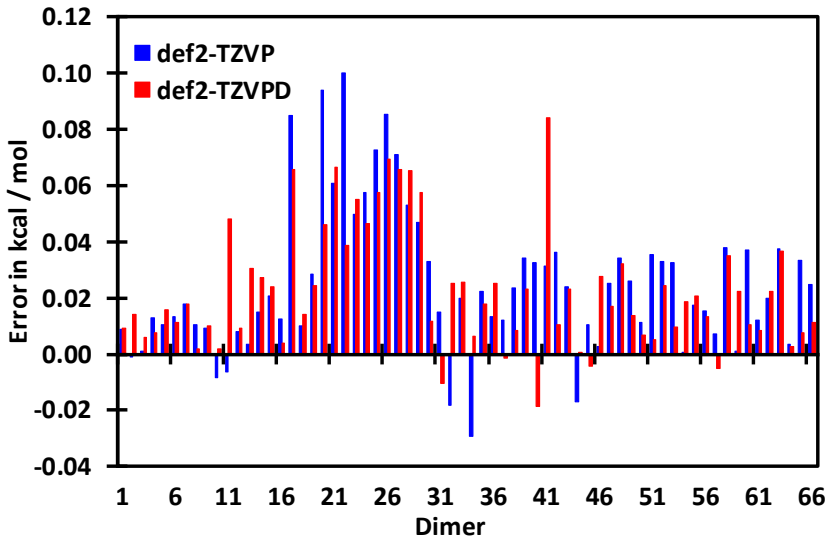

(b) Deviations of DLPNO-MP2 dimerisation energies from RI-MP2, each calculated with counterpoise corrections.

Figure 2.13: Errors in dimer interaction energies for the S66 set calculated with the def2-TZVP and def2-TZVPD basis sets.

With the counterpoise correction used for both DLPNO-MP2 and RI-MP2, the maximal error reduces to 0.1 kcal mol^{-1} (Figure 2.13b). The mean absolute error is below 0.03 kcal mol^{-1}; again, however, the averaged value is of limited meaning in this context. As before, the binding strength of the monomers is underestimated slightly in most cases.

The closer agreement between the counterpoise-corrected DLPNO-MP2 and RI-MP2 dimerisation energies appears to be the consequence of a more fortuitous error cancel-

lation. In the dimer basis, the relative error in the correlation energy of the monomers is close to that of the dimers, so that approximately 99.9 % of the respective RI-MP2 correlation energy is reproduced for both the monomers and the dimers in the larger examples. Without counterpoise correction, a larger proportion of the RI-MP2 energy is recovered in the monomer basis than in the dimer basis, leading to a systematic lowering of the monomer energies relative to the dimer.

2.3.5 Computational efficiency

2.3.5.1 Scaling of the integral transformation routine

Achieving optimal efficiency in a sparse integral transformation requires a compromise. On the one hand, truncating quantities to the largest possible extent may reduce the formal operation count and the amount of raw data that needs to be handled. On the other hand, using the efficient BLAS level 3 operations, in particular matrix multiplication, requires retaining a block-structure of the data. The computational effort for the integral transformation will be compared with the non-local routine implemented in ORCA, which is used for RI-MP2.

Figure 2.14 compares the performance of the local and non-local integral transformation routines for linear alkane chains with the implementation that we used in ref. [43]. Each calculation was performed on one CPU core using the def2-TZVP basis and the associated auxiliary basis set. With the relatively conservative thresholds used for DLPNO-MP2, linear scaling sets in beyond about 60 carbon atoms. For smaller systems we observed little discernible overhead for the local transformation compared with the non-local one.

With default truncation thresholds, the domains quickly reached a constant size, encompassing PAOs from about 16 atoms per orbital, and the fitting domains contained auxiliary functions from six atoms per orbital. On the other hand, the maps $\mathbf{L}(i \to \mu)$ and $\mathbf{L}(\tilde{\mu}' \to \nu)$ contained functions from about 45 atoms (MO to AO) and 70 atoms (PAO to AO), respectively, thus emphasising the extent of the tails of the localised MOs and of the PAOs. The extended domains reached constant sizes of 80 atoms in the

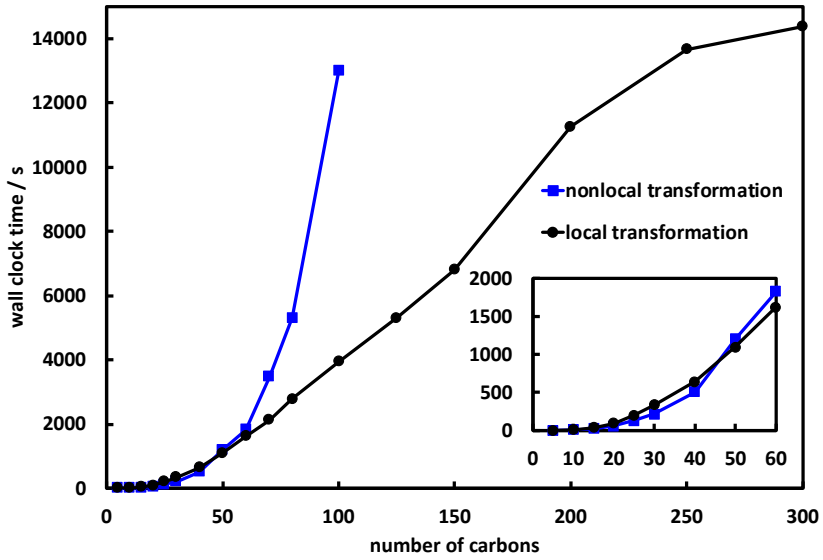

Figure 2.14: Timings for the transformation of RI integrals from $(\mu\nu|K)$ to $(i\tilde{\mu}'|K)$ for linear alkane chains. The calculations were performed with the def2-TZVP basis on one CPU core. All geometries were constructed with bond lengths $r_{\mathrm{C-C}} = 1.55\,\text{Å}$ and $r_{\mathrm{C-H}} = 1.09\,\text{Å}$, and with tetrahedral angles of 109.4712°. Inset: crossover between the local and non-local transformation routines.

case of $\mathbf{L}_{\mathrm{ext}}\,(i \to \tilde{\mu}')$ (MOs to PAOs), and 70 atoms for $\mathbf{L}_{\mathrm{ext}}\,(i \to K)$ (MOs to auxiliary functions).

2.3.5.2 Scaling of the DLPNO-MP2 algorithm

Linear alkane chains were used to examine the scaling of the DLPNO-MP2 method with system size. Figure 2.15 shows wall clock times determined with the def2-TZVP basis. The efficient RIJCOSX approximation[145] was used to accelerate the Hartree-Fock calculations. "VeryTightSCF" convergence criteria as documented for ORCA were used together with a standard model potential guess.

The crossover between wall clock times for canonical RI-MP2 and for DLPNO-MP2 occurs at a chain length of around 25 carbon atoms. More importantly, the DLPNO-MP2 calculations required consistently less computational effort than the preceding RHF calculations, even though the latter were accelerated with the RIJCOSX method.

In typical calculations, the three most expensive components are the transformation of the three-centre electron repulsion integrals; the calculation of the semicanonical amplitudes with PNO generation; and the iterative solution of the residual equations in

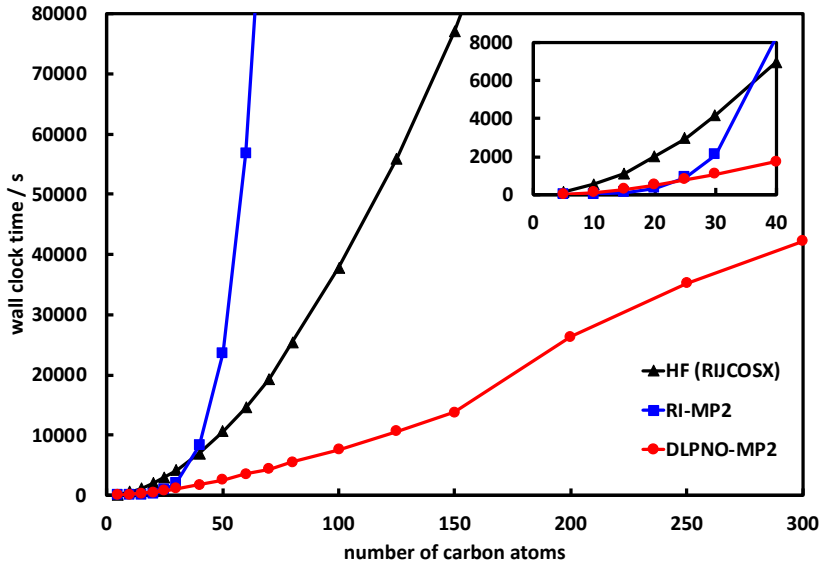

Figure 2.15: Wall clock times needed to perform DLPNO-MP2, RI-MP2 and Hartree-Fock calculations for linear alkane chains using the def2-TZVP basis. The HF calculations were performed with the efficient RIJCOSX approximation. Inset: crossover between DLPNO-MP2 and RI-MP2.

PNO basis. All of these exhibit an asymptotically linear scaling.

A breakdown of timings for different chain lengths is provided in Table A.7 in the Appendix. There are further parts of the calculation which do not scale linearly with system size. These include localisation of the occupied orbitals, calculation of the Fock and overlap matrices between all redundant PAOs in the system, calculation of the dipole integrals $\langle i|\mathbf{r}|\tilde{\mu}'\rangle$, grid setup for numerical evaluation of the differential overlap integrals, and the prescreening of orbital pairs. Orbital localisation can be made linear scaling in principle.[156]

2.3.5.3 Timings for representative systems

Alkane chains represent an ideal case for local correlation methods, as their linear structure permits a large number of contributions to be screened out. While this makes them well-suited to examine the asymptotic scaling behaviour of the algorithm, they are not representative for practical applications.

Table 2.7 contains detailed timings for several molecules, among which sildenafil, vancomycin and crambin possess a three-dimensional structure. In particular, the calculation

	$C_{150}H_{302}$	Sildenafil	Vancomycin	PVC_{75}	Crambin (def2-SVP)	Crambin (def2-TZVP)
No. of basis functions	6462	1209	3592	8787	6187	12 075
HF (RIJCOSX)	77 149	6644	68 591	[I]27 241	[II]18 461	[II]70 982
MO localisation	715	14	255	20 868	2160	10 608
DOI	948	34	274	1263	2387	4973
Dipole integrals	178	4.6	75	1371	460	3098
Prescreening	65	0.2	18	172	54	302
Screened out pairs / %	87	7	44	87	72	71
Three-index integral transformation	6801	303	13 995	22 754	177 756	1 601 289
Semicanonical amplitudes	2353	1696	21 139	14 320	54 814	372 503
PNO generation	930	663	7389	4834	4587	59 930
LMP2 iterations	1313	1575	15 250	16 517	24 925	164 886
No. of iterations	8	12	13	22	13	13
LMP2 (total)	13 768	4296	58 510	83 790	268 021	2 223 402

Table 2.7: Detailed timings in seconds for some selected systems. Unless noted otherwise, the calculations were performed with the def2-TZVP basis on one CPU core. (PVC_{75}: A $H-(CH_2CHCl)_{75}-H$ chain.) Default cutoffs were used in all calculations.
[I]Parallel execution on eight cores.
[II]Parallel execution on 16 cores.

for crambin (644 atoms) with the def2-TZVP basis is the most demanding single-point energy calculation performed in this work.

The time required to calculate the DLPNO-MP2 correlation energy is comparable to or even below that of the preceding Hartree-Fock calculation (multiplied with the number of CPU cores where appropriate). Note that the SCF procedure in these calculations was accelerated with the RIJCOSX approximation. Approximately comparable amounts of time were typically spent on the three major parts of the algorithm: the three-index integral transformation; formation of the semicanonical amplitudes together with PNO generation; and the LMP2 iterations in PNO basis. However, the timing for crambin is dominated by the computational cost of the RI integral transformation.

Finally, it is worth noting that the three major steps—performing the integral transformation, calculating the semicanonical amplitudes with the PNOs, and performing the LMP2 iterations—taken together account for over 97 % of the wall clock time. All of these components were shown to exhibit an asymptotically linear scaling with system size.

2.3.5.4 Memory requirements

Two major aspects determine the memory requirements of large-scale DLPNO-MP2 calculations, the first of which are various two-index integrals stored in global matrices. These include the overlap and Fock matrices in redundant PAO basis, the repulsion integrals $(K|L)$ between auxiliary functions, and the dipole integrals $\langle i|\mathbf{r}|\tilde{\mu}'\rangle$, which are used during orbital pair prescreening. These quantities are calculated initially for the entire system, and local matrices for specific domains are subsequently extracted during the calculation.

While the number of operations to calculate these matrices scales with up to $O(N^3)$, they did not appear as a major contribution to the overall wall clock times, even for the largest systems investigated. The $O(N^2)$ size of these quantities in memory eventually becomes a determining factor. This was most apparent for the linear systems, which place comparably modest requirements otherwise. The maximum amount of memory used by

the MP2 module during calculations with the def2-TZVP basis was 4.2 GB for $C_{150}H_{302}$ (6462 basis functions), 8.5 GB for $C_{150}H_{227}Cl_{75}$ (8787 basis functions), and 16.3 GB for $C_{300}H_{602}$ (12 912 basis functions).

Transforming the three-centre electron repulsion integrals is the second step which determines the memory footprint. It is dominant for calculations on large, three-dimensional systems.

In the first phase of the integral transformation (calculation of the integrals), a matrix of size $N(\mu) \times N(\nu)$ needs to be stored in memory for each auxiliary function K in a given shell. The superblock of basis functions μ to expand the occupied molecular orbitals is encoded by the sparse map $\mathbf{L}_{\text{ext}}\,(K \to i) \circ \mathbf{L}\,(i \to \mu_{\text{A}})$. For the PAOs, the sparse map $\mathbf{L}_{\text{ext}}\,(K \to i) \circ \mathbf{L}_{\text{ext}}\,(i \to \tilde{\mu}'_{\text{A}}) \circ \mathbf{L}_{\text{ext}}\,(\tilde{\mu}'_{\text{A}} \to \nu_{\text{A}})$ provides the superblock of atomic basis functions ν. Once an index has been transformed to the occupied MO basis, a much smaller amount of memory is required for the integrals.

In the second phase of the integral transformation (sorting of the already computed integrals), at least one matrix of size $N(K) \times N(\tilde{\mu}')$ needs be stored in memory for each occupied orbital i at a time. The numbers of auxiliary functions K and PAOs $\tilde{\mu}'$ are determined by the sparse lists $L_{\text{ext}}\,(i \to K)$ and $L_{\text{ext}}\,(i \to \tilde{\mu}')$, respectively. Asymptotically, the sizes of these matrices would become independent of the molecular size. The routine uses all available memory up to a user-specified threshold to store the sorted integrals in memory, which minimises the number of requests for disk access.

In order to perform a DLPNO-MP2 calculation without abortion or performance penalties due to lack of memory, 2.1 GB were sufficient for vancomycin in def2-TZVP basis (3593 basis functions), and 6.5 GB for crambin in def2-SVP basis (6187 basis functions). Even though the memory consumption for crambin in def2-TZVP (12 075 basis functions) was not monitored at the point of performing this single-point energy calculation, we estimate it at ca. 25 GB.

2.4 Unrestricted local MP2 with pair natural orbitals

2.4.1 Møller-Plesset theory with unrestricted orbitals

In the unrestricted Hartree-Fock method (UHF), spin up and spin down orbitals have different spatial components. The UHF energy is represented in the following equation,[128]

$$E_{\mathrm{UHF}} = V_{\mathrm{NN}} + \sum_{\sigma=\alpha,\beta} \sum_{i}^{\sigma} h_{ii} + \frac{1}{2} \sum_{\sigma=\alpha,\beta} \sum_{\tau=\alpha,\beta} \sum_{i}^{\sigma} \sum_{j}^{\tau} (ii|jj) - \frac{1}{2} \sum_{\sigma=\alpha,\beta} \sum_{ij}^{\sigma} (ij|ij)\,, \quad (2.65)$$

with spin orbitals labelled as i, j. A superscript in each summation sign indicates if the orbitals are of α spin or of β spin. Only real orbitals are considered in this work.

The ground-state Slater determinant is an eigenfunction of the unrestricted Fock operator:

$$\begin{aligned} \hat{F} &= \sum_{\sigma=\alpha,\beta} \sum_{pq}^{\sigma} F_{pq}^{\sigma} \hat{a}_p^\dagger \hat{a}_q \\ F_{pq}^{\sigma} &= h_{pq} + \sum_{\tau=\alpha,\beta} \sum_{i}^{\tau} (ii|pq) - \sum_{i}^{\sigma} (ip|iq) \end{aligned} \quad (2.66)$$

Similar to the spin-restricted case, the MP2 energy in a basis of unrestricted canonical orbitals is provided in the following equation:[128]

$$E^{(2)} = -\frac{1}{2} \sum_{\sigma,\tau} \sum_{ia}^{\sigma} \sum_{jb}^{\tau} \frac{(ia|jb)^2}{\varepsilon_a + \varepsilon_b - \varepsilon_i - \varepsilon_j} + \frac{1}{2} \sum_{\sigma} \sum_{ijab}^{\sigma} \frac{(ia|jb)\,(ib|ja)}{\varepsilon_a + \varepsilon_b - \varepsilon_i - \varepsilon_j} \quad (2.67)$$

In a non-canonical basis of molecular orbitals, the MP2 energy can be calculated via the Hylleraas functional:[157]

$$E_2 = \sum_{ijab} (ia|jb)\, T_{ab}^{ij} + \frac{1}{2} \sum_{ijabc} F_{cb} T_{ab}^{ij} T_{ac}^{ij} - \frac{1}{2} \sum_{ijkab} F_{kj} T_{ab}^{ij} T_{ab}^{ik} \quad (2.68)$$

For simplicity, the labels i, j, k and a, b, c refer to the respective occupied and virtual orbitals of both α and β spin. As a consequence of the antisymmetry of a Slater determinant, the amplitudes are bound to the following permutation relation:

$$T_{ab}^{ij} = -T_{ba}^{ij} = -T_{ab}^{ji} = T_{ba}^{ji} \quad (2.69)$$

The set of amplitudes that minimises the Hylleraas functional is found by solving the residual equations $R_{ab}^{ij} = 0$, with the residual

$$R_{ab}^{ij} = (ia|jb) - (ib|ja) + \sum_c F_{ac} T_{cb}^{ij} + \sum_c T_{ac}^{ij} F_{cb} - \sum_k F_{ik} T_{ab}^{kj} - \sum_k F_{kj} T_{ab}^{ik}. \quad (2.70)$$

After the set of equations has been solved, the amplitudes can be used to calculate the second-order energy:

$$E^{(2)} = \frac{1}{2} \sum_{ijab} (ia|jb)\, T_{ab}^{ij} \quad (2.71)$$

2.4.2 Approximations in the unrestricted local MP2 method

Following an unrestricted Hartree-Fock calculation, different sets of orbitals i_α and i_β are obtained for the spin up and spin down electrons. Accordingly, the two orbitals sets are localised separately. The unoccupied space is represented using projected atomic orbitals:

$$|\tilde{\mu}'_\sigma\rangle = N_{\tilde{\mu}'_\sigma} \left[1 - \sum_i^\sigma |i\rangle \langle i| \right] |\mu\rangle \quad (2.72)$$

Note that the α PAOs $\tilde{\mu}'_\alpha$ are obtained by a projection of the atomic orbitals onto the space spanned by the virtual α MOs, and the β PAOs likewise by a projection onto the unoccupied β space.

In consequence, there are four types of pair domains:

1. Domains of α PAOs for pairs of two α MOs: $\{i_\alpha j_\alpha\} = \{i_\alpha\}^\alpha \cup \{j_\alpha\}^\alpha$
2. Domains of β PAOs for pairs of two β MOs: $\{i_\beta j_\beta\} = \{i_\beta\}^\beta \cup \{j_\beta\}^\beta$
3. Domains of α PAOs for opposite-spin pairs: $\{i_\alpha j_\beta\}^\alpha = \{i_\alpha\}^\alpha \cup \{j_\beta\}^\alpha$
4. Domains of β PAOs for opposite-spin pairs: $\{i_\alpha j_\beta\}^\beta = \{i_\alpha\}^\beta \cup \{j_\beta\}^\beta$

Because the differential overlap criterion takes into account the properties of the virtual functions, a domain of α PAOs obtained for a given α MO, $\{i_\alpha\}^\alpha$, is different from the domain of β PAOs $\{i_\alpha\}^\beta$ for the same α spin MO. Likewise, two different domains $\{i_\alpha\}^\beta$

and $\{i_\beta\}^\alpha$ are obtained for each β MO. However, there is only one fitting domain $\{i_\sigma\}_{\mathrm{RI}}$ for each spin orbital, as it is determined using the populations of each MO.

RI integrals contain only combinations of orbitals and PAOs with the same spin. The extended maps, which are used in the integral transformation, need to include PAOs of both same-spin and opposite-spin molecular orbital pairs:

$$L_{\mathrm{ext}}\left(i_\alpha \to \tilde{\mu}'_\alpha\right) = L\left(i_\alpha \to j_\alpha\right) \circ \mathbf{L}\left(j_\alpha \to \tilde{\mu}'_\alpha\right) \cup L\left(i_\alpha \to j_\beta\right) \circ \mathbf{L}\left(j_\beta \to \tilde{\mu}'_\alpha\right) \tag{2.73}$$

$$L_{\mathrm{ext}}\left(i_\alpha \to K\right) = L\left(i_\alpha \to j_\alpha\right) \circ \mathbf{L}\left(j_\alpha \to K\right) \cup L\left(i_\alpha \to j_\beta\right) \circ \mathbf{L}\left(j_\beta \to K\right) \tag{2.74}$$

The preceding examples for α spin apply in an identical manner to β spin. Truncation of the atomic orbital coefficients during the integral transformation is performed in an analogous manner to the closed-shell DLPNO-MP2 method.

Pair natural orbitals are constructed similarly to Hansen and co-workers' unrestricted local pair natural orbital (UHF-LPNO-CCSD) approach.[158] Semicanonical amplitudes for same-spin pairs are calculated in a non-redundant virtual basis spanned by the PAOs in the pair domain $\{i_\sigma j_\sigma\}$:

$$\breve{T}^{i_\sigma j_\sigma}_{\tilde{\mu}_\sigma \tilde{\nu}_\sigma} = -\frac{(i_\sigma \tilde{\mu}_\sigma | j_\sigma \tilde{\nu}_\sigma) - (i_\sigma \tilde{\nu}_\sigma | j_\sigma \tilde{\mu}_\sigma)}{\varepsilon_{\tilde{\mu}_\sigma} + \varepsilon_{\tilde{\nu}_\sigma} - F_{i_\sigma i_\sigma} - F_{j_\sigma j_\sigma}} \tag{2.75}$$

For opposite-spin pairs, the semicanonical amplitudes are rectangular matrices. The virtual spaces for spin up and spin down electrons are spanned by PAOs in the domains $\{i_\alpha j_\beta\}^\alpha$ and $\{i_\alpha j_\beta\}^\beta$, respectively:

$$\breve{T}^{i_\alpha j_\beta}_{\tilde{\mu}_\alpha \tilde{\nu}_\beta} = -\frac{(i_\alpha \tilde{\mu}_\alpha | j_\beta \tilde{\nu}_\beta)}{\varepsilon_{\tilde{\mu}_\alpha} + \varepsilon_{\tilde{\nu}_\beta} - F_{i_\alpha i_\alpha} - F_{j_\beta j_\beta}} \tag{2.76}$$

PNOs for same-spin pairs are calculated through diagonalisation of their virtual pair density contribution:

$$\breve{\mathbf{D}}^{i_\sigma j_\sigma} = \breve{\mathbf{T}}^{i_\sigma j_\sigma} \breve{\mathbf{T}}^{i_\sigma j_\sigma \dagger} \tag{2.77}$$

Two sets of PNOs need to be constructed for opposite-spin pairs. They are obtained from

the respective virtual pair density contributions in α PAO basis,

$$\breve{\mathbf{D}}^{i_\alpha j_\beta(\alpha)} = \breve{\mathbf{T}}^{i_\alpha j_\beta} \breve{\mathbf{T}}^{i_\alpha j_\beta \dagger}, \tag{2.78}$$

and in β PAO basis:

$$\breve{\mathbf{D}}^{i_\alpha j_\beta(\beta)} = \breve{\mathbf{T}}^{i_\alpha j_\beta \dagger} \breve{\mathbf{T}}^{i_\alpha j_\beta}. \tag{2.79}$$

A significant shortcoming of the unrestricted PNO construction scheme is its inconsistency with the restricted closed-shell approach. Given a set of orbitals for a closed-shell system without any symmetry breaking, UHF-DLPNO-MP2 produces a different energy than the RHF-DLPNO-MP2 method. This is an inherent feature of the UHF-based PNO construction scheme, which cannot be made universally consistent with the RHF case simply by using a different truncation threshold. All other approximations in the RHF and UHF variants of DLPNO-MP2 are consistent, though.

To circumvent the difficulties resulting from PNO construction for unrestricted occupied orbitals, Saitow and co-workers implemented the DLPNO-CCSD method with a PNO construction scheme derived from n-electron valence state perturbation theory (NEVPT).[46] This approach requires a set of restricted open-shell reference orbitals. The doubly occupied and unoccupied orbitals are treated analogously to the inactive occupied and virtual orbitals in a NEVPT2 calculation based on a CASSCF reference wave function, while the singly occupied molecular orbitals are treated analogously to the active space. While this approach to construct PNOs is substantially more complicated than straightforward unrestricted Møller-Plesset perturbation theory, it produces only one set of PNOs for each spin-free orbital pair, and it is consistent with the closed-shell variant of DLPNO-CCSD. Krause and Werner developed a spin-restricted open-shell variant of PNO-based local MP2.[61] Their method constructs the perturbed wave function in terms of spin-adapted configurations, and thereby also uses only one set of PNOs per orbital pair.

Residual equations analogous to Eq. (2.70) need to be solved to determine the ampli-

tudes. The specific expression for same-spin pairs is

$$R_{\tilde{a}_\sigma \tilde{b}_\sigma}^{i_\sigma j_\sigma} = \left(i\tilde{a}\middle|j\tilde{b}\right) - \left(i\tilde{b}\middle|j\tilde{a}\right) + \left[\varepsilon_{\tilde{a}} + \varepsilon_{\tilde{b}} - F_{ii} - F_{jj}\right] T_{\tilde{a}\tilde{b}}^{ij} - \sum_{k\neq i}^{\sigma} F_{ik} \sum_{\tilde{c}\tilde{d}}^{\sigma} S_{\tilde{a}\tilde{c}} T_{\tilde{c}\tilde{d}}^{kj} S_{\tilde{d}\tilde{b}} - \sum_{k\neq j}^{\sigma} F_{kj} \sum_{\tilde{c}\tilde{d}}^{\sigma} S_{\tilde{a}\tilde{c}} T_{\tilde{c}\tilde{d}}^{ik} S_{\tilde{d}\tilde{b}} \quad \text{with} \quad \sigma = \alpha, \beta, \quad (2.80)$$

and for opposite-spin pairs it is:

$$R_{\tilde{a}_\alpha \tilde{b}_\beta}^{i_\alpha j_\beta} = \left(i\tilde{a}\middle|j\tilde{b}\right) + \left[\varepsilon_{\tilde{a}} + \varepsilon_{\tilde{b}} - F_{ii} - F_{jj}\right] T_{\tilde{a}\tilde{b}}^{ij} - \sum_{k\neq i}^{\alpha} F_{ik} \sum_{\tilde{c}}^{\alpha} \sum_{\tilde{d}}^{\beta} S_{\tilde{a}\tilde{c}} T_{\tilde{c}\tilde{d}}^{kj} S_{\tilde{d}\tilde{b}} - \sum_{k\neq j}^{\beta} F_{kj} \sum_{\tilde{c}}^{\alpha} \sum_{\tilde{d}}^{\beta} S_{\tilde{a}\tilde{c}} T_{\tilde{c}\tilde{d}}^{ik} S_{\tilde{d}\tilde{b}}. \quad (2.81)$$

Unambiguous spin indices have been omitted on the right-hand sides of the equations for simplicity. There are three sets of linear equations to be solved independently: to determine the amplitudes for α-α pairs, for β-β pairs, and for α-β pairs. As in the closed-shell DLPNO-MP2 method, negligible internal Fock matrix elements are dropped during the residual construction.

Same-spin amplitudes are stored only for $i_\sigma > j_\sigma$, exploiting their permutational symmetry $\mathbf{T}^{ji} = -\mathbf{T}^{ij}$. A full square matrix is stored for each pair, as this format is most suited for matrix operations, even though this leads to a redundancy with respect to the exchange of the virtual indices, $T_{\tilde{a}\tilde{b}}^{ij} = -T_{\tilde{b}\tilde{a}}^{ij}$. Opposite-spin pair amplitudes are handled via their permutationally unique components $T_{\tilde{a}_\alpha \tilde{b}_\beta}^{i_\alpha j_\beta}$.

After the amplitudes have been determined, the second-order correlation energy is calculated via:

$$E^{(2)} = \sum_{\sigma=\alpha,\beta} \sum_{i>j}^{\sigma} \sum_{\tilde{a}\tilde{b}}^{\sigma} \left(i\tilde{a}\middle|j\tilde{b}\right) T_{\tilde{a}\tilde{b}}^{ij} + \sum_{i\tilde{a}}^{\alpha} \sum_{j\tilde{b}}^{\beta} \left(i\tilde{a}\middle|j\tilde{b}\right) T_{\tilde{a}\tilde{b}}^{ij} \quad (2.82)$$

An energy correction for PNO truncation, ΔE_{PNO}, is included similarly as in the closed-shell method. For this purpose, the difference is taken between the energies calculated with the semicanonical amplitudes before and after their projection to the truncated PNO basis.

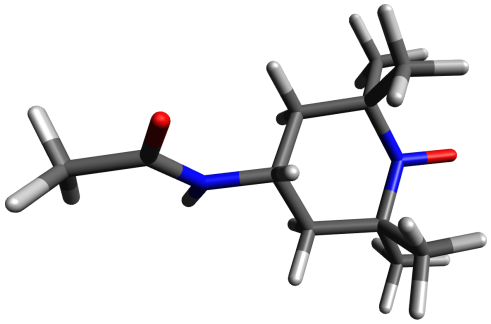

Figure 2.16: Structure of the 4-acetamido-TEMPO radical.

The pair-prescreening procedure has been defined in a consistent way with its closed-shell counterpart. Firstly, an orbital pair is screened out only if the differential overlap of the spatial components, as defined in Eq. (2.39), is below the threshold T_{CutDOij}. Secondly, the collinear dipole energy of the pair is calculated:

$$\varepsilon_{ij}^{\mathrm{COL(UHF)}} = -\frac{4}{|\mathbf{R}^{ij}|^6} \sum_{\tilde{\mu}\tilde{\nu}} \frac{|\langle i|\mathbf{r}|\tilde{\mu}\rangle|^2 \, |\langle j|\mathbf{r}|\tilde{\nu}\rangle|^2}{\varepsilon_{\tilde{\mu}} + \varepsilon_{\tilde{\nu}} - F_{ii} - F_{jj}} \tag{2.83}$$

Since $\varepsilon_{ij}^{\mathrm{COL(UHF)}}$ is related by a factor of $\frac{1}{4}$ to its closed-shell counterpart in Eq. (2.40), a spin orbital pair is screened out only if $\left|\varepsilon_{ij}^{\mathrm{COL(UHF)}}\right| < \frac{1}{4} T_{\mathrm{CutPre}}$.

All orbital pairs that have been excluded from the subsequent MP2 calculations are accounted for with the contribution

$$\varepsilon_{ij}^{\mathrm{DIP(UHF)}} = -\sum_{\tilde{\mu}_i\tilde{\nu}_j} \frac{\left(M_{\tilde{\mu}_i\tilde{\nu}_j}^{ij}\right)^2}{\varepsilon_{\tilde{\mu}_i} + \varepsilon_{\tilde{\nu}_j} - F_{ii} - F_{jj}}. \tag{2.84}$$

It is related to the expression for spatial orbitals in Eq. (2.37) by a factor of $\frac{1}{4}$.

2.4.3 Thresholds and performance

With the exception of the PNO truncation, all other approximations in the UHF-DLPNO-MP2 method are consistent with its RHF counterpart, and therefore the associated thresholds are left unchanged. The PNO truncation threshold is investigated in this section.

The influence of T_{CutPNO} was examined for the 4-acetamido-TEMPO radical, which is depicted in Figure 2.16. All other truncation thresholds were set to zero. The calculations

$E_C(\alpha\alpha)/E_h$	$E_C(\beta\beta)/E_h$	$E_C(\alpha\beta)/E_h$	$E_C(\text{total})/E_h$
−0.333 983	−0.330 999	−2.025 985	−2.690 968

(a) RI-MP2 correlation energy and its spin components.

T_{CutPNO}	% of E_C(RI-MP2)			
	$\alpha\alpha$	$\beta\beta$	$\alpha\beta$	total
10^{-7}	99.55	99.53	99.71	99.67
10^{-8}	99.74	99.73	99.87	99.84
10^{-9}	99.86	99.86	99.95	99.92
10^{-10}	99.94	99.93	99.98	99.97

(b) Percentages of the RI-MP2 correlation energy recovered with different pair natural orbital truncation thresholds. The energy correction for PNO truncation ΔE_{PNO} has been included.

T_{CutPNO}	PNOs ($\alpha\alpha$)	PNOs ($\beta\beta$)	α-PNOs ($\alpha\beta$)	β-PNOs ($\alpha\beta$)
10^{-7}	11.3	11.7	10.0	10.0
10^{-8}	22.1	22.7	20.5	20.5
10^{-9}	40.7	41.7	38.7	38.7
10^{-10}	70.1	71.6	67.6	67.6

(c) Average number of PNOs per pair.

Table 2.8: Pair natural orbital truncation examined for the 4-acetamido-TEMPO radical (doublet state) using the def2-TZVP basis. All other truncation thresholds were set to zero.

were performed with the def2-TZVP basis, and the core orbitals were frozen.

Table 2.8b shows the recovered percentages of the total RI-MP2 correlation energy, and of its contributions by same-spin and opposite-spin pairs. Despite including the PNO truncation correction ΔE_{PNO}, a smaller fraction of the total correlation energy is recovered than would be expected with RHF-DLPNO-MP2 using the same threshold. A second observation is that a smaller percentage of the energy is recovered for same-spin pairs than for opposite-spin pairs. However, the former contribute a much smaller part of the total energy than the latter. Counterintuitively, similar numbers of PNOs are obtained on average for same-spin and opposite-spin pairs with the same T_{CutPNO}, as shown in Table 2.8c.

For a direct comparison between the RHF and UHF variants of DLPNO-MP2, the calculations were repeated with the cation of 4-acetamido-TEMPO. The behaviour of

$E_C(\alpha\alpha/\beta\beta)/E_h$	$E_C(\alpha\beta)/E_h$	$E_C(\text{total})/E_h$
−0.331 442	−2.032 541	−2.695 424

(a) RI-MP2 correlation energy and its spin components.

T_{CutPNO}	% of E_C(RI-MP2)			
	$\alpha\alpha/\beta\beta$	$\alpha\beta$	total	RHF-DLPNO-MP2
10^{-7}	99.54	99.72	99.68	99.90
10^{-8}	99.74	99.88	99.84	99.96
10^{-9}	99.86	99.95	99.93	99.99
10^{-10}	99.94	99.98	99.97	100.00

(b) Percentages of the RI-MP2 correlation energy recovered with different pair natural orbital truncation thresholds. The energy correction for PNO truncation ΔE_{PNO} has been included.

T_{CutPNO}	UHF-DLPNO-MP2		RHF-DLPNO-MP2
	PNOs ($\alpha\alpha/\beta\beta$)	PNOs ($\alpha\beta$)	PNOs
10^{-7}	11.7	10.3	23.6
10^{-8}	22.9	21.1	44.2
10^{-9}	42.2	39.9	77.8
10^{-10}	72.8	70.0	127.7

(c) Average number of PNOs per pair.

Table 2.9: Pair natural orbital truncation examined for the closed-shell 4-acetamido-TEMPO cation using the def2-TZVP basis. All other truncation thresholds were set to zero.

UHF-DLPNO-MP2 for the doublet radical in Table 2.8 and for the singlet cation in Table 2.9 is very similar. In a calculation with a UHF reference, T_{CutPNO} needs to scaled with a factor of 0.1 to obtain a comparable number of PNOs per pair as with an RHF reference (Table 2.9b). Nevertheless, the percentage of the total correlation energy recovered with the tighter threshold is still somewhat smaller than in the RHF case.

A comparison of the RHF and UHF variants of DLPNO-MP2 for the closed-shell molecule sildenafil is presented in Table 2.11. In these calculations, the differential overlap threshold for domain selection T_{CutDO} was set to its respective "LoosePNO", "NormalPNO" and "TightPNO" values, and the influence of T_{CutPNO} on the correlation energy and the wall clock time was examined. Default values were used for all remaining cutoffs. As an additional modification, calculations were performed not only with identical values of

Threshold	LoosePNO	NormalPNO	TightPNO
T_{CutPNO}	1×10^{-8}	1×10^{-9}	1×10^{-10}
T_{CutDO}	2×10^{-2}	1×10^{-2}	5×10^{-3}

Table 2.10: Truncation thresholds in the UHF-DLPNO-MP2 method.

T_{CutPNO} for all pairs, but also with a tighter threshold for same-spin pairs to recover their energy more accurately.

As previously, the calculations confirm that the T_{CutPNO} settings used in RHF-DLPNO-MP2 are not adequate for the UHF variant, and even scaling them with a factor of 0.1 still leads to somewhat less accurate energies. This finding is qualitatively consistent with the observations of Hansen and co-workers for the UHF-LPNO-CCSD method.[158] The computational expense for the entire UHF-DLPNO-MP2 calculation with this tighter cutoff is by a factor of 3 to 5 larger than that for RHF-DLPNO-MP2. Choosing a tighter threshold for the same-spin pairs than for opposite-spin pairs does not lead to a worthwhile improvement in the relation between accuracy and performance; therefore, T_{CutPNO} is assigned the same value for all valence pairs. In this context, it is worth mentioning that spin component-scaled MP2[116] and related schemes reduce the same-spin contribution and increase the opposite-spin contribution with empirical parameters.

The chosen default settings are summarised in Table 2.10. As in the case of RHF-DLPNO-MP2, the threshold for pairs with one or two core orbitals is obtained by scaling T_{CutPNO} with a factor of 0.01.

T_{CutPNO}		% of E_{C}(RI-MP2)			$t_{\mathrm{DLPNO-MP2}}$ / s
$\alpha\alpha/\beta\beta$	$\alpha\beta$	$\alpha\alpha/\beta\beta$	$\alpha\beta$	total	
10^{-7}	10^{-7}	99.43	99.56	99.53	2152
10^{-8}	10^{-7}	99.65	99.56	99.59	2343
10^{-8}	10^{-8}	99.65	99.74	99.71	2595
10^{-9}	10^{-8}	99.79	99.74	99.75	2898

(a) UHF-DLPNO-MP2 calculations with $T_{\mathrm{CutDO}} = 2 \times 10^{-2}$ to determine a T_{CutPNO} value for "LoosePNO" settings.

T_{CutPNO}		% of E_{C}(RI-MP2)			$t_{\mathrm{DLPNO-MP2}}$ / s
$\alpha\alpha/\beta\beta$	$\alpha\beta$	$\alpha\alpha/\beta\beta$	$\alpha\beta$	total	
10^{-8}	10^{-8}	99.70	99.81	99.78	3662
10^{-9}	10^{-8}	99.84	99.81	99.82	4214
10^{-9}	10^{-9}	99.84	99.89	99.88	4541
10^{-10}	10^{-9}	99.91	99.89	99.90	5531

(b) UHF-DLPNO-MP2 calculations with $T_{\mathrm{CutDO}} = 1 \times 10^{-2}$ to determine a T_{CutPNO} value for "NormalPNO" settings.

T_{CutPNO}		% of E_{C}(RI-MP2)			$t_{\mathrm{DLPNO-MP2}}$ / s
$\alpha\alpha/\beta\beta$	$\alpha\beta$	$\alpha\alpha/\beta\beta$	$\alpha\beta$	total	
10^{-9}	10^{-9}	99.85	99.91	99.90	6461
10^{-10}	10^{-9}	99.93	99.91	99.92	7610
10^{-10}	10^{-10}	99.93	99.95	99.95	9434
10^{-11}	10^{-10}	99.97	99.95	99.96	11 005

(c) UHF-DLPNO-MP2 calculations with $T_{\mathrm{CutDO}} = 5 \times 10^{-3}$ to determine a T_{CutPNO} value for "TightPNO" settings.

	T_{CutPNO}	T_{CutDO}	% of E_{C}(RI-MP2)	$t_{\mathrm{DLPNO-MP2}}$ / s
LoosePNO	10^{-7}	2×10^{-2}	99.77	590
NormalPNO	10^{-8}	1×10^{-2}	99.92	1070
TightPNO	10^{-9}	5×10^{-3}	99.97	3396

(d) Closed-shell calculations with RHF-DLPNO-MP2 using its default settings.

Table 2.11: Percentages of the correlation energy recovered with UHF-DLPNO-MP2 for sildenafil (closed-shell), and the total wall clock times for the MP2 module. The calculations were performed with the def2-TZVP basis using four parallel processes. Default values were used for the remaining thresholds. The domain cutoff T_{CutDO} was set as specified in the descriptions.

Chapter 3

Analytical gradient for domain-based local pair natural orbital Møller-Plesset perturbation theory

3.1 Theory

3.1.1 Introductory aspects of derivative theory

3.1.1.1 The Lagrangian method for derivatives

As a convenient, powerful and general tool, the Lagrangian approach is well-established in the theory of analytical derivatives for quantum chemical methods. However, literature that can act as an accessible introduction is scarce, and often limited to lecture notes or proceedings such as in ref. [88]. Therefore, a brief introduction will be provided in this section.

Consider an energy expression E that is subject to external variables $\mathbf{x}$, and is parameterised using a set of variables $\mathbf{t}$:

$$E = E(\mathbf{x}, \mathbf{t}(\mathbf{x})) \tag{3.1}$$

$\mathbf{x}$ represents external variables entering the molecular Hamiltonian, such as nuclear coor-

dinates or an external field. Parameters may include, for example, coefficients of molecular orbitals, or excitation amplitudes in the case of a correlated method; for the sake of simplicity, all of them are represented as $\mathbf{t}$ in this argument. Differentiation of the energy expression yields by the chain rule:

$$\frac{dE}{d\mathbf{x}} = \frac{\partial E}{\partial \mathbf{x}} + \frac{\partial E}{\partial \mathbf{t}} \frac{d\mathbf{t}}{d\mathbf{x}} \tag{3.2}$$

In fully variational methods the energy expression is stationary with respect to all parameters, $\frac{\partial E}{\partial \mathbf{t}} = 0$, which permits a relatively straightforward evaluation of derivatives. If the method builds upon an atomic orbital basis with the one-electron integrals $h_{\mu\nu}$, the two-electron integrals $(\mu\nu|\eta\lambda)$ and the overlap integrals $S_{\mu\nu}$, the derivative expression becomes:

$$\frac{dE}{d\mathbf{x}} = \frac{\partial V_{\mathrm{NN}}}{\partial \mathbf{x}} + \sum_{\mu\nu} D_{\mu\nu} \frac{\partial h_{\mu\nu}}{\partial \mathbf{x}} + \sum_{\mu\nu\eta\lambda} \Gamma^{\eta\lambda}_{\mu\nu} \frac{\partial \left(\mu\nu|\eta\lambda\right)}{\partial \mathbf{x}} + \sum_{\mu\nu} W_{\mu\nu} \frac{\partial S_{\mu\nu}}{\partial \mathbf{x}} \tag{3.3}$$

$\mathbf{D}$ is the reduced one-particle density matrix. Similarly, $\mathbf{\Gamma}$ is the two-particle density tensor, and $\mathbf{W}$ is the energy-weighted density matrix:

$$D_{\mu\nu} = \frac{\partial E}{\partial h_{\mu\nu}} \tag{3.4}$$

$$\Gamma^{\eta\lambda}_{\mu\nu} = \frac{\partial E}{\partial \left(\mu\nu|\eta\lambda\right)} \tag{3.5}$$

$$W_{\mu\nu} = \frac{\partial E}{\partial S_{\mu\nu}} \tag{3.6}$$

V_{NN} represents the internuclear repulsion.

Many correlated methods, for example Møller-Plesset perturbation theory or coupled cluster, are not variational. A naïve implementation of derivatives would need to calculate the response $\frac{d\mathbf{t}}{d\mathbf{x}}$ in Eq. (3.2) for each perturbation. In practice, this is not necessary to obtain first derivatives. Handy and Schaefer developed the Z-vector method: by identifying a set of suitable intermediates, they showed that it is sufficient to solve only one set of coupled-perturbed self-consistent field (CP-SCF) equations instead of calculating the

response of the molecular orbitals for each perturbation.[159] Similarly, it was shown for coupled cluster theory that the response of the amplitudes does not need to be determined to calculate first derivatives.[160–162]

Rice and Amos realised that integral derivatives in atomic orbital basis never need to be transformed or stored to calculate an analytical gradient.[163] The Lagrangian method was developed by Jørgensen and Helgaker, who constructed a formalism that conveniently and methodically incorporates the aforementioned advantages.[164, 165]

Suppose that the parameters $\mathbf{t}$ in Eq. (3.1) are determined entirely through a set of constraints g_n:

$$g_n(\mathbf{x}, \mathbf{t}(\mathbf{x})) = 0 \tag{3.7}$$

A Lagrangian function can thus be constructed for the energy:

$$\mathcal{L}(\mathbf{x}, \mathbf{t}(\mathbf{x}), \boldsymbol{\lambda}(\mathbf{x})) = E(\mathbf{x}, \mathbf{t}(\mathbf{x})) + \sum_n \lambda_n(\mathbf{x}) g_n(\mathbf{x}, \mathbf{t}(\mathbf{x})) \tag{3.8}$$

Since each constraint $g_n(\mathbf{x})$ is zero, its total derivative with respect to the external parameters vanishes, $\frac{dg_n}{d\mathbf{x}} = 0$. Therefore, the total derivative of the Lagrangian equals that of the energy:

$$\frac{d\mathcal{L}}{d\mathbf{x}} = \frac{dE}{d\mathbf{x}} \tag{3.9}$$

The Lagrangian is made stationary with respect to the parameters $\mathbf{t}$, which leads to a set of linear equations to determine the Lagrange multipliers λ_n:

$$\frac{\partial \mathcal{L}}{\partial \mathbf{t}} = \frac{\partial E}{\partial \mathbf{t}} + \sum_n \lambda_n \frac{\partial g_n}{\partial \mathbf{t}} = 0 \tag{3.10}$$

As a consequence of the stationarity, the total derivative of the Lagrangian with respect to the external parameters equals the partial derivative:

$$\frac{d\mathcal{L}}{d\mathbf{x}} = \frac{\partial \mathcal{L}}{\partial \mathbf{x}} + \frac{\partial \mathcal{L}}{\partial \mathbf{t}} \frac{d\mathbf{t}}{d\mathbf{x}} + \frac{\partial \mathcal{L}}{\partial \boldsymbol{\lambda}} \frac{d\boldsymbol{\lambda}}{d\mathbf{x}} = \frac{\partial \mathcal{L}}{\partial \mathbf{x}} \tag{3.11}$$

Combining Eq. (3.9) and Eq. (3.11) shows that the total derivative of the energy equals

the partial derivative of the Lagrangian:

$$\frac{dE}{d\mathbf{x}} = \frac{\partial \mathcal{L}}{\partial \mathbf{x}} \tag{3.12}$$

In order to obtain the derivatives of a nonvariational method, it is thus necessary to construct a Lagrangian with a sufficient set of constraints for all parameters first. Second, equations for the Lagrange multipliers need to be derived by ensuring stationarity with respect to all parameters (Eq. (3.10)). Finally, it becomes possible to calculate derivatives of the energy through an expression equivalent to Eq. (3.3) by taking the partial derivative of the Lagrangian (Eq. (3.12)). The quantity

$$D_{\mu\nu} = \frac{\partial \mathcal{L}}{\partial h_{\mu\nu}} \tag{3.13}$$

assumes the character of a response density, which is the counterpart of the reduced one-particle density matrix in variational methods.

3.1.1.2 Orthogonal parameterisation of molecular orbitals

The setup of a Lagrangian is facilitated by choosing a convenient parameterisation for the molecular orbitals. Molecular orbital coefficients $C^{(0)}_{\mu p}$, which solve the self-consistent field equations for the unperturbed problem, do not represent an orthogonal set of functions if the basis functions change, e.g. following a displacement of the nuclei. One possibility is to parameterise the perturbed coefficients through a general matrix $\mathbf{V}$, so that $\mathbf{C} = \mathbf{C}^{(0)}\mathbf{V}$. This parameterisation requires an additional orthogonality constraint $\mathbf{C}^\dagger\mathbf{S}\mathbf{C} = \mathbf{1}$ in the Lagrangian.

In this work we follow a different approach by Helgaker and Almlöf.[166] The unperturbed coefficients $\mathbf{C}^{(0)}$ are first subject to symmetric orthogonalisation to produce a set of orthonormal molecular orbitals (OMO):

$$|\mathrm{OMO}_i\rangle = \sum_\mu \sum_j C^{(0)}_{\mu j} \left(\boldsymbol{\mathcal{S}}^{-\frac{1}{2}}\right)_{ji} |\mu\rangle \tag{3.14}$$

The matrix $\boldsymbol{\mathcal{S}}$ contains the overlap of the unperturbed orbitals in the perturbed basis:

$$\boldsymbol{\mathcal{S}} = \mathbf{C}^{(0)\dagger}\mathbf{S}\mathbf{C}^{(0)} \tag{3.15}$$

The actual perturbed molecular orbitals are obtained from the OMOs via a unitary transformation:

$$|i\rangle = \sum_j U_{ji} |j\rangle \tag{3.16}$$

In order to parameterise the unitary matrix $\mathbf{U}$, the exponential of an antihermitian matrix $\boldsymbol{\kappa}$ is used:

$$\mathbf{U} = \exp(\boldsymbol{\kappa}) \quad \text{with} \quad \boldsymbol{\kappa}^\dagger = -\boldsymbol{\kappa} \tag{3.17}$$

A full parameterisation of molecular orbitals is thus given as follows:

$$\mathbf{C} = \mathbf{C}^{(0)}\boldsymbol{\mathcal{S}}^{-\frac{1}{2}} \exp(\boldsymbol{\kappa}) \quad \text{with} \quad \boldsymbol{\kappa}^\dagger = -\boldsymbol{\kappa} \tag{3.18}$$

Derivatives of the molecular orbital coefficients with respect to the parameters $\boldsymbol{\kappa}$ are given by the expression

$$\left.\frac{\partial C_{\mu r}}{\partial \kappa_{pq}}\right|_{\boldsymbol{\kappa}=0} = C_{\mu p}\delta_{qr} - C_{\mu q}\delta_{pr}. \tag{3.19}$$

The only independent parameters are in the upper triangle of $\boldsymbol{\kappa}$.

3.1.1.3 Closed-shell coupled-perturbed Hartree-Fock equations

Each self-consistent RHF solution satisfies Brillouin's theorem:

$$F_{ia} = 0 \tag{3.20}$$

For a set of orthonormal orbitals, this is a necessary and sufficient condition. Differentiating it with respect to an arbitrary external perturbation $\mathbf{x}$ leads to equations that determine the first-order response of the molecular orbital parameters:

$$\frac{\partial F_{ia}}{\partial \mathbf{x}} + \sum_{p<q} \frac{\partial F_{ia}}{\partial \kappa_{pq}} \frac{d\kappa_{pq}}{d\mathbf{x}} = 0 \tag{3.21}$$

The derivative with respect to the rotation parameters $\boldsymbol{\kappa}$ is taken using Eq. (3.19). While the Brillouin condition is invariant to first order with respect to purely occupied or virtual rotations,

$$\frac{\partial F_{ia}}{\partial \kappa_{jk}} = \frac{\partial F_{ia}}{\partial \kappa_{bc}} = 0, \tag{3.22}$$

stationarity with respect to the mixing of occupied and virtual orbitals leads to the coupled-perturbed Hartree-Fock equations,[167, 168] which are expressed in terms of the exponential parameters $\boldsymbol{\kappa}$ below:

$$(\varepsilon_a - \varepsilon_i)\,\kappa_{ia}^{(1)} + \sum_{jb} A_{ia,jb}\kappa_{jb}^{(1)} = \mathcal{F}_{ia}^{(1)} \tag{3.23}$$

It was assumed that the unperturbed orbitals are canonical. $\boldsymbol{\mathcal{F}}$ is the Fock matrix calculated using the unperturbed molecular orbital coefficients together with the perturbed AO basis integrals. The derivative $\frac{d\boldsymbol{\kappa}}{d\mathbf{x}}$ was replaced with the first-order response $\boldsymbol{\kappa}^{(1)}$, and $\frac{\partial \mathbf{F}}{\partial \mathbf{x}}$ with $\boldsymbol{\mathcal{F}}^{(1)}$. $A_{pq,rs}$ is the Fock response tensor:

$$A_{pq,rs} = 4\,(pq|rs) - (pr|qs) - (ps|qr) \tag{3.24}$$

If a general matrix $\mathbf{V}$ is used to parameterise the orbitals $\mathbf{C} = \mathbf{C}^{(0)}\mathbf{V}$ instead of the matrix exponential in Eq. (3.18), then the relation between the respective first-order response expressions is given by:

$$\mathbf{V}^{(1)} = \boldsymbol{\kappa}^{(1)} - \frac{1}{2}\boldsymbol{\mathcal{S}}^{(1)} \tag{3.25}$$

Eq. (3.23) determines the rotation parameters $\kappa_{ia}^{(1)}$ between occupied and virtual orbitals. The diagonal elements are fixed by definition, since $\boldsymbol{\kappa}$ is antihermitian:

$$\kappa_{pp}^{(1)} = 0 \tag{3.26}$$

This leaves the off-diagonal occupied and virtual rotation parameters $\kappa_{i\neq j}^{(1)}$ and $\kappa_{a\neq b}^{(1)}$ undefined. Since the Hartree-Fock energy is invariant to unitary transformations in the

occupied or virtual orbital subspaces, these may be chosen arbitrarily.

A stronger constraint could be imposed by enforcing that the perturbed orbitals remain canonical, thus leaving the perturbed Fock matrix in a diagonal shape:

$$F_{pq} = 0 \qquad p \neq q \tag{3.27}$$

Determining the response of this equation as before leads to additional expressions for the occupied and virtual orbital rotation coefficients:

$$\kappa_{ij}^{(1)} = \frac{\mathcal{F}_{ij}^{(1)} - \sum_{kc} A_{ij,kc}\kappa_{kc}^{(1)}}{\varepsilon_j - \varepsilon_i} \qquad i < j \tag{3.28}$$

$$\kappa_{ab}^{(1)} = \frac{\mathcal{F}_{ab}^{(1)} - \sum_{kc} A_{ab,kc}\kappa_{kc}^{(1)}}{\varepsilon_b - \varepsilon_a} \qquad a < b \tag{3.29}$$

Under the condition that the perturbed orbitals remain canonical, the coupled-perturbed Hartree-Fock equations become singular in the presence of degenerate orbitals $\varepsilon_i = \varepsilon_j$ or $\varepsilon_a = \varepsilon_b$. In practice, it is therefore preferable to avoid this requirement.

3.1.1.4 Construction of a Lagrangian for canonical MP2

In their early contribution, Pople and co-workers developed an approach to calculate the MP2 gradient through direct differentiation of the energy in a basis of canonical orbitals.[169] This requires the coupled-perturbed self-consistent field (CP-SCF) equations to be solved separately for each perturbation, in the case of the gradient $3N$ times if the system contains N nuclei. As shown by Handy and Schaefer, this is unnecessary: only a single set of CP-SCF-type equations needs to be solved if the gradient is calculated via the Z-vector approach.[159]

Jørgensen and Helgaker introduced the Lagrangian method in the context of the canonical MP2 energy.[164] Following the first variant of their approach loosely, the Lagrangian for the RHF formulation of MP2 with orbitals parameterised as in Eq. (3.18)

and nuclei at positions $\mathbf{R}$ becomes:

$$\mathcal{L}(\mathbf{R}, \boldsymbol{\kappa}, \boldsymbol{\varepsilon}, \mathbf{z}) = E_{\mathrm{RHF}} + \sum_{ijab} \frac{\left[2\,(ia|jb) - (ib|ja)\right](ia|jb)}{\varepsilon_i + \varepsilon_j - \varepsilon_a - \varepsilon_b} + \sum_{p \geq q} z_{pq}\left(F_{pq} - \varepsilon_p \delta_{pq}\right) \tag{3.30}$$

The constraint ensures that the perturbed orbitals remain canonical, and the orbital energies are introduced as an additional set of parameters. As pointed out by Handy and co-workers, a strictly canonical coupled-perturbed self-consistent field approach is unstable due to singularities caused by degenerate orbitals.[170] This was elaborated upon in Section 3.1.1.3.

Since derivatives of degenerate eigenvalues (and hence of orbital energies) are not generally well-defined, Helgaker and co-workers introduced an improved Lagrangian for MP2.[165] The constraint on the orbitals is made weaker, such that they are only required to satisfy Brillouin's theorem. This, in turn, requires an expression for the MP2 energy that is invariant to unitary transformations among the occupied or virtual orbital subspaces. The Hylleraas functional, which was discussed earlier, is particularly suited for this purpose.[9] A Lagrangian for the closed-shell energy may be written down in the following form, which is somewhat different from the original expression in ref. [165]:

$$\mathcal{L}(\mathbf{R}, \boldsymbol{\kappa}, \mathbf{z}, \mathbf{T}) = E_{\mathrm{RHF}} + E_2^{\mathrm{MP2}} + \sum_{ia} z_{ia} F_{ia} \tag{3.31}$$

$$E_2^{\mathrm{MP2}} = \sum_{i \geq j} \sum_{ab} 2\,(ia|jb)\,\tilde{T}_{ab}^{ij} + \sum_{ab} F_{ab} D_{ab} - \sum_{ij} F_{ij} D_{ij} \tag{3.32}$$

$$D_{ab} = \sum_{i \geq j} \sum_{c} \left[T_{ac}^{ij} \tilde{T}_{bc}^{ij} + T_{ca}^{ij} \tilde{T}_{cb}^{ij} \right] \tag{3.33}$$

$$D_{ij} = \sum_{k} (1 + \delta_{ik}) \sum_{ab} T_{ab}^{kj} \tilde{T}_{ab}^{ik} \tag{3.34}$$

Since the Lagrangian functional $\mathcal{L}$ contains the Hylleraas functional, it is stationary with respect to the amplitudes T_{ab}^{ij} by construction. Derivatives of $\mathcal{L}$ with respect to occupied and virtual orbital rotation parameters κ_{ij} and κ_{ab} vanish as a consequence of the orbital invariance. The remaining Lagrange multipliers z_{ia} are determined through the stationarity requirement for the Lagrangian with respect to the parameters κ_{ia}.

3.1.2 Lagrangian approach for the DLPNO-MP2 gradient

As the starting point in the derivation of the analytical gradient for DLPNO-MP2, an appropriate Lagrangian needs to be defined, which contains all necessary constraints for the approximations involved. The molecular orbitals are parameterised through symmetric orthogonalisation of the unperturbed coefficients, followed by a rotation with a matrix exponential as defined in Eq. (3.18).

In the formulation of the gradient, the truncated PNOs $\tilde{a}_{ij}$ will be used, and in addition also the discarded set of PNOs $\tilde{a}'_{ij}$ for each pair. We refer to this set of functions as the complementary PNOs. The two sets of retained and discarded PNOs taken together correspond to untruncated PNOs $\tilde{a}''_{ij}$:

$$\{\, \tilde{a}''_{ij} \,\} = \{\, \tilde{a}_{ij} \,\} \cup \{\, \tilde{a}'_{ij} \,\} \tag{3.35}$$

The full set of PNOs is represented in a basis of redundant PAOs through the coefficients $d''^{ij}_{\tilde{\mu}'\tilde{a}''}$:

$$|\tilde{a}''_{ij}\rangle = \sum_{\tilde{\mu}'} d''^{ij}_{\tilde{\mu}'\tilde{a}''} \, |\tilde{\mu}'\rangle \tag{3.36}$$

As a consequence of the PNO truncation, the matrix $\mathbf{d}''^{ij}$ can be grouped into columns containing the coefficients of the retained PNOs $\mathbf{d}^{ij}$, and the remaining columns $\mathbf{d}'^{ij}$ representing the complementary PNOs:

$$\begin{pmatrix} \mathbf{d}''^{ij} \end{pmatrix} = \begin{pmatrix} \mathbf{d}^{ij} & \mathbf{d}'^{ij} \end{pmatrix} \tag{3.37}$$

There is no obvious closed-form function to express PNOs as a function of the molecular orbitals. Therefore, we introduce an exponential parameterisation of the coefficients for the untruncated PNOs:

$$\mathbf{d}''^{ij} = \mathbf{d}''^{ij(0)} \boldsymbol{\mathcal{S}}^{-\frac{1}{2}} \exp\left(\boldsymbol{\theta}^{ij}\right) \quad \text{with} \quad \boldsymbol{\theta}^{ij} = -\boldsymbol{\theta}^{ij\dagger} \tag{3.38}$$

The matrix $\boldsymbol{\theta}^{ij}$ is antisymmetric and specific to each orbital pair. $\boldsymbol{\mathcal{S}}$ represents the overlap

matrix of the unperturbed PNO coefficients $\mathbf{d}''^{ij(0)}$ in a basis of perturbed PAOs:

$$\mathcal{S}_{\tilde{a}''\tilde{b}''} = \sum_{\tilde{\mu}'\tilde{\nu}'} d''^{ij(0)}_{\tilde{\mu}'\tilde{a}''} S_{\tilde{\mu}'\tilde{\nu}'} d''^{ij(0)}_{\tilde{\nu}'\tilde{b}''} \tag{3.39}$$

Evidently, the idea for the parameterisation of the PNOs in Eq. (3.38) is closely related to the MO parameterisation in Eq. (3.18). However, further explanation is needed, as the redundant PAOs are linearly dependent. The set of non-redundant PAOs—which span the same space as the untruncated PNOs—is determined through diagonalisation of the matrix $S_{\tilde{\mu}'\tilde{\nu}'}$, where the redundant PAOs $\tilde{\mu}', \tilde{\nu}'$ are restricted to the pair domain $\{ij\}$. The eigenvectors of $S_{\tilde{\mu}'\tilde{\nu}'}$ with non-zero associated eigenvalues represent an orthonormal set of non-redundant PAOs in the space spanned by the redundant PAO basis. By construction, the overlap matrix $S^{(0)}_{\tilde{a}''\tilde{b}''}$ for the unperturbed system is of full rank. Provided that the eigenvalues of the matrix $\mathcal{S}_{\tilde{a}''\tilde{b}''}$ evolve continuously upon an infinitesimal perturbation, the rank of $\mathcal{S}_{\tilde{a}''\tilde{b}''}$ does not change, and $\sum_{\tilde{\mu}'} d''^{ij(0)}_{\tilde{\mu}'\tilde{a}''} |\tilde{\mu}'\rangle$ thus represents a linearly independent set of functions for the pair domain in the perturbed system. Discontinuities may occur after a reassignment of the domain $\{ij\}$, but this requires a finite perturbation, which does not concern this argument. This linearly independent set of functions is then subjected to symmetric orthogonalisation, and an orthogonal transformation to the final set of perturbed PNOs.

Orbital prescreening employs small domains of PAOs for each orbital. The corresponding matrix $\pi^i_{\tilde{\mu}'\tilde{\nu}}$ transforming redundant to non-redundant PAOs is parameterised as follows:

$$\boldsymbol{\pi}^i = \boldsymbol{\pi}^{i(0)} \boldsymbol{\mathcal{S}}^{-\frac{1}{2}} \quad \text{with} \quad \mathcal{S}_{\tilde{\mu}\tilde{\nu}} = \sum_{\tilde{\eta}'\tilde{\lambda}'} \pi^{i(0)}_{\tilde{\eta}'\tilde{\mu}} S_{\tilde{\eta}'\tilde{\lambda}'} \pi^{i(0)}_{\tilde{\lambda}'\tilde{\nu}} \tag{3.40}$$

It differs from the PNO parameterisation in two regards. Firstly, non-redundant PAOs are determined for the domain of each orbital i individually, whereas pair domains are not used in prescreening. Secondly, there is no further rotation of the orthogonalised functions, since the entire non-redundant PAO space of each orbital domain is used to calculate the pair energy contribution.

The function presented in Eq. (3.41) contains the complete Lagrangian for DLPNO-

MP2 including all of its energy contributions. Its individual components will be explained one-by-one in the remainder of this section.

$$\mathcal{L}\left(\mathbf{R}, \boldsymbol{\kappa}, \boldsymbol{\theta}^{ij}, \mathbf{T}^{ij}, \hat{\mathbf{T}}^{ij}, \mathbf{t}^{ij}, \mathbf{z}, \mathbf{z}^{\mathrm{Loc}}, \mathbf{v}^{ij}, \mathbf{w}^{ij}\right) = E_{\mathrm{RHF}} + E_2^{\mathrm{DLPNO}} + \Delta E_{\mathrm{PNO}} + \Delta E_2^{\mathrm{Pre}} + \sum_{ia} z_{ia} F_{ia} + \sum_{i<j} z_{ij}^{\mathrm{Loc}} s_{ij} + \sum_{i \geq j} \left[\sum_{\tilde{a}\tilde{b}'} v_{\tilde{a}\tilde{b}'}^{ij} \breve{D}_{\tilde{a}\tilde{b}'}^{ij} + \sum_{\tilde{a}''\tilde{b}''} w_{\tilde{a}''\tilde{b}''}^{ij} \breve{R}_{\tilde{a}''\tilde{b}''}^{ij} \right] \quad (3.41)$$

$\mathbf{z}$, $\mathbf{z}^{\mathrm{Loc}}$, $\mathbf{v}^{ij}$ and $\mathbf{w}^{ij}$ are Lagrange multipliers for a total of four different constraints. The closed-shell Hartree-Fock energy function E_{RHF} (Eq. (2.1)) is included as part of the total energy.

E_2^{DLPNO} is the Hylleraas functional in PNO basis representing the DLPNO-MP2 energy. It is a special case of Eq. (2.19) for pair natural orbitals:

$$E_2^{\mathrm{DLPNO}} = \sum_{i \geq j} \sum_{\tilde{a}\tilde{b}} \left[2 \left(i\tilde{a} \middle| j\tilde{b} \right) \tilde{T}_{\tilde{a}\tilde{b}}^{ij} + F_{\tilde{a}\tilde{b}} D_{\tilde{a}\tilde{b}}^{ij} \right] - \sum_{ij} F_{ij} D_{ij} \quad (3.42)$$

$D_{\tilde{a}\tilde{b}}^{ij}$ and D_{ij} represent the virtual pair contribution and the occupied contribution to the unrelaxed density, respectively:

$$D_{\tilde{a}\tilde{b}}^{ij} = \sum_{\tilde{c}} \left[T_{\tilde{a}\tilde{c}}^{ij} \tilde{T}_{\tilde{b}\tilde{c}}^{ij} + T_{\tilde{c}\tilde{a}}^{ij} \tilde{T}_{\tilde{c}\tilde{b}}^{ij} \right] \quad (3.43)$$

$$D_{ij} = \sum_{k} (1 + \delta_{ik}) \sum_{\tilde{a}\tilde{b}} \sum_{\tilde{c}\tilde{d}} T_{\tilde{a}\tilde{b}}^{jk} S_{\tilde{b}\tilde{c}} \tilde{T}_{\tilde{c}\tilde{d}}^{ki} S_{\tilde{d}\tilde{a}} \quad (3.44)$$

Pair natural orbitals $\tilde{a}$ and $\tilde{b}$ in Eq. (3.44) belong to pair kj, whereas $\tilde{c}$ and $\tilde{d}$ belong to pair ik. Note that all PNOs of the same orbital pair are orthogonal. Importantly, the functional is invariant with respect to orthogonal transformations among PNOs belonging to the same orbital pair.

Unlike the canonical MP2 energy in its orbital-invariant formulation, the DLPNO-MP2 energy depends on the specific choice of localised orbitals. This mandates an additional constraint ensuring that the perturbed occupied orbitals satisfy the appropriate localisation criterion.[89, 90] In this work we use Foster-Boys orbitals,[132, 133] which

maximise the localisation sum $\sum_i \langle i \,|\, \mathbf{r} \,|\, i\rangle^2$. The second constraint is thus obtained by requiring that the localisation sum is stationary with respect to orthogonal transformations among occupied orbitals:

$$s_{ij} = \mathbf{r}^{ij} \left[\mathbf{r}^{ii} - \mathbf{r}^{jj}\right] = 0 \quad \text{with} \quad \mathbf{r}^{pq} = \langle p|\mathbf{r}|q\rangle \tag{3.45}$$

Its associated Lagrange multipliers are z_{ij}^{Loc}. The set of constraints actually implemented in the code is slightly more complicated:

1. Separation of valence and core orbitals needs to be ensured via a constraint $F_{mi} = 0$, where m represents core orbitals and i valence orbitals. This is not only necessary in frozen core calculations, but also if all electrons are correlated, as different PNO cutoffs apply to both sets of orbitals.

2. The constraint $s_{ij} = 0$ needs to be satisfied for the valence orbitals i, j.

3. If all electrons are correlated, the constraint $s_{mn} = 0$ needs to be satisfied for the core orbitals m, n, as the valence and core orbitals are localised separately. This condition is not needed for frozen core calculations.

For simplicity, the equations presented in this document will be derived with the constraint in Eq. (3.45), however, the actual implementation makes use of the three conditions explained above.

A further set of constraints is needed for the additional variables that were introduced to parameterise the pair natural orbitals. The subset of retained PNOs is selected through the eigenvalues of the semicanonical virtual pair density matrix $\breve{\mathbf{D}}^{ij}$ (see Eq. (2.31)). However, an eigenvalue constraint should not be used, as the derivative of degenerate eigenvalues is not well-defined in general. Instead, we introduce a block-diagonality constraint for the semicanonical density: $\breve{D}^{ij}_{\tilde{a}\tilde{b}'} = 0$. It is analogous to the Brillouin condition for the orbitals, and it ensures that the two eigenvector subspaces of retained and discarded PNOs do not mix upon a perturbation. The associated pair-specific Lagrange multipliers are $v^{ij}_{\tilde{a}\tilde{b}'}$. As the Hylleraas functional in PNO basis (Eq. (3.42)) is invariant to

orthogonal transformations within the subspace of retained PNOs, the block-diagonality constraint is both necessary and sufficient.

Semicanonical amplitudes $\breve{\mathbf{T}}^{ij}$ are introduced as an additional set of parameters via the semicanonical density in the PNO constraint. They minimise the Hylleraas functional

$$E_2^{\mathrm{SC}} = \sum_{i\geq j} \left[2 \sum_{\tilde{a}''\tilde{b}''} \left(i\tilde{a}'' \middle| j\tilde{b}'' \right) \breve{\tilde{T}}^{ij}_{\tilde{a}''\tilde{b}''} + \sum_{\tilde{a}''\tilde{b}''} F_{\tilde{a}''\tilde{b}''} \breve{D}^{ij}_{\tilde{a}''\tilde{b}''} - (F_{ii} + F_{jj}) \sum_{\tilde{a}''\tilde{b}'} \breve{T}^{ij}_{\tilde{a}''\tilde{b}''} \breve{\tilde{T}}^{ij}_{\tilde{a}''\tilde{b}''} \right], \quad (3.46)$$

and therefore the perturbed $\breve{\mathbf{T}}^{ij}$ need to satisfy the semicanonical residual equation as the fourth constraint, with associated Lagrange multipliers $\mathbf{w}^{ij}$:

$$\breve{R}^{ij}_{\tilde{a}\tilde{b}} = \left(i\tilde{a}'' \middle| j\tilde{b}'' \right) + \sum_{\tilde{c}} \left[F_{\tilde{a}''\tilde{c}''} \breve{T}^{ij}_{\tilde{c}''\tilde{b}''} + \breve{T}^{ij}_{\tilde{a}''\tilde{c}''} F_{\tilde{c}''\tilde{b}''} \right] - (F_{ii} + F_{jj}) \breve{T}^{ij}_{\tilde{a}''\tilde{b}''} = 0 \quad (3.47)$$

We found that the equations to determine the Lagrange multipliers become redundant if the amplitudes $\breve{\mathbf{T}}^{ij}$ are used as parameters in the Lagrangian. This is resolved through a reparameterisation of the amplitudes in terms of the variables $\hat{\mathbf{T}}^{ij}$:

$$\breve{\mathbf{T}}^{ij} = \exp\left(-\boldsymbol{\theta}^{ij}\right) \hat{\mathbf{T}}^{ij} \exp\left(\boldsymbol{\theta}^{ij}\right) \quad (3.48)$$

To account for the energy error caused by PNO truncation, the contribution ΔE_{PNO} is included in the Lagrangian, as defined in Eq. (2.34):

$$\Delta E_{\mathrm{PNO}} = \sum_{i\geq j} \left[\sum_{\tilde{a}''\tilde{b}''} \left(i\tilde{a}'' \middle| j\tilde{b}'' \right) \breve{\tilde{T}}^{ij}_{\tilde{a}''\tilde{b}''} - \sum_{\tilde{a}\tilde{b}} \left(i\tilde{a} \middle| j\tilde{b} \right) \breve{\tilde{T}}^{ij}_{\tilde{a}\tilde{b}} \right] \quad (3.49)$$

The first term represents the semicanonical correlation energy in the untruncated PNO space, and it is therefore invariant to any PNO rotations. In the second term, the energy contribution is obtained by projecting the semicanonical amplitudes to the truncated PNO basis. It is invariant to orthogonal transformations among the retained PNOs.

The expression to estimate the energy of screened-out pairs in Eq. (2.37) uses pseudo-canonical non-redundant PAOs, which were constructed for prescreening domains. To be included as part of the Lagrangian, the energy is reformulated in terms of a Hylleraas

functional, which is invariant with respect to orthogonal transformations among the non-redundant PAOs:

$$\Delta E_2^{\mathrm{Pre}} = \sum_{i>j} \mathbf{1}_S(ij) \left[8 \sum_{\tilde{\mu}\tilde{\nu}} M^{ij}_{\tilde{\mu}\tilde{\nu}} t^{ij}_{\tilde{\mu}\tilde{\nu}} + \sum_{\tilde{\mu}'\tilde{\nu}'} F_{\tilde{\mu}'\tilde{\nu}'} D^{\mathrm{v(Pre)}}_{\tilde{\mu}'\tilde{\nu}'} - \sum_{ij} F_{ij} D^{\mathrm{o(Pre)}}_{ij} \right] \tag{3.50}$$

The indicator function $\mathbf{1}_S$ has a value of 1 if the pair ij was screened out, and 0 otherwise. $M^{ij}_{\tilde{\mu}\tilde{\nu}}$ is the dipole approximation for the two-electron integrals $(i\tilde{\mu}|j\tilde{\nu})$ as defined in Eq. (2.38). The functional includes the virtual contribution $D^{\mathrm{v(Pre)}}_{\tilde{\mu}'\tilde{\nu}'}$ and the occupied contribution $D^{\mathrm{o(Pre)}}_{ij}$ to the unrelaxed density matrix:

$$D^{\mathrm{v(Pre)}}_{\tilde{\mu}'\tilde{\nu}'} = 4 \sum_{ij} \mathbf{1}_S(ij) \sum_{\tilde{\eta}\tilde{\lambda}\tilde{\rho}} \pi^i_{\tilde{\mu}'\tilde{\eta}} t^{ij}_{\tilde{\eta}\tilde{\lambda}} t^{ij}_{\tilde{\rho}\tilde{\lambda}} \pi^i_{\tilde{\nu}'\tilde{\rho}} \tag{3.51}$$

$$D^{\mathrm{o(Pre)}}_{ij} = 4\delta_{ij} \sum_{k} \mathbf{1}_S(ik) \sum_{\tilde{\mu}\tilde{\nu}} \left(t^{ik}_{\tilde{\mu}\tilde{\nu}} \right)^2 \tag{3.52}$$

The amplitudes $t^{ij}_{\tilde{\mu}\tilde{\nu}}$ have been introduced in the Hylleraas functional for prescreening as a new set of parameters.

To summarise, the independent parameters in the Lagrangian $\mathcal{L}$ are the MO rotation coefficients κ_{pq}, the PNO rotation coefficients $\theta^{ij}_{\tilde{a}''\tilde{b}''}$, the PNO-basis amplitudes $T^{ij}_{\tilde{a}\tilde{b}}$, the variables $\hat{T}^{ij}_{\tilde{a}''\tilde{b}''}$ to parameterise the semicanonical amplitudes, and the amplitudes $t^{ij}_{\tilde{\mu}\tilde{\nu}}$ to estimate the energy contribution of screened-out pairs. z_{ia}, z^{Loc}_{ij}, $v^{ij}_{\tilde{a}\tilde{b}'}$ and $w^{ij}_{\tilde{a}''\tilde{b}''}$ are Lagrange multipliers. As will be illustrated below, all of the energy contributions E_{RHF}, E_2^{DLPNO}, ΔE_{PNO} and $\Delta E_2^{\mathrm{Pre}}$ have well-defined values if the four constraints in the Lagrangian are satisfied:

1. The Hartree-Fock energy E_{RHF} is constant subject to all orbital parameter variations $\delta\boldsymbol{\kappa}$ that satisfy the Brillouin condition $F_{ia} = 0$.

2. The value of the DLPNO-MP2 energy E_2^{DLPNO} depends, firstly, on the localised orbitals, which are fully constrained through the Brillouin and the localisation conditions. Secondly, it depends on the choice of PNOs through $\boldsymbol{\theta}^{ij}$, which is subject to the block-diagonality condition for the semicanonical density matrix. Thirdly, the

amplitudes $T_{\tilde{a}\tilde{b}}^{ij}$ appear only in this functional. Thus, $\mathcal{L}$ and E_2^{DLPNO} are minimised by identical sets of parameters.

3. The PNO correction ΔE_{PNO} depends, firstly, on the choice of occupied molecular orbitals, which are fully constrained. Secondly, it depends on the PNOs and on the semicanonical amplitudes, both of which are subject to the appropriate conditions. Therefore, the value of ΔE^{PNO} is constant subject to permissible parameter variations $\delta\boldsymbol{\kappa}$, $\delta\boldsymbol{\theta}^{ij}$ and $\delta\hat{\mathbf{T}}^{ij}$.

4. The value of the prescreening correction $\Delta E_2^{\mathrm{Pre}}$ is determined by the fully constrained localised MOs, and by the amplitudes $\mathbf{t}^{ij}$, which appear only in the Hylleraas functional for prescreening. Therefore, $\mathcal{L}$ and $\Delta E_2^{\mathrm{Pre}}$ are minimised by identical parameters.

3.1.3 Expressions for the nuclear gradient

As per Eq. (3.12), an expression for the DLPNO-MP2 gradient is obtained after taking the partial derivative of the Lagrangian with respect to external perturbations. The quantities that depend on nuclear coordinates explicitly are primarily the integrals in AO basis, thus leading to the following equation for the derivative E^x:

$$\begin{aligned} E^x =& V_{\mathrm{NN}}^x + \sum_{\mu\nu} \left[P_{\mu\nu}^{\mathrm{SCF}} + D''_{\mu\nu}\right] h_{\mu\nu}^x + \sum_{\mu\nu} W_{\mu\nu} S_{\mu\nu}^x + \sum_{n=1}^{3} \sum_{\mu\nu} Q_{\mu\nu}^n \langle\mu|r_n|\nu\rangle^x \\ &+ \sum_{\mu\nu\eta\lambda} \left[\frac{1}{2} P_{\mu\nu}^{\mathrm{SCF}} P_{\eta\lambda}^{\mathrm{SCF}} - \frac{1}{4} P_{\mu\eta}^{\mathrm{SCF}} P_{\nu\lambda}^{\mathrm{SCF}} + P_{\mu\nu}^{\mathrm{SCF}} D''_{\eta\lambda} - \frac{1}{2} P_{\mu\eta}^{\mathrm{SCF}} D''_{\nu\lambda}\right] (\mu\nu|\eta\lambda)^x \\ &+ \sum_{K} \sum_{\mu\nu} \Gamma_{\mu\nu}^K (\mu\nu|K)^x + \sum_{KL} \gamma_{KL} (K|L)^x \end{aligned} \tag{3.53}$$

V_{NN}^x is the derivative of the nuclear repulsion energy, and, likewise, the superscript x indicates the corresponding derivatives of the integrals in AO basis.

The total one-electron density matrix is a sum of the density of the reference wave function,

$$P_{\mu\nu}^{\mathrm{SCF}} = 2 \sum_i C_{\mu i} C_{\nu i}, \tag{3.54}$$

and the orbital-relaxed MP2 difference density

$$D''_{\mu\nu} = D'_{\mu\nu} + \frac{1}{2}\left[\sum_{ia} C_{\mu i} z_{ia} C_{\nu a} + \sum_{ia} C_{\nu i} z_{ia} C_{\mu a}\right]. \tag{3.55}$$

We refer to $D'_{\mu\nu}$ as the PNO-relaxed difference density, as it is the sum of the unrelaxed difference density and another contribution originating from the constraint for the semicanonical amplitudes. The PNO-relaxed density is a sum of a purely occupied contribution D'^{o}_{ij} and a purely virtual contribution $D'^{\mathrm{v}}_{\tilde{\mu}'\tilde{\nu}'}$ in redundant PAO basis:

$$D'_{\mu\nu} = \sum_{\tilde{\eta}'\tilde{\lambda}'} \tilde{P}_{\mu\tilde{\eta}'} D'^{\mathrm{v}}_{\tilde{\eta}'\tilde{\lambda}'} \tilde{P}_{\nu\tilde{\lambda}'} - \sum_{ij} C_{\mu i} D'^{\mathrm{o}}_{ij} C_{\nu j} \tag{3.56}$$

The virtual part is further partitioned into a sum over PNO-relaxed density contributions $D'^{ij}_{\tilde{\mu}'\tilde{\nu}'}$ and an unrelaxed prescreening density component $D^{\mathrm{v(Pre)}}_{\tilde{\mu}'\tilde{\nu}'}$:

$$D'^{\mathrm{v}}_{\tilde{\mu}'\tilde{\nu}'} = \sum_{i\geq j} \left[D'^{ij}_{\tilde{\mu}'\tilde{\nu}'} + D^{\mathrm{v(Pre)}}_{\tilde{\mu}'\tilde{\nu}'}\right] \tag{3.57}$$

$$D'^{ij}_{\tilde{\mu}'\tilde{\nu}'} = \sum_{\tilde{a}\tilde{b}} d^{ij}_{\tilde{\mu}'\tilde{a}} D^{ij}_{\tilde{a}\tilde{b}} d^{ij}_{\tilde{\nu}'\tilde{b}} + \frac{1}{2}\sum_{\tilde{\eta}\tilde{\lambda}\tilde{\rho}} d''^{ij}_{\tilde{\mu}'\tilde{\eta}} \left[w^{ij}_{\tilde{\eta}\tilde{\lambda}} \breve{T}^{ij}_{\tilde{\rho}\tilde{\lambda}} + w^{ij}_{\tilde{\lambda}\tilde{\eta}} \breve{T}^{ij}_{\tilde{\lambda}\tilde{\rho}} + \breve{T}^{ij}_{\tilde{\eta}\tilde{\lambda}} w^{ij}_{\tilde{\rho}\tilde{\lambda}} + \breve{T}^{ij}_{\tilde{\lambda}\tilde{\eta}} w^{ij}_{\tilde{\lambda}\tilde{\rho}}\right] d''^{ij}_{\tilde{\nu}'\tilde{\rho}} \tag{3.58}$$

Eq. (3.58) contains non-redundant PAO indices $\tilde{\mu}$, since they span the same space as the untruncated PNOs $\tilde{a}''$; this reflects the way that the equation is implemented in the code. $D^{ij}_{\tilde{a}\tilde{b}}$ is the unrelaxed pair density defined in Eq. (3.43).

Similarly, the occupied contribution D'^{o}_{ij} contains the two unrelaxed difference density contributions $D^{ij}_{\tilde{a}\tilde{b}}$ and $D^{\mathrm{o(Pre)}}_{ij}$, which originate from the two respective Hylleraas functionals for the MP2 energy in PNO basis, and for the prescreening contribution to the energy. The middle term accounts for the relaxation of the PNOs:

$$D'^{\mathrm{o}}_{ij} = D_{ij} + \sum_{k\geq l} \delta_{ij}\left(\delta_{ik} + \delta_{il}\right) \sum_{\tilde{\mu}\tilde{\nu}} w^{kl}_{\tilde{\mu}\tilde{\nu}} \breve{T}^{kl}_{\tilde{\mu}\tilde{\nu}} + D^{\mathrm{o(Pre)}}_{ij} \tag{3.59}$$

Note that the energy correction for PNO truncation, ΔE_{PNO}, contributes to the density only indirectly, as it affects the values of the Lagrange multipliers.

The contributions of the three-centre electron repulsion integrals to the gradient are

calculated by contracting the integral derivatives with the two-body density tensor

$$\Gamma^K_{i\tilde{\mu}'} = \sum_j (1+\delta_{ij})\, G^{i(ij)}_{K\tilde{\mu}'}. \tag{3.60}$$

Each orbital pair ij contributes individual terms to the two-body density defined as follows:

$$\begin{aligned} G^{i(ij)}_{K\tilde{\mu}'} &= \sum_{\tilde{\nu}\tilde{\eta}} X^j_{K\tilde{\nu}} g^{ij}_{\tilde{\eta}\tilde{\nu}} d''^{ij}_{\tilde{\mu}'\tilde{\eta}} \\ G^{j(ij)}_{K\tilde{\mu}'} &= \sum_{\tilde{\nu}\tilde{\eta}} X^i_{K\tilde{\nu}} g^{ij}_{\tilde{\nu}\tilde{\eta}} d''^{ij}_{\tilde{\mu}'\tilde{\eta}} \end{aligned} \tag{3.61}$$

Density-fitted three-centre integrals are represented by $X^i_{K\tilde{\mu}}$:

$$X^i_{K\tilde{\mu}} = \sum_L \left(\mathbf{V}^{-1}\right)_{KL} (i\tilde{\mu}|L) \quad \text{with} \quad V_{KL} = (K|L) \tag{3.62}$$

The intermediate $g^{ij}_{\tilde{\mu}\tilde{\nu}}$, which is defined in Eq. (3.63), contains a contribution from the PNO-basis Hylleraas functional in the first term, from the constraint for the semicanonical amplitudes in the second term, and from the PNO truncation energy correction in the third and fourth terms:

$$g^{ij}_{\tilde{\mu}\tilde{\nu}} = 2\sum_{\tilde{a}\tilde{b}} S_{\tilde{\mu}\tilde{a}} \tilde{T}^{ij}_{\tilde{a}\tilde{b}} S_{\tilde{\nu}\tilde{b}} + w^{ij}_{\tilde{\mu}\tilde{\nu}} + \tilde{\tilde{T}}^{ij}_{\tilde{\mu}\tilde{\nu}} - \sum_{\tilde{a}\tilde{b}} S_{\tilde{\mu}\tilde{a}} \tilde{\tilde{T}}^{ij}_{\tilde{a}\tilde{b}} S_{\tilde{\nu}\tilde{b}} \tag{3.63}$$

In order to calculate the gradient contribution by the three-centre integrals, a transformation of the two-body density tensor to the atomic orbital basis is performed:

$$\Gamma^K_{\mu\nu} = \sum_{i\tilde{\eta}'} C_{\mu i} \Gamma^K_{i\tilde{\eta}'} \tilde{P}_{\nu\tilde{\eta}'} \tag{3.64}$$

Two-centre electron repulsion integrals between auxiliary basis functions are contracted with the matrix $\boldsymbol{\gamma}$:

$$\gamma_{KL} = -\sum_{i\geq j} X^i_{K\tilde{\mu}} g^{ij}_{\tilde{\mu}\tilde{\nu}} X^j_{L\tilde{\nu}} \tag{3.65}$$

Dipole integrals $\langle \mu \,|\, \mathbf{r} \,|\, \nu \rangle$ contribute to the DLPNO-MP2 energy through the Foster-Boys localisation constraint, and as part of the energy correction for prescreening ΔE_2^{Pre}.

The derivatives of these integrals are contracted with the dipole density matrices $Q^n_{\mu\nu}$, with the index n representing x, y, z-coordinates:

$$Q^n_{\mu\nu} = \frac{1}{2}\sum_{ij} C_{\mu i} C_{\nu j} z^{\mathrm{Loc}}_{ij} \left(r^{ii}_n - r^{jj}_n\right) + \sum_i C_{\mu i} C_{\nu i} \sum_j z^{\mathrm{Loc}}_{ij} r^{ij}_n + Q^{n(\mathrm{Pre})}_{\mu\nu} \tag{3.66}$$

In this expression, $Q^{n(\mathrm{Pre})}_{\mu\nu}$ represents a contribution which originates from the prescreening correction,

$$Q^{n(\mathrm{Pre})}_{\mu\nu} = \frac{1}{2}\left\{\sum_{i\tilde{\eta}'}\left[C_{\mu i} y^{\alpha,n}_{i\tilde{\eta}'} \tilde{P}_{\nu\tilde{\eta}'} + C_{\nu i} y^{\alpha,n}_{i\tilde{\eta}'} \tilde{P}_{\mu\tilde{\eta}'}\right] + \sum_i C_{\mu i} y^{\beta,n}_i C_{\nu i}\right\}. \tag{3.67}$$

The intermediate $\mathbf{y}^{\alpha,n}$ contains dipole contributions in a mixed basis of MOs and PAOs,

$$y^{\alpha,n}_{i\tilde{\mu}'} = 8\sum_j \mathbf{1}_S(ij) \sum_{\tilde{\nu}\tilde{\eta}} \pi^i_{\tilde{\mu}'\tilde{\nu}} t^{ij}_{\tilde{\nu}\tilde{\eta}} \left[\frac{r^{j\tilde{\eta}}_n}{|\mathbf{R}^{ij}|^3} - 3\frac{\left(\mathbf{R}^{ij}\mathbf{r}^{j\tilde{\eta}}\right) R^{ij}_n}{|\mathbf{R}^{ij}|^5}\right], \tag{3.68}$$

while the intermediate $\mathbf{y}^{\beta,n}$ contains contributions purely in MO basis:

$$\begin{aligned} y^{\beta,n}_i = \sum_j \mathbf{1}_S(ij) \Bigg[\frac{48}{|\mathbf{R}^{ij}|^5} \sum_{\tilde{\mu}\tilde{\nu}} \left(\mathbf{r}^{i\tilde{\mu}}\mathbf{r}^{j\tilde{\nu}}\right) t^{ij}_{\tilde{\mu}\tilde{\nu}} - \frac{240}{|\mathbf{R}^{ij}|^7} \sum_{\tilde{\mu}\tilde{\nu}} \left(\mathbf{R}^{ij}\mathbf{r}^{i\tilde{\mu}}\right)\left(\mathbf{R}^{ij}\mathbf{r}^{j\tilde{\nu}}\right) t^{ij}_{\tilde{\mu}\tilde{\nu}}\Bigg] R^{ji}_n \\ - \sum_j \mathbf{1}_S(ij) \frac{48}{|\mathbf{R}^{ij}|^5} \sum_{\tilde{\mu}\tilde{\nu}} \left[\left(\mathbf{R}^{ij}\mathbf{r}^{i\tilde{\mu}}\right) t^{ij}_{\tilde{\mu}\tilde{\nu}} r^{j\tilde{\nu}}_n + r^{i\tilde{\mu}}_n t^{ij}_{\tilde{\mu}\tilde{\nu}} \left(\mathbf{R}^{ij}\mathbf{r}^{j\tilde{\nu}}\right)\right] \end{aligned} \tag{3.69}$$

In order to calculate the gradient contributions of the overlap integrals, the energy-weighted density $\mathbf{W}$ needs to be computed. Overlap matrices appear explicitly in the pair projection terms of the PNO-basis Hylleraas functional E_2^{DLPNO} and as part of the redundant PAOs, but they are also introduced through the orthogonal parameterisations of the MO and PNO coefficients.

In order to collect contributions to the energy-weighted density $\mathbf{W}$, terms originating from the symmetric orthogonalisation of the MOs are identified through the derivative of the MO parameterisation in Eq. (3.18):

$$\left.\frac{\partial C_{\mu p}}{\partial x}\right|_{\boldsymbol{\kappa}=0} = -\frac{1}{2}\sum_{\nu\eta}\sum_q C_{\mu q} C_{\nu q} S^x_{\nu\eta} C_{\eta p} \tag{3.70}$$

A slightly more complicated expression is obtained for the derivatives of the normalised redundant PAO coefficients in atomic orbital basis:

$$\left.\frac{\partial \tilde{P}_{\mu\tilde{\nu}'}}{\partial x}\right|_{\boldsymbol{\kappa}=0} = -\frac{1}{2}\sum_{\eta\lambda}\sum_{p} C_{\mu p} C_{\eta p} S^{x}_{\eta\lambda} \tilde{P}_{\lambda\tilde{\nu}'} + \frac{1}{2} N_{\tilde{\nu}'} \sum_{\eta}\sum_{a} C_{\mu a} C_{\eta a} S^{x}_{\eta\nu} - \frac{1}{2} N_{\tilde{\nu}'} \tilde{P}_{\mu\tilde{\nu}'} \sum_{\eta} S^{x}_{\nu\eta} \tilde{P}_{\eta\tilde{\nu}'} \quad (3.71)$$

Finally, quantities in a basis of PNOs—or non-redundant PAOs—introduce contributions to the energy-weighted density via the derivatives of redundant PAO coefficients (see Eq. (3.71)) and of the overlap matrix in AO basis:

$$\left.\frac{\partial d''^{ij}_{\tilde{\mu}'\tilde{a}''}}{\partial x}\right|_{\boldsymbol{\kappa}=0,\boldsymbol{\theta}^{ij}=0} = -\frac{1}{2}\sum_{\tilde{b}''}\sum_{\tilde{\nu}'\tilde{\eta}'} d''^{ij}_{\tilde{\mu}'\tilde{b}''} d''^{ij}_{\tilde{\nu}'\tilde{b}''} \frac{\partial}{\partial x}\left[\sum_{\lambda\rho} \tilde{P}_{\lambda\tilde{\nu}'} S_{\lambda\rho} \tilde{P}_{\rho\tilde{\eta}'}\right] d''^{ij}_{\tilde{\eta}'\tilde{a}''} \quad (3.72)$$

Non-redundant PAO coefficient matrices $\pi^{i}_{\tilde{\mu}'\tilde{\nu}}$ in the Hylleraas functional for screened-out pairs contribute to $\mathbf{W}$ analogously to Eq. (3.72).

The expression for the complete energy-weighted density is collected in the following equation with intermediates $\mathbf{Y}^{\alpha}$ to $\mathbf{Y}^{\varepsilon}$ that will be defined below:

$$W_{\mu\nu} = \frac{1}{2}\left[\sum_{ip} C_{\mu i} Y^{\alpha}_{ip} C_{\nu p} - \sum_{p}\sum_{\tilde{\eta}'} C_{\mu p} Y^{\beta}_{p\tilde{\eta}'} \tilde{P}_{\nu\tilde{\eta}'} + \sum_{a} C_{\mu a} N_{\tilde{\nu}'} Y^{\beta}_{a\tilde{\nu}'} - \sum_{\tilde{\nu}'} \tilde{P}_{\mu\tilde{\nu}'} N_{\tilde{\nu}'} Y^{\gamma}_{\tilde{\nu}'} + \sum_{\tilde{\eta}'\tilde{\lambda}'} \tilde{P}_{\mu\tilde{\eta}'} Y^{\delta}_{\tilde{\eta}'\tilde{\lambda}'} \tilde{P}_{\nu\tilde{\lambda}'} - \sum_{ip} C_{\mu i} Y^{\varepsilon}_{ip} C_{\nu p}\right] \quad (3.73)$$

The intermediate $\mathbf{Y}^{\alpha}$ originates from matrices with molecular orbital indices:

$$Y^{\alpha}_{ip} = -\sum_{K}\sum_{\tilde{\mu}'} \Gamma^{K}_{i\tilde{\mu}'} (p\tilde{\mu}'|K) - \sum_{\mu\nu} A_{ip,\mu\nu} D'_{\mu\nu} + \sum_{k} A^{\mathrm{Loc}}_{ip,k} z^{\mathrm{Loc}}_{ik} - \sum_{\tilde{\mu}'}\sum_{n=1}^{3} y^{\alpha,n}_{i\tilde{\mu}'} r^{p\tilde{\mu}'}_{n} - \sum_{n=1}^{3} y^{\beta,n}_{i} r^{ip}_{n} \quad (3.74)$$

$\mathbf{A}$ is the Fock response tensor, which has been defined in Eq. (3.24). The Foster-Boys

localisation constraint gives rise to terms containing the localisation response tensor $\mathbf{A}^{\mathrm{Loc}}$:

$$A^{\mathrm{Loc}}_{ip,k} = \mathbf{r}^{kp}\left(\mathbf{r}^{kk} - \mathbf{r}^{ii}\right) - 2\mathbf{r}^{ik}\mathbf{r}^{ip} \tag{3.75}$$

We have defined $\mathbf{z}^{\mathrm{Loc}}$ as an antisymmetric matrix to simplify the equations,

$$\mathbf{z}^{\mathrm{Loc}} = -\mathbf{z}^{\mathrm{Loc}\dagger}, \tag{3.76}$$

even though only the entries in its upper diagonal appear as an independent set of multipliers in the Lagrangian.

Intermediate $\mathbf{Y}^{\varepsilon}$ contains further contributions originating from derivatives of MO coefficients. Unlike $\mathbf{Y}^{\alpha}$, it is only needed to calculate the energy-weighted density for the gradient, but not for solving the Z-vector equations (Section 3.1.4):

$$\begin{aligned} Y^{\varepsilon}_{ij} &= 4F_{ij} - 2\sum_{k} D'^{\mathrm{o}}_{ik}F_{kj} + \sum_{kc} A_{ij,kc}z_{kc} \\ Y^{\varepsilon}_{ia} &= \sum_{k} F_{ik}z_{ka} + \sum_{b} z_{ib}F_{ba} + \sum_{kc} A_{ia,kc}z_{kc} \end{aligned} \tag{3.77}$$

The intermediate $\mathbf{Y}^{\beta}$ originates from derivatives of redundant PAO coefficients:

$$Y^{\beta}_{p\tilde{\mu}'} = \sum_{i}\sum_{K} \Gamma^{K}_{i\tilde{\mu}'}\,(ip|K) + 2\sum_{\tilde{\nu}'} F_{p\tilde{\nu}'}D'^{\mathrm{v}}_{\tilde{\nu}'\tilde{\mu}'} + \sum_{\tilde{\nu}'} S_{p\tilde{\nu}'}Y^{\delta}_{\tilde{\nu}'\tilde{\mu}'} + \sum_{i}\sum_{n=1}^{3} y^{\alpha,n}_{i\tilde{\mu}'}r^{ip}_{n} \tag{3.78}$$

Clearly, the Fock and overlap matrix elements in the second and third terms of Eq. (3.78) vanish if p is an occupied orbital, so that $Y^{\beta}_{i\tilde{\mu}'}$ only contains the first and the fourth term.

$\mathbf{Y}^{\gamma}$ is an intermediate connected to the normalisation factors of redundant PAOs:

$$Y^{\gamma}_{\tilde{\mu}'} = \sum_{i}\sum_{K} \Gamma^{K}_{i\tilde{\mu}'}\,(i\tilde{\mu}'|K) + 2\sum_{\tilde{\nu}'} F_{\tilde{\mu}'\tilde{\nu}'}D'^{\mathrm{v}}_{\tilde{\mu}'\tilde{\nu}'} + \sum_{\tilde{\nu}'} S_{\tilde{\mu}'\tilde{\nu}'}Y^{\delta}_{\tilde{\mu}'\tilde{\nu}'} + \sum_{i}\sum_{n=1}^{3} y^{\alpha,n}_{i\tilde{\mu}'}r^{i\tilde{\mu}'}_{n} \tag{3.79}$$

Finally, intermediate $\mathbf{Y}^{\delta}$ originates from derivatives of terms containg overlap matrices

in a redundant PAO basis. This includes matrices in PNO basis via $\mathbf{d}^{ij\dagger}\mathbf{S}\mathbf{d}^{ij}$:

$$Y^{\delta}_{\tilde{\mu}'\tilde{\nu}'} = \sum_{i\geq j}\left[\xi^{ij}_{\tilde{\mu}'\tilde{\nu}'} + \xi^{ij}_{\tilde{\nu}'\tilde{\mu}'} - 2\sum_{\tilde{a}} d^{ij}_{\tilde{\mu}'\tilde{a}}\tau^{ij}_{\tilde{a}\tilde{\nu}'}\right] - y^{\delta}_{\tilde{\mu}'\tilde{\nu}'} - y^{\delta}_{\tilde{\nu}'\tilde{\mu}'} \tag{3.80}$$

The preceding equation contains the intermediate $\boldsymbol{\tau}^{ij}$, which is defined as follows:

$$\begin{aligned}\tau^{ij}_{\tilde{a}\tilde{\mu}'} = \sum_k \sum_{\tilde{b}\tilde{c}\tilde{e}} F_{ik}\left[\tilde{T}^{ij}_{\tilde{a}\tilde{b}} S_{\tilde{b}\tilde{c}} T^{jk}_{\tilde{c}\tilde{e}} + \tilde{T}^{ji}_{\tilde{a}\tilde{b}} S_{\tilde{b}\tilde{c}} T^{kj}_{\tilde{c}\tilde{e}}\right] d^{kj}_{\tilde{\mu}'\tilde{e}} \\ + \sum_k \sum_{\tilde{b}\tilde{c}\tilde{e}} F_{kj}\left[\tilde{T}^{ij}_{\tilde{a}\tilde{b}} S_{\tilde{b}\tilde{c}} T^{ki}_{\tilde{c}\tilde{e}} + \tilde{T}^{ji}_{\tilde{a}\tilde{b}} S_{\tilde{b}\tilde{c}} T^{ik}_{\tilde{c}\tilde{e}}\right] d^{ik}_{\tilde{\mu}'\tilde{e}}\end{aligned} \tag{3.81}$$

$\tau^{ij}_{a\tilde{\mu}'}$ needs to be determined for all indices $\tilde{\mu}'$ that are members of the domains of the pairs ik and kj with all possible k: $\tilde{\mu}' \in \bigcup_k \{\{ik\} \cup \{kj\}\}$. Exceptions are pairs ik and kj that have been screened out, or if an associated Fock matrix elements F_{kj} or F_{ik} is below the corresponding cutoff.

Further intermediates entering $\mathbf{Y}^{\delta}$ are

$$\begin{aligned}\xi^{ij}_{\tilde{\mu}'\tilde{\nu}'} = \sum_{\tilde{\eta}} \sum_{\tilde{\lambda}'} d''^{ij}_{\tilde{\mu}'\tilde{\eta}} d''^{ij}_{\tilde{\lambda}'\tilde{\eta}} \Bigg\{ -\frac{1}{2}\sum_K \left[G^{i(ij)}_{\tilde{\nu}'K}\left(i\tilde{\lambda}'\middle|K\right) + G^{j(ij)}_{\tilde{\nu}'K}\left(j\tilde{\lambda}'\middle|K\right)\right] \\ - \sum_{\tilde{\rho}'} F_{\tilde{\lambda}'\tilde{\rho}'} D'^{ij}_{\tilde{\rho}'\tilde{\nu}'} + \sum_{\tilde{\rho}'}\sum_{\tilde{a}} S_{\tilde{\lambda}'\tilde{\rho}'}\tau^{ij}_{\tilde{a}\tilde{\rho}'} d^{ij}_{\tilde{\nu}'\tilde{a}}\Bigg\}\end{aligned} \tag{3.82}$$

and another contribution originating from the prescreening energy correction:

$$y^{\delta}_{\tilde{\mu}'\tilde{\nu}'} = 4\sum_{ij} \mathbf{1}_S(ij) \sum_{\tilde{\eta}\tilde{\lambda}\tilde{\rho}\tilde{\chi}} \pi^{i}_{\tilde{\mu}'\tilde{\eta}} F_{\tilde{\eta}\tilde{\lambda}} t^{ij}_{\tilde{\lambda}\tilde{\rho}} t^{ij}_{\tilde{\chi}\tilde{\rho}} \pi^{i}_{\tilde{\nu}'\tilde{\chi}}, \tag{3.83}$$

3.1.4 Expressions for the Z-vector equations

The Lagrange multipliers are determined by making the Lagrangian stationary with respect to its parameters. For the PNO block-diagonality condition, a set of stationarity equations needs to be derived with respect to variations of the PNO coefficients,

$\frac{\partial \mathcal{L}}{\partial \theta^{ij}_{\tilde{a}''\tilde{b}''}} = 0$. Derivatives of the PNO coefficients in Eq. (3.38) are given by the expression

$$\left.\frac{\partial d''^{ij}_{\tilde{\mu}'\tilde{c}''}}{\partial \theta^{ij}_{\tilde{a}''\tilde{b}''}}\right|_{\boldsymbol{\theta}^{ij}=0} = d''^{ij}_{\tilde{\mu}'\tilde{a}''}\delta_{\tilde{b}''\tilde{c}''} - d''^{ij}_{\tilde{\mu}'\tilde{b}''}\delta_{\tilde{a}''\tilde{c}''}, \tag{3.84}$$

which can be used directly to take the derivative of the Lagrangian.

Derivatives of $\mathcal{L}$ with respect to parameters mixing retained PNOs $\theta^{ij}_{\tilde{a}\tilde{b}}$ or discarded PNOs $\theta^{ij}_{\tilde{a}'\tilde{b}'}$ among themselves are zero by construction. Therefore, the equations to determine $v^{ij}_{\tilde{a}\tilde{b}'}$ originate from stationarity with respect to parameters $\theta^{ij}_{\tilde{a}\tilde{b}'}$ mixing the two subspaces,

$$\sum_{\tilde{c}} \breve{D}^{ij}_{\tilde{a}\tilde{c}} v^{ij}_{\tilde{c}\tilde{b}'} - \sum_{\tilde{c}'} v^{ij}_{\tilde{a}\tilde{c}'} \breve{D}^{ij}_{\tilde{c}'\tilde{b}'} = -\frac{\partial E_2^{\mathrm{DLPNO}}}{\partial \theta^{ij}_{\tilde{a}\tilde{b}'}} - \frac{\partial \Delta E_{\mathrm{PNO}}}{\partial \theta^{ij}_{\tilde{a}\tilde{b}'}}. \tag{3.85}$$

The left-hand side of Eq. (3.85) is the derivative of the block-diagonality constraint for PNOs, which contains the semicanonical density that is parameterised through the amplitudes defined in Eq. (3.48):

$$\breve{\mathbf{D}}^{ij} = \exp\left(-\boldsymbol{\theta}^{ij}\right)\left[\hat{\mathbf{T}}^{ij\dagger}\tilde{\hat{\mathbf{T}}}^{ij} + \hat{\mathbf{T}}^{ij}\tilde{\hat{\mathbf{T}}}^{ij\dagger}\right]\exp\left(\boldsymbol{\theta}^{ij}\right) \tag{3.86}$$

Since the semicanonical residual equation is invariant to PNO rotations, $\frac{\partial \breve{\mathbf{R}}^{ij}}{\partial \boldsymbol{\theta}^{ij}} = 0$, the contributing terms on the right-hand side of Eq. (3.85) are the derivatives of the PNO-basis Hylleraas functional and of the energy correction for PNO truncation:

$$\frac{\partial E_2^{\mathrm{DLPNO}}}{\partial \theta^{ij}_{\tilde{a}\tilde{b}'}} = -2\sum_{\tilde{c}}\left[\tilde{T}^{ij}_{\tilde{a}\tilde{c}}\left(i\tilde{b}'\middle|j\tilde{c}\right) + \tilde{T}^{ij}_{\tilde{c}\tilde{a}}\left(i\tilde{c}\middle|j\tilde{b}'\right) + D^{ij}_{\tilde{a}\tilde{c}}F_{\tilde{c}\tilde{b}'}\right] + 2\sum_{\tilde{\mu}'}\tau^{ij}_{\tilde{a}\tilde{\mu}'}S_{\tilde{\mu}'\tilde{b}'} \tag{3.87}$$

$$\frac{\partial \Delta E_{\mathrm{PNO}}}{\partial \theta^{ij}_{\tilde{a}\tilde{b}'}} = \sum_{\tilde{c}}\left[(i\tilde{a}|j\tilde{c})\,\tilde{\breve{T}}^{ij}_{\tilde{b}'\tilde{c}} + (i\tilde{c}|j\tilde{a})\,\tilde{\breve{T}}^{ij}_{\tilde{c}\tilde{b}'} + \left(i\tilde{b}'\middle|j\tilde{c}\right)\tilde{\breve{T}}^{ij}_{\tilde{a}\tilde{c}} + \left(i\tilde{c}\middle|j\tilde{b}'\right)\tilde{\breve{T}}^{ij}_{\tilde{c}\tilde{a}}\right] \tag{3.88}$$

The PNO Z-vector equations in Eq. (3.85) are most easily solved for the Lagrange multipliers $v^{ij}_{\tilde{a}\tilde{b}'}$ by transforming the set of functions $\tilde{a}$ and $\tilde{b}'$ to the eigenvector representation of the semicanonical density $\breve{\mathbf{D}}^{ij}$, such that the left-hand side becomes $n_{\tilde{a}}v^{ij}_{\tilde{a}\tilde{b}'} - v^{ij}_{\tilde{a}\tilde{b}'}n_{\tilde{b}'}$. Eq. (3.87) contains the quantity $\tau^{ij}_{\tilde{a}\tilde{\mu}'}$, which has been defined previously in Eq. (3.81).

Equations to determine the Lagrange multipliers $w^{ij}_{\tilde{a}''\tilde{b}''}$ associated with the semicanonical residual constraint are derived from the stationarity condition $\frac{\partial \mathcal{L}}{\partial \hat{T}^{ij}_{\tilde{a}''\tilde{b}''}} = 0$ of

the Lagrangian with respect to the semicanonical amplitude parameters. Since the non-redundant PAOs span the same space as the untruncated PNOs, it is most convenient to represent the semicanonical Z-vector equations in a basis of pseudo-canonical non-redundant PAOs, which diagonalise the Fock matrix with eigenvalues $\varepsilon_{\tilde{\mu}}$:

$$\left(\varepsilon_{\tilde{\mu}} + \varepsilon_{\tilde{\nu}} - F_{ii} - F_{jj}\right) w^{ij}_{\tilde{\mu}\tilde{\nu}} = -\frac{\partial \sum_{\tilde{a}\tilde{b}'} v^{ij}_{\tilde{a}\tilde{b}'} \breve{D}^{ij}_{\tilde{a}\tilde{b}'}}{\partial \hat{T}^{ij}_{\tilde{\mu}\tilde{\nu}}} - \frac{\partial \Delta E^{\mathrm{PNO}}}{\partial \hat{T}^{ij}_{\tilde{\mu}\tilde{\nu}}} \tag{3.89}$$

The right-hand side of the equations contains the derivatives of the PNO block-diagonality constraint with respect to the semicanonical amplitude parameters

$$\frac{\partial \sum_{\tilde{c}\tilde{d}'} v^{ij}_{\tilde{c}\tilde{d}'} \breve{D}^{ij}_{\tilde{c}\tilde{d}'}}{\partial \hat{T}^{ij}_{\tilde{\mu}\tilde{\nu}}} = \sum_{\tilde{\eta}} \left[\left(\bar{v}^{ij}_{\tilde{\mu}\tilde{\eta}} + \bar{v}^{ij}_{\tilde{\eta}\tilde{\mu}} \right) \breve{\tilde{T}}^{ij}_{\tilde{\eta}\tilde{\nu}} + \breve{\tilde{T}}^{ij}_{\tilde{\mu}\tilde{\eta}} \left(\bar{v}^{ij}_{\tilde{\eta}\tilde{\nu}} + \bar{v}^{ij}_{\tilde{\nu}\tilde{\eta}} \right) \right]$$

$$\text{with} \quad \bar{v}^{ij}_{\tilde{\mu}\tilde{\nu}} = \sum_{\tilde{a}\tilde{b}'} S_{\tilde{\mu}\tilde{a}} v^{ij}_{\tilde{a}\tilde{b}'} S_{\tilde{\nu}\tilde{b}'}, \tag{3.90}$$

and of the energy correction for PNO truncation:

$$\frac{\partial \Delta E^{\mathrm{PNO}}}{\partial \hat{T}^{ij}_{\tilde{\mu}\tilde{\nu}}} = \frac{4\,(i\tilde{\mu}|j\tilde{\nu}) - 2\,(i\tilde{\nu}|j\tilde{\mu}) - \sum_{\tilde{a}\tilde{b}} S_{\tilde{\mu}\tilde{a}} \left[4\left(i\tilde{a}\middle|j\tilde{b}\right) - 2\left(i\tilde{b}\middle|j\tilde{a}\right) \right] S_{\tilde{\nu}\tilde{b}}}{1 + \delta_{ij}}. \tag{3.91}$$

Eqs. (3.85) and (3.89) determine the Lagrange multipliers for the PNO and semicanonical constraints. Importantly, the equations sets are solved independently for each pair of orbitals.

In order to calculate the multipliers $\mathbf{z}$ and $\mathbf{z}^{\mathrm{Loc}}$ associated with the Brillouin constraint and the orbital localisation constraint, respectively, the Lagrangian needs to be made stationary with respect to the molecular orbital variations $\frac{\partial \mathcal{L}}{\partial \kappa_{pq}}$. With the derivative of MO coefficients $\frac{\partial \mathbf{C}}{\partial \boldsymbol{\kappa}}$ that was provided in Eq. (3.19), the following expression is obtained for the derivative of redundant PAO coefficients:

$$\begin{gathered}\frac{\partial \tilde{P}_{\mu\tilde{\nu}'}}{\partial \kappa_{ia}} = N_{\tilde{\nu}'} \left(C_{\mu i} S_{a\nu} + C_{\mu a} S_{i\nu} \right) - N_{\tilde{\nu}'} S_{i\nu} S_{a\tilde{\nu}'} \tilde{P}_{\mu\tilde{\nu}'} \quad \text{with} \quad S_{p\nu} = \sum_{\eta} C_{\eta p} S_{\eta\nu} \\ \frac{\partial \tilde{P}_{\mu\tilde{\nu}'}}{\partial \kappa_{ij}} = \frac{\partial \tilde{P}_{\mu\tilde{\nu}'}}{\partial \kappa_{ab}} = 0\end{gathered} \tag{3.92}$$

Projected atomic orbitals are invariant with respect to orthogonal transformations among occupied or among virtual molecular orbitals.

PNO coefficients depend upon molecular orbital parameters via the symmetric orthogonalisation in their parameterisation, which contains a matrix in PAO basis. This introduces a non-vanishing derivative with respect to MO rotations mixing occupied and virtual contributions:

$$\begin{aligned}\frac{\partial d''^{kl}_{\tilde{\mu}'\tilde{b}''}}{\partial \kappa_{ia}} = -\frac{1}{2}\sum_{\tilde{\nu}'\tilde{\eta}'} N_{\tilde{\nu}'} S_{i\nu} S_{a\tilde{\eta}'} \sum_{\tilde{c}''} d''^{kl}_{\tilde{\nu}'\tilde{c}''} \Big[d''^{kl}_{\tilde{\nu}'\tilde{c}''} \Big(d''^{kl}_{\tilde{\eta}'\tilde{b}''} - S_{\tilde{\nu}'\tilde{b}''}\delta_{\tilde{\nu}'\tilde{\eta}'} \Big) \\ + d''^{kl}_{\tilde{\nu}'\tilde{b}''} \Big(d''^{kl}_{\tilde{\eta}'\tilde{c}''} - S_{\tilde{\nu}'\tilde{c}''}\delta_{\tilde{\nu}'\tilde{\eta}'} \Big) \Big] \\ \frac{\partial d''^{kl}_{\tilde{\mu}'\tilde{c}''}}{\partial \kappa_{ij}} = \frac{\partial d''^{kl}_{\tilde{\mu}'\tilde{c}''}}{\partial \kappa_{ab}} = 0\end{aligned} \tag{3.93}$$

The Z-vector equations are thus derived by substituting Eqs. (3.19), (3.92) and (3.93). A set of coupled-perturbed localisation (CP-L) equations needs to be solved to determine the orbital localisation Lagrange multipliers $\mathbf{z}^{\mathrm{Loc}}$:

$$\sum_k \left[A^{\mathrm{Loc}}_{ij,k} z^{\mathrm{Loc}}_{ik} - A^{\mathrm{Loc}}_{ji,k} z^{\mathrm{Loc}}_{jk} \right] = -L_{ij} \tag{3.94}$$

$A_{ip,k}$ is the localisation response tensor defined in Eq. (3.75). The right-hand side of the CP-L equations contains the derivative of the remaining terms in the Lagrangian with respect to rotation parameters among occupied orbitals,

$$L_{ij} = \sum_{\tilde{\mu}'}\sum_K \Gamma^K_{j\tilde{\mu}'}\,(i\tilde{\mu}'|K) - \sum_{\tilde{\mu}'}\sum_K \Gamma^K_{i\tilde{\mu}'}\,(j\tilde{\mu}'|K) - 2\sum_k F_{ik} D'^{\mathrm{o}}_{kj} + 2\sum_k F_{kj} D'^{\mathrm{o}}_{ik} + L^{\mathrm{Pre}}_{ij}. \tag{3.95}$$

$\Gamma^K_{i\tilde{\mu}'}$ was introduced as the two-body density in Eq. (3.60). $\mathbf{D}'^{\mathrm{o}}$ is the occupied orbital block of the PNO-relaxed density defined in Eq. (3.59), which includes the prescreening contribution to the unrelaxed density.

An additional term originating from the energy correction for screened-out pairs is

contained in L_{ij}:

$$L_{ij}^{\mathrm{Pre}} = \sum_{\tilde{\mu}'} \sum_{n=1}^{3} \left[y_{j\tilde{\mu}'}^{\alpha,n} r_n^{i\tilde{\mu}'} - y_{i\tilde{\mu}'}^{\alpha,n} r_n^{j\tilde{\mu}'} \right] + \sum_{n=1}^{3} r_n^{ij} \left[y_j^{\beta,n} - y_i^{\beta,n} \right]. \tag{3.96}$$

Finally, the Lagrange multipliers associated with the Brillouin condition are determined through stationarity of the Lagrangian with respect to the mixing of occupied and virtual orbitals:

$$\sum_b z_{ib} F_{ba} - \sum_j F_{ij} z_{ja} + \sum_{jb} A_{ia,jb} z_{jb} = L_{ia} \tag{3.97}$$

The Fock response tensor $A_{pq,rs}$ was defined in Eq. (3.24).

Derivatives of the remaining terms in the Lagrangian with respect to κ_{ia} are contained on the right-hand side of the equation:

$$L_{ia} = Y_{ia}^{\alpha} + \sum_{\tilde{\mu}'} \left[Y_{i\tilde{\mu}'}^{\beta} N_{\tilde{\mu}'} S_{a\mu} + Y_{a\tilde{\mu}'}^{\beta} N_{\tilde{\mu}'} S_{i\mu} \right] - \sum_{\tilde{\mu}'} Y_{\tilde{\mu}'}^{\gamma} N_{\tilde{\mu}'}^2 S_{i\mu} S_{a\mu} \tag{3.98}$$

The intermediate quantities $\mathbf{Y}^{\alpha}$, $\mathbf{Y}^{\beta}$ and $\mathbf{Y}^{\gamma}$ were introduced in Eqs. (3.74), (3.78) and (3.79), respectively.

It is most convenient to solve the Z-vector equations (3.97) in a basis of canonical molecular orbitals. In that case, the left-hand side of the equations becomes identical with that of the coupled-perturbed Hartree-Fock equations (3.23). The canonical CP-SCF equations can be solved using well-established procedures.

3.1.5 Treatment of localisation orbital Hessian singularities

Under specific circumstances, the coupled-perturbed localisation equations can become singular. This subsection elaborates on the underlying cause, and presents a solution that was developed as part of this work.

Orthogonal transformations among occupied orbitals can be parameterised through the exponential of a matrix κ'_{ij}. Note that it is a different set of parameters from the matrix $\boldsymbol{\kappa}$ that was introduced to parameterise the full orbital space, and the indices of $\boldsymbol{\kappa}'$

are restricted to the occupied space:

$$C_{\mu i} = \sum_j C^0_{\mu j} \left[\exp\left(\boldsymbol{\kappa}'\right)\right]_{ji} \quad \text{with} \quad \kappa'_{ji} = -\kappa'_{ij} \tag{3.99}$$

The localisation constraint in the Lagrangian is derived by ensuring stationarity of the Foster-Boys localisation criterion with respect to variations of the parameters $\boldsymbol{\kappa}'$:

$$\begin{aligned} \frac{\partial}{\partial \kappa'_{ij}} \sum_k \left|\mathbf{r}^{kk}\right|^2 &= 4\mathbf{r}^{ij}\left(\mathbf{r}^{jj} - \mathbf{r}^{ii}\right) \\ &= -4s_{ij} \end{aligned} \tag{3.100}$$

s_{ij} in Eq. (3.45) is, thus, simply the orbital gradient scaled by a factor of $-\frac{1}{4}$.

The orbital Hessian of the Foster-Boys criterion in this parameterisation takes the following form:

$$\begin{aligned} H^{\mathrm{Loc}}_{ij,kl} = & \frac{\partial^2}{\partial \kappa'_{ij} \partial \kappa'_{kl}} \sum_m \left|\mathbf{r}^{mm}\right|^2 \Bigg|_{\boldsymbol{\kappa}'=0} \\ =& 8\left[\delta_{ik} - \delta_{il} - \delta_{jk} + \delta_{jl}\right]\mathbf{r}^{ij}\mathbf{r}^{kl} + 4\left[\delta_{ik} + \delta_{jl}\right]\mathbf{r}^{ik}\mathbf{r}^{jl} - 4\left[\delta_{il} + \delta_{jk}\right]\mathbf{r}^{il}\mathbf{r}^{jk} \\ & - 2\delta_{ik}\mathbf{r}^{jl}\left[\mathbf{r}^{jj} + \mathbf{r}^{ll}\right] + 2\delta_{il}\mathbf{r}^{jk}\left[\mathbf{r}^{jj} + \mathbf{r}^{kk}\right] \\ & + 2\delta_{jk}\mathbf{r}^{il}\left[\mathbf{r}^{ii} + \mathbf{r}^{ll}\right] - 2\delta_{jl}\mathbf{r}^{ik}\left[\mathbf{r}^{ii} + \mathbf{r}^{kk}\right] \end{aligned} \tag{3.101}$$

Provided that the orbital gradient is zero, the response matrix of $\mathbf{s}$, which is contained in the coupled-perturbed localisation equations, is identical with the orbital Hessian up to a constant prefactor:

$$\left.\frac{\partial s_{ij}}{\partial \kappa_{kl}}\right|_{\boldsymbol{\kappa}=0} = -\frac{1}{4} H^{\mathrm{Loc}}_{ij,kl} \quad \text{if} \quad \mathbf{s}\left(\boldsymbol{\kappa}=0\right) = 0 \tag{3.102}$$

The CP-L equations (3.94) for an appropriate set of localised orbitals may be expressed in terms of $\mathbf{H}^{\mathrm{Loc}}$:

$$\frac{1}{4}\sum_{k<l} H^{\mathrm{Loc}}_{ij,kl} z^{\mathrm{Loc}}_{kl} = L_{ij} \tag{3.103}$$

Eq. (3.102) is not true if the orbital gradient of the localisation criterion does not equal

zero; this would be the case if the orbitals did not originate from a converged localisation procedure. Such a special case will not be considered in this work, as the starting point is assumed to be a set of well-defined localised orbitals.

Since Foster-Boys orbitals maximise $\sum_i |\mathbf{r}^{ii}|^2$, all eigenvalues of the matrix $\mathbf{H}^{\mathrm{Loc}}$ are negative (with each row or column corresponding to one independent parameter κ'_{ij} for $i < j$). The CP-L equations (3.94) are a system of linear equations with a positive-semidefinite coefficient matrix, since the response of $\mathbf{s}$ is just the orbital Hessian of the localisation sum multiplied by $-\frac{1}{4}$.

Under specific circumstances, some eigenvalues of $\mathbf{H}^{\mathrm{Loc}}$ may be small or zero, which leads to singular CP-L equations. In the following analysis, eigenvectors are labelled as $\mathbf{u}^n$ and eigenvectors as ω_n:

$$\sum_{k<l} H^{\mathrm{Loc}}_{ij,kl} u^n_{kl} = \omega_n u^n_{ij} \quad \text{with} \quad u^n_{ji} = -u^n_{ij} \tag{3.104}$$

Eigenvalues $\omega_n = 0$ commonly occur as the consequence of a continuous degeneracy. In such a case there is not a discrete set of solutions to the orbital localisation problem, but instead there is an entire continuum of orthogonal transformations that satisfy the localisation criterion.

As a trivial example for a continuous degeneracy, the orbitals of a linear molecule can be rotated collectively around the internuclear axis by an arbitrary angle without affecting the localisation criterion. More complicated cases of continuous degeneracy may occur in specific symmetry groups, which was recognised by England.[171] Later, Scheurer and Schwarz derived rules for the Foster-Boys, Von Niessen and Edmiston-Ruedenberg schemes, which specify if a continuous degeneracy is allowed or forbidden depending on the symmetry group of the electronic density. Rather interestingly, they found that the symmetry groups with either allowed or forbidden continuous degeneracy are identical among all three localisation methods.[172, 173]

The CP-L equations are analysed most conveniently by transforming Eq. (3.103) into

the eigenvector basis of $\mathbf{H}^{\mathrm{Loc}}$. This leads to the transformed right-hand side vector

$$\bar{L}_n = \sum_{i<j} L_{ij} u_{ij}^n, \tag{3.105}$$

and to the transformed Lagrange multipliers

$$\bar{z}_n^{\mathrm{Loc}} = \sum_{i<j} z_{ij}^{\mathrm{Loc}} u_{ij}^n = 4\frac{\bar{L}_n}{\omega_n}. \tag{3.106}$$

Two different cases can be distinguished for an eigenvalue $\omega_n = 0$ from a formal viewpoint:

- $\bar{L}_n = 0$ means that the energy is invariant to orbital variations along $\mathbf{u}^n$. Constraining the first-order response, $\boldsymbol{\kappa}^{(1)}$, in the direction of this eigenvector is unnecessary. A valid solution is to relax the constraint by eliminating the transformed multiplier $\bar{z}_n^{\mathrm{Loc}} = 0$. Along the remaining directions, the multipliers $\bar{z}_{m\neq n}^{\mathrm{Loc}}$ are determined as usual.

- $\bar{L}_n \neq 0$ is a pathologic case: the energy is not constant for different orbitals that belong to the same continuously degenerate set, making it ill-defined.

In practice, a numerically sound distinction between these two cases may not always exist. Moreover, an energy calculated using continuously degenerate localised orbitals may nonetheless be physically meaningful, provided that it changes sufficiently little with other orbitals from the same set.

Singular CP-L equations are the consequence of an unfortunate interplay between the localisation criterion and the orbital-dependence of the local correlation energy. However, using a different localisation criterion is not an acceptable solution, unless it artificially breaks the symmetry of the molecule.

The π orbitals of benzene in the Pipek-Mezey localisation scheme are a notorious example for continuously degenerate orbitals (whereas in the Foster-Boys scheme there is a discrete two-fold degeneracy). Werner and Pflüger suggested domain merging as a workaround in local correlation methods for this case.[138] Toyota and co-workers proposed the minimum orbital-deformation method, which effectively maps a set of localised

reference orbitals onto slightly perturbed geometries, and thereby aims to circumvent discontinuous localised orbitals along a potential energy surface.[174, 175] All of these methods require some degree of user intervention.

In the context of the DLPNO-MP2 gradient, a more general and automatic approach is introduced through a modification of the localisation condition in the Lagrangian. The localisation sum is constrained to remain stationary along modes of the orbital Hessian with a non-zero eigenvalue only,

$$\bar{s}_n = \sum_{i<j} s_{ij} u_{ij}^n = 0 \quad \text{for} \quad |\omega_n| > 0. \tag{3.107}$$

It is assumed that the eigenvectors are constant, so that determining their response is not necessary to calculate the gradient. In addition, the response of the orbital parameters is restricted to remain orthogonal to eigenvectors with singular eigenvalues:

$$\bar{\kappa}_{n'} = \sum_{i<j} \kappa_{ij} u_{ij}^{n'} = 0 \quad \text{for} \quad |\omega_{n'}| \approx 0 \tag{3.108}$$

The underlying idea is that the perturbed orbitals should remain similar to the original orbitals, which is achieved by eliminating the response $\boldsymbol{\kappa}^{(1)}$ along continuously degenerate modes. Both conditions together define the modified localisation constraint for the DLPNO-MP2 Lagrangian:

$$\begin{aligned}\mathcal{L} \leftarrow & \sum_n \bar{z}_n^{\mathrm{Loc}} \bar{s}_n + \sum_{n'} \bar{z}_{n'}^{\mathrm{Loc}} \bar{\kappa}_{n'} \\ & = \sum_{i<j} \sum_{k<l} z_{ij}^{\mathrm{Loc}} \left[\delta_{ij,kl} - \sum_{n'} u_{ij}^{n'} u_{kl}^{n'} \right] s_{kl} + \sum_{i<j} \sum_{k<l} \sum_{n'} z_{ij}^{\mathrm{Loc}} u_{ij}^{n'} u_{kl}^{n'} \kappa_{kl}\end{aligned} \tag{3.109}$$

n' enumerates the eigenvectors associated with singular eigenvalues.

In the resulting procedure, a modified set of CP-L equations is solved to determine the Lagrange multipliers:

$$\frac{1}{4} \sum_{k<l} \tilde{H}_{ij,kl}^{\mathrm{Loc}} z_{kl}^{\mathrm{Loc}} = L_{ij}, \tag{3.110}$$

This is directly related to Eq. (3.103). However, $\tilde{\mathbf{H}}^{\mathrm{Loc}}$ corresponds to an orbital Hessian

of the Foster-Boys localisation sum with its singular eigenvalues shifted to one:

$$\tilde{H}^{\mathrm{Loc}}_{ij,kl} = \sum_{\bar{i}<\bar{j}} \sum_{\bar{k}<\bar{l}} \left[\delta_{ij,\bar{i}\bar{j}} - \sum_{n'} u^{n'}_{ij} u^{n'}_{\bar{i}\bar{j}} \right] H^{\mathrm{Loc}}_{\bar{i}\bar{j},\bar{k}\bar{l}} \left[\delta_{kl,\bar{k}\bar{l}} - \sum_{n'} u^{n'}_{kl} u^{n'}_{\bar{k}\bar{l}} \right] + \sum_{n'} u^{n'}_{ij} u^{n'}_{kl} \tag{3.111}$$

After the modified CP-L equations have been solved, the final Lagrange multipliers are replaced by a projection:

$$z^{\mathrm{Loc}}_{ij} \rightarrow \sum_{k<l} z^{\mathrm{Loc}}_{kl} \left[\delta_{kl,ij} - \sum_{n'} u^{n'}_{kl} u^{n'}_{ij} \right]. \tag{3.112}$$

Specifically, this affects the density matrix for the dipole integrals in Eq. (3.66) and the intermediate quantity in Eq. (3.74), where $\mathbf{z}^{\mathrm{Loc}}$ is used.

This resulting procedure may be understood as shifting the singular eigenvalues of the Foster-Boys orbital Hessian in the CP-L equations, and then removing components of the solution along the singular eigenvectors by projection.

3.2 Implementation

3.2.1 General aspects

As the DLPNO-MP2 method itself, the gradient for DLPNO-MP2 was implemented within the ORCA package.[35, 36] The four different types of Z-vector equations need to be solved in the following order:

1. The PNO equations to calculate $\mathbf{v}^{ij}$ for each pair.
2. The semicanonical equations to calculate $\mathbf{w}^{ij}$ for each pair.
3. The coupled-perturbed localisation (CP-L) equations to determine $\mathbf{z}^{\mathrm{Loc}}$.
4. A set of coupled-perturbed self-consistent field (CP-SCF) equations to determine $\mathbf{z}$.

Each of these steps requires the Lagrange multipliers of the previous equation set to be determined, e.g. $\mathbf{v}^{ij}$ (1) is needed to solve the semicanonical equations (2) for the same pair, which determine $\mathbf{w}^{ij}$. On the other hand, the solutions of the equations

appearing lower in the list do not affect any of their preceding equation sets, so that the semicanonical or PNO equations are not coupled backwards to the solution of the CP-L or CP-SCF procedures.

Algorithm 3 Outline of the overall procedure to calculate the DLPNO-MP2 gradient.

1: Energy calculation ▷ Details in Algorithm 1
2: Processing of pair-specific gradient terms ▷ Details in Algorithm 4
3: Calculate RI metric gradient $\sum_{KL} \gamma_{KL} \left(K|L\right)^x$
4: Calculate prescreening contributions: $\mathbf{D}^{\mathrm{v(Pre)}}, \mathbf{D}^{\mathrm{o(Pre)}}, \mathbf{Q}^{n\mathrm{(Pre)}}, \mathbf{y}^{\alpha,n}, \mathbf{y}^{\beta,n}, \mathbf{y}^{\delta}, L_{ij}^{\mathrm{Pre}}$
5: Sort two-body density $\Gamma^i_{K\tilde{\mu}'} \rightarrow \Gamma^K_{i\tilde{\mu}'}$
6: Calculate $\sum_{K\tilde{\mu}'} \Gamma^K_{i\tilde{\mu}'} \left(p\tilde{\mu}'|K\right), \sum_{iK} \Gamma^K_{i\tilde{\mu}'} \left(ip|K\right)$ (integral direct) for $\mathbf{Y}^{\alpha}, \mathbf{Y}^{\beta}, L_{ij}$
7: Three-index integral gradient $\sum_{\mu\nu} \sum_K \Gamma^K_{\mu\nu} \left(\mu\nu|K\right)^x$
8: Solve CP-L equations for $\mathbf{z}^{\mathrm{Loc}}$
9: Calculate Fock response $\sum_{\mu\nu} A_{ip,\mu\nu} D'_{\mu\nu}$ for Y^{α}_{ip}
10: Finalise contributions for $\mathbf{Y}^{\alpha}$, $\mathbf{Y}^{\beta}$, L_{ia} and $\mathbf{W}$
11: Solve CP-SCF equations for $\mathbf{z}$
12: Calculate Fock response $\sum_{\mu\nu} A_{ip,jb} z_{jb}$ for Y^{ϵ}_{ip} in $\mathbf{W}$
13: Dipole gradient $\sum_{n=1}^{3} \sum_{\mu\nu} Q^n_{\mu\nu} \left\langle \mu|r_n|\nu \right\rangle^x$
14: Gradient contributions $\sum_{\mu\nu} \left[P^{\mathrm{SCF}}_{\mu\nu} + D''_{\mu\nu}\right] h^x_{\mu\nu}, \sum_{\mu\nu} W_{\mu\nu} S^x_{\mu\nu}$
15: Calculate Fock gradient with $\left(\mu\nu|\eta\lambda\right)^x$

An outline of the complete procedure is provided in Algorithm 3. After the energy has been calculated, all pair-dependent quantities involving PNOs are processed in the beginning of the gradient calculation. All subsequent steps (except for the inexpensive prescreening contributions) involve only processing of global quantities without further reference to pair-specific information. This includes solving the CP-L and CP-SCF equations, and calculating the derivatives of integrals in an atomic orbital basis.

The CP-L equations feature a quadratic matrix of size $\frac{n(n-1)}{2}$, where n is the number of occupied orbitals in the relevant sub-block. Therefore, the equation system is solved iteratively using the conjugate gradient algorithm with diagonal preconditioning (see ref. [176] for an introduction). Note that the CP-L equations can be expressed in terms of a positive-definite quadratic matrix (Eq. (3.103)). An iterative Jacobi algorithm with DIIS extrapolation was found to exhibit inferior performance. In addition, it is possible to construct the full Hessian matrix to apply a LAPACK linear equation solver via Cholesky decomposition, but this approach is only feasible for sufficiently small systems.

Before solving the CP-L equations, singular and near-singular eigenvalues of the or-

bital localisation Hessian are removed using the procedure described in Section 3.1.5. Since the number of rows and columns of the Hessian matrix each grow quadratically with system size and only its few smallest eigenvalues are needed, it is diagonalised using the Davidson method by default.[177, 178] The eigenvectors need to be determined to a sufficiently high precision; otherwise, singular and non-singular components could be mixed, and numerical artefacts propagated to the CP-L equations.

By default, the eigenvalues are converged to an accuracy of 10^{-6} times the singular eigenvalue threshold, which will be determined in Section 3.3.3. The diagonalisation residual is converged to 0.1 times the threshold for the iterative solution of the CP-L equations. As an alternative to Davidson diagonalisation, it is also possible to build the full Hessian matrix for diagonalisation via the appropriate LAPACK solver, but this option is only attractive for sufficiently small systems.

The time needed to solve the Hartree-Fock and the CP-SCF equations has a large impact on the overall cost of the calculation. Our implementation fully integrates the RIJCOSX technique,[145] which accelerates the evaluation of the Fock response function and the solution of the CP-SCF equations; the computation of Fock matrix gradient; and, of course, the SCF procedure itself. The integration of RIJCOSX with the RI-MP2 method has been described in an earlier publication,[179] so that it could be interfaced with the DLPNO-MP2 gradient via the appropriate function calls. Derivatives of the dipole integrals have been implemented analytically using the McMurchie-Davidson scheme[180] for the final version of the DLPNO-MP2 gradient, while numerical integration on a grid was performed in preliminary implementations.

The correctness of the gradient was verified by comparison with numerical derivatives, and by ensuring convergence to the RI-MP2 gradient with tightening thresholds. Since this thesis contains results obtained with different software versions, the interested reader is referred to ref. [110, 111] for details on the numerical verification of the respective gradient implementations.

The DLPNO-MP2 gradient supports spin-component scaling and double-hybrid density functionals. An implementation of the DHDF gradient with RI-MP2 in ORCA has

been described previously,[181] and the DLPNO-MP2 gradient interfaces the same code to calculate additional terms for the Fock response function and the gradient.

3.2.2 Processing of pair-dependent terms in the DLPNO-MP2 gradient

The first part of the gradient calculation, shown in Algorithm 4, processes pair-specific terms in PNO basis and their related contributions. From the DLPNO-MP2 energy calculation, the PNO-basis amplitudes $T^{ij}_{\tilde{a}\tilde{b}}$ and the integrals $\left(i\tilde{a}\middle|j\tilde{b}\right)$ are carried forward to the gradient on disk alongside the matrices $d^{ij}_{\tilde{\mu}'\tilde{a}}$, which transform the redundant PAOs of domain $\{\tilde{\mu}'\}_{ij}$ to the truncated set of PNOs $\tilde{a}$. In order to avoid potentially excessive storage requirements, pair-specific matrices that are entirely in non-redundant PAOs basis are not stored on disk. Therefore, non-redundant PAOs and the semicanonical amplitudes $\hat{T}^{ij}_{\tilde{\mu}\tilde{\nu}}$ are recalculated for each pair and processed in memory only.

Solving the PNO-specific Z-vector equations requires a set of complementary PNOs (CPNOs) $\tilde{a}'$. Even though they are readily available as a by-product during PNO construction, in the gradient calculation they need to be reconstructed as the orthogonal complement to the PNOs that were stored on disk.

Different numerical procedures could be used for complementary PNO construction, e.g. singular value decomposition or QR factorisation of the overlap matrix $\langle\tilde{\mu}|\tilde{a}\rangle$, which is identical with the matrix $\bar{d}^{ij}_{\tilde{\mu}\tilde{a}_{ij}}$ defined in Eq. (2.31). An alternative is to diagonalise $\bar{\mathbf{d}}^{ij}\bar{\mathbf{d}}^{ij\dagger}$, since all its eigenvalues are either 1 (for PNOs) or 0 (for CPNOs). Neither singular value decomposition nor diagonalisation (in their LAPACK implementations) were sufficiently stable in practice, failing on some occasions for this highly degenerate problem. A fully reliable procedure was arrived at through the diagonalisation of the matrix

$$\left(\mathbf{1}-\bar{\mathbf{d}}^{ij}\bar{\mathbf{d}}^{ij\dagger}\right)\mathbf{B}\left(\mathbf{1}-\bar{\mathbf{d}}^{ij}\bar{\mathbf{d}}^{ij\dagger}\right)-\bar{\mathbf{d}}^{ij}\bar{\mathbf{d}}^{ij\dagger}\mathbf{B}\bar{\mathbf{d}}^{ij}\bar{\mathbf{d}}^{ij\dagger}=\mathbf{B}-\bar{\mathbf{d}}^{ij}\bar{\mathbf{d}}^{ij\dagger}\mathbf{B}-\mathbf{B}\bar{\mathbf{d}}^{ij}\bar{\mathbf{d}}^{ij\dagger}, \quad (3.113)$$

with a suitable positive-definite matrix $\mathbf{B}$ chosen to lift the degeneracy of the eigenvalues.

Algorithm 4 Computation of pair-dependent quantities for the DLPNO-MP2 gradient.

if size($\mathbf{\Gamma}$) $<$ available memory **then**
  for all $i \geq j$ **do**
    PairContributions(i, j, ...)
    $\mathbf{\Gamma}^i := \mathbf{\Gamma}^i + \mathbf{G}^{i(ij)}$ ▷ Eq. (3.60)
    $\mathbf{\Gamma}^j := \mathbf{\Gamma}^j + \mathbf{G}^{j(ij)}$
  end for
else
  for all i **do**
    for all j **do**
      PairContributions(i, j, ...)
      $\mathbf{\Gamma}^i := \mathbf{\Gamma}^i + (1 + \delta_{ij})\, \mathbf{G}^{i(ij)}$ ▷ Eq. (3.60)
    end for
  end for
end if

function PairContribution(i, j, ...)
  Calculate non-redundant PAOs for pair ij
  Calculate semicanonical amplitudes $\breve{\mathbf{T}}^{ij}$ ▷ Eq. (2.29)
  Calculate intermediate quantity $\boldsymbol{\tau}^{ij}$ ▷ Eq. (3.81)
  Calculate complementary PNOs $\mathbf{d}'^{ij}$ ▷ PNOs $\mathbf{d}^{ij}$ from disk
  Solve the PNO Z-vector equations to obtain $\mathbf{v}^{ij}$ ▷ Eq. (3.85)
  Solve the semicanonical Z-vector equations to obtain $\mathbf{w}^{ij}$ ▷ Eq. (3.89)
  Calculate $\mathbf{G}^{i(ij)}$ ▷ Eq. (3.61)
  if $i \geq j$ **then** ▷ Quantities not needed to compute $\mathbf{G}^{i(ij)}$
    Calculate $\mathbf{G}^{j(ij)}$
    Add pair contribution to $\boldsymbol{\gamma}$ ▷ Eq. (3.65)
    Add pair contributions to the density $\mathbf{D}'^{\mathrm{v}}$ and $\mathbf{D}'^{\mathrm{o}}$ ▷ Eqs. (3.57, 3.59)
    Calculate pair contributions to $\mathbf{Y}^{\gamma}$ and $\mathbf{Y}^{\delta}$ ▷ Eqs. (3.79, 3.80)
  end if
end function

In our implementation, $\mathbf{B}$ was simply chosen as a diagonal matrix with its elements evenly spaced between 1 and 2. As a result, CPNOs are obtained as eigenvectors with associated eigenvalues distributed between 1 and 2 (while eigenvalues associated with PNOs are found between -2 and -1); numerical problems with highly degenerate eigenvalues are circumvented.

Implementing an efficient algorithm to calculate the two-body density $\Gamma^K_{i\tilde{\mu}'}$ is not entirely straightforward, as a compromise between the demands for memory, disk and the number of calculated terms needs to be achieved. Further constraints are imposed by the parallelisation concept of the ORCA software, which uses the Message Passing Interface (MPI) for communication and replicates data structures across processes. During the

construction of the two-body density, it is most convenient to store it as a set of matrices $\Gamma^i_{K\tilde{\mu}'}$, meaning that for each orbital there is one matrix with its rows indexed by auxiliary functions and its columns indexed by redundant PAOs. A number of quantities need to be calculated to determine the two-body density contribution by each pair: this includes re-determining the non-redundant PAOs and complementary PNOs, and solving the Z-vector equations for the PNOs and the semicanonical amplitudes. Because of the overhead associated with these steps, it is preferable to perform them only once for each pair, though in practice it is always possible to do so no more than twice. We investigated the following algorithms to accumulate contributions by each pair:

1. Provided that the entire two-body density $\Gamma^K_{i\tilde{\mu}'}$ tensor can be stored in memory by each process, random access is possible to any of its elements, so that the contributions $\mathbf{G}^{i(ij)}$ and $\mathbf{G}^{j(ij)}$ by each pair can be added in memory. As shown in Algorithm 4, this results in an efficient and simple procedure which iterates over each pair ij only once, but it can only be used for sufficiently small systems. The program automatically selects this procedure if sufficient memory is available to store the entire two-body density in memory.

2. For larger systems, it becomes inevitable to store the two-body density on disk. A simple algorithm can be implemented by nesting loops iterating over the occupied orbitals i and j, so that contributions $\mathbf{G}^{i(ij)}$ are accumulated for all j, but only one i at a time. As shown in Algorithm 4, this is the procedure selected automatically if the entire two-body density $\mathbf{\Gamma}$ is too large to be stored in the memory allocated to a single process. A disadvantage of this approach is that all quantities necessary to calculate $\mathbf{G}^{i(ij)}$, such as the non-redundant PAOs and the semicanonical amplitudes, or the Lagrange multipliers associated with the PNO and semicanonical constraints, need to be calculated twice for all pairs with $i \neq j$. The calculation is parallelised by splitting the outermost loop over orbitals i. Pair-specific contributions that are not required to construct the two-body density are calculated only for pairs with $i \geq j$. Therefore, the orbitals i need to be distributed appropriately over the parallel processes such that the load is balanced adequately.

3. An experimental algorithm was tested, which passes all pairs only once, but can be used regardless of the system size. It is shown in the scheme Algorithm 5. Required fragments of the two-body density are read from disk and retained in a memory buffer. Once the buffer fills all available memory, its contents are written back to disk. A disadvantage of this algorithm is the increased demand for disk read and write access via the operating system. Moreover, each parallel process needs to store a fully dimensioned local copy of the $\mathbf{\Gamma}$ contributions for all indices.

Algorithm 5 Experimental buffering algorithm to compute the two-body density (not used in practice).

```
Initialise buffer (Γ)
for all i ≥ j do
    ...
    Estimate memory for the following steps
    if necessary memory > available memory then
        Write buffer content to disk, empty buffer
    end if
    for all K ∈ {ij}_RI do
        if Γ^i_{Kμ̃'} not in buffer then
            Load entire row Γ^i_{Kμ̃'} for i and K into buffer
        end if
        if Γ^j_{Kμ̃'} not in buffer then
            Load entire row Γ^j_{Kμ̃'} for j and K into buffer
        end if
    end for
    Add G^{i(ij)} to buffered Γ^i
    Add G^{j(ij)} to buffered Γ^j
    ...
end for
Write buffer to disk, empty buffer
```

Variant (3) was the first to be implemented for the DLPNO-MP2 gradient. However, its performance with several parallel processes on one node was found to be somewhat unpredictable for larger systems, and often limited by disk access. Therefore, it was abandoned in favour of automatically using one out of variants (1) or (2). Approach (2) is sufficiently general for all system sizes; modest performance improvements can be achieved by switching to (1) whenever possible, as shown by the results in Section 3.3.8. After completion of this step, the two-body density is reordered such that the associated

container indexes matrices by auxiliary functions, storing them as $\Gamma^K_{i\tilde{\mu}'}$.

Matrix containers in ORCA are usually read by retrieving an entire matrix at once. When accessing the RI integrals $(i\tilde{\mu}'|K)$ for a specific orbital i, this implies reading all entries mapped by $L_{\text{ext}}\,(i \to \tilde{\mu}')$ and $L_{\text{ext}}\,(i \to K)$. Compared with the actual sizes of the pair domains $\{ij\}$ and $\{ij\}_{\text{RI}}$, it results in reading more data than necessary; for large systems with several thousand basis functions, only a few percent of the data read from disk for each pair ij is actually used. On the other hand, retrieving only the necessary matrix elements selectively would result in an excessive number of operating system calls.

A suitable compromise was achieved by reading the entire row of a matrix from the container if at least one entry from the respective row is required. Blocks of adjacent rows are always read in a single operation. Basis functions belonging to the same shell and to the same atoms are stored sequentially. Therefore, at most one reading operation per atom is required to retrieve the integrals $(i\tilde{\mu}'|K)$ for a specific orbital i with a given pair domain $\tilde{\mu}' \in \{ij\}$ and fitting domain $K \in \{ij\}_{\text{RI}}$, but reading of unnecessary data is reduced substantially.

3.2.3 Sparse maps

As shown in Section 2.1.6, the RI integrals required to calculate the DLPNO-MP2 energy are determined by the extended maps $\mathbf{L}_{\text{ext}}\,(i \to \tilde{\mu}')$ and $\mathbf{L}_{\text{ext}}\,(i \to K)$. Since the integrals in AO basis $(\mu\nu|K)$ are transformed by matrix multiplications for each K, a complete list of all generated integrals is not given by the preceding maps, but rather by $\mathbf{L}\,(K \to i)$ and $\mathbf{L}\,(K \to \tilde{\mu}')$ as specified in Eqs. (2.57, 2.58). Accordingly, the full set of AO basis integrals that are calculated prior to the transformation is mapped by $\mathbf{L}\left(K \to \mu^{\text{MO}}\right)$ and $\mathbf{L}\left(K \to \nu^{\text{PAO}}\right)$ in Eqs. (2.59, 2.60).

Next, the necessary maps for the gradient will be examined. The two-body density is first generated as a set of matrices $\Gamma^i_{K\tilde{\mu}'}$ indexed by the MO i. Inspection of Eq. (3.60) shows that all indices $\tilde{\mu}'$ and K are members of pair domains $\{ij\}$ or fitting pair domains $\{ij\}_{\text{fit}}$. Therefore, the complete lists are given by $L_{\text{ext}}\,(i \to \tilde{\mu}')$ and $L_{\text{ext}}\,(i \to K)$, the same as for the RI integrals. After the reordering procedure $\Gamma^i_{K\tilde{\mu}'} \to \Gamma^K_{i\tilde{\mu}'}$, the matrices for each

Algorithm 6 Algorithm to contract the two-body density with RI integrals.

$B^{\alpha}_{ip} := 0$ ▷ Buffer matrices $\mathbf{B}^{\alpha}, \mathbf{B}^{\beta}$
$B^{\beta}_{p\tilde{\mu}'} := 0$
for all auxiliary basis function shells K_S **do**
  for all basis function shells μ_S in $L\left(K_\mathrm{S} \to \mu_\mathrm{S}\right)$ **do** ▷ Primitive integrals
    for all basis function shells ν_S in $L\left(K_\mathrm{S} \to \nu_\mathrm{S}\right)$ **do**
      if $(\mu\nu|\mu\nu) >$ Schwarz screening threshold **then**
        Compute integrals $(\mu\nu|K)$
      end if
    end for
  end for
  for all functions K in K_S **do**
    $\Gamma^{K}_{i\nu} := \sum_{\tilde{\mu}'}^{L(K\to\tilde{\mu}')} \Gamma^{K}_{i\tilde{\mu}'} \tilde{P}'_{\nu\tilde{\mu}'}$ ▷ Terms in $(p\tilde{\mu}'|K)$
    $\mathrm{I}_{\eta i} := \sum_{\nu}^{L\left(K\to\nu^{\mathrm{PAO}}\right)} \Gamma^{K}_{i\nu} \left(\eta\nu|K\right)$ ▷ Buffer matrix $\mathbf{I}$
    $B^{\alpha}_{ip} := B^{\alpha}_{ip} + \sum_{\eta}^{L\left(K\to\eta^{\mathrm{MO}}\right)} C_{\eta p} \mathrm{I}_{\eta i}$
    $(i\nu|K) := \sum_{\eta}^{L\left(K\to\eta^{\mathrm{MO}}\right)} C_{\eta i} \left(\eta\nu|K\right)$ ▷ Terms in $(ip|K)$
    $(ip|K) := \sum_{\nu}^{L\left(K\to\nu^{\mathrm{PAO}}\right)} C_{\nu p} \left(i\nu|K\right)$
    $B^{\beta}_{p\tilde{\mu}'} := B^{\beta}_{p\tilde{\mu}'} + \sum_{i}^{L(K\to i)} \Gamma^{K}_{i\tilde{\mu}'} \left(ip|K\right)$
  end for
end for
$Y^{\alpha}_{ip} := Y^{\alpha}_{ip} - B^{\alpha}_{ip}$
$Y^{\beta}_{p\tilde{\mu}'} := Y^{\beta}_{p\tilde{\mu}'} + B^{\beta}_{p\tilde{\mu}'}$
$L_{ij} := L_{ij} - B^{\alpha}_{ij} + B^{\alpha}_{ji}$

K have row indices i and column indices $\tilde{\mu}'$, which are members of the maps $\mathbf{L}\left(K \to i\right)$ and $\mathbf{L}\left(K \to \tilde{\mu}'\right)$. These maps are more complete, as the chaining step introduces combinations of i and $\tilde{\mu}'$ for a given K that may not have been present in the original maps. The missing elements in $\Gamma^{K}_{i\tilde{\mu}'}$ are included as zeros.

In order to calculate the three-centre integral gradient, each matrix $\mathbf{\Gamma}^{K}$ is transformed to AO basis as in Eq. (3.64), and directly summed together with the integral derivatives $(\mu\nu|K)^{x}$. As for the integrals themselves, the maps of AO indices for the derivatives are $\mathbf{L}\left(K \to \mu^{\mathrm{MO}}\right)$ and $\mathbf{L}\left(K \to \nu^{\mathrm{PAO}}\right)$. In addition, all three-centre integrals used at any stage of the energy or gradient calculation are subject to Schwarz screening in the final implementation. It would also be possible to define separate screening criteria for derivatives of integrals, but this approach was not followed in the present work.

An additional set of integrals is calculated for the term $\sum_{K} \sum_{\tilde{\mu}'} \Gamma^{K}_{i\tilde{\mu}'} \left(p\tilde{\mu}'|K\right)$, which contributes to Y^{α}_{ip} in Eq. (3.74). Evidently, the respective PAOs are members of the map

$\mathbf{L}\,(K \to \tilde{\mu}')$, whereas the index p includes all occupied and virtual molecular orbitals. As the term originates from orbital rotations, the appropriate maps for the AOs are $\mathbf{L}\left(K \to \mu^{\mathrm{MO}}\right)$ and $\mathbf{L}\left(K \to \nu^{\mathrm{PAO}}\right)$. The processing is performed through an integral direct procedure. Optimal performance is achieved by arranging the matrix multiplications such that one index is always in the occupied orbital basis, as shown in the pseudocode in Algorithm 6. The computational expense of this procedure is comparable with the in-memory transformation of the RI integrals $(i\tilde{\mu}'|K)$, while the more expensive explicit formation of the two-external integrals $(a\tilde{\mu}'|K)$ is circumvented.

Another set of integrals is needed for the term $\sum_i \sum_K \Gamma^K_{i\tilde{\mu}'}\,(ip|K)$ contributing to $Y^{\beta}_{p\tilde{\mu}'}$ in Eq. (3.78). The occupied indices i are members of $\mathbf{L}\,(K \to i)$, while p enumerates all occupied and virtual orbitals. As before, the necessary AO basis RI integrals $(\mu\nu|K)$ are listed by the maps $\mathbf{L}\left(K \to \mu^{\mathrm{MO}}\right)$ and $\mathbf{L}\left(K \to \nu^{\mathrm{PAO}}\right)$. In this step, the most efficient procedure is to perform an integral direct transformation to $(ip|K)$, followed by summation over i (Algorithm 6).

3.2.4 Rational function optimisation of localised orbitals

Calculating accurate derivatives requires well-converged localised orbitals, as the Lagrangian includes the orbital gradient of the localisation criterion, Eq. (3.45), among its constraints. However, the commonly employed method of Jacobi sweeps[135, 182, 183] is, under practical circumstances, often not suited to find a solution with a vanishing orbital gradient.

Leonard and Luken suggested a combined approach of a first-order method for the initial iterations and a second-order method for later iterations of a localisation procedure.[184] Specific modifications needed to be made for systems with a singular or near-singular orbital Hessian of the localisation criterion. Subotnik and co-workers developed a first-order method in combination with DIIS to localise orbitals.[185] Later, they published a modification of the algorithm that can rectify convergence to a saddle point by a displacement along a normal mode, which is determined by Davidson diagonalisation.[186] A trust-region Newton-Raphson method for orbital localisation was im-

plemented by Høyvik and co-workers.[12] Sun described the "co-iterative augmented Hessian" method, which couples the optimisation step in the augmented Hessian method to Davidson diagonalisation, and demonstrated its performance for orbital localisation.[187]

The Newton-Raphson method for minimisation of a function f approximates the latter as a second-order Taylor series,

$$f(\mathbf{x}) \approx f_0 + \mathbf{g}^\dagger \mathbf{x} + \frac{1}{2}\mathbf{x}^\dagger \mathbf{H} \mathbf{x}, \tag{3.114}$$

with the gradient $\mathbf{g}$ and the Hessian matrix $\mathbf{H}$ of f. An iterative step is determined as the minimum of the quadratic model function, provided that $\mathbf{H}$ is positive definite:

$$\mathbf{x} = -\mathbf{H}^{-1}\mathbf{g} \tag{3.115}$$

A disadvantage of this second-order local optimisation method is the need to introduce explicit step size control for poorly behaved f and, more crucially, its inability to deal with functions that feature a singular (or near-singular) Hessian matrix. Moreover, the optimisation may converge to saddle points if there are positive and negative eigenvalues of $\mathbf{H}$.

Rational function optimisation (RFO) approximates the target function f through

$$f(\mathbf{x}) \approx f_0 + \frac{\mathbf{g}^\dagger \mathbf{x} + \frac{1}{2}\mathbf{x}^\dagger \mathbf{H} \mathbf{x}}{1 + \mathbf{x}^\dagger \mathbf{x}}, \tag{3.116}$$

which is identical with the quadratic Taylor series up to second order. An accessible explanation of the method was published by Banerjee and co-workers.[188]

The minimum of this function is found by solving the following eigenvalue problem:

$$\begin{pmatrix} H_{11} & \dots & H_{1n} & g_1 \\ \vdots & \ddots & \vdots & \vdots \\ H_{n1} & \dots & H_{nn} & g_n \\ g_1 & \dots & g_n & 0 \end{pmatrix} \begin{pmatrix} x_1 \\ \vdots \\ x_n \\ 1 \end{pmatrix} = \lambda \begin{pmatrix} x_1 \\ \vdots \\ x_n \\ 1 \end{pmatrix}. \tag{3.117}$$

For a function f of n variables $x_1, \ldots, x_n$, the left-hand matrix is an "augmented" Hessian of dimension $(n+1) \times (n+1)$. Note the unusual normalisation of the eigenvectors, which have a scaling factor that makes the $n+1$-th element equal to 1.

The eigenvalues of the augmented Hessian bracket the eigenvalues h_i of the Hessian $\mathbf{H}$, so that $\lambda_i \leq h_i \leq \lambda_{i+1}$. At a stationary point with $\mathbf{g} = 0$, one of the eigenvalues equals zero, whereas the remaining values λ become identical with the eigenvalues of the Hessian $\mathbf{H}$. A local minimum is found by following the vector $\mathbf{x}$ associated with the lowest eigenvalue λ_1, whereas vectors associated with eigenvalues $\lambda_2, \ldots, \lambda_n$ lead towards saddle points and λ_{n+1} towards a maximum. This ability to converge towards specific stationary points of the target functions, and to optimise functions with a singular Hessian, makes rational function optimisation an attractive choice for orbital localisation.

An orbital optimisation procedure based on RFO was implemented to obtain well-converged localised orbitals for correlated calculations. The orthogonal transformation of the occupied orbitals may be parameterised as $C_{\mu i} = \sum_j C^0_{\mu j} \left[\exp\left(\boldsymbol{\kappa}'\right)\right]_{ji}$ following Eq. (3.99), with an antisymmetric matrix $\kappa'_{ji} = -\kappa'_{ij}$. The only independent parameters are thus in the upper triangle of the matrix, $\kappa'_{i<j}$, and the gradient and Hessian of the Foster-Boys localisation criterion are given in Eq. (3.100) and Eq. (3.101), respectively.

With n occupied orbitals, the augmented Hessian is a square matrix of size $\frac{n(n-1)}{2} + 1$. Forming the full matrix and diagonalising it becomes unfeasible for a large number of orbitals. On the other hand, most elements of the Hessian are zero, and only one eigenvalue needs to be determined, which makes the problem well-suited for the Davidson diagonalisation method without explicit formation of the full matrix.[177, 178]

An outline of the orbital localisation routine is provided in Algorithm 7. The initial set of localised orbitals is determined using a conventional procedure with Jacobi sweeps (which in turn uses pivoted Cholesky decomposition as a guess[189]). These already local orbitals are refined through RFO. Depending on the size of the augmented Hessian matrix, the algorithm either forms the full matrix for diagonalisation via LAPACK, or employs Davidson diagonalisation; the default boundary for switching between the two diagonalisation methods is set at a size of 2000×2000.

Algorithm 7 Rational function optimisation of Foster-Boys orbitals. Several default thresholds have been included as numbers.

Determine guess orbitals with Jacobi sweeps
TolE := 1.0×10^{-6} ▷ eigenvalue tolerance for Davidson diag.
TolR := 1.0×10^{-6} ▷ residual tolerance for Davidson diag.
CorrectStructure := false ▷ eigenvalue structure
Newton := false ▷ flag for Newton-Raphson iterations
for iter < MaxIter **do**
    Calculate $\mathbf{g}$
    if $|\mathbf{g}|$ < TolG **and** CorrectStructure **then**
        break
    end if
    TolR := $\min\left(1.0 \times 10^{-3} \times |\mathbf{g}|, \text{TolR}\right)$ ▷ threshold adjustment
    if Newton **then**
        Solve $\mathbf{Hx} = -\mathbf{g}$
    else
        Diagonalisation: $-\begin{pmatrix} \mathbf{H} & \mathbf{g} \\ \mathbf{g}^\dagger & 0 \end{pmatrix} \begin{pmatrix} \mathbf{x} \\ x' \end{pmatrix} = \lambda \begin{pmatrix} \mathbf{x} \\ x' \end{pmatrix}$ ▷ thresholds TolE, TolR
        if $\mathbf{g}^\dagger\mathbf{x} < 0$ **then**
            $\mathbf{x} := -\mathbf{x}$
        end if
        if $|\mathbf{x}| > 0.2$ **then**
            Scale to $|\mathbf{x}| = 0.2$
        end if
        TolE := $\min\left(1.0 \times 10^{-3} \times |\lambda_1|, \text{TolE}\right)$ ▷ threshold adjustment
        CorrectStructure := false
        if $\lambda_2 > 0$ **and** $|\lambda_1| < 1.0 \times 10^{-3} \times \lambda_2$ **then**
            CorrectStructure := true
        end if
        if CorrectStructure **and** slow convergence **then**
            Newton := true
        end if
    end if
    Cayley update of the orbitals with the parameters $\mathbf{x}$
end for

Since the Foster-Boys criterion is maximised, the optimisation needs to follow the largest eigenvalue, or alternatively the smallest eigenvalue of minus the augmented Hessian matrix. The convergence thresholds of the iterative Davidson diagonalisation are set to successively tighter values as the optimisation progresses: the eigenvalue threshold by default to 10^{-3} times the smallest eigenvalue from the previous iterations, and the residual threshold to 10^{-3} times the smallest gradient norm.

The implementation deviates from Eq. (3.117) in determining the length and direction

of the step. First, the parameters are scaled down if the resulting step length exceeds a predefined threshold, by default 0.2. Second, the product of the gradient with the step vector is used to assess if the localisation criterion would be increased to first order, and the sign is flipped if necessary.

Convergence of the localisation procedure is determined firstly using the norm of the gradient, and secondly by ascertaining that the eigenvalues have the correct signs. Singular eigenvalues are ignored in this analysis. With Davidson diagonalisation of the augmented Hessian matrix, the RFO may fail to achieve sufficiently tight convergence due to numerical noise. If the correct eigenvalue structure has already been verified and slow convergence is detected using a set of heuristic criteria, the algorithm switches to Newton-Raphson optimisation instead of RFO. The linear equation system is solved iteratively to avoid formation of the full Hessian matrix.

Precise numerical evaluation of a matrix exponential is not straightforward, even though solutions have been developed and implemented.[190] Instead, the orbital update in the localisation is performed via the Cayley transform:

$$\mathrm{Cay}\left(\frac{1}{2}\boldsymbol{\kappa}'\right) = \left(\mathbf{1} - \frac{1}{2}\boldsymbol{\kappa}'\right)^{-1}\left(\mathbf{1} + \frac{1}{2}\boldsymbol{\kappa}'\right) \tag{3.118}$$

The matrix defined thereby is orthogonal[191]. Moreover, its Taylor expansion,

$$\mathrm{Cay}\left(\frac{1}{2}\boldsymbol{\kappa}'\right) = \mathbf{1} + \boldsymbol{\kappa}' + \frac{1}{2}\boldsymbol{\kappa}'^2 + \frac{1}{4}\boldsymbol{\kappa}'^3 + \ldots, \tag{3.119}$$

shows that it is identical with the matrix exponential of $\boldsymbol{\kappa}'$ up to second order. These properties permit the Cayley transform to be used instead of the matrix exponential for an orbital update with the same parameters, but the orthogonal matrix in Eq. (3.118) is determined straightforwardly by solving a linear equation system.

Unlike Jacobi sweeps, the localisation method described in this section systematically determines a local maximum of the Foster-Boys criterion, and converges its orbital gradient to high precision. The choice of a well-behaved numerical procedure to obtain localised orbitals can influence even the single-point energies calculated with a local cor-

relation method significantly. Appendix C demonstrates this using DLPNO-CCSD(T) energies calculated for two benchmark sets.

3.2.5 Scaling of the computational cost

The major components of a DLPNO-MP2 energy calculation, which are the RI integral transformation, the PNO construction and the MP2 iterations, are formally linear scaling. This was verified in Section 2.3.5 for alkane chains as a model system. However, large-scale calculations on systems of practical relevance with a more complicated structure usually do not operate in the asymptotic regime, and therefore exhibit a higher-than-linear scaling. Second, otherwise unimportant components with a higher-order scaling become relevant in calculations on very long linear chains, thereby defying an analysis of the "asymptotic" scaling. Nevertheless, this subsection considers the scaling of different steps in the DLPNO-MP2 gradient implementation from a formal viewpoint, which will be verified with calculations at a later stage.

Pair-dependent contributions for the gradient are evaluated in one or two loops over all orbital pairs. The number of quantities per pair are limited by the sizes of the domains of PAOs and auxiliary functions, and the respective number of PNOs, all of which become asymptotically constant with increasing system size. Due to orbital pair prescreening, the number of remaining orbital pairs, and hence the computational expense for this part of the calculation, has an $O(N)$ scaling. Pair prescreening itself, and the associated contributions to the gradient, scale quadratically with the number of orbitals, but their overall impact on the computational expense is insignificant.

The cost of the RI integral gradient, $\sum_{\mu\nu K} \Gamma^K_{\mu\nu} (\mu\nu|K)^x$, is $O(N)$. Calculating terms involving the integrals $(p\tilde{\mu}'|K)$ and $(ip|K)$ leads to an $O(N^2)$ scaling, as p stands for all molecular orbitals in the system. The number of MOs i, PAOs $\tilde{\mu}'$, and associated atomic basis functions connected to a specific auxiliary function K become asymptotically constant (albeit only for very large systems).

A substantial amount of the computational cost is incurred by the Fock response function and the CP-SCF equations, as well as the gradient of the two-electron integrals

in the Fock operator. The scaling of these components will generally depend on any approximations taken to accelerate Fock matrix construction, and therefore it is not specific to DLPNO-MP2. The $O(N^4)$ scaling of Hartree-Fock is reduced to $O(N^2)$ with the help of integral screening techniques.[146, 192] While the cost to calculate the exchange energy formally reduces to $O(N)$ in the large-scale limit, actual linear scaling is not achieved in practical applications.[143] RIJCOSX typically features an $O(N^2)$ scaling in practice, even though the chain-of-spheres exchange integration itself is asymptotically linear scaling in principle.

An $O(N^3)$ expense is incurred from calculating the residual of the coupled-perturbed localisation equations (3.94). Likewise, the cost to diagonalise the Hessian of the Foster-Boys criterion with the Davidson method scales with the third power of the system size, since the number of trial vectors is system-independent. As a consequence, the rational function optimisation of the localised orbitals, which performs several diagonalisations, has an $O(N^3)$ scaling.

There is a fixed number of further steps, which involve operations on matrices or vectors in a non-truncated basis. For example, multiplications of matrices that are in a basis of all AOs, MOs or redundant PAOs of a given system scale with the third power of the system size. Generally, these steps account only for a small part of the overall cost.

3.3 Results

3.3.1 Electric field gradients with exact and approximate energy derivatives

The purpose of this subsection is to assess the quality of the relaxed DLPNO-MP2 density for first-order property calculations, and to examine the importance of individual constraints in the DLPNO-MP2 Lagrangian.

Different quantities could be used, for example electrostatic multipole moments, root mean square deviations of natural occupation numbers from RI-MP2, or the integrated root-mean-square error of the density itself. We chose electric field gradients (EFGs),

which were found to be very sensitive regarding different factors such as the electronic structure method, the basis set, the molecular geometry, or relativistic corrections.[193–195]

A molecule with nuclei of atomic number Z_A at positions $\mathbf{R}^A$ and an electronic particle density ρ generates an electrostatic potential V,

$$V(\mathbf{r}) = \sum_B \frac{Z_B}{|\mathbf{r} - \mathbf{R}^B|} - \int \frac{\rho(\mathbf{r}')}{|\mathbf{r} - \mathbf{r}'|} d\mathbf{r}', \tag{3.120}$$

where the total DLPNO-MP2 electron density is given through the respective SCF and relaxed MP2 contributions:

$$\rho(\mathbf{r}) = \sum_{\mu\nu} \left(P_{\mu\nu}^{\mathrm{SCF}} + D''_{\mu\nu} \right) \mu^*(\mathbf{r}) \nu(\mathbf{r}) \tag{3.121}$$

Nuclei with an electric quadrupole moment interact with an inhomogeneous electric field, leading to quadrupole splitting interactions that are relevant in the context of several spectroscopic techniques, e.g. nuclear magnetic resonance (NMR), nuclear quadrupole resonance (NQR), rotational and Mössbauer spectroscopies. The interaction strength of an electric quadrupole with the electric field is determined by the electric field gradient, i.e. the Hessian matrix of the electrostatic potential:

$$V_{mn}(\mathbf{r}) = \frac{\partial^2 V(\mathbf{r})}{\partial r_m \partial r_n} \tag{3.122}$$

Specifically, the EFG at nucleus A due to the electrons and all remaining nuclei is given by:

$$\begin{aligned} V_{mn}^A(\mathbf{R}^A) = -\sum_{B \neq A} Z_B \left[\frac{\delta_{mn}}{|\mathbf{R}^A - \mathbf{R}^B|^3} - 3\frac{(R_m^A - R_m^B)(R_n^A - R_n^B)}{|\mathbf{R}^A - \mathbf{R}^B|^5} \right] \\ + \int \rho(\mathbf{r}) \left[\frac{\delta_{mn}}{|\mathbf{r} - \mathbf{R}^A|^3} - 3\frac{(r_m - R_m^A)(r_n - R_n^A)}{|\mathbf{r} - \mathbf{R}^A|^5} \right] d\mathbf{r} \end{aligned} \tag{3.123}$$

A representation of the EFG tensor, which is independent of the absolute orientation of the coordinate system, is obtained by diagonalising $\mathbf{V}^A$. The eigenvectors are taken as

local x-, y-, and z-axes, assigned by the magnitudes of the eigenvalues:

$$|V_{zz}| \geq |V_{yy}| \geq |V_{xx}| \tag{3.124}$$

The largest eigenvalue determines the nuclear quadrupole coupling constant (NQCC) C_{Q}:

$$C_{\mathrm{Q}} = \frac{eQV_{zz}}{h} \tag{3.125}$$

In the preceding equation, Q is the nuclear quadrupole moment of the nucleus in question. Furthermore, the eigenvalues determine the asymmetry parameter η:

$$\eta = \frac{V_{yy} - V_{xx}}{V_{zz}} \tag{3.126}$$

We calculated electric field gradients for the Cl nucleus of chlorothiazide and the S nucleus of the taurine zwitterion. Nuclear quadrupole coupling constants derived from solid-state NMR measurements have been reported for chlorothiazide with the ^{35}Cl isotope[196] and for taurine with the ^{33}S isotope.[197]

Molecular geometries for both compounds are available in the Cambridge Structural Database.[198] The atomic coordinates in chlorothiazide were extracted from the X-ray diffraction structure[199] (CSD reference QQQAUG18), and the hydrogen positions were refined using a constrained optimisation with the BP86 functional[200, 201] together with the D3BJ dispersion correction[202, 203] and the def2-TZVP basis set. Atomic coordinates for taurine were obtained from neutron diffraction data[204] (CSD reference TAURIN03) without further optimisation.

In order to isolate the influence of the PNO-specific constraints on the overall accuracy, calculations were first performed using different values for T_{CutPNO}, while all other thresholds were set to zero. Densities were calculated using the complete Lagrangian, and separately by omitting specific constraints. Figure 3.1 shows the MP2 contribution to the principal component V_{zz} of the electric field gradient as a function of the PNO truncation threshold. These calculations were performed for isolated molecules of chlorothiazide

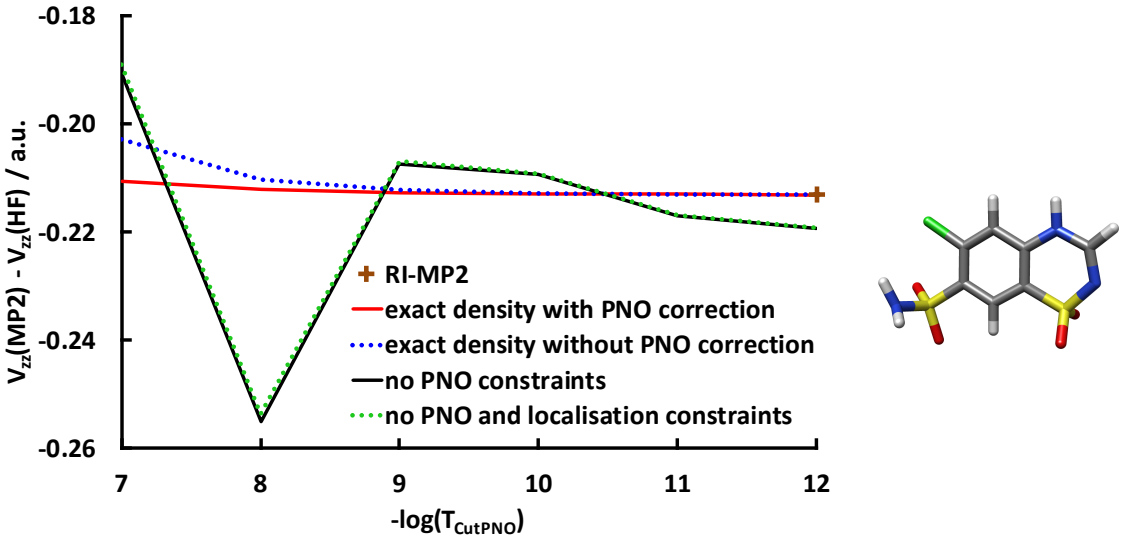

(a) Electric field gradient at the Cl nucleus of chlorothiazide.

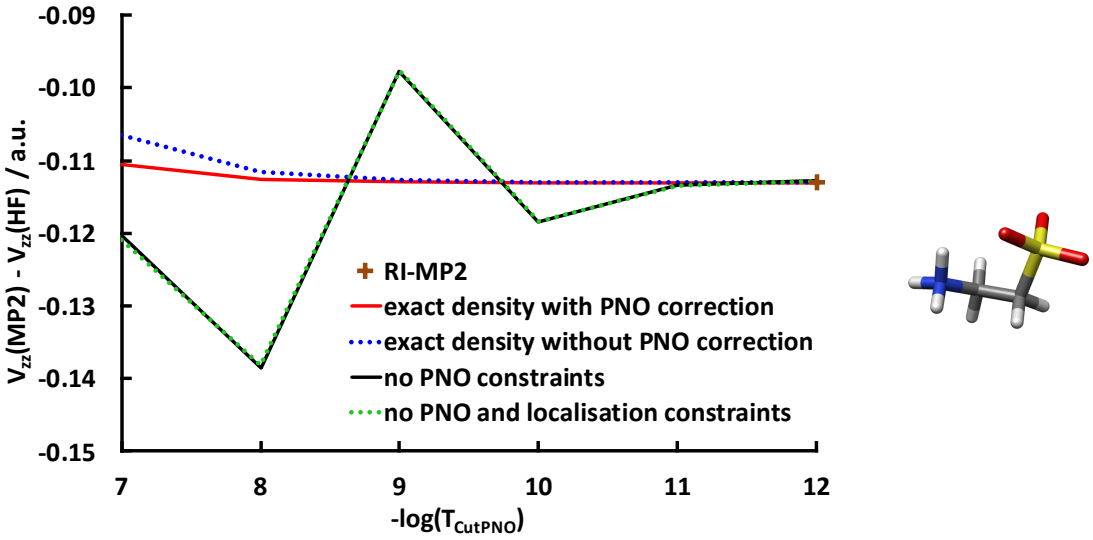

(b) Electric field gradient at the S nucleus of taurine.

Figure 3.1: MP2 contribution to the largest principal component of the electric field gradient (V_{zz}) as a function of T_{CutPNO}. The cc-pwCVTZ basis set was employed.

or taurine in vacuum using the cc-pwCVTZ basis set for all non-hydrogen atoms[205] and cc-pVTZ for the hydrogens,[206] with appropriate auxiliary sets for correlation fitting.[207, 208] All electrons were correlated in the EFG calculations.

There is a good agreement between the EFGs calculated using the formally complete relaxed DLPNO-MP2 and RI-MP2 densities. Especially for loose values of T_{CutPNO}, results are improved by including the derivative of the PNO energy correction ΔE_{PNO}. On the other hand, omitting the constraints for the PNOs and for the semicanonical ampli-

tudes introduces unacceptably large errors and an erratic, non-monotonous convergence behaviour. With the default threshold $T_{\mathrm{CutPNO}} = 10^{-8}$, the errors in the correlation contribution to the electric field gradient amount to 20 % when these constraints are omitted, whereas errors of only ca. 1 % are incurred using a Lagrangian with the full set of constraints.

The observed large errors resulting from omitted constraints originate primarily from valence pair contributions. At the point of performing these calculations, the gradient for DLPNO-MP2 with frozen core orbitals had not been implemented yet; however, we performed calculations with $T_{\mathrm{CutPNO(Core)}} = 0$, which eliminated any virtual space truncation for all pairs involving at least one core orbital. As shown in Appendix B.1.1, this only had a small influence on the EFG errors with a given PNO truncation threshold for valence orbital pairs.

While the preceding results were obtained with PNO truncation only, for practical applications it is more relevant to examine EFGs with standard settings for all thresholds. In addition, the intrinsic MP2 error relative to experimental results should be taken into account. To reproduce the experimental nuclear quadrupole coupling constant of chlorothiazide with RI-MP2, it was sufficient to perform a calculation with an isolated molecule in vacuum using the cc-pwCVQZ set[205] (with cc-pVQZ[206] for the hydrogen atoms). For ^{35}Cl we used the quadrupole moment of $-81.7(8)$ mb determined by Sundholm and Olsen,[209] as recommended in the tabulation by Stone.[210] According to Eq. (3.125), RI-MP2 yields a nuclear quadrupole coupling constant of -74.59 MHz, which is in a fair agreement with the experimentally derived value of $-73.04(8)$ MHz for chlorothiazide in the solid state.[196]

Since taurine is present as a zwitterion in the solid state, there is a large intermolecular contribution to the electric field gradient. In consequence, calculations performed with an isolated molecule do not reproduce the experimental value: while the nuclear quadrupole coupling constant was determined as 1.36(2) MHz experimentally,[197] a value of -6.75 MHz was obtained using RI-MP2 with cc-pwCVQZ. We used $-69.4(4)$ mb as the quadrupole moment of the ^{33}S nucleus, which was obtained by Stopkowicz and Gauss.[194]

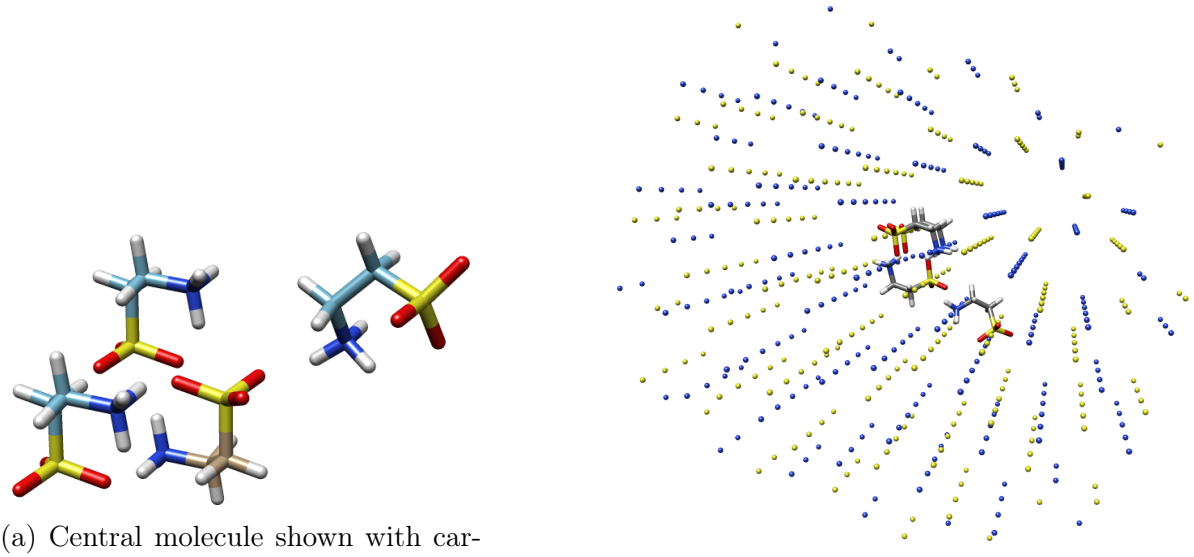

(a) Central molecule shown with carbon atoms in bronze colour, spectator molecules with carbons in light blue.

(b) The four taurine molecules embedded in point charges.

Figure 3.2: Model to calculate the nuclear quadrupole moment of taurine.

In order to calculate a more realistic value for the nuclear quadrupole coupling constant, an adequate representation of the environment needed to be created, which also accounted for the computational limitations of the preliminary DLPNO-MP2 derivatives implementation that the EFG calculations were performed with. A central taurine molecule in cc-pwCVQZ basis (with cc-pVQZ basis for the hydrogens) was supplemented with three neighbouring molecules in cc-pVTZ basis (Figure 3.2a). Two of the molecules are hydrogen-bonded to the SO_3^- group of the central molecule. The third molecule has a hydrogen atom of its NH_3^+ group at a distance of 2.79 Å to the central sulphur nucleus. In addition, the four molecules were embedded in 470 point charges representing additional 235 molecules (Figure 3.2b): a charge of -0.938 was placed at the positions of sulphur atoms, and the opposite charge at the nitrogen atom positions. The values were chosen to reproduce the calculated dipole moment of a taurine zwitterion in vacuum. All atomic coordinates were extracted from neutron diffraction data.[204] The RIJCOSX method was used with the GridX6 settings to accelerate the SCF and CP-SCF procedures, which we found to give negligible errors for the electric field gradient.

Figure 3.3 shows nuclear quadrupole coupling constants calculated for chlorothiazide and taurine with LoosePNO, NormalPNO and TightPNO settings (as defined in Table 2.2) using the complete and approximate Lagrangians. Corresponding data tables

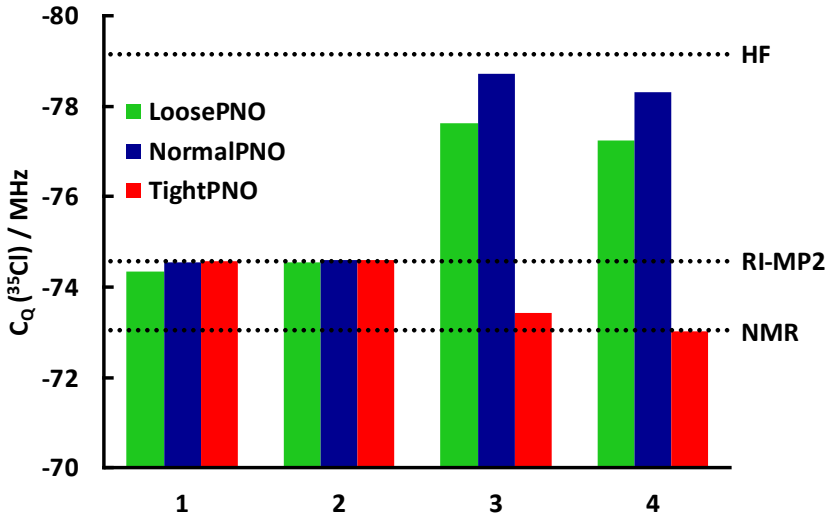

(a) Quadrupole coupling constant at the ^{35}Cl nucleus of chlorothiazide.

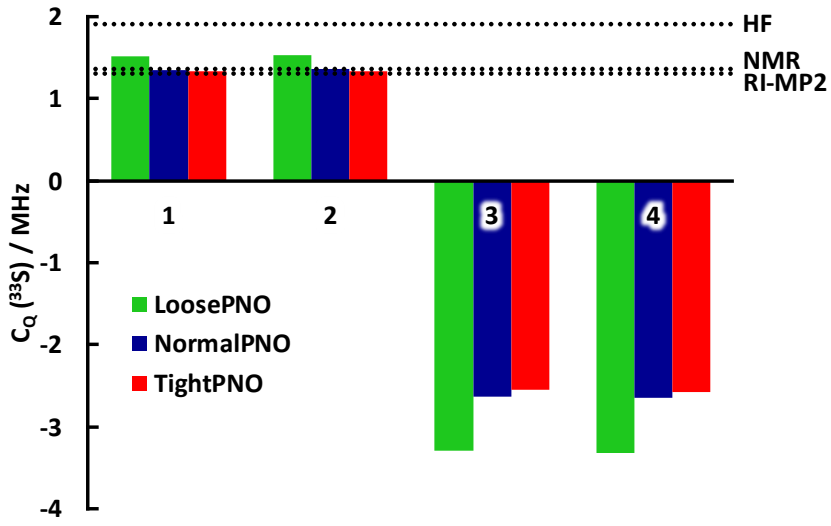

(b) Quadrupole coupling constant at the ^{33}S nucleus of taurine.

Figure 3.3: Nuclear quadrupole coupling constants calculated with DLPNO-MP2 using different threshold settings and the cc-pwCVQZ basis. The horizontal dotted lines mark results calculated with Hartree-Fock and RI-MP2, and experimental values from solid-state NMR experiments.[196, 197]
Grouping of the DLPNO-MP2 results: (1) charge density calculated with all constraints, and including the derivative of the PNO correction ΔE_{PNO}, (2) charge density calculated with all constraints, but without the derivative of ΔE_{PNO}, (3) constraints specific to PNOs and the semicanonical amplitudes are omitted, but the localisation constraint is considered, (4) the localisation constraint is also omitted.

are provided in Appendix B.1.2. With default (NormalPNO) and tight thresholds, the NQCC of taurine deviates from the canonical RI-MP2 result by 0.05 MHz and 0.03 MHz, respectively, which is somewhat smaller than the difference to the experimental result. A

somewhat larger deviation of 0.2 MHz is observed with loose settings. Errors for chlorothiazide are in a similar range, showing that EFGs can be calculated reliably using the relaxed DLPNO-MP2 density with default or tight thresholds.

Omitting constraints for the PNOs and for the semicanonical amplitudes leads to very large errors: for chlorothiazide, the deviations from RI-MP2 are comparable to the entire MP2 correlation contribution to the NQCC (Figure 3.3a). The NQCCs of taurine have not only a wrong absolute value, but also the wrong sign if constraints related to the PNOs are omitted (Figure 3.3b).

EFGs of chlorothiazide and taurine are two selected examples with particularly dramatic errors caused by a simplified Lagrangian. In preliminary calculations, we found that such cases represent a minority, whereas the errors were much smaller for many other examples. However, a general derivatives implementation needs to produce accurate results without exceptions, which means that the complete set of constraints, including relaxation of the PNOs, is needed to calculate the orbital-relaxed density.

Datta and co-workers used an implementation of the orbital-unrelaxed closed-shell DLPNO-CCSD density to calculate electric dipole moments.[107] They found that wave function truncation in local correlation methods can have a strong influence on the accuracy of correlation contributions to orbital-unrelaxed molecular properties. This finding is in agreement with results by other authors: e.g. Saitow and Neese, who calculated hyperfine couplings using an implementation of the unrelaxed density for open-shell DLPNO-CCSD;[108] McAlexander and Crawford, who calculated dynamic polarisabilities and optical rotations using a simulated CCSD code with PAOs, OSVs and PNOs;[109] Kumar and Crawford, who calculated dynamic polarisabilities using a frozen virtual natural orbital approach;[211] and Korona and co-workers, who calculated static polarisabilities using numerical derivatives of the PAO-based local CCSD energy.[212]

While the results presented in our work show that relaxation of PNOs is important for orbital-relaxed properties, it does not lead to the conclusion that this is necessarily also the case for the orbital-unrelaxed density. To the contrary, numerically calculated orbital-unrelaxed DLPNO-CCSD dipole moments—which thereby include PNO relaxation—by

Datta and co-workers suggest that a deeper understanding of contributions beyond PNO relaxation may be necessary to improve the accuracy of unrelaxed properties.[107]

The preliminary implementation used to calculate the EFGs reported in this subsection did not yet include a derivative of the energy correction for screened-out orbital pairs. However, the corresponding energy contributions were $-2\,\mu E_\mathrm{h}$ for the chlorothiazide molecule, and $-37\,\mu E_\mathrm{h}$ for the system of four taurine molecules embedded in point charges. Repeating the calculation for taurine without orbital prescreening did not result in any significant numerical difference for the electric field gradient.

3.3.2 Molecular geometries with exact and approximate gradient schemes

This subsection investigates the influence of constraints in the Lagrangian on the equilibrium structures of a few organic systems. The geometry optimisations were performed with the def2-TZVP basis. Because of the limitations of the preliminary gradient implementation used for these calculations, all electron were correlated, and the derivative of the prescreening contribution to the energy was not included in the gradient. The calculations were performed for four systems: 1,5-dibromo-4,8-dichloronaphthalene and RESVAN, each with starting geometries from the LB12 set by Grimme and coworkers[213]; and 1,1'-bi-2-naphthol (BINOL) and the adenine-thymine dimer, with their starting geometries determined using HF-3c.[214] Unless noted otherwise, all geometry optimisations were performed with the TightOpt convergence settings.

Figure 3.4 shows the structures of the four systems. The accuracy of the optimised geometries was judged by comparing selected interatomic distances, or the dihedral angle in the case of BINOL, between DLPNO-MP2 and RI-MP2. NormalPNO and TightPNO settings lead to accurate structures, which reproduce covalent bond lengths in RI-MP2 equilibrium geometries to well within 0.1 pm. Larger errors are caused by LoosePNO settings, which are not intended for general production use.

Table 3.1 shows geometric parameters determined using the gradient with complete and approximate Lagrangians. As for the electric field gradients (Section 3.3.1), the

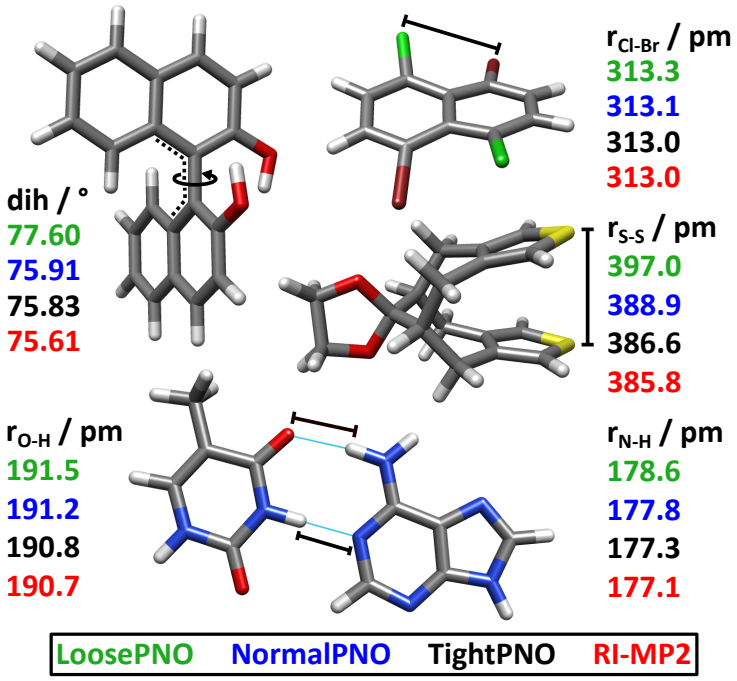

Figure 3.4: Structures optimised with RI-MP2 and DLPNO-MP2 in comparison. The calculations were performed with the def2-TZVP basis, and all electrons were correlated.

calculations were performed using (1) a complete Lagrangian with all constraints, (2) a Lagrangian with the full set of constraints, but without the derivative of the PNO energy correction ΔE_{PNO}, (3) a Lagrangian without constraints specific to PNOs and the semicanonical amplitudes, and (4) a Lagrangian with the Brillouin constraint only.

Omitting the gradient contribution $\nabla \Delta E_{\mathrm{PNO}}$ somewhat increases the deviations from RI-MP2 geometries with a given set of DLPNO-MP2 truncation thresholds. Leaving out the PNO-specific constraints further increases errors, and may also lead to convergence difficulties of geometry optimisations, as is the case for the adenine-thymine dimer with NormalPNO settings (Table 3.1c). Unlike for EFGs, no catastrophic failures were observed; however, establishing this as a general conclusion for an approximate nuclear gradient without PNO-specific constraints would require much more extensive testing. On the other hand, geometry optimisations performed without the localisation constraint converge to structures with very large errors, most blatantly evident for the dihedral angle in BINOL (Table 3.1d).

Screened-out orbital pairs contribute $-1\,\mu E_{\mathrm{h}}$ to the total correlation energy of the adenine-thymine dimer, $-0.4\,\mu E_{\mathrm{h}}$ for RESVAN, $-0.1\,\mu E_{\mathrm{h}}$ for BINOL, and $-0.2\,\mu E_{\mathrm{h}}$ for

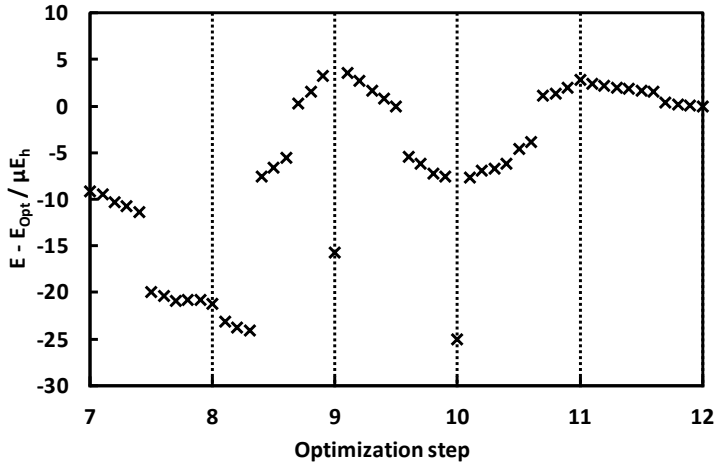

(a) LoosePNO (NormalOpt)

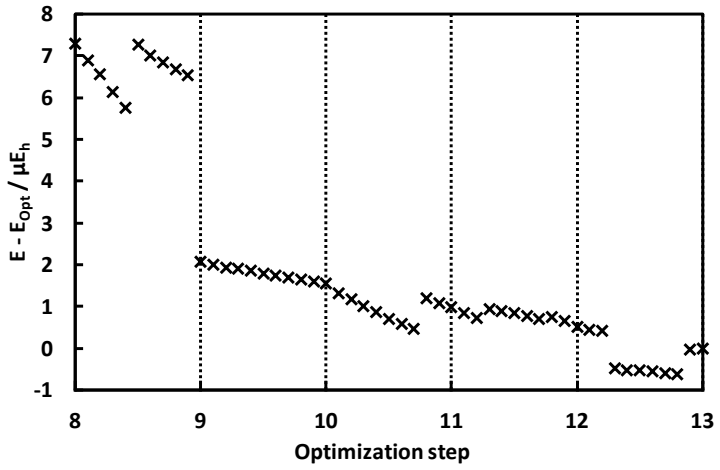

(b) NormalPNO (TightOpt)

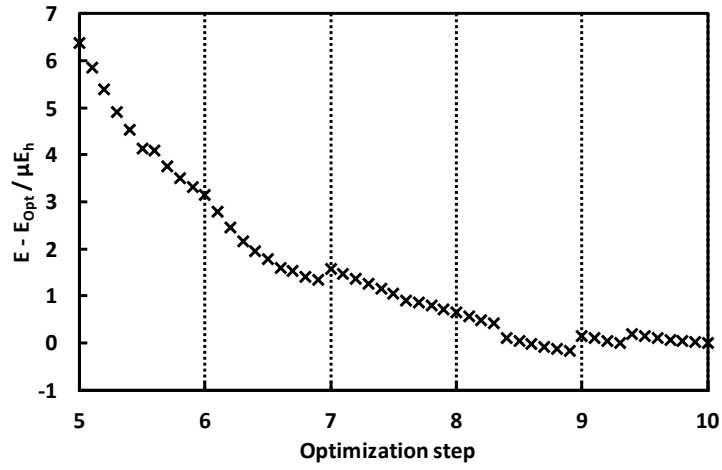

(c) TightPNO (TightOpt)

Figure 3.5: Electronic energy of the adenine-thymine dimer in the last steps of the respective geometry optimisations. The energy of the final step (E_{Opt}) has been subtracted from all values. In between the geometries of the optimisation steps, single-point energies were calculated for linearly interpolated coordinates, $\mathbf{R}(\alpha) = (1-\alpha)\mathbf{R}_k + \alpha\mathbf{R}_{k+1}$.

	$r_{\mathrm{Br\cdots Cl}}$ / pm			
Settings	(1)	(2)	(3)	(4)
LoosePNO	313.3	313.5	313.9	313.1
NormalPNO	313.1	313.1	313.2	312.3
TightPNO	313.0	313.0	313.0	312.2
RI-MP2		313.0		

(a) Distance between the Br and Cl atoms in 1,5-dibromo-4,8-dichloronaphthalene.

	$r_{\mathrm{S\cdots S}}$ / pm			
Settings	(1)	(2)	(3)	(4)
LoosePNO	397.0	401.5	401.7	399.7
NormalPNO	388.9	390.5	389.9	385.4
TightPNO	386.7	387.0	387.2	383.0
RI-MP2		385.8		

(b) Distance between the S atoms in RESVAN.

	$r_{\mathrm{N-H\cdots O}}$ / pm				$r_{\mathrm{N-H\cdots N}}$ / pm			
Settings	(1)	(2)	(3)	(4)	(1)	(2)	(3)	(4)
LoosePNO	[I]191.5	[I]192.3	[II]–	185.8	[I]178.6	[I]179.8	[II]–	175.2
NormalPNO	191.2	191.3	[I]190.3	184.0	177.8	178.1	[I]178.5	173.7
TightPNO	190.8	190.9	190.8	184.1	177.3	177.4	177.4	172.8
RI-MP2		190.7				177.1		

(c) Hydrogen bond lengths in the adenine-thymine dimer.
[I]Converged only with "NormalOpt" settings, but not with "TightOpt".
[II]Did not converge.

	dihedral / °			
Settings	(1)	(2)	(3)	(4)
LoosePNO	77.60	78.87	78.33	105.34
NormalPNO	75.91	76.31	77.81	106.30
TightPNO	75.83	75.92	75.93	107.30
RI-MP2		75.61		

(d) Dihedral angle in BINOL.

Table 3.1: Geometric parameters obtained with exact and approximate gradients of the DLPNO-MP2 energy (see Figure 3.4). Meaning of the column labels:
(1) Including all constraints and the derivative of ΔE_{PNO}.
(2) Including all constraints without the derivative of ΔE_{PNO}.
(3) Excluding the constraints for the PNOs and the semicanonical amplitudes.
(4) As in (3), but also excluding the localisation constraint.

1,5-dibromo-4,8-dichloronaphthalene. Accordingly, the change in the energy contribution ΔE_{Pre} is significantly below $1\,\mu E_{\mathrm{h}}$ in each case, and thus irrelevant in these geometry optimisations.

In order to gain more insight into the geometry convergence difficulties observed for the adenine-thymine dimer with loose thresholds (Table 3.1c), we have analysed single-point energies for the final steps of the geometry optimisation. Figure 3.5 shows energies of linearly interpolated structures between subsequent optimisation steps. LoosePNO thresholds lead to steps of up to $20\,\mu E_{\mathrm{h}}$ in the potential energy surface, and convergence of a geometry optimisation is rather based on a coincidental fulfilment of the criteria. With NormalPNO settings the discontinuities are reduced to a few μE_{h}, and the endpoint of the optimisation is more clearly identifiable as a minimum, even though there are a few lower-lying points in its vicinity. TightPNO settings reduce the steps in the PES to $< 1\,\mu E_{\mathrm{h}}$, and the continuous parts of the curve possess a more uniform slope.

3.3.3 Singularities of the localisation orbital Hessian

This subsection investigates systems with a singular or near-singular orbital Hessian of the Foster-Boys localisation scheme: a weakly bonded dimer of benzene and ethyne (system 50 from the S66 benchmark set[155]), bis(cyclopentadienyl)magnesium ($MgCp_2$), and the transition metal complex KAMDOR from the LB12 set of Grimme and co-workers[213]. The systems are depicted in Figure 3.6.

Foster-Boys localisation of the valence orbitals of ethyne leads to a set of two orbitals that are purely of σ-character, and three bent orbitals that mix σ- and π-contributions (Figure 3.7). Rotating those three orbitals collectively around the molecular axis by any angle leaves the localisation criterion unchanged. Accordingly, the orbital Hessian of the localisation function has one eigenvalue of zero, corresponding to the rotation mode. This is not a unique feature of the Foster-Boys scheme: any localisation method that does not artificially break the symmetry of linear molecules would lead to this type of continuous rotational degeneracy. On the other hand, rotating all orbitals together around the internuclear axis also leaves the DLPNO-MP2 energy unchanged.

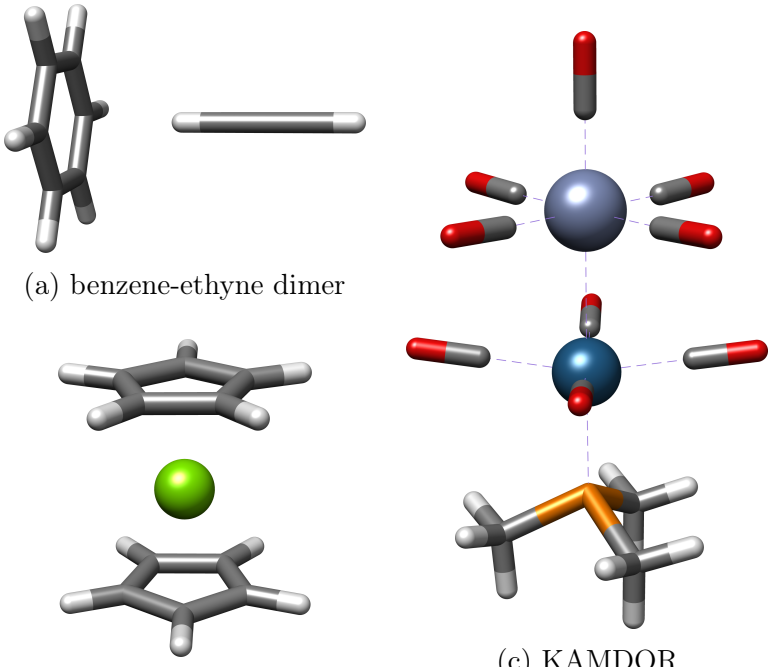

(a) benzene-ethyne dimer

(b) $MgCp_2$

(c) KAMDOR

Figure 3.6: Structures of systems used to investigate singularities of the orbital Hessian of the localisation criterion.

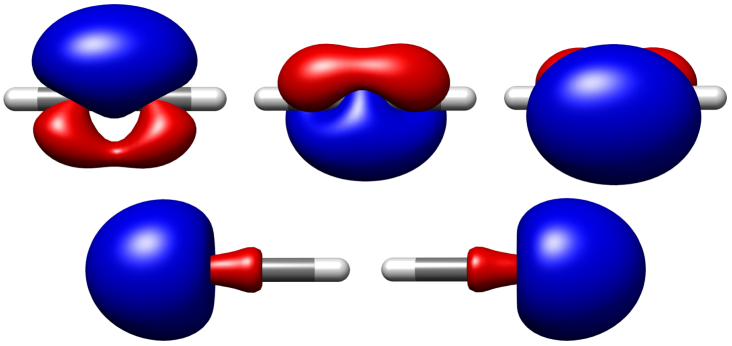

(a) The five localised valence orbitals.

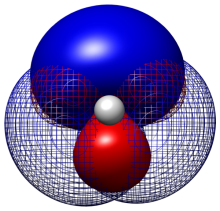

(b) The three bent orbitals can be rotated collectively around the molecular axis without affecting the localisation criterion.

Figure 3.7: Molecular orbitals of ethyne after Foster-Boys localisation.

The point group of the benzene-ethyne dimer is C_{6v}. According to Scheurer and Schwarz, continuous degeneracy may occur in molecules belonging to this group.[173] While most eigenvalues of the Foster-Boys localisation Hessian were in a range of about -2 to -500, one had a value of -4×10^{-7}. The latter results in an instability of the DLPNO-MP2 derivatives for the dimer.

The lowest and highest natural occupation numbers of the relaxed DLPNO-MP2 density matrix in def2-TZVP basis with NormalPNO thresholds are -0.58 and -2.52, respectively. This is not caused by any intrinsic pathology of the MP2 method for this

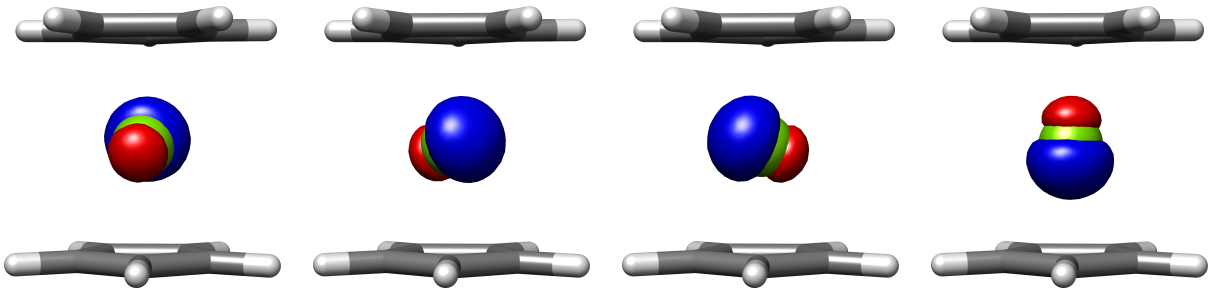

Figure 3.8: Foster-Boys orbitals representing the second shell of magnesium in $MgCp_2$.

system, since all eigenvalues of the relaxed RI-MP2 density are between 0.0000 and 2.0000. After eliminating the eigenvector of the localisation Hessian associated with the near-zero eigenvalue, the lowest and highest occupation numbers of the relaxed DLPNO-MP2 density are also recovered as 0.0000 and 2.0000, respectively.

Calculations for $MgCp_2$ were performed with the cc-pwCVTZ basis, and all electrons were correlated. We found that the pathological effects were more pronounced with this basis than with def2-TZVP. Natural occupation numbers of the relaxed RI-MP2 density were in a range of 0.0000 to 1.9997, while the smallest and largest values of the DLPNO-MP2 (NormalPNO) density were -0.23 and 2.22, respectively.

We used an $MgCp_2$ structure in a staggered arrangement of D_{5d} symmetry, for which a continuous degeneracy is possible.[173] Among the Foster-Boys LMOs, four orbitals can be identified as the subvalence shell of Mg, with a shape resembling sp^3 hybrid orbitals of 2s and 2p contributions (Figure 3.8). The smallest eigenvalue of the localisation Hessian (-5×10^{-7}) corresponds to a rotation of the three orbitals that point toward the edges of the upper cyclopentadienyl ring. Two further small eigenvalues (-2×10^{-5} each) are associated with an eigenvector that mixes all four orbitals.

After removing the respective three eigenvectors corresponding to the smallest eigenvalues, lowest and highest natural occupation numbers of -0.0002 and 1.9997 are obtained for the relaxed DLPNO-MP2 density; the same result is achieved even by eliminating only the one eigenvector associated with the smallest eigenvalue. As the core definition for Mg in ORCA includes the 1s orbital only, the same pathological effects would occur in a frozen-core calculation.[150]

KAMDOR is a complex of chromium and osmium with nine carbonyl ligands, and

one trimethylphosphine ligand bound to the Os atom. In def2-TZVP basis, the natural occupation numbers of the RI-MP2 density are in a range of -0.0578 to 2.0114. The lowest and highest natural occupation numbers of the DLPNO-MP2 (NormalPNO) are -0.21 and 2.15, which are much further outside the range between zero and two.

The smallest eigenvalue of the localisation Hessian is -4×10^{-5}, associated with a rotation of the three bent valence orbitals of the CO ligand that is on the same axis as the two metal atoms (the upper ligand in Figure 3.6c). The structure of the KAMDOR complex is of C_s symmetry, for which a continuous degeneracy is not allowed.[173] However, disregarding the trimethylphosphine ligand at the opposite end of the molecule, the remaining fragment is of $C_{4\mathrm{v}}$ symmetry, for which a continuous degeneracy is possible. This may explain the existence of the small eigenvalue of -4×10^{-5}, which is sufficiently close to zero, but larger than comparable values between 10^{-7} and 10^{-6} obtained for the other two systems. After removing the eigenvector associated with this eigenvalue, the lowest and highest natural occupation numbers of the relaxed DLPNO-MP2 density are -0.0572 and 2.0119, which is close to the RI-MP2 results.

In order to establish an automatic procedure for eigenvector removal, we will next examine a quantitative relationship between small eigenvalues and errors in the density. For this purpose, we created distorted structures of the three systems. Each atom was displaced by a step of 0.1 pm, 0.3 pm, 1 pm, 2 pm and 5 pm in a randomly chosen direction. Breaking the symmetry of these systems with small displacements permits very small eigenvalues of the localisation Hessian to be examined more systematically.

For each structure, an "uncorrected" relaxed density matrix was calculated using the unmodified localisation constraint in the Lagrangian. In addition, a "corrected" density was calculated by removing only the one eigenvector of the localisation Hessian that is associated with the smallest eigenvalue. Even though it may be necessary to remove several eigenvectors for a given system in practice, this investigation is limited to one eigenvector for simplicity.

Root mean square deviations (RMSD) between natural occupation numbers calculated with RI-MP2 and DLPNO-MP2 are shown in Figure 3.9. In the presence of a very small

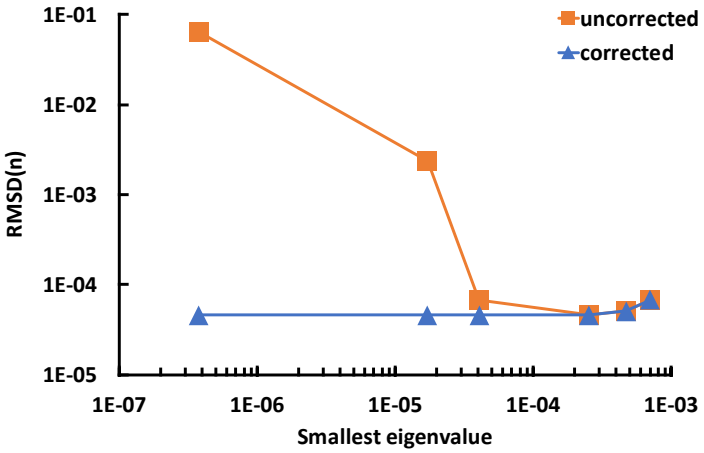

(a) benzene-ethyne dimer

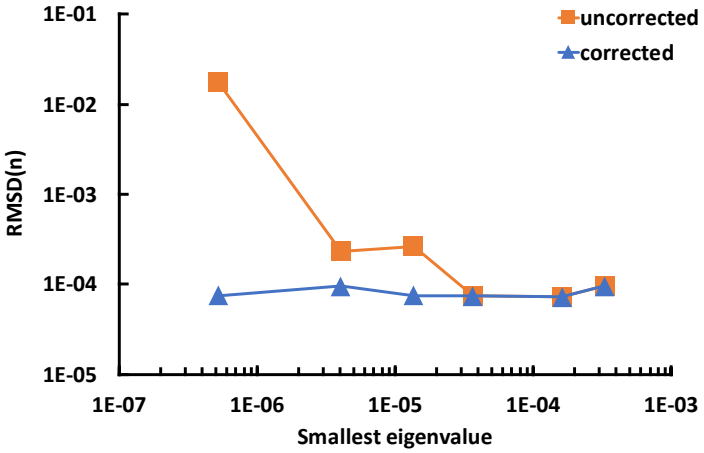

(b) $MgCp_2$

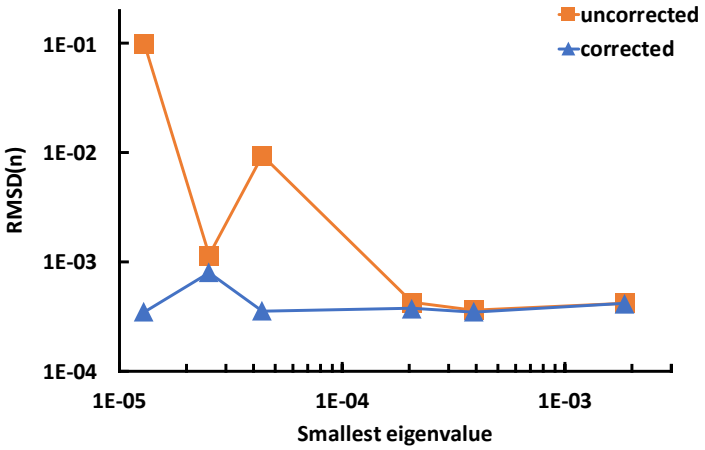

(c) KAMDOR

Figure 3.9: Root mean square deviation of the natural occupation numbers between the DLPNO-MP2 and RI-MP2 relaxed densities. Each system is represented by an undistorted and five slightly distorted geometries. The position of each point on the horizontal axis is determined by the magnitude of the smallest eigenvalue of the localisation Hessian. "Corrected" density matrices were calculated after removing one eigenvector associated with the smallest eigenvalue, whereas the "uncorrected" data points represent raw DLPNO-MP2 results without removing any eigenvectors.

localisation Hessian eigenvalue there is a very large deviation of the natural occupation numbers from the RI-MP2 reference. However, with increasing magnitude of the smallest eigenvalue, the RMSD decreases strongly. Correcting the localisation constraint in the Lagrangian by removing the eigenvector associated with the smallest eigenvalue leads to density matrices that are in close agreement with the RI-MP2 natural occupation numbers in every case. If the smallest eigenvalue has a sufficiently large magnitude, the "corrected" and "uncorrected" results become almost indistinguishable.

We conclude from the data shown in Figure 3.9 that 3×10^{-4} is an appropriate eigenvalue cutoff. However, all calculations of the DLPNO-MP2 gradient in the remainder of this work and in the production implementation remove eigenvectors associated with *all* eigenvalues below the given threshold, not only with the smallest one.

3.3.4 Accuracy of the gradient

As it was shown before that DLPNO-MP2 reproduces RI-MP2 energies closely, one may assume that standard settings such as "NormalPNO" or "TightPNO" also lead to an accurate analytical gradient. This will be verified below with single-point gradient calculations using structures from the Baker[215] and S66x8 sets[155]. Data tables are presented in Appendix B.3.

The Baker set contains 30 structures ranging from three (water) to 29 atoms (menthone). As it was originally designed to test geometry optimisers, the nuclear coordinates differ strongly from their equilibrium positions. Figure 3.10 shows the root mean square deviations between the DLPNO-MP2 and RI-MP2 gradients calculated for each structure.

Whereas the gradients are almost identical for the smallest molecules, the deviation converges to a range of $10^{-4}\,E_\mathrm{h}\,{a_0}^{-1}$ to $10^{-5}\,E_\mathrm{h}\,{a_0}^{-1}$ for the larger systems with NormalPNO or TightPNO thresholds. Larger errors are encountered for benzidine, where most of the deviation from the RI-MP2 gradient is caused by a slight distorting force with DLPNO-MP2 towards an alternating lengthening and shortening of aromatic bonds between carbon atoms. This is likely an artefact of the interplay between the Foster-Boys orbitals (resembling a Lewis structure of benzene) and the DLPNO approximations.

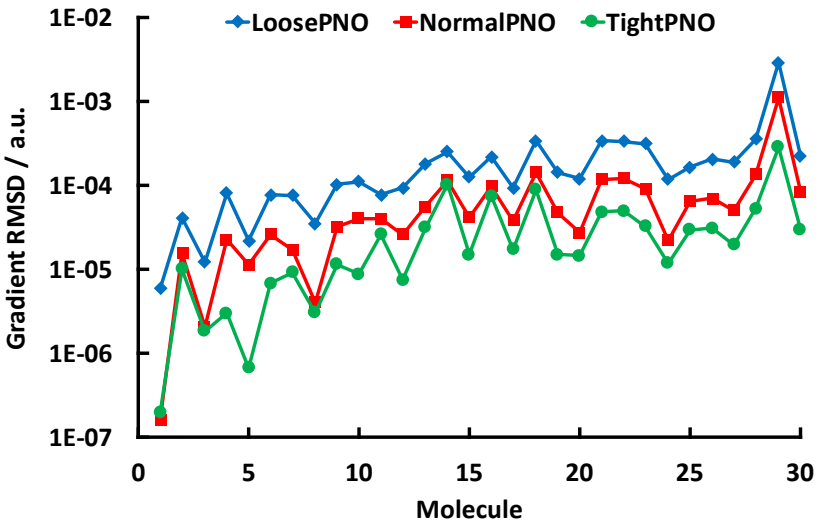

Figure 3.10: Root mean square deviations between the DLPNO-MP2 and RI-MP2 gradients for the Baker test set. Each data point corresponds to one system. The molecules are ordered by their number of atoms, increasing from left to right.

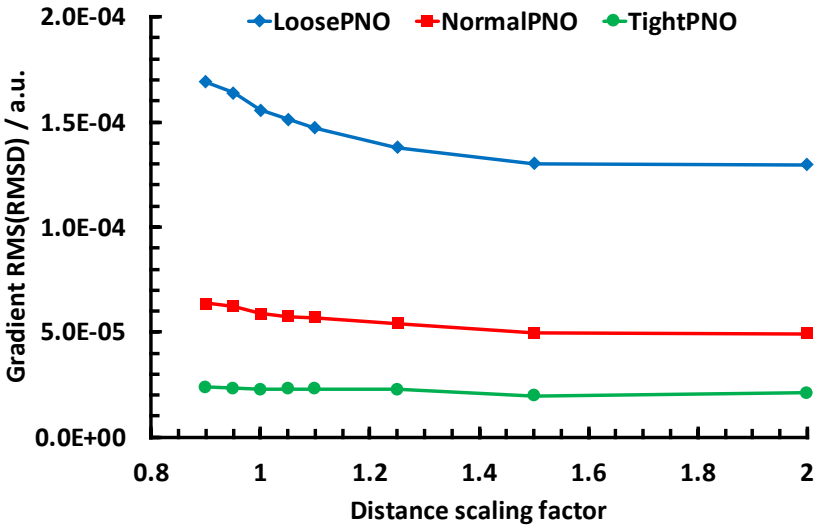

Figure 3.11: Root mean square deviation between the DLPNO-MP2 and the RI-MP2 gradients over all dimers in the S66x8 test set [RMS(RMSD)]. The position of the data points on the horizontal axis is determined by the distance scaling factor.

The S66x8 set was designed to examine the performance of quantum chemical methods for potential energy surfaces of weakly interacting systems. It contains the dimers of the S66 set,[155], but the distances of the monomers are scaled by eight different factors between 0.9 and 2. To represent the data for the 528 structures in a condensed and meaningful way, we calculated the root mean square of the root mean square gradient

deviations, RMS(RMSD), for the 66 dimers at each of the eight different distances:

$$\mathrm{RMS(RMSD)} = \sqrt{\frac{1}{66}\sum_{s}^{66}\frac{\left[\nabla E_{\mathrm{DLPNO\text{-}MP2}}(s) - \nabla E_{\mathrm{RI\text{-}MP2}}(s)\right]^2}{N_{\mathrm{Atoms}}(s)}} \tag{3.127}$$

Figure 3.11 shows RMS(RMSD) values for DLPNO-MP2 with different threshold settings. Close to the equilibrium distances, the typical errors are $1.5 \times 10^{-4}\,E_\mathrm{h}\,{a_0}^{-1}$, $6 \times 10^{-5}\,E_\mathrm{h}\,{a_0}^{-1}$ and $2 \times 10^{-5}\,E_\mathrm{h}\,{a_0}^{-1}$ for LoosePNO, NormalPNO and TightPNO, respectively. The errors tend decrease slightly from shorter to longer distances between the monomers.

3.3.5 Geometry optimisation benchmarks

The most important practical application of the nuclear gradient is likely to perform geometry optimisations of molecular systems. In this regard, two questions need to be answered: is the convergence of geometry optimisations comparable to RI-MP2, and how large are the errors relative to RI-MP2 equilibrium geometries?

To address these questions, we have performed optimisations of the structures from the Baker set,[215] the ROT34 set,[122, 123] the S66 set,[155] the LB12 set,[213] and a few organometallic compounds containing main group metals and zinc. All calculations were performed using the def2-TZVP basis and with the frozen core approximation. Unless noted otherwise, the optimisations were carried out in redundant internal coordinates, with the "TightOpt" settings to enforce strict convergence criteria which permit even small deviations between molecular structures to be identified. By default, ORCA employs "tight" SCF settings in all geometry optimisations.

3.3.5.1 Rotational constants of molecules

The ROT34 set by Grimme and co-workers[122, 123] contains twelve organic molecules with 18 to 35 atoms each. It was designed to examine rotational constants as an indirect measure for the quality of equilibrium geometries. Geometry optimisations were performed using both DLPNO-MP2 and RI-MP2, and the results of the DLPNO-MP2

Thresholds	MRE (%)	SD (%)	Min (%)	Max (%)
LoosePNO	−0.157	0.106	−0.404	0.053
NormalPNO	−0.064	0.049	−0.170	0.025
TightPNO	−0.025	0.022	−0.070	−0.017

Table 3.2: Error statistics for equilibrium constants B_e in the ROT34 set as computed with DLPNO-MP2, using RI-MP2 as a reference: $\Delta B_e = B_e^{\text{DLPNO-MP2}} - B_e^{\text{RI-MP2}}$. MRE: mean relative error, SD: standard deviation of the relative error, and Min/Max: minimal and maximal relative errors

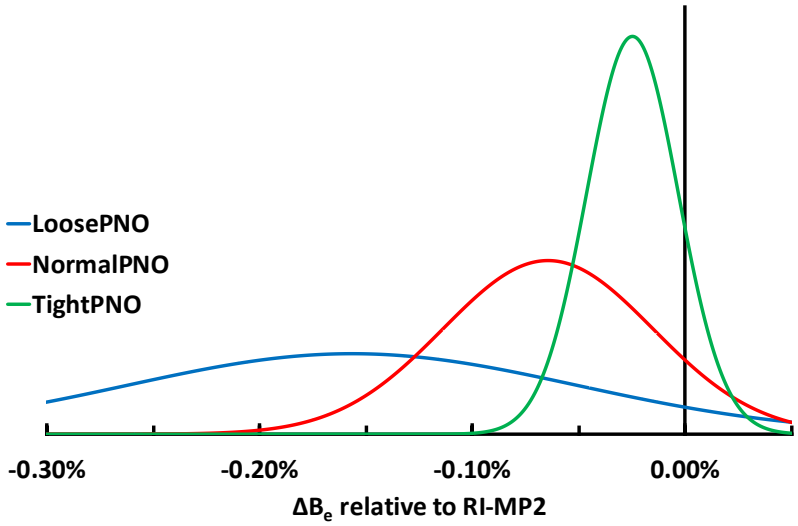

Figure 3.12: Errors in rotation constants for the ROT34 represented as normal distributions, with RI-MP2 as the reference. The corresponding numerical data is shown in Table 3.2.

calculations were compared to RI-MP2 as a reference. For consistency with the original publications on ROT34, only the largest rotational constant of triethylamine is included in the statistics (and hence there is a total of 34 rotational constants to compare instead of 36).

As shown in Table 3.2 and Figure 3.12, DLPNO-MP2 slightly underestimates rotational constants in comparison with RI-MP2, which means that the structures are somewhat larger than the MP2 equilibrium geometries. The magnitudes of the mean relative errors are 0.16 % with LoosePNO, 0.06 % with NormalPNO, and 0.03 % with TightPNO. A comparison with the deviations from experimentally derived rotation constants puts these values into context: Risthaus and co-workers determined that the overall deviations for this benchmark set are 0.45 % with RI-MP2/def2-QZVP, and 0.21 % with the

Basis set	MRE (%)	SD (%)	Min (%)	Max (%)
def2-SVP	−0.043	0.034	−0.106	0.027
def2-TZVP	−0.064	0.049	−0.170	0.025
def2-QZVPP	−0.050	0.044	−0.138	0.052

Table 3.3: Error statistics for equilibrium constants B_e in the ROT34 set as computed with DLPNO-MP2, using RI-MP2 as a reference. MRE: mean relative error, SD: standard deviation of the relative error, and Min/Max: minimal and maximal relative errors

dispersion-corrected double-hybrid density functional RI-B2PLYP-D3/def2-QZVP.[123] Errors incurred by truncations with NormalPNO or TightPNO settings are thus substantially smaller than the method-specific errors of MP2 itself, or of typical empirical schemes based on MP2.

Upon analysing bond lengths for part of the molecules in the Baker test set, Frank and Hättig reported that errors in geometries optimised with their PNO-MP2 method increase with basis set size.[112] To investigate a possible basis set dependence, we have performed additional optimisation for the ROT34 set with basis sets of double zeta and quadruple zeta quality using NormalPNO thresholds. The statistical results in Table 3.3 do not show any clear tendency with the size of the basis set, but the errors always stay in the small range observed with def2-TZVP.

3.3.5.2 Structures of organic molecules

Baker's test set[215] was originally designed to investigate the performance of algorithms for geometry optimisation. Hence, the starting coordinates differ substantially from the corresponding equilibrium structures. In some cases, we encountered convergence difficulties, which required a few manual interventions to obtain comparable geometries:

- Benzidine, pterin and ACANIL01, all of which contain amino groups, feature planar starting structures in the Baker set. In their MP2 minimum geometries, however, the amino groups are not planar; the RI-MP2 optimisations of these three molecules with the planar starting structures converged to saddle points. On the other hand, the LoosePNO-level optimisations of benzidine and pterin converged directly to the non-planar minima with lower energies, which were used as starting points to obtain

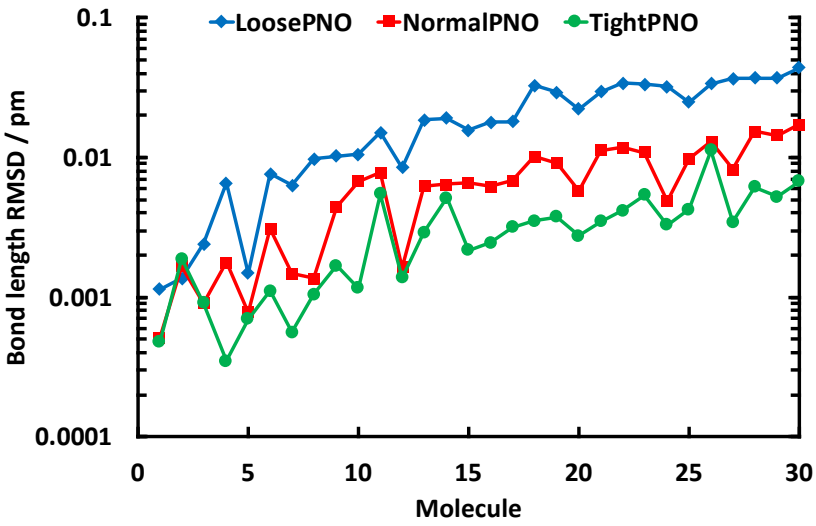

Figure 3.13: Baker test set: root mean square deviation of all covalent bond lengths in each molecule between DLPNO-MP2 and RI-MP2. The molecules are ordered by their number of atoms, increasing from left to right.

structures with RI-MP2 and with NormalPNO and TightPNO settings.

A LoosePNO optimisation of ACANIL01 led to an initially unconverged structure. The latter was used as a starting point for the RI-MP2 optimisation and for further DLPNO-MP2 optimisations with LoosePNO, NormalPNO and TightPNO settings, all of which then converged to the correct minima.

- No convergence with "TightOpt" settings could be achieved for caffeine with thresholds at LoosePNO level. In this case, the geometry convergence criteria needed to be relaxed to "NormalOpt".

An automated analysis of the optimised geometries was performed using a script. Covalent bonds were assigned between all atoms that were separated by no more than 1.2 times the sum of their covalent atomic radii. All angles and dihedrals between bonds in this framework were calculated, too.

Figure 3.13 shows root mean square deviations over all bond lengths in each molecule. All RMSDs are below 0.02 pm with NormalPNO thresholds and 0.01 pm with TightPNO thresholds. As a further trend evident from the graph, errors are almost negligible for smaller molecules, but increase towards the larger systems where the local approximations become more effective. Therefore, it is not particularly meaningful to perform a statistical

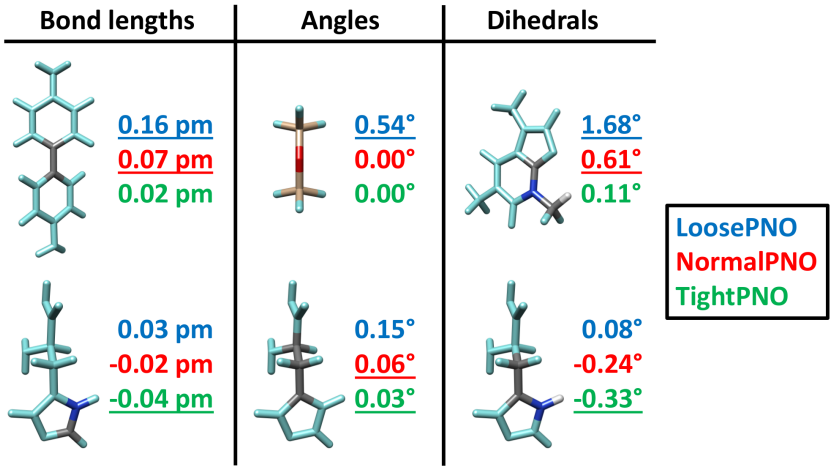

Figure 3.14: Largest errors occurring in any molecules of the Baker test set. The underlined values highlight the maximal errors determined among all bond lengths, angles and dihedrals in all of the structures. Values that are not underlined are only shown for comparison. Atoms belonging to the respective bonds, angles and dihedrals are shown in their element colours, whereas all remaining atoms are coloured in light cyan.

analysis for the Baker set with DLPNO-MP2, but instead it is more interesting to examine the largest errors occurring in any of the molecules.

Figure 3.14 illustrates the largest errors in bond lengths, bond angles and dihedrals that were observed in any of the molecules. Relative to RI-MP2, the magnitudes of the respective largest errors with NormalPNO/TightPNO thresholds are 0.07 pm/0.04 pm for bond lengths, 0.06°/0.03° for bond angles and 0.6°/0.3° for dihedrals.

Even though the single-point gradient at the starting geometry of benzidine is slightly imbalanced (see Section 3.3.4), there is no significant tendency towards bond length alternation in the aromatic rings of the optimised structure: the largest deviations of intra-ring bond lengths between DLPNO-MP2 and RI-MP2 are 0.04 pm with LoosePNO thresholds, 0.01 pm with NormalPNO thresholds and 0.005 pm with TightPNO thresholds. All of these errors are well within the overall accuracy margins observed for DLPNO-MP2 equilibrium geometries with the respective threshold settings.

In their recent investigation of the OSV-MP2 gradient, Yang and co-workers included a comparison with the DLPNO-MP2 method for geometry optimisations of molecules from the Baker test set.[113] For the dihedral angle in benzidine they report a deviation of the DLPNO-MP2 geometries by 1° to 2° from the RI-MP2 result, which is an order of magnitude larger than observed in the present work. However, they used RIJCOSX

with unreported grid settings for the DLPNO-MP2 calculations only, which is a possible cause of significant errors in torsional angles that exceed the intrinsic error of DLPNO-MP2.[123] In addition, a geometry optimisation of benzidine with the starting structure from the test set may accidentally converge to a saddle point with planar amino groups, or to one of the different local minima.

3.3.5.3 Non-covalently bonded dimers

Geometry optimisations of the dimers in the S66 set[155] were performed to investigate the performance of the DLPNO-MP2 gradient for weakly interacting systems. In a few cases, ensuing difficulties required manual intervention to obtain comparable equilibrium structures:

- The optimisation of the water-methylamine dimer in its geometry from the S66 set failed to converge to a minimum with RI-MP2/def2-TZVP. Instead, we flipped the water molecule around the O−H···N hydrogen bond in the starting geometry for all optimisations of this dimer.

- An initially unconverged geometry of the peptide-ethene dimer with LoosePNO settings was found to possess a lower RI-MP2 single point energy than the converged structure from the RI-MP2 optimisation. Therefore, the RI-MP2 optimisation and all DLPNO-MP2 optimisations were restarted from that structure, and convergence was subsequently achieved in all cases.

- All optimisations of the pentane-acetamide dimer were restarted from an initially unconverged TightPNO structure, as it was found to have the lowest RI-MP2 single-point energy. Convergence was subsequently achieved in all cases.

- Optimisations of the cyclopentane-neopentane dimer with LoosePNO and NormalPNO settings converged to a higher-lying point than the RI-MP2 and TightPNO optimisations. Therefore, the LoosePNO and NormalPNO optimisations were restarted with the converged RI-MP2 structure.

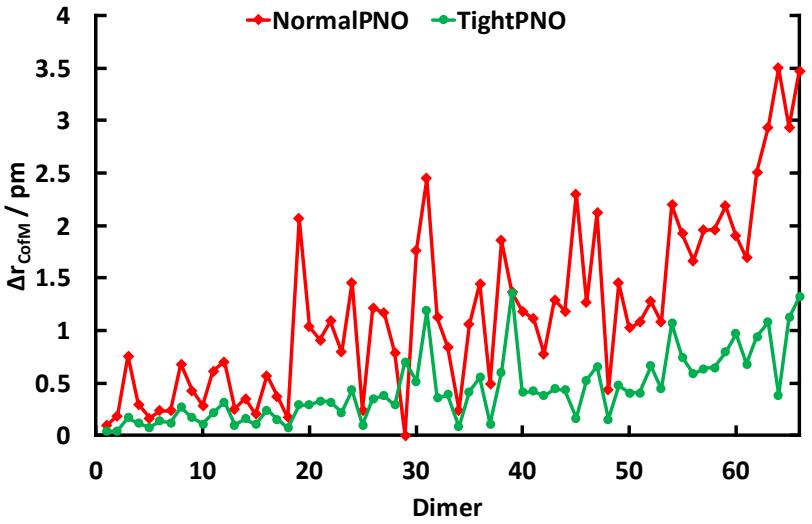

Figure 3.15: S66 set: errors in centre-of-mass distances between monomers in DLPNO-MP2 equilibrium geometries. RI-MP2 dimer geometries were taken as the reference. The dimers are ordered by their total number of atoms, increasing from left to right.

The accuracy of the dimer equilibrium geometries was assessed via the distances between the respective monomers. Figure 3.15 shows the errors in centre-of-mass distances calculated using DLPNO-MP2. LoosePNO results have been omitted from the graph, but all numbers are reported in Appendix B.4. The error range varies across the set, increasing from the smallest system (water dimer) to the largest dimers, which contain 34 atoms.

As before, the most useful quantities are the maximum errors: the largest absolute and relative deviations in centre-of-mass distances are 3.5 pm and 0.91 %, respectively, with NormalPNO, and 1.4 pm and 0.34 % with TightPNO. Unacceptably large errors are encountered with LoosePNO (10 pm or 2 %), which is certainly not a suitable set of thresholds for noncovalent interactions. DLPNO-MP2 tends to predict slightly larger distances between monomers than RI-MP2.

3.3.5.4 Long bonds in molecules

The LB12 set contains twelve molecules compiled by Grimme and co-workers to test the geometry optimisation of structures that present a challenge to electronic structure methods.[213] For each structure, they specified an interatomic distance which should be examined, typically representing either a long covalent bond or a short distance between

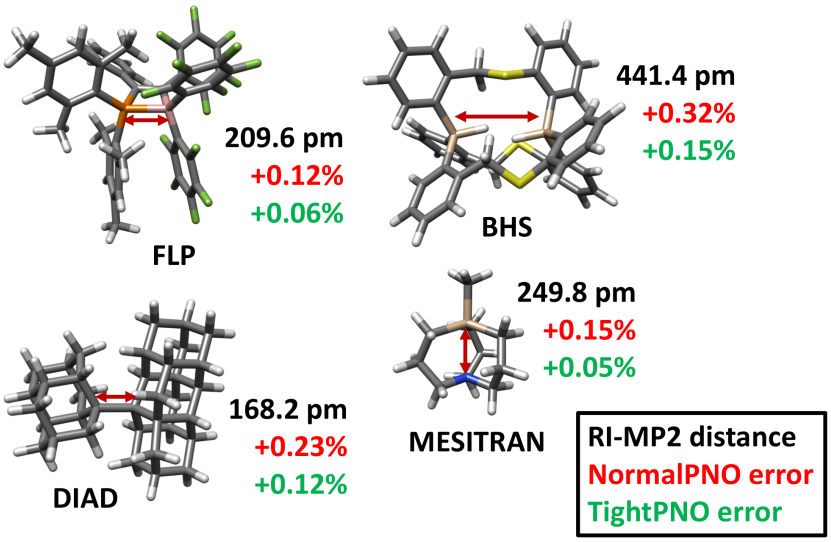

Figure 3.16: A few example structures from the LB12 benchmark set. RI-MP2 distances and signed relative deviations of DLPNO-MP2 are provided for the highlighted distances. The full set of results is provided in Table 3.4.

noncovalently interacting molecule fragments. While ten of the structures contain main group elements only, two systems are organometallic complexes containing either Rh and Cr (HAPPOD) or Os and Cr (KAMDOR). Table 3.4 reports distances in the equilibrium structures optimised with RI-MP2, and the corresponding DLPNO-MP2 errors. A few examples are illustrated in Figure 3.16.

The following complications were encountered during the geometry optimisations:

- In order to converge the HAPPOD structure with LoosePNO thresholds, the geometry convergence settings needed to be relaxed to "NormalOpt", while the SCF convergence criteria needed to be tightened to "VeryTightSCF".

- Geometry convergence could not be achieved for KAMDOR with LoosePNO or NormalPNO settings.

- Initially, the RI-MP2 and DLPNO-MP2 optimisations of BHS converged to a geometry which, as the starting structure, was of C_3 symmetry with the Si−H bonds on a straight line. Subsequent DLPNO-MP2 optimisations performed with RIJCOSX to determine timings, however, led to a structure of C_1 symmetry with a shorter Si···Si distance. Even without RIJCOSX, the geometry featured a lower RI-MP2 energy than the C_3 structure, suggesting that the latter is an unstable stationary

			Δr/pm			r/pm
Name	Atoms	Distance	LoosePNO	NormalPNO	TightPNO	RI-MP2
DIAD	82	C–C	0.66	0.39	0.20	168.23
FLP	88	P–B	0.54	0.25	0.12	209.57
DTFS	14	Si–N	1.94	0.78	0.33	214.91
MESITRAN	33	Si–N	0.93	0.37	0.13	249.80
S_8^{2+}	8	S–S	0.28	0.17	0.07	329.82
HAPPOD	28	Rh–Cr	[I]4.53	1.82	0.81	284.77
KAMDOR	33	Os–Cr	[II]–	[II]–	0.64	269.28
PP	32	C–C	0.58	0.16	0.05	307.91
BRCLNA	18	Br–Cl	0.30	0.11	0.05	313.82
C_2Br_6	8	Br–Br	0.42	0.22	0.08	341.73
RESVAN	39	S–S	9.36	2.98	0.91	390.66
BHS	76	Si–Si	3.17	1.40	0.63	433.37

Table 3.4: Interatomic distances in the LB12 test set. The reference values for the specified interatomic distances (r) were obtained with RI-MP2. Errors in distances (Δr) are reported for DLPNO-MP2.
[I]Convergence was achieved with "NormalOpt" settings.
[II]Geometry optimisations did not converge.

point on the potential energy surface. Therefore, the RI-MP2 and DLPNO-MP2 optimisations of BHS without RIJCOSX were started from the structure optimised using DLPNO-MP2(RIJCOSX).

In comparison with RI-MP2, DLPNO-MP2 predicts slightly larger interatomic distances. The largest errors were found to be below 0.8 % with NormalPNO settings and below 0.3 % with TightPNO settings.

3.3.5.5 Structures of metal-containing compounds

In order to examine the accuracy of the DLPNO-MP2 gradient for systems with some degree of ionic bonding, further optimisations were performed for compounds containing main group metals or zinc. The structures are illustrated in Figure 3.17. For each system, we specify a distance to be compared between geometries optimised with DLPNO-MP2 and RI-MP2:

1. Trimethylaluminium dimer (Al_2Me_6): the distance between the aluminium atoms is inspected.

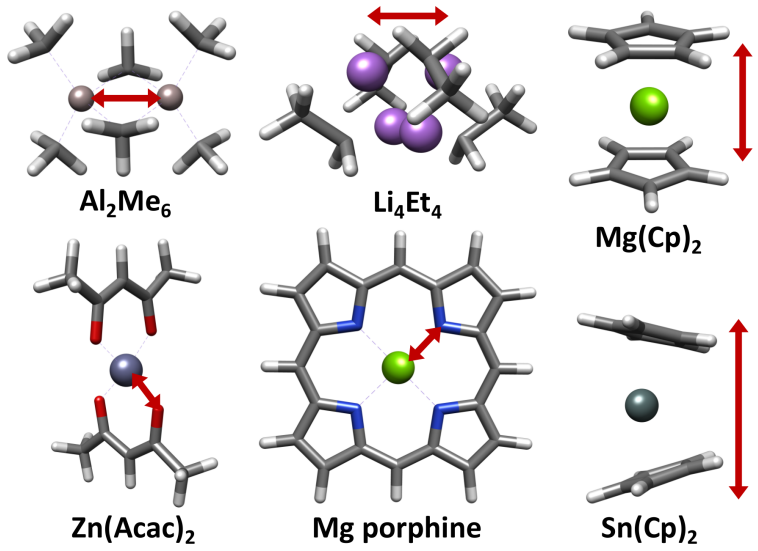

Figure 3.17: Structures of systems used to examine the geometry optimisation of metal-containing compounds. The arrows indicate distances that are used to compare structures optimised with different methods.

2. Ethyllithium tetramer (Li_4Et_4): the lithium atoms are in a tetrahedral arrangement, and the entire complex is of D_{2d} symmetry. There are two types of symmetry-equivalent bonds between Li atoms: two bonds of equal length, which are inspected here, and four further bonds.

3. Bis(cyclopentadienyl)magnesium ($MgCp_2$): the distance between the centres of mass of the Cp ligands is inspected.

4. Bis(cyclopentadienyl)tin ($SnCp_2$): the distance between the centres of mass of the Cp ligands is inspected.

5. Magnesium porphine: the Mg–N distance is inspected.

6. Zinc acetylacetonate ($Zn(acac)_2$): the Zn–O distance is inspected.

The starting structures for the geometry optimisations were pre-optimised with the PBEh-3c method.[213] Results for specific distances in the optimised structures are shown in Table 3.5. Generally, the errors for the six systems are in a range that would be expected from the preceding benchmark calculations. In DLPNO-MP2 optimisations

		Δr/pm			r/pm
Name	Distance	LoosePNO	NormalPNO	TightPNO	RI-MP2
Al_2Me_6	Al−Al	0.36	0.11	0.03	261.58
Li_4Et_4	Li−Li	0.44	0.17	0.10	237.10
$MgCp_2$	Cp−Cp	[I]0.47	0.16	0.03	397.07
$SnCp_2$	Cp−Cp	2.85	1.51	0.60	467.05
Mg porphine	Mg−N	0.1	<0.05	<0.03	205.0
$Zn(acac)_2$	Zn−O	[I]0.3	0.1	<0.05	194.7

Table 3.5: Specific distances in compounds containing metal atoms. Total distances (r) are reported for RI-MP2, and deviations (Δr) for DLPNO-MP2.
[I]Geometry optimised with "NormalOpt" settings.

	LoosePNO	NormalPNO	TightPNO	RI-MP2
r(Cp−Cp)/pm	469.90	468.56	467.65	467.05
r(Sn−Cp)/pm	237.99	237.80	237.70	237.64
∠(Cp−Sn−Cp)/°	161.67	160.25	159.27	158.64

Table 3.6: Geometric parameters in $SnCp_2$ optimised with DLPNO-MP2 using different thresholds, and with RI-MP2. The table shows the distance between the centres of mass of the Cp ligands; the distance of the Sn atom to the centres of the Cp rings; and, for illustration purposes, also the angle between the lines connecting the Sn atom to the Cp ring centres.

of $MgCp_2$ and $Zn(acac)_2$ with LoosePNO thresholds, the geometry convergence settings needed to be relaxed to "NormalOpt".

The largest errors were observed for the distance between the cyclopentadienyl ligands in $SnCp_2$. As demonstrated in Table 3.6, this is primarily a consequence of an increase in the angle between the two lines connecting the Sn atom to the centres of the Cp ligands. On the other hand, the variation in the distance of the Sn atoms to the ligands is significantly smaller.

3.3.6 Geometry optimisation with double-hybrid density functionals

A particularly interesting use case of DLPNO-MP2 is its combination with double-hybrid density functionals. While hybrid functionals mix the "DFT" component of the exchange energy E_X^{DFT} with a portion a_X of Hartree-Fock exchange E_X^{HF}, in double-hybrids the

correlation functional E_{C} is mixed with an MP2-like energy contribution $E_{\mathrm{C}}^{\mathrm{MP2}}$:

$$E_{\mathrm{XC}} = (1 - a_{\mathrm{X}})\, E_{\mathrm{X}}^{\mathrm{DFT}} + a_{\mathrm{X}} E_{\mathrm{X}}^{\mathrm{HF}} + (1 - a_{\mathrm{C}})\, E_{\mathrm{C}}^{\mathrm{DFT}} + a_{\mathrm{C}} E_{\mathrm{C}}^{\mathrm{MP2}} \tag{3.128}$$

The orbitals are determined self-consistently using the exchange-correlation functional E_{XC} without the MP2-type contribution. Afterwards, the perturbative correction is added using the previously converged orbitals and orbital energies. Since the RI-MP2 gradient had been combined with double-hybrid density functionals before,[181] extending the procedure to the DLPNO-MP2 gradient was straightforward.

Geometry optimisations were performed using the functionals B2PLYP,[119] B2GP-PLYP,[216] DSD-BLYP[217] and DSD-PBEP86.[218] In all cases, the D3 correction with Becke-Johnson damping was included.[202, 203] Note that the ORCA software contains several different parameterisations of the DSD functionals: this work used the versions documented as combinations of the "DSD-BLYP" and "DSD-PBEP86" keywords together with "D3" in ORCA 4.1. The calculations were performed with the def2-TZVP basis set, and core orbitals were frozen. In order to reduce the impact of grid artefacts, the "Grid7" setting in ORCA was used.

Figure 3.18 shows the error distributions obtained in geometry optimisations of the molecules in the ROT34 set. The reference geometries were obtained using the respective functionals with RI-MP2 employed for the perturbative contribution. While B2PLYP and B2GP-PLYP build upon "regular" MP2, in the DSD functionals the spin components are scaled differently. For comparison, therefore, we include DLPNO-SCS-MP2 results with Grimme's original scaling parameters[116] alongside the previously discussed DLPNO-MP2 error distributions.

A fair comparison of a DHDF result to experiment needs to be made with a sufficiently large basis set. While data on the performance of DHDFs for geometries is less extensive than for energetics, the ROT34 set has been examined previously with the B2PLYP-D3 functional using the def2-QZVP basis set.[123] This yielded relative errors in rotational constants of 0.21(23) % to within a standard deviation, and a total spread of 1.1 %. Even with "LoosePNO" thresholds, a narrower error distribution is obtained with all

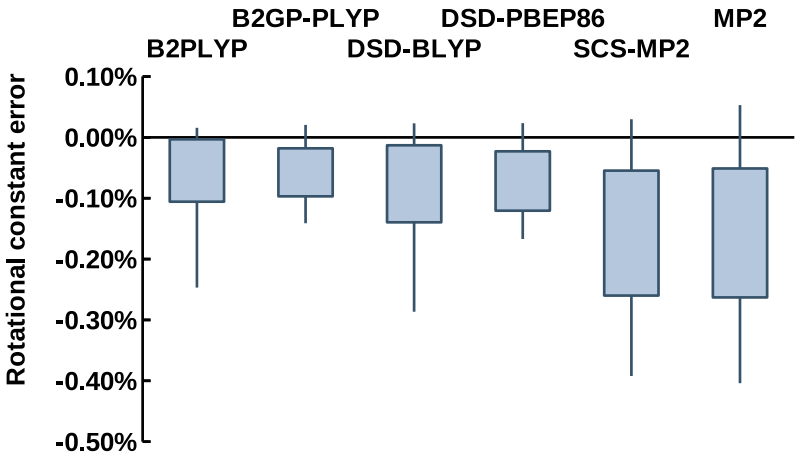

(a) LoosePNO settings for DLPNO-MP2

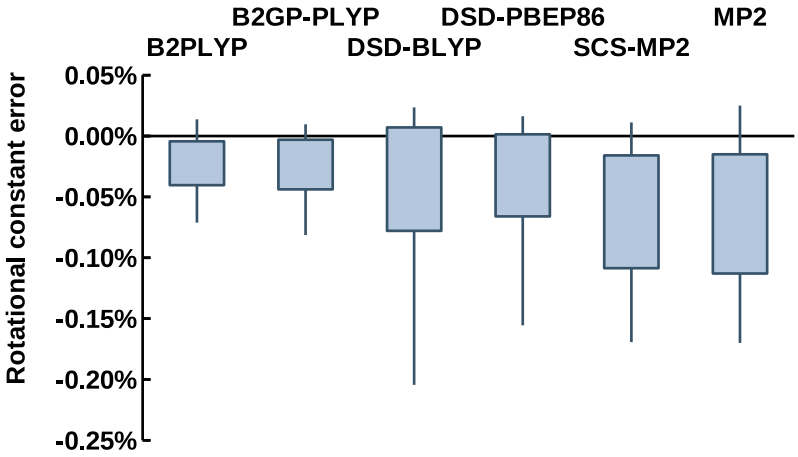

(b) NormalPNO settings for DLPNO-MP2

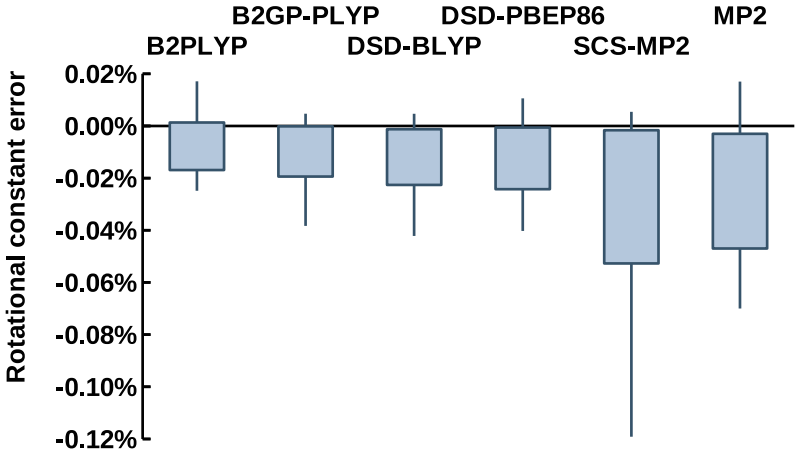

(c) TightPNO settings for DLPNO-MP2

Figure 3.18: Errors in rotational constants for the ROT34 set with double-hybrid density functionals and SCS-MP2. In each case, values obtained using the respective method without DLPNO approximations serve as the reference.
Boxes: relative errors within one standard deviation of the mean.
Whiskers: complete range of relative errors.

functionals. With "NormalPNO" thresholds, only a few outliers are in a similar range as the intrinsic B2PLYP-D3 error; and with "TightPNO", the errors become negligible without exception.

The errors of DHDFs with DLPNO approximations are usually smaller than those of DLPNO-MP2, and in the remaining cases do not exceed the latter by a big margin. Among the DHDFs, the DSD functionals tend to be more sensitive to the local approximations. We note in passing that the error distributions of DLPNO-SCS-MP2 are mostly comparable to those of DLPNO-MP2.

Among the benchmark systems used to examine the performance of the DLPNO-MP2 gradient, the ROT34 set was one of the less challenging. Therefore, an equally good performance of DLPNO-based double-hybrid density functionals in more difficult applications cannot be taken for granted. Nonetheless, the results suggest that the combination of DLPNO-MP2 with double-hybrid density functionals is a worthwhile approach for the geometry optimisation of large systems, and encourage further exploration.

3.3.7 Domain sizes and basis set superposition error

In multiple past publications on local correlation methods with small domains, the respective authors concluded that domain truncation reduces the extent of the basis set superposition error (BSSE).[219–221] This idea gained popularity in parts of the local correlation community, anecdotally evidenced by the fact that two anonymous peer-reviewers of our publication in ref. [111] commented independently upon a possible reduction of the BSSE (or lack thereof) in DLPNO-MP2. Indeed, one of the reviewers suggested that recovering the BSSE is actually a disadvantage of DLPNO-MP2 compared to methods that employ smaller domains: since the approximations behind DLPNO-MP2 were designed with the goal to reproduce RI-MP2 as closely as possible, the same would apply to pathologies such as the basis set superposition error. This section investigates how the BSSE and the overall accuracy are affected by the domain size for a few selected cases.

The electronic contribution to the dimerisation energy of two monomers is given by

the difference

$$\Delta E = E^{\mathrm{AB}}(\mathrm{AB}) - E^{\mathrm{A}}(\mathrm{A}) - E^{\mathrm{B}}(\mathrm{B}). \tag{3.129}$$

In this equation, $E^{\mathrm{AB}}(\mathrm{AB})$ represents the energy of the dimer AB. Likewise, $E^{\mathrm{A}}(\mathrm{A})$ and $E^{\mathrm{B}}(\mathrm{B})$ are the energies of the monomers calculated with their respective sets of basis functions. With finite basis sets, this expression tends to overestimate the binding strength. If one calculates the energy of one monomer using the basis functions of both monomers taken together, then, because of the variational principle, the resulting energy is lower than that of the monomer in its own basis. This effect introduces an additional bias known as the basis set superposition error, caused by the "more complete" basis of the dimer relative to the monomers.

To address this problem, Boys and Bernardi suggested the counterpoise correction,[222] whereby the electronic contribution to the dimerisation energy is determined with monomer energies $E^{\mathrm{AB}}(\mathrm{A})$ and $E^{\mathrm{AB}}(\mathrm{B})$ calculated using the basis set of the dimer AB:

$$\Delta E_{\mathrm{CP}} = E^{\mathrm{AB}}(\mathrm{AB}) - E^{\mathrm{AB}}(\mathrm{A}) - E^{\mathrm{AB}}(\mathrm{B}) \tag{3.130}$$

Even though the counterpoise correction sometimes exhibits a tendency to underbind dimers,[223, 224] we take the difference

$$\delta E_{\mathrm{BSSE}} = \Delta E_{\mathrm{CP}} - \Delta E \tag{3.131}$$

as an estimate for the extent of the intermolecular BSSE.

Potential energy curves were calculated for three systems in the S66 set:[155] (a) the water dimer, (b) a dimer of methanol with methylamine, and (c) the neopentane dimer (Figure 3.19). To construct coordinates for dimers (a) and (b), the lengths of the hydrogen bonds were varied in steps of 0.1 pm, while the structures of the monomers themselves and their relative orientations were kept fixed. For the neopentane dimer (c), the distance between the centres of the monomers was varied in steps of 1 pm.

This approach is consistent with the S66x8 set; however, instead of calculating an

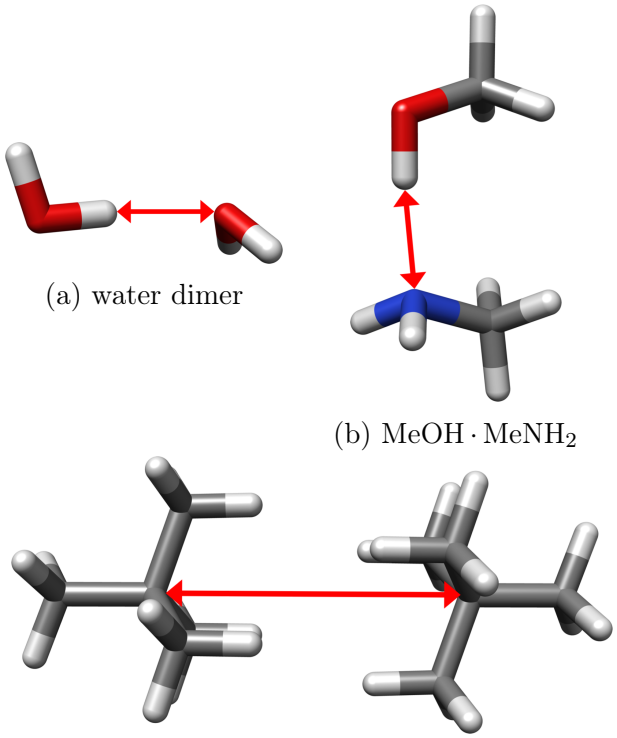

(a) water dimer

(b) $MeOH \cdot MeNH_2$

(c) neopentane dimer

Figure 3.19: Non-covalently bonded dimers used to investigate the basis set superposition error with different domain sizes.

interpolated potential energy surface using only a few points, the energy curve can be examined closely for discontinuities. At each of the geometries, we calculated single-point DLPNO-MP2 energies with different domain cutoffs T_{CutDO}. Default values ("NormalPNO") were used for all other thresholds.

At first, the effect of the basis set superposition error will be investigated for energies. Table 3.7 shows dimerisation energies ΔE and counterpoise contributions δE_{BSSE} for those geometries which are closest to the S66 reference coordinates. All DLPNO-MP2 calculations were performed with the def2-TZVP basis. For comparison, the table also includes values calculated with RI-MP2, and at SCF level.

To estimate the basis set incompleteness error, explicitly correlated calculations were performed using RI-MP2-F12 with and without counterpoise correction (the implementation of MP2-F12 in ORCA is described in ref. [226] and the references therein). For the latter calculations, we used the cc-pVTZ-F12 basis[227] together with the complementary auxiliary basis set cc-pVTZ-F12/OptRI[228] and the auxiliary set aug-cc-pVQZ/C.[208]

	$(H_2O)_2$		$MeOH \cdot MeNH_2$		$(C_5H_{12})_2$	
T_{CutDO}	ΔE	δE_{BSSE}	ΔE	δE_{BSSE}	ΔE	δE_{BSSE}
0.01	−23.49	3.37	−34.42	5.33	−6.63	2.00
0.02	−23.48	3.36	−34.29	5.26	−5.40	0.95
0.04	−23.44	3.32	−33.87	4.71	−3.95	0.14
0.06	−23.35	3.25	−33.85	4.52	−3.42	0.02
0.08	−23.35	3.25	−32.01	3.51	−2.58	0.12
0.10	−23.32	3.21	−31.10	2.93	−2.58	0.12
0.15	−21.68	2.00	−30.05	2.87	−2.58	0.12
0.20	−21.68	2.00	−30.05	2.87	−2.58	0.12
SCF	−18.28	1.39	−20.14	1.97	6.89	0.13
RI-MP2	−23.57	3.40	−34.57	5.44	−6.98	2.24
RI-MP2-F12	−20.95	0.27	−32.50	0.26	−7.34	0.13
CCSD(T)/CBS[I]	−20.83		−31.90		−7.30	

Table 3.7: Interaction energies ΔE and BSSE error estimates δE_{BSSE} for non-covalently bonded dimers with different DLPNO-MP2 domain thresholds T_{CutDO}. All energies are reported in $\mathrm{kJ\,mol^{-1}}$.
SCF, RI-MP2 and DLPNO-MP2 energies were calculated using the def2-TZVP basis.
RI-MP2-F12 energies were calculated with the cc-pVTZ-F12 basis.
[I]The reported Coupled Cluster results are revised S66 reference values from ref. [225].

Comparing results with and without counterpoise correction shows that most of the BSSE is eliminated in the explicitly correlated calculations. Finally, Table 3.7 also includes coupled cluster results obtained by Kesharwani and co-workers.[225]

With the default threshold of $T_{\mathrm{CutDO}} = 0.01$, dimerisation energies ΔE calculated with DLPNO-MP2 are in a reasonably good agreement with RI-MP2; likewise, the extent of the BSSE is similar. Increasing the domain threshold T_{CutDO} reduces the extent of the counterpoise correction δE_{BSSE}, but at different rates for the three systems:

- The water dimer was studied with local correlation methods by Saebø and co-workers,[219] and by Schütz and co-workers.[220] Increasing the T_{CutDO} from the default value of 0.01 to 0.10 leads to compact domains, each of which spans the three atoms of the water molecule where the respective molecular orbital resides. Nonetheless, a large part of the BSSE is recovered. Increasing T_{CutDO} even further to 0.15 or 0.20 leads to the smallest domains that are still viable in a chemical sense: each domain contains PAOs from only one or two atoms in the case of oxygen lone pairs or O–H bonding orbitals, respectively. This leads to a significant reduction

of the BSSE from $3.4\,\mathrm{kJ\,mol^{-1}}$ to $2.0\,\mathrm{kJ\,mol^{-1}}$. However, $1.4\,\mathrm{kJ\,mol^{-1}}$ of δE_{BSSE} are accounted for by the Hartree-Fock energy, whereas the remaining $0.7\,\mathrm{kJ\,mol^{-1}}$ originate from the local MP2 contribution even with such small domains. Dimerisation energies approach the RI-MP2-F12 and CCSD(T)/CBS results with decreasing domain size, likely as a result of error cancellation.

- For the dimer of MeOH with $MeNH_2$, a reduction of δE_{BSSE} is achieved with decreasing domain sizes. Unlike for the water dimer, a domain threshold of $T_{\mathrm{CutDO}} = 0.10$ (leading to domains of two to three atoms) already achieves the largest possible part of the reduction in δE_{BSSE}. Again, however, the BSSE is only lowered from $5.4\,\mathrm{kJ\,mol^{-1}}$ to $2.9\,\mathrm{kJ\,mol^{-1}}$, of which $2.0\,\mathrm{kJ\,mol^{-1}}$ are due to the SCF contribution. While RI-MP2 in def2-TZVP basis overbinds the dimer, reducing the domain size ultimately leads to underbinding compared with both RI-MP2-F12 and CCSD(T)/CBS.

- For the neopentane dimer, the contribution δE_{BSSE} is halved with $T_{\mathrm{CutDO}} = 0.02$, which is used in combination with a different PNO cutoff in the "LoosePNO" settings, and the correlation contribution is effectively eliminated with $T_{\mathrm{CutDO}} = 0.04$. Rather curiously, with even smaller domains the SCF and correlation contributions to δE_{BSSE} have opposite signs: with such small domains, DLPNO-MP2 produces monomer correlation energies that are *higher* in the dimer basis than in the monomer basis. While RI-MP2/def2-TZVP slightly underbinds the two monomers (in comparison with both the complete basis and the coupled cluster results), reducing domain sizes leads to a much more severe underestimation of the bonding strength.

Particularly in the case of the two hydrogen-bonded dimers, it is unsurprising that a significant fraction of the basis set superposition error remains even with minimalistic domains that span PAOs from two atoms for covalent orbitals, and from only one atom for lone pairs: while PAOs $\tilde{\mu}'$ are centred on the same atoms as the localised MOs, significant AO coefficients $\tilde{P}_{\nu\tilde{\mu}'}$ may still spread over the entire dimer. Likewise, orthogonalisation

	$(H_2O)_2$		$MeOH \cdot MeNH_2$		$(C_5H_{12})_2$	
T_{CutDO}	r	r_{CP}	r	r_{CP}	r	r_{CP}
0.01	195.4	201.7	192.0	198.4	533	545
0.02	195.4	202.6	192.0	198.4	539	545
0.04	195.6	203.5	192.0	198.0	549	550
0.06	196.1	201.8	192.0	198.4	554	554
0.08	196.2	201.8	194.7	200.7	559	560
0.10	196.3	201.8	195.8	199.0	559	560
0.15	198.7	202.9	197.4	200.4	559	560
0.20	198.7	202.9	197.4	200.4	559	560
RI-MP2	195.3	201.7	192.5	198.3	531	544
RI-MP2-F12	195.1	195.4	191.6	191.8	525	525
CCSD(T)/CBS[I]	195.8		193.4		526	

Table 3.8: Optimal distances between monomers in non-covalently bonded dimers along a one-dimensional potential energy curve. DLPNO-MP2 results were calculated with different domain thresholds T_{CutDO}. Distances r were calculated without the counterpoise correction, whereas r_{CP} represent the minimum of the counterpoise-corrected energy. All distances are reported in pm.
SCF, RI-MP2 and DLPNO-MP2 energies were calculated using the def2-TZVP basis.
RI-MP2-F12 energies were calculated with the cc-pVTZ-F12 basis.
[I]The reported Coupled Cluster results are revised S66 reference values from ref. [229]

.

tails of occupied molecular orbitals may extend beyond one monomer.

The features of the potential energy surfaces will be examined next. Graphs with sections of dissociation curves calculated using selected domain thresholds are shown in Figure 3.20. Table 3.8 lists minimum energy distances determined for the three dimers using DLPNO-MP2, RI-MP2 and RI-MP2-F12. Counterpoise-corrected distances were determined in addition. Revised distances reported for the S66 set by Brauer and co-workers[229] have been included in Table 3.8 for comparison.

- Water dimer: despite the basis set incompleteness and superposition errors, RI-MP2/def2-TZVP agrees very well with RI-MP2-F12. On the other hand, the minimum of the counterpoise-corrected energy, r_{CP}, overestimates the hydrogen bond length by more than 6 pm. While DLPNO-MP2 with default thresholds is in good agreement with the RI-MP2 result, reducing the domain size leads to an overestimation of the interatomic distance by several pm.

  Boese and co-workers performed unconstrained geometry optimisations of the wa-

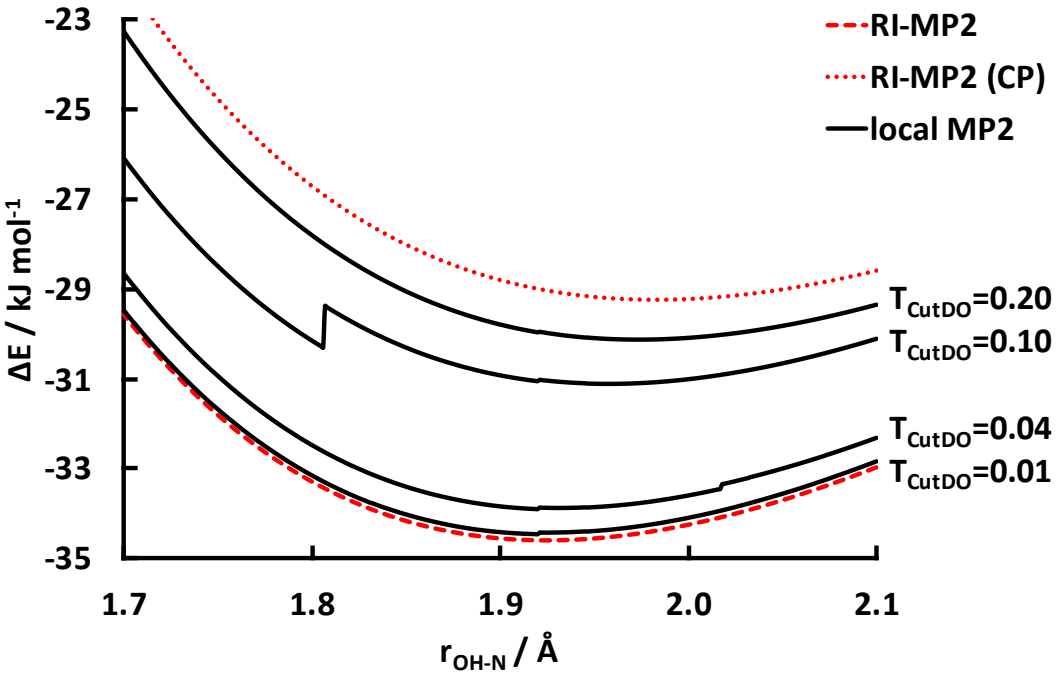

(a) PES of the dimer $MeOH \cdot MeNH_2$.

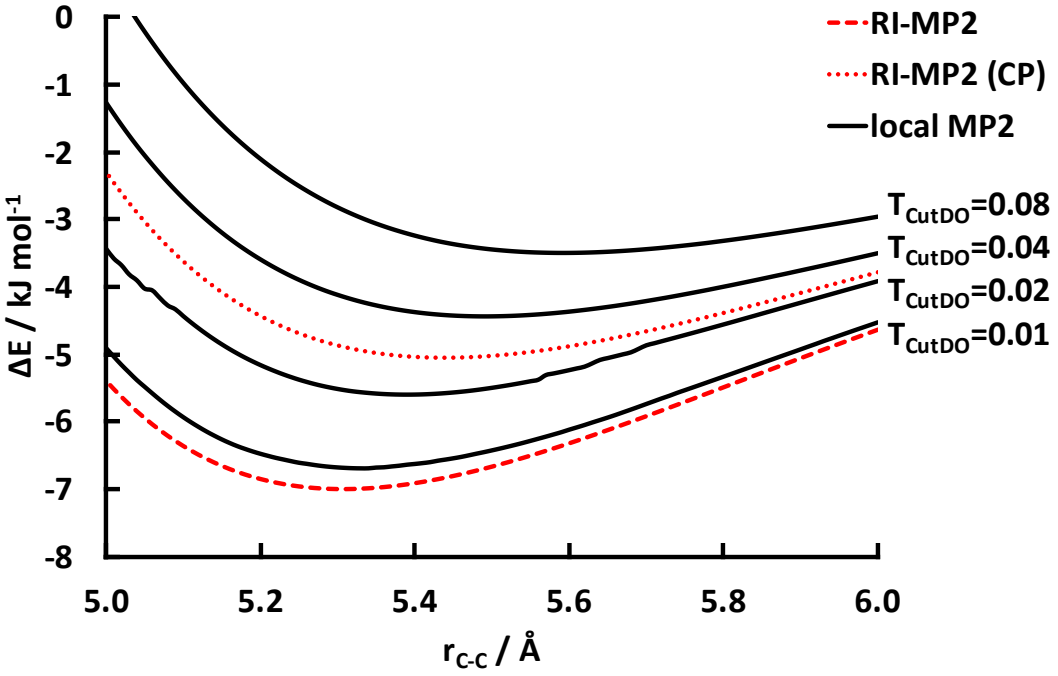

(b) PES of the neopentane dimer.

Figure 3.20: Potential energy surfaces calculated using DLPNO-MP2 with different domain selection thresholds T_{CutDO} are represented by black solid lines. For comparison, the red dashed lines show RI-MP2 energies, and the red dotted lines show counterpoise-corrected RI-MP2 energies. All values represent dimerisation energies relative to the separated monomers.

ter dimer with MP2 close to the basis set limit, obtaining an equilibrium distance of 290.5 pm to 290.7 pm between the two oxygen atoms. In much earlier work, Schütz and co-workers determined O···O distances using their local MP2 method with basis sets of triple-ζ or quadruple-ζ quality, which overestimate the complete basis set result by 2 pm to 5 pm.[220] Since their canonical MP2 results calculated with the same basis sets are in much better agreement with the numbers by Boese and co-workers, this supports our finding that small domains lead to a substantial overestimation of the hydrogen bond length.

- $MeOH \cdot MeNH_2$ dimer: with relatively large domains, DLPNO-MP2 predicts a slightly too short hydrogen bond for $T_{\mathrm{CutDO}} \leq 0.06$. This is an artefact of a small roughness in the potential energy surface, since the overall minimum at 192.0 pm coincides with a discontinuity of 14 μE_{h} in the energy. It is caused by a reassignment of the auxiliary function domains, and would therefore be present even if the PAO domains were not truncated altogether. On the other hand, unconstrained geometry optimisation of the $MeOH \cdot MeNH_2$ dimer, which includes the gradient and the step size among its convergence criteria, leads to very similar hydrogen bond lengths of 191.7 pm and 191.9 pm with RI-MP2 and DLPNO-MP2 using default thresholds, respectively.

  With reduced domain sizes the discontinuities become much larger, as shown in Figure 3.20a: with $T_{\mathrm{CutDO}} = 0.10$, PAO domain reassignment causes a step of 0.35 mE_{h} in the energy at a distance of approximately 1.8 Å.

- Neopentane dimer: DLPNO-MP2 with default thresholds is in good agreement with RI-MP2 for the distance between the centres of the monomers. The basis set incompleteness error with RI-MP2/def2-TZVP is 6 pm, whereas the counterpoise-corrected result overestimates the distance by 20 pm. Even the domain threshold $T_{\mathrm{CutDO}} = 0.02$, used as part of the "LoosePNO" settings, leads to a visible roughness in the potential energy surface (Figure 3.20b). Smaller domains cause errors of ca. 20 pm to 30 pm in the distance between the monomers.

While structures optimised using DLPNO-MP2 with default thresholds are in a reasonably good agreement with RI-MP2, the shortcomings of local MP2 with smaller domains are consistent with the literature. Liakos and Neese compared structures of alkane chains in hairpin conformations, which were optimised using different methods. These included geometries calculated with the local correlation method DF-LMP2 using the cc-pVTZ basis set by Lüttschwager and co-workers;[230] and equivalent structures optimised by Byrd and co-workers using RI-MP2 with the same basis set.[231] Distances between carbon atoms in the DF-LMP2 structures deviated by up to 0.5 Å from their RI-MP2 counterpart, which is 13 % of the interatomic distance. The authors argued that there are substantial errors in the coordinates obtained with DF-LMP2.[232]

Our results confirm the assumption that sufficiently small domains reduce the extent of the BSSE in the correlation energy, but without eliminating it completely. As demonstrated for non-covalently interacting systems, however, the overall truncation errors become very substantial, and can vastly exceed any errors that are inherent to basis set incompleteness or the MP2 method itself. On the other hand, DLPNO-MP2 reproduces RI-MP2 closely, including most of the BSSE. In our opinion, it is preferable to reproduce the canonical method with all its shortcomings, and to eliminate basis set artefacts systematically where necessary, rather than by cancellation of different errors. Moreover, it is possible to perform a basis set extrapolation of the gradient.[233] Explicitly correlated variants of local correlation methods have been developed successfully to perform energy calculations;[48, 58, 63] however, implementing an analytical gradient for such methods would likely amount to a difficult undertaking.

To conclude our case against local correlation methods with small domains, we will refer to the recent work by Dornbach and Werner, who reported difficulties performing geometry optimisations of some conjugated molecules: in particular, they found that large errors occur with small domains for 1,3,5-heptatriyne, and that optimisations are difficult to converge for anthracene.[91] To resolve the latter problem, the authors perform a symmetry adaption of the starting structure.

To examine if the same problems occur with DLPNO-MP2, we performed optimisa-

tions of these systems using identical starting geometries (obtained from the benchmark set by Friedrich and Hänchen[152]) and the same basis set (aug-cc-pVTZ[234] for the carbon atoms and cc-pVTZ[206] for the hydrogens). The DLPNO-MP2 calculations were performed with default thresholds. Reassuringly, the optimisations of both molecules converged within an identical number of steps as the respective RI-MP2 calculations, without needing to modify the starting structure. The deviations in any carbon-carbon bond length relative to the RI-MP2 structure did not exceed 0.04 pm, and were thus effectively negligible. This illustrates that combining large domains with pair natural orbitals paves an efficient and robust pathway towards obtaining accurate structures.

3.3.8 Computational performance of the DLPNO-MP2 gradient

To investigate the computational performance of the DLPNO-MP2 gradient, we performed single-point calculations and geometry optimisations of large systems. Wall-clock times for single-point energy and gradient calculations are presented in Table 3.9. The calculations were performed for cassyrane (structure from the ROT34 set[123]), sildenafil (structure from ref. [43]), BHS, DIAD and FLP from the LB12 set,[213] taxol and vancomycin (structures calculated with PBEh-3c from ref. [235]), and the host-guest completes C_{60}@catcher, morpholine@RA4, BQ@mcycle and DAAD@ADDA from the S30L test set.[236]

All calculations were performed using the def2-TZVP basis set and the RIJCOSX approximation. The GridX7 settings was used for chain-of-spheres-exchange (COSX) integration, as it is, in our experience, the least expensive option which is not prone to produce artefacts in optimised geometries. Nonetheless, it offers a substantial speedup over regular Hartree-Fock with basis sets of at least triple-ζ quality. To examine the behaviour of the code under realistic conditions, each calculation was performed on one cluster node with 24 CPU cores and 256 GB of memory; each process was permitted to use up to 8 GB of memory with the "MaxCore" setting in ORCA. A graphical representation of data is provided in Figure 3.21.

For smaller systems, the computational cost of gradient calculations with DLPNO-

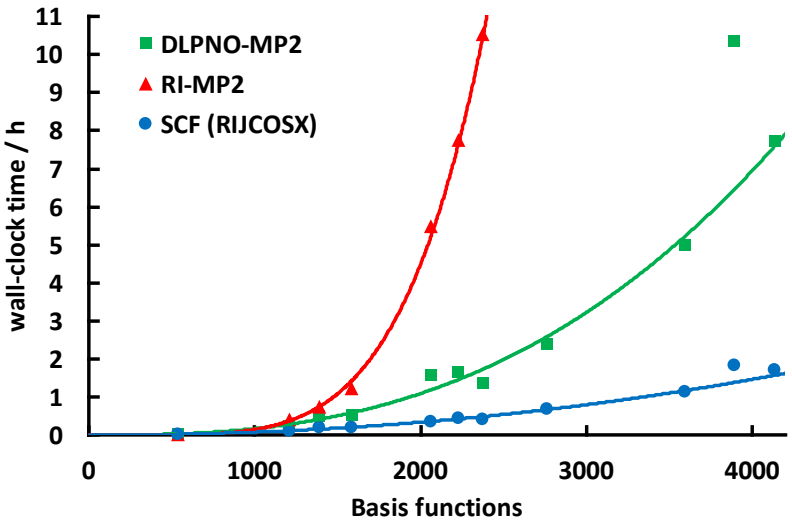

Figure 3.21: Wall-clock times to perform single-point energy and gradient calculations for representative systems on 24 CPU cores. DLPNO-MP2 and RI-MP2 data includes all steps in the respective energy and gradient calculations, but excludes the time for the SCF procedure. For comparison, the time for a single-point SCF energy and gradient calculation is shown by the blue line. All calculations were performed with def2-TZVP and RIJCOSX (GridX7). Default settings were used for DLPNO-MP2.

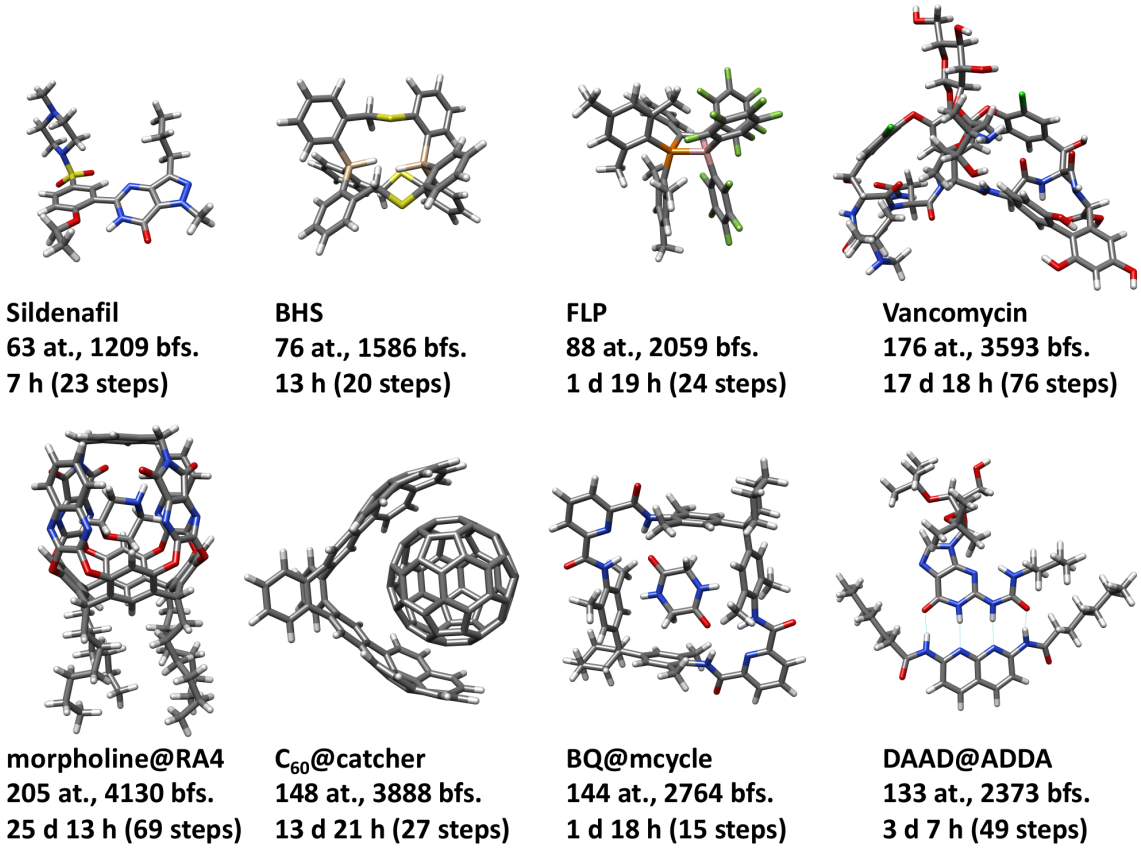

Figure 3.22: Wall-clock times to perform geometry optimisations of various systems. All calculations were performed with the def2-TZVP basis, "NormalPNO" settings and RIJCOSX (GridX7) using 24 parallel processes on one node.

System properties			Wall-clock time / s				
Name	Atoms	Basis functions	NormalPNO	TightPNO	RI-MP2	SCF iterations	SCF gradient
cassyrane	35	535	114	135	128	58	17
sildenafil	63	1209	889	1136	1490	291	76
DIAD	82	1392	1848	2392	2675	560	176
BHS	76	1586	1906	2559	4388	548	153
FLP	88	2059	5680	9091	19 742	1036	280
taxol	113	2228	5906	8453	27 959	1210	337
DAAD@ADDA	133	2373	4958	6143	37 915	1171	307
BQ@mcycle	144	2764	8697	12 216	-	1886	514
vancomycin	176	3593	17 969	23 774	-	3217	845
C_{60}@catcher	148	3888	37 255	86 394	-	5221	1374
morpholine@RA4	205	4130	27 817	42 391	-	4867	1301

Table 3.9: Timings for single-point energy and gradient calculations for representative systems on one node with 24 CPU cores. For DLPNO-MP2 and RI-MP2, the time to perform the SCF calculation has been excluded. All calculations were performed with the def2-TZVP basis and RIJCOSX (GridX7).

	% of the wall-clock time						
Name	Energy[I]	Pair loop (#passes)	$(p\tilde{\mu}'\|K)$, $(ip\|K)$	$(\mu\nu\|K)^x$	CP-L[II]	CP-SCF[III]	Fock gradient
cassyrane	13	11 (1)	1	1	0.7	41	29
BHS	17	17 (1)	2	1	0.3	43	17
FLP	18	36 (2)	2	1	0.6	30	10
C_{60}@catcher	20	38 (2)	3	1	0.4	28	8
morpholine@RA4	15	23 (2)	6	2	0.5	41	11

Table 3.10: Contributions of major steps to the overall computational cost of calculations with "NormalPNO" thresholds.
[I]Including all steps necessary to calculate the correlation energy, e.g. localising the orbitals and calculating $(i\tilde{\mu}'|K)$.
[II]Including diagonalisation of the Foster-Boys orbital Hessian.
[III]Including standalone Fock response evaluation.

MP2 is comparable to RI-MP2. Significant gains over RI-MP2 are made for sildenafil, which contains 63 atoms. For systems with around 80 to 90 atoms or more, the cost of the RI-MP2 calculations increases very rapidly.

Using DLPNO-MP2 with default thresholds, on the other hand, calculating the entire single-point gradient, including the SCF iterations, typically requires four to six times as long as a comparable calculation at the SCF level, even with the efficient RIJCOSX approximation. This permits single-point calculations for systems containing as many as 200 atoms to be performed at triple-ζ level within one working day. Increasing the accuracy level to "TightPNO" increases the cost by a factor of about 1.5 to 2.

Contributions of individual steps to the cost of the DLPNO-MP2 gradient are shown in Table 3.10. With "NormalPNO" settings, 40 % to 60 % of the time are needed to calculate the DLPNO-MP2 energy (including all necessary steps such as orbital localisation and the RI integral transformation), and to process the pair-specific contributions in the gradient calculation. With the given computational resources, calculations for systems containing up to ca. 80 atoms were performed with the memory-based algorithm, which passes all pairs only once, whereas for larger systems the code switched to the disk-based algorithm, which passes pairs twice.

Contracting the two-body density with the appropriate three-centre integrals (and derivatives thereof) amounts to a modest fraction of the overall cost at about 5 % to 10 %. Less than 1 % of the total time was needed for steps towards solving the CP-L equations; around 80 % to 90 % of that time was spent diagonalising the orbital Hessian of the Foster-Boys localisation criterion to remove potential singularities, and only the remaining fraction was needed for the actual CP-L solution.

Ca. 40 % to 60 % of the overall time were expended to calculate the Fock response, to solve the CP-SCF equations, and to compute the gradient of the Fock operator. These steps are identical in the DLPNO-MP2 and RI-MP2 gradients, and independent of any approximations taken for DLPNO-MP2 itself. On the other hand, choosing a technique that is efficient for Fock matrix formation and Fock response construction is beneficial for the overall performance of the DLPNO-MP2 gradient.

Figure 3.22 depicts structures of systems for which geometry optimisations were performed, and lists the elapsed wall-clock times. The optimisations were performed with default convergence settings ("NormalOpt") in redundant internal coordinates. With the exception of the C_{60}@catcher complex, which consists of very rigid fragments, we used additional features to enhance the convergence behaviour of the geometry optimisations. First, automatic trust radius adjustment was specified with a starting value of 0.1 a.u. Second, the newly implemented "AddExtraBonds" feature of ORCA [C. Riplinger, 2018] was used to enforce sufficient connectivity in redundant internal coordinates: additional bonds were added automatically, so that all atoms within a distance of 5 Å were connected by a path of no more than 8 bonds. This feature was incorporated in ORCA in order to reduce oscillations of molecular fragments, which occur in optimisations of large systems with methods such as density functional theory or semiempirical approaches; it is not specific to DLPNO-MP2. The results show that MP2 geometry optimisations of systems containing 100 to 200 atoms can be performed with a triple-ζ basis within a timespan of a few days to a few weeks on a single cluster node.

While they are hardly representative examples for actual applications, linear alkane chains are particularly suited to investigate the scaling behaviour of the code with system size. We have performed single-point energy and gradient calculations with the def2-TZVP basis. As the COSX integration in the CP-SCF solver incurred very high memory demands for chains with more than 100 carbon atoms, the RIJONX method was used to solve the SCF and CP-SCF equations instead: it employs the RI approximation for the Coulomb integrals in the Fock operator, but applies only conventional screening techniques for the exchange integrals.

Figure 3.23 shows results for timings calculated using eight parallel processes on one compute node with 128 GB of memory; each processes was restricted to occupy up to 12 GB of memory. The RI-MP2 method incurs a very steep increase in its cost for chains containing more than 20 carbon atoms. Indeed, calculating the gradient for $C_{50}H_{102}$ with RI-MP2 requires as much time as for $C_{200}H_{402}$ with DLPNO-MP2 (Figure 3.23a). Processing all pair-specific quantities is associated with a linearly scaling cost (Figure 3.23b),

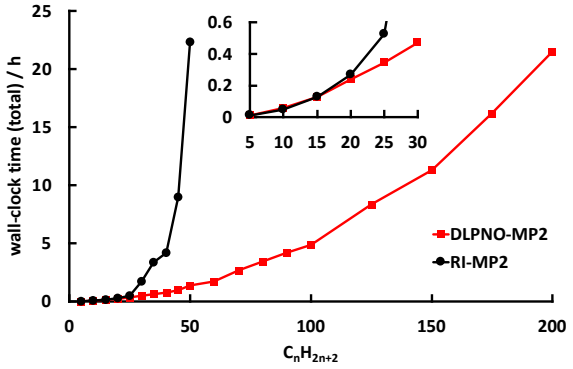

(a) Total time to calculate the single-point energy and gradient with DLPNO-MP2, in comparison to RI-MP2.

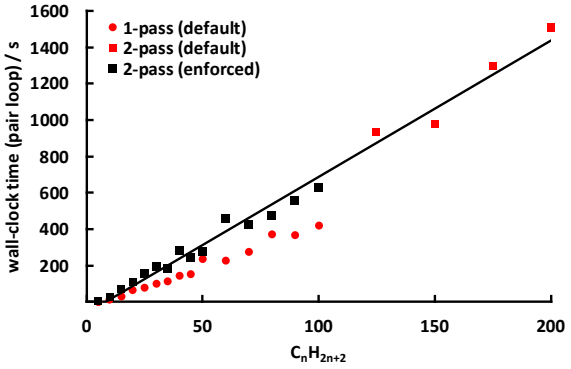

(b) Time to process the pair-specific quantities in the DLPNO-MP2 gradient. Circles show the time for the one-pass algorithm (if applicable), squares the time for the two-pass algorithm.

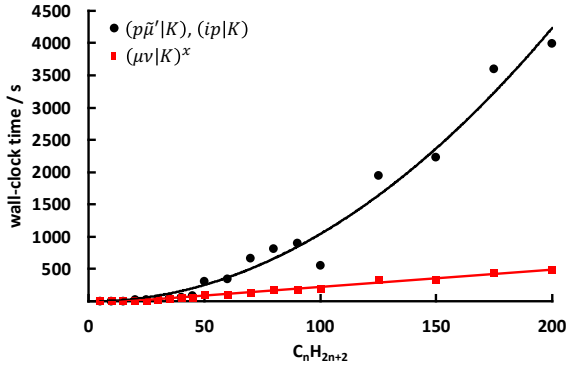

(c) Time to perform the integral-direct contraction of the two-body density with the three-centre integrals, and to calculate the RI gradient.

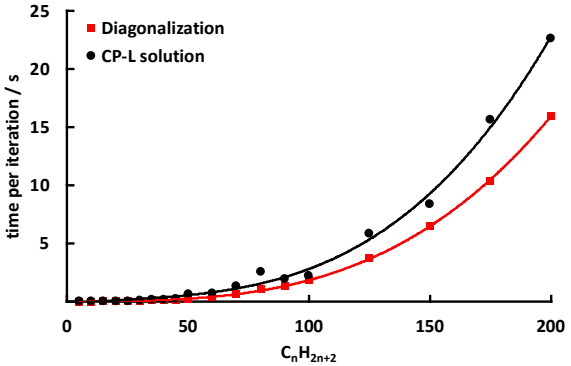

(d) Time per iteration to diagonalise the localisation function orbital Hessian with the Davidson algorithm, and to perform one conjugate gradient step to solve the coupled-perturbed localisation equations.

Figure 3.23: Scaling behaviour of the DLPNO-MP2 gradient for linear alkane chains, calculated with the def2-TZVP basis and RIJONX on eight CPU cores.

as the number of screened pairs grows linearly. Up to $C_{100}H_{202}$, the program was able to store the two-body density in memory, thus requiring only one pass over all pairs.

As discussed previously, the cost to contract the two-body density with the integrals $(p\tilde{\mu}'|K)$ and $(ip|K)$ scales quadratically, whereas the RI integral gradient $(\mu\nu|K)^x$ scales linearly (Figure 3.23c). We experienced difficulties to converge the Davidson diagonalisation of the localisation Hessian for very long alkane chains, presumably due to a large number of similar eigenvalues. This was resolved by reducing the number of requested roots from the default value of 32 to eight: even though the localisation orbital Hessian of an alkane chain is not singular, this still permitted us to compute the cost scaling.

	Insulin	Crambin
Atoms	787	644
Basis	cc-pVDZ	def2-TZVP
Basis functions	7604	12 075
SCF / h	[I]17	[I]57
DLPNO-MP2 / h	[I]69	[II]194
DLPNO-MP2 steps / %		
Energy[III]	25	11
Pair loop	10	6
$(p\tilde{\mu}'\|K)$, $(ip\|K)$	6	9
$(\mu\nu\|K)^x$	2	3
Hessian diagonalisation	17	1
CP-L	1	0.2
CP-SCF[IV]	32	64
Fock gradient	5	6

Table 3.11: Times to perform a single-point energy and gradient calculation for insulin and crambin. Each calculation was executed on one node with 24 CPU cores and 384 GB of memory.
[I]24 cores used
[II]12 cores used
[III]Including all necessary steps to calculate the DLPNO-MP2 correlation energy.
[IV]Including standalone Fock response evaluation.

Figure 3.23d shows the time per iteration for the Davidson solver to diagonalise the localisation Hessian, and the time per step to solve the CP-L equations with the conjugate gradient method, both of which scale cubically with the system size.

Finally, two large-scale single-point gradient evaluations were performed to demonstrate the capabilities of the implementation. Using the divide-expand-consolidate RI-MP2 (DEC-RI-MP2) method, Bykov and co-workers calculated the gradient of insulin ($C_{257}H_{382}N_{65}O_{77}S_6^-$) with the cc-pVDZ basis in 10 h on 6000 nodes of a supercomputer.[103]

We repeated the calculation using the atomic coordinates from their work. Two-electron integrals in the SCF and CP-SCF procedures were subject to a regular treatment. On one compute node with 24 processor cores and 384 GB of memory, the entire DLPNO-MP2 calculation with "NormalPNO" thresholds finished in 69 h (see Table 3.11). Further 17 h were spent on the Hartree-Fock calculation. There is a reassuring agreement with the gradient published by Bykov and co-workers: with a root mean square deviation of

$6 \times 10^{-4}\, E_\mathrm{h}\, {a_0}^{-1}$, the two gradients agree within the accuracy range that was reported for the DEC-RI-MP2 gradient.

In addition, we calculated the gradient for crambin ($C_{202}H_{317}N_{55}O_{64}S_6{}^{2+}$) with the def2-TZVP basis using "NormalPNO" thresholds. The SCF calculation with the RIJONX approximation finished in 57 h with 24 parallel processes. Because of its larger memory demands, the subsequent DLPNO-MP2 calculation was performed with 12 parallel processes on a compute node with 384 GB of memory. This calculation finished in eight days. Almost two thirds of the time were required to compute the Fock response and to solve the CP-SCF equations with the RIJONX approximation (Table 3.11).

Chapter 4

Conclusion

The first part of this thesis describes the implementation of DLPNO-MP2.[43] It is closely related to the previously developed DLPNO-CCSD method,[37] but improves several technical aspects. A major bottleneck in large-scale calculations with DLPNO-CCSD used to be the transformation of the three-index RI integrals, which we replaced with a formally linear scaling routine. Reduced scaling transformation of integrals was also discussed by Werner and co-workers.[19, 55] Interrelations between sparse quantities are complex to discuss and error-prone to implement, but this task is greatly facilitated by the sparse maps formalism.

By means of the differential overlap integral between MOs and PAOs, a new domain construction scheme was introduced, which is based upon the spatial extent of both the occupied and the virtual functions. As it was discovered that the prescreening method used originally with DLPNO-CCSD significantly underestimates the energies of many orbital pairs, a new procedure was introduced that significantly reduces the associated error.

The DLPNO-MP2 method shares many similarities with the PNO-LMP2 method by Werner and co-workers, but also a number of differences.[55] DLPNO-MP2 expands the PNOs directly in a basis of PAOs, while PNO-LMP2 uses OSVs as an intermediate basis. The domain selection scheme in PNO-LMP2 is based on populations and interatomic connectivity. An important conceptual difference concerns the threshold selection: whereas

standard settings for DLPNO-MP2 ("NormalPNO") have been chosen to reproduce ca. 99.9 % of the total RI-MP2 correlation energy for mid-sized molecules, the PNO-LMP2 method of Werner and co-workers recovers 99.7 % of the canonical correlation energy by default. In principle, both methods are systematically improvable by choosing tighter thresholds. Werner and co-workers advocate the viewpoint that local truncation errors can and should be removed together with the basis set incompleteness error through an F12 correction,[55] but this opinion is disputed by other authors.[48, 237] In addition, derivatives of explicitly correlated methods are complicated to implement in general.[238]

A simple unrestricted variant of DLPNO-MP2 was introduced for open-shell calculations, with a PNO construction scheme based on the work of Hansen and co-workers.[158] A disadvantage of the method is that the pair natural orbitals are inconsistent with the closed-shell scheme. As a consequence, the energies of both closed-shell and open-shell species need to be calculated with the unrestricted formalism when targeting energy differences. An approximately fourfold computational expense is required to obtain an almost comparable accuracy as with the RHF-based method. In this regard, PNO construction schemes working with a restricted open-shell reference offer a better trade-off between accuracy and computational expense.[46, 61]

The core part of this thesis is the implementation of the analytical gradient for the closed-shell DLPNO-MP2 method. Complete derivatives were taken for all energy contributions, leading to the exact gradient of the DLPNO-MP2 energy. To the best of our knowledge, our publications in ref. [110, 111] were the first to describe the analytical derivatives for a PNO-based method without neglecting terms or introducing further approximations.

The impact of individual Lagrangian constraints and derivative contributions was examined with electric field gradient calculations and geometry optimisations of several systems. While the relevance of the localisation constraint was well-known beforehand,[89] an appropriate treatment of PNO relaxation can also be necessary to calculate sensitive first-order properties accurately. Since the correction term for PNO truncation increases the accuracy of the energy, its derivative improves optimised geometries somewhat. On

the other hand, the correction for screened out pairs contributes relatively little to the total gradient or the density, possibly as a consequence of the very conservative truncation criteria.

Localised orbitals of systems belonging to specific symmetry groups may be continuously degenerate. In those cases, the second derivative matrix of the localisation criterion with respect to orbital variations has one or several eigenvalues of zero, which causes singular coupled-perturbed localisation equations. We circumvented the ensuing difficulties by introducing a modification of the localisation constraint in the Lagrangian. Since this finding is not directly related to the PNO approximation or to other truncations that are specific to DLPNO-MP2, it is of general relevance for derivatives of local correlation methods that are not invariant to the choice of localised orbitals.

Testing geometry optimisations extensively shows that RI-MP2 equilibrium structures are reproduced accurately. The investigated systems span a wide variety of bonding situations, predominantly between main group elements. Errors in the lengths of covalent bonds are usually below 0.1 pm with default thresholds. In more complicated situations with a substantial influence of weak interactions on the structure, interatomic distances are typically reproduced with errors of up to 1 % using "NormalPNO" settings and up to 0.3 % with "TightPNO" settings. Molecular sizes are usually slightly overestimated in comparison with RI-MP2.

Discontinuities of the potential energy surface represent a well-known problem of local correlation methods.[239] To circumvent the ensuing difficulties, Werner and co-workers suggested domain merging as a workaround.[240] Subotnik and Head-Gordon proposed introducing smoothing functions into residual equations for amplitudes.[73, 241] While small discontinuities are present in potential energy surfaces calculated with DLPNO-MP2, owing to the large domains they are usually on a scale of a few μE_h and can be reduced systematically by choosing tighter thresholds. Reassuringly, our geometry optimisations were not subject to significant convergence problems when performed with "NormalPNO" or "TightPNO" settings, while "LoosePNO" cannot be recommended for broad usage. This is not unlike choosing an appropriate integration grid for the exchange-

correlation functional in DFT calculations, or for the exchange integrals calculated with the COSX method. When difficulties with geometry optimisations occurred despite adequate threshold settings, they were often connected either to the starting structure or to the geometry optimiser.

The time needed to perform a DLPNO-MP2 gradient calculation for modestly sized systems is comparable to RI-MP2. With increasing system size, however, the cost remains within the same order of magnitude as for a Hartree-Fock calculation: even with the efficient RIJCOSX approximation for the Coulomb and exchange integrals in the Fock matrix, computing the energy and gradient with default DLPNO settings typically requires 4-5 times as long as a comparable calculation at SCF level. We were able to perform DLPNO-MP2 optimisations of systems containing more than 100 atoms in a few days, and up to 200 atoms with ca. 4000 basis functions in a few weeks with the def2-TZVP basis on a single cluster node. The most demanding single-point gradient calculation was completed for the small protein crambin with the def2-TZVP basis, containing 644 atoms and over 12 000 basis functions.

Unlike the impressive large-scale computations performed with the divide-expand-consolidate method on thousands of supercomputer nodes,[103] the calculations reported in this work used regular cluster hardware. In comparison with methods that expand the virtual space directly in projected atomic orbitals, a higher accuracy and greater robustness of the results can be expected for DLPNO-MP2. While there is a popular belief that small domains reduce the BSSE,[219–221] they also lead to large errors and markedly discontinuous potential energy surfaces. In combination with pair natural orbitals, DLPNO-MP2 uses domain sizes that would be very costly or prohibitive otherwise.

In a very recent publication, Yang and co-workers reported the analytical gradient for the OSV-MP2 method, which expands the truncated orbital-specific virtuals in the full basis of virtual molecular orbitals.[113] The working equations are derived directly via the appropriate response equations, which is more similar to the Z-vector method by Handy and Schäfer.[159] Relaxation of the OSVs is accounted for in a comparable way to the approach for the PNOs in the DLPNO-MP2 gradient. The conclusions of Yang and

co-workers about the accuracy of DLPNO-MP2 geometries are potentially misleading, as they employed the RIJCOSX approximation with unreported grid settings in their own DLPNO-MP2 calculations (see Section 3.3.5.2). Both the DLPNO-MP2 and OSV-MP2 gradients were found to offer substantial computational savings over RI-MP2 for systems with up to 116 atoms, while the cost of DLPNO-MP2 scales more favourably for glycine chains in the reported timings.

Benchmark sets for local correlation methods need to include systems that are not only varied and challenging, but that also contain a sufficiently large number of atoms to produce meaningful results. In the case of DLPNO-MP2, the local approximations do not become fully effective for molecules containing less than ca. 20 to 30 atoms. Results obtained from calculations on significantly smaller systems may underestimate errors encountered in a more realistic scenario, and thereby also distort a statistical analysis.

While the MP2 method often falls short of achieving chemical accuracy, it is the building component of empirical schemes such as SCS-MP2 or double-hybrid density functionals. In particular, DHDFs were shown to outperform lower DFT rungs consistently for main group compounds.[121] For this reason, one of the likeliest application scenarios of this work is to make gradient calculations with double-hybrid DFT feasible for larger systems. Preliminary results for geometry optimisations suggest that the errors incurred by the DLPNO approximations are comparable to or smaller than for plain DLPNO-MP2, and significantly smaller than the intrinsic errors of DHDFs.

Despite the continuously evolving power of broadly available computational systems, in the near future the DLPNO-MP2 gradient is most likely to remain useful for geometry optimisations of structures containing ca. 70 to 150 main group element atoms. Several such calculations have been performed with a triple-zeta basis in a few days or less, and are therefore within reach for routine calculations if particularly accurate results are desired. Another possible application area is to calculate properties for large systems.

Appendix A

Data tables: DLPNO-MP2 energy

A.1 Threshold selection

Tables A.1 to A.3 show the correlation energy calculated with different PNO truncation thresholds T_{CutPNO}. All other truncation thresholds were set to zero. A graphical representation of the data is provided in Figure 2.3.

Correlation energies obtained with different fitting domain truncation thresholds are shown in Table A.4. In those calculations, the PNO truncation threshold was set to its default value of $T_{\mathrm{CutPNO}} = 1 \times 10^{-8}$, while the remaining truncation thresholds were left at a value of zero. The data was plotted in Figure 2.4.

Table A.5 lists correlation energies calculated with different domain truncation thresholds T_{CutDO}. The PNO and fitting domain cutoffs were set to their default values of $T_{\mathrm{CutPNO}} = 1 \times 10^{-8}$ and $T_{\mathrm{CutMKN}} = 1 \times 10^{-3}$, while the remaining truncation thresholds were set to zero. A plot of the data is provided in Figure 2.5.

T_{CutPNO}	def2-TZVP def2-TZVP/C		def2-TZVPD def2-TZVP/C		def2-TZVPD aug-cc-pVTZ/C	
	E_{C} / E_{h}	%	E_{C} / E_{h}	%	E_{C} / E_{h}	%
$10^{-6.5}$	−5.838 439 0	99.4349	−5.878 387 4	99.4186	−5.879 051 3	99.4195
$10^{-7.0}$	−5.855 111 7	99.7189	−5.895 528 9	99.7086	−5.896 188 2	99.7093
$10^{-7.5}$	−5.863 327 2	99.8588	−5.904 114 4	99.8538	−5.904 749 9	99.8541
$10^{-8.0}$	−5.867 394 9	99.9281	−5.908 324 0	99.9250	−5.908 938 9	99.9249
$10^{-8.5}$	−5.869 460 7	99.9633	−5.910 475 6	99.9613	−5.911 085 7	99.9613
$10^{-9.0}$	−5.870 518 0	99.9813	−5.911 583 3	99.9801	−5.912 192 1	99.9800
$10^{-9.5}$	−5.871 059 1	99.9905	−5.912 155 9	99.9898	−5.912 765 7	99.9897
$10^{-10.0}$	−5.871 334 9	99.9952	−5.912 449 8	99.9947	−5.913 061 1	99.9947
$10^{-10.5}$	−5.871 474 2	99.9976	−5.912 600 7	99.9973	−5.913 213 6	99.9972
$10^{-11.0}$	−5.871 545 1	99.9988	−5.912 678 8	99.9986	−5.913 292 8	99.9986
$10^{-11.5}$	−5.871 580 8	99.9994	−5.912 718 6	99.9993	−5.913 333 5	99.9993
$10^{-12.0}$	−5.871 598 4	99.9997	−5.912 739 0	99.9996	−5.913 354 3	99.9996

(a) Correlation energy $E_{\mathrm{DLPNO-MP2}}$, omitting the correction for PNO truncation.

T_{CutPNO}	def2-TZVP def2-TZVP/C		def2-TZVPD def2-TZVP/C		def2-TZVPD aug-cc-pVTZ/C	
	E_{C} / E_{h}	%	E_{C} / E_{h}	%	E_{C} / E_{h}	%
$10^{-6.5}$	−5.859 414 0	99.7922	−5.900 210 0	99.7877	−5.900 814 4	99.7876
$10^{-7.0}$	−5.864 313 2	99.8756	−5.905 247 3	99.8729	−5.905 874 5	99.8731
$10^{-7.5}$	−5.867 184 7	99.9245	−5.908 205 9	99.9230	−5.908 812 6	99.9228
$10^{-8.0}$	−5.869 021 5	99.9558	−5.910 064 6	99.9544	−5.910 663 8	99.9541
$10^{-8.5}$	−5.870 142 7	99.9749	−5.911 208 3	99.9737	−5.911 809 7	99.9735
$10^{-9.0}$	−5.870 795 6	99.9860	−5.911 885 0	99.9852	−5.912 489 4	99.9850
$10^{-9.5}$	−5.871 168 6	99.9924	−5.912 275 7	99.9918	−5.912 883 6	99.9917
$10^{-10.0}$	−5.871 377 1	99.9959	−5.912 496 4	99.9955	−5.913 106 9	99.9954
$10^{-10.5}$	−5.871 490 4	99.9978	−5.912 618 8	99.9976	−5.913 231 2	99.9975
$10^{-11.0}$	−5.871 551 2	99.9989	−5.912 685 6	99.9987	−5.913 299 5	99.9987
$10^{-11.5}$	−5.871 583 0	99.9994	−5.912 721 1	99.9993	−5.913 336 0	99.9993
$10^{-12.0}$	−5.871 599 2	99.9997	−5.912 740 0	99.9996	−5.913 355 2	99.9996

(b) Correlation energy $E_{\mathrm{DLPNO-MP2}} + \Delta E_{\mathrm{PNO}}$, which includes the correction for PNO truncation.

Table A.1: Correlation energy calculated for sildenafil using different thresholds T_{CutPNO}. No other truncations were applied. In addition, the percentage of the RI-MP2 correlation energy recovered is shown.

T_{CutPNO}	def2-TZVP def2-TZVP/C		def2-TZVPD def2-TZVP/C		def2-TZVPD aug-cc-pVTZ/C	
	E_{C} / E_{h}	%	E_{C} / E_{h}	%	E_{C} / E_{h}	%
$10^{-6.5}$	−4.345 718 7	99.3260	−4.370 899 0	99.3024	−4.371 571 2	99.3029
$10^{-7.0}$	−4.360 462 3	99.6630	−4.386 225 0	99.6506	−4.386 883 6	99.6507
$10^{-7.5}$	−4.367 793 3	99.8306	−4.393 843 6	99.8236	−4.394 510 6	99.8240
$10^{-8.0}$	−4.371 323 9	99.9113	−4.397 540 2	99.9076	−4.398 196 1	99.9077
$10^{-8.5}$	−4.373 197 6	99.9541	−4.399 484 2	99.9518	−4.400 144 4	99.9519
$10^{-9.0}$	−4.374 153 3	99.9759	−4.400 486 0	99.9745	−4.401 140 2	99.9746
$10^{-9.5}$	−4.374 657 3	99.9875	−4.401 017 0	99.9866	−4.401 667 5	99.9865
$10^{-10.0}$	−4.374 913 8	99.9933	−4.401 290 7	99.9928	−4.401 941 7	99.9928
$10^{-10.5}$	−4.375 050 3	99.9964	−4.401 435 9	99.9961	−4.402 087 3	99.9961
$10^{-11.0}$	−4.375 124 0	99.9981	−4.401 514 7	99.9979	−4.402 166 6	99.9979
$10^{-11.5}$	−4.375 163 7	99.9990	−4.401 557 7	99.9989	−4.402 210 3	99.9989
$10^{-12.0}$	−4.375 184 7	99.9995	−4.401 581 1	99.9994	−4.402 234 1	99.9994

(a) Correlation energy $E_{\mathrm{DLPNO-MP2}}$, omitting the correction for PNO truncation.

T_{CutPNO}	def2-TZVP def2-TZVP/C		def2-TZVPD def2-TZVP/C		def2-TZVPD aug-cc-pVTZ/C	
	E_{C} / E_{h}	%	E_{C} / E_{h}	%	E_{C} / E_{h}	%
$10^{-6.5}$	−4.364 374 3	99.7524	−4.390 489 3	99.7474	−4.391 133 6	99.7473
$10^{-7.0}$	−4.368 777 4	99.8531	−4.395 016 9	99.8503	−4.395 662 8	99.8501
$10^{-7.5}$	−4.371 260 0	99.9098	−4.397 539 1	99.9076	−4.398 183 9	99.9074
$10^{-8.0}$	−4.372 802 7	99.9451	−4.399 120 3	99.9435	−4.399 765 1	99.9433
$10^{-8.5}$	−4.373 813 2	99.9682	−4.400 148 5	99.9669	−4.400 801 7	99.9669
$10^{-9.0}$	−4.374 399 2	99.9816	−4.400 754 6	99.9806	−4.401 404 4	99.9806
$10^{-9.5}$	−4.374 753 1	99.9896	−4.401 122 6	99.9890	−4.401 770 9	99.9889
$10^{-10.0}$	−4.374 950 7	99.9942	−4.401 331 4	99.9938	−4.401 981 5	99.9937
$10^{-10.5}$	−4.375 064 1	99.9968	−4.401 451 3	99.9965	−4.402 102 3	99.9964
$10^{-11.0}$	−4.375 129 1	99.9982	−4.401 520 3	99.9980	−4.402 172 1	99.9980
$10^{-11.5}$	−4.375 165 5	99.9991	−4.401 559 8	99.9989	−4.402 212 3	99.9989
$10^{-12.0}$	−4.375 185 3	99.9995	−4.401 581 9	99.9994	−4.402 234 8	99.9994

(b) Correlation energy $E_{\mathrm{DLPNO-MP2}} + \Delta E_{\mathrm{PNO}}$, which includes the correction for PNO truncation.

Table A.2: Correlation energy calculated for the anthrecene dimer using different thresholds T_{CutPNO}. No other truncations were applied. In addition, the percentage of the RI-MP2 correlation energy recovered is shown.

T_{CutPNO}	def2-TZVPD def2-TZVP/C		def2-TZVPD aug-cc-pVTZ/C	
	E_{C} / E_{h}	%	E_{C} / E_{h}	%
$10^{-6.5}$	−6.164 746 0	99.4964	−6.164 902 1	99.4975
$10^{-7.0}$	−6.180 405 7	99.7491	−6.180 537 3	99.7498
$10^{-7.5}$	−6.188 222 2	99.8753	−6.188 346 2	99.8758
$10^{-8.0}$	−6.192 057 2	99.9372	−6.192 147 4	99.9372
$10^{-8.5}$	−6.193 969 8	99.9680	−6.194 052 3	99.9679
$10^{-9.0}$	−6.194 930 0	99.9835	−6.195 012 7	99.9834
$10^{-9.5}$	−6.195 430 0	99.9916	−6.195 515 0	99.9915
$10^{-10.0}$	−6.195 684 3	99.9957	−6.195 770 6	99.9957
$10^{-10.5}$	−6.195 814 1	99.9978	−6.195 901 4	99.9978
$10^{-11.0}$	−6.195 879 9	99.9989	−6.195 968 3	99.9989
$10^{-11.5}$	−6.195 914 0	99.9994	−6.196 002 9	99.9994
$10^{-12.0}$	−6.195 931 4	99.9997	−6.196 020 7	99.9997

(a) Correlation energy $E_{\mathrm{DLPNO-MP2}}$, omitting the correction for PNO truncation.

T_{CutPNO}	def2-TZVPD def2-TZVP/C		def2-TZVPD aug-cc-pVTZ/C	
	E_{C} / E_{h}	%	E_{C} / E_{h}	%
$10^{-6.5}$	−6.185 037 6	99.8239	−6.185 153 1	99.8243
$10^{-7.0}$	−6.189 477 7	99.8955	−6.189 573 6	99.8957
$10^{-7.5}$	−6.192 043 0	99.9370	−6.192 128 1	99.9369
$10^{-8.0}$	−6.193 659 2	99.9630	−6.193 731 5	99.9628
$10^{-8.5}$	−6.194 641 9	99.9789	−6.194 714 2	99.9786
$10^{-9.0}$	−6.195 211 7	99.9881	−6.195 289 6	99.9879
$10^{-9.5}$	−6.195 542 2	99.9934	−6.195 624 9	99.9933
$10^{-10.0}$	−6.195 728 0	99.9964	−6.195 813 4	99.9964
$10^{-10.5}$	−6.195 830 9	99.9981	−6.195 918 0	99.9980
$10^{-11.0}$	−6.195 886 3	99.9990	−6.195 974 6	99.9990
$10^{-11.5}$	−6.195 916 4	99.9995	−6.196 005 3	99.9995
$10^{-12.0}$	−6.195 932 2	99.9997	−6.196 021 5	99.9997

(b) Correlation energy $E_{\mathrm{DLPNO-MP2}} + \Delta E_{\mathrm{PNO}}$, which includes the correction for PNO truncation.

Table A.3: Correlation energy calculated for the ATP^{4-} anion using different thresholds T_{CutPNO}. No other truncations were applied. In addition, the percentage of the RI-MP2 correlation energy recovered is shown.

T_{CutMKN}	def2-TZVP def2-TZVP/C		def2-TZVPD def2-TZVP/C		def2-TZVPD aug-cc-pVTZ/C	
	E_{C} / E_{h}	%	E_{C} / E_{h}	%	E_{C} / E_{h}	%
$10^{-2.0}$	−5.866 583 8	99.9585	−5.906 067 5	99.9324	−5.908 073 1	99.9562
$10^{-2.5}$	−5.868 316 3	99.9880	−5.909 574 3	99.9917	−5.910 412 1	99.9957
$10^{-3.0}$	−5.868 756 7	99.9955	−5.909 805 4	99.9956	−5.910 524 1	99.9976
$10^{-3.5}$	−5.868 922 8	99.9983	−5.909 953 9	99.9981	−5.910 603 7	99.9990
$10^{-4.0}$	−5.868 977 4	99.9992	−5.910 023 7	99.9993	−5.910 635 3	99.9995
0	−5.869 021 5	100.0000	−5.910 064 6	100.0000	−5.910 663 8	100.0000

(a) Energies for sildenafil.

T_{CutMKN}	def2-TZVP def2-TZVP/C		def2-TZVPD def2-TZVP/C		def2-TZVPD aug-cc-pVTZ/C	
	E_{C} / E_{h}	%	E_{C} / E_{h}	%	E_{C} / E_{h}	%
$10^{-2.0}$	−4.369 661 6	99.9282	−4.396 899 9	99.9495	−4.398 789 5	99.9778
$10^{-2.5}$	−4.372 263 9	99.9877	−4.398 577 8	99.9877	−4.399 521 8	99.9945
$10^{-3.0}$	−4.372 637 0	99.9962	−4.398 936 2	99.9958	−4.399 691 4	99.9983
$10^{-3.5}$	−4.372 745 5	99.9987	−4.399 029 7	99.9979	−4.399 723 3	99.9990
$10^{-4.0}$	−4.372 773 3	99.9993	−4.399 107 6	99.9997	−4.399 751 5	99.9997
0	−4.372 802 7	100.0000	−4.399 120 3	100.0000	−4.399 765 1	100.0000

(b) Energies for the anthracene dimer.

T_{CutMKN}	def2-TZVPD def2-TZVP/C		def2-TZVPD aug-cc-pVTZ/C	
	E_{C} / E_{h}	%	E_{C} / E_{h}	%
$10^{-2.0}$	−6.192 282 5	99.9778	−6.193 104 7	99.9899
$10^{-2.5}$	−6.193 131 5	99.9915	−6.193 474 3	99.9958
$10^{-3.0}$	−6.193 408 2	99.9959	−6.193 610 5	99.9980
$10^{-3.5}$	−6.193 541 4	99.9981	−6.193 673 3	99.9991
$10^{-4.0}$	−6.193 623 3	99.9994	−6.193 711 7	99.9997
0	−6.193 659 2	100.0000	−6.193 731 5	100.0000

(c) Energies for the ATP^{4-} anion.

Table A.4: Correlation energies calculated with different thresholds T_{CutMKN}. The PNO threshold was set to the standard value $T_{\mathrm{CutPNO}} = 1 \times 10^{-8}$, but no other truncation were applied. The percentages are those of the DLPNO-MP2 energy with $T_{\mathrm{CutMKN}} = 0$ and the specified T_{CutPNO}.

T_{CutDO}	def2-TZVP def2-TZVP/C		def2-TZVPD def2-TZVP/C		def2-TZVPD aug-cc-pVTZ/C	
	E_{C} / E_{h}	%	E_{C} / E_{h}	%	E_{C} / E_{h}	%
$10^{-1.50}$	−5.857 221 5	99.8034	−5.894 660 1	99.7437	−5.895 271 0	99.7419
$10^{-1.75}$	−5.864 982 8	99.9357	−5.903 002 1	99.8849	−5.903 665 8	99.8840
$10^{-2.00}$	−5.867 185 4	99.9732	−5.905 739 4	99.9312	−5.906 419 5	99.9306
$10^{-2.25}$	−5.868 201 8	99.9905	−5.907 873 0	99.9673	−5.908 572 2	99.9670
$10^{-2.50}$	−5.868 571 8	99.9968	−5.908 934 0	99.9853	−5.909 643 9	99.9851
$10^{-2.75}$	−5.868 691 3	99.9989	−5.909 366 0	99.9926	−5.910 078 7	99.9925
$10^{-3.00}$	−5.868 735 4	99.9996	−5.909 607 1	99.9966	−5.910 322 4	99.9966
0	−5.868 756 7	100.0000	−5.909 805 4	100.0000	−5.910 524 1	100.0000

(a) Energies for sildenafil.

T_{CutDO}	def2-TZVP def2-TZVP/C		def2-TZVPD def2-TZVP/C		def2-TZVPD aug-cc-pVTZ/C	
	E_{C} / E_{h}	%	E_{C} / E_{h}	%	E_{C} / E_{h}	%
$10^{-1.50}$	−4.358 174 6	99.6693	−4.380 173 1	99.5735	−4.380 814 4	99.5709
$10^{-1.75}$	−4.367 982 2	99.8935	−4.392 401 3	99.8514	−4.393 108 8	99.8504
$10^{-2.00}$	−4.371 472 3	99.9734	−4.396 432 6	99.9431	−4.397 160 7	99.9425
$10^{-2.25}$	−4.372 289 9	99.9921	−4.398 008 1	99.9789	−4.398 752 0	99.9786
$10^{-2.50}$	−4.372 537 8	99.9977	−4.398 585 2	99.9920	−4.399 335 1	99.9919
$10^{-2.75}$	−4.372 618 6	99.9996	−4.398 883 2	99.9988	−4.399 636 1	99.9987
$10^{-3.00}$	−4.372 634 4	99.9999	−4.398 932 5	99.9999	−4.399 687 6	99.9999
0	−4.372 637 0	100.0000	−4.398 936 2	100.0000	−4.399 691 4	100.0000

(b) Energies for the anthracene dimer.

T_{CutDO}	def2-TZVPD def2-TZVP/C		def2-TZVPD aug-cc-pVTZ/C	
	E_{C} / E_{h}	%	E_{C} / E_{h}	%
$10^{-1.50}$	−6.184 588 2	99.8576	−6.184 751 9	99.8570
$10^{-1.75}$	−6.189 325 0	99.9341	−6.189 500 3	99.9336
$10^{-2.00}$	−6.191 812 5	99.9742	−6.192 001 1	99.9740
$10^{-2.25}$	−6.192 817 4	99.9905	−6.193 014 5	99.9904
$10^{-2.50}$	−6.193 135 8	99.9956	−6.193 336 7	99.9956
$10^{-2.75}$	−6.193 266 1	99.9977	−6.193 467 1	99.9977
$10^{-3.00}$	−6.193 362 2	99.9993	−6.193 564 0	99.9992
0	−6.193 408 2	100.0000	−6.193 610 5	100.0000

(c) Energies for the ATP^{4-} anion.

Table A.5: Correlation energy calculated with different thresholds T_{CutDO}. The PNO and fitting domain threshold were set to their respective default values, and no other truncation were applied. The percentages are those of the DLPNO-MP2 energy with $T_{\mathrm{CutDO}} = 0$.

Energies calculated with different occupied Fock matrix truncation thresholds F_{Cut} are shown in Table A.6 for vancomycin with the def2-TZVP basis. The truncation thresholds for PNOs, PAOs and auxiliary functions were set to their default values of $T_{\mathrm{CutPNO}} = 1 \times 10^{-8}$, $T_{\mathrm{CutMKN}} = 1 \times 10^{-3}$ and $T_{\mathrm{CutDO}} = 1 \times 10^{-2}$. All remaining thresholds were set to zero. The data is represented graphically in Figure 2.6.

F_{Cut}	energy / E_{h}	truncation error / E_{h}
$10^{-2.00}$	−18.306 593 079 605	4.825×10^{-3}
$10^{-2.50}$	−18.311 034 733 384	3.834×10^{-4}
$10^{-3.00}$	−18.311 415 790 297	2.350×10^{-6}
$10^{-3.25}$	−18.311 432 610 517	-1.447×10^{-5}
$10^{-3.50}$	−18.311 428 233 514	-1.009×10^{-5}
$10^{-3.75}$	−18.311 422 910 129	-4.770×10^{-6}
$10^{-4.00}$	−18.311 420 523 158	-2.383×10^{-6}
$10^{-4.25}$	−18.311 418 984 655	-8.447×10^{-7}
$10^{-4.50}$	−18.311 418 463 731	-3.238×10^{-7}
$10^{-4.75}$	−18.311 418 261 340	-1.214×10^{-7}
$10^{-5.00}$	−18.311 418 184 232	-4.426×10^{-8}
$10^{-5.50}$	−18.311 418 143 703	-3.734×10^{-9}
$10^{-6.00}$	−18.311 418 140 262	-2.930×10^{-10}
0	−18.311 418 139 969	0.0

Table A.6: Energies for vancomycin with the def2-TZVP calculated with different F_{Cut}. The thresholds T_{CutPNO}, T_{CutMKN} and T_{CutDO} were set to their default values. No other truncations were applied.

A.2 Timing results

Table A.7 shows wall clock times for individual components of the DLPNO-MP2 energy calculation determined for alkane chains of different length.

	wall clock times / s				
	$C_{100}H_{202}$	$C_{150}H_{302}$	$C_{200}H_{402}$	$C_{250}H_{502}$	$C_{300}H_{602}$
no. of basis functions	4312	6462	8612	10 762	12 912
HF (RIJCOSX)	44 071	77 149	128 912	199 392	[I]63 262
MO localization	215	715	1992	3234	4888
F and **S** in AO basis	73	242	671	1206	1831
calculation of PAOs	21	70	208	363	547
F and **S** in PAO basis	27	91	267	461	703
grid setup for DOI	284	873	2648	4880	6890
DOI calculation	44	75	157	196	212
dipole integrals	58	178	499	831	1255
prescreening	27	65	151	215	276
screened out pairs / %	81	87	90	92	94
map setup	36	116	353	520	731
$(i\tilde{\mu}'\|K)$ transformation	3937	6801	11 256	13 671	14 381
semicanonical amplitudes	1466	2353	4144	4831	5575
PNO generation	529	818	1435	1597	1678
LMP2 iterations	804	1313	2404	2887	2819
no. of iterations	8	8	9	9	9
LMP2 (total)	7543	13 768	26 350	35 203	42 190

Table A.7: Breakdown of the DLPNO-MP2 timings on one CPU core for long alkane chains.
[I]Execution in parallel on 16 cores.

Appendix B

Data tables: DLPNO-MP2 gradient

B.1 Electric field gradient calculations

B.1.1 Convergence of electric field gradient errors with the PNO truncation threshold

Table B.1 shows electric field gradients computed with different pair natural orbital truncation thresholds for chlorothiazide and taurine, as presented in Figure 3.1. It includes results calculated with the complete Lagrangian and with approximate schemes. Results were calculated with the cc-pwCVTZ basis, and all truncation thresholds except for T_{CutPNO} were set to zero. As defined in the default settings, the PNO truncation threshold for pairs involving at least one core orbital was adjusted to $T_{\mathrm{CutPNO(Core)}} = 10^{-2} \times T_{\mathrm{CutPNO}}$.

In addition, results are shown with $T_{\mathrm{CutPNO(Core)}} = 0$: this reproduces the full virtual space for pairs involving at least one core orbital, and permits PNO truncation only for pure valence pairs.

B.1.2 Electric field gradients with standard threshold settings

Table B.2 shows nuclear quadrupole coupling constants calculated for chlorothiazide and taurine in cc-pwCVQZ basis. The taurine molecule was supplemented with three spectator molecules and embedded in point charges, as shown in Figure 3.2.

	$T_{\text{CutPNO(Core)}} = 10^{-2} \times T_{\text{CutPNO}}$				$T_{\text{CutPNO(Core)}} = 0$			
T_{CutPNO}	(1)	(2)	(3)	(4)	(1)	(2)	(3)	(4)
10^{-7}	3.9331	3.9407	3.9528	3.9547	3.9327	3.9400	3.9590	3.9604
10^{-8}	3.9315	3.9333	3.8885	3.8899	3.9316	3.9334	3.8942	3.8953
10^{-9}	3.9309	3.9314	3.9362	3.9368	3.9309	3.9314	3.9369	3.9374
10^{-10}	3.9307	3.9307	3.9343	3.9344	3.9307	3.9307	3.9344	3.9346
10^{-11}	3.9306	3.9306	3.9267	3.9267	3.9306	3.9306	3.9267	3.9268
10^{-12}	3.9305	3.9305	3.9243	3.9244	3.9305	3.9305	3.9244	3.9244
HF	4.1436							
RI-MP2	3.9305							

(a) Cl nucleus of chlorothiazide

	$T_{\text{CutPNO(Core)}} = 10^{-2} \times T_{\text{CutPNO}}$				$T_{\text{CutPNO(Core)}} = 0$			
T_{CutPNO}	(1)	(2)	(3)	(4)	(1)	(2)	(3)	(4)
10^{-7}	0.4570	0.4610	0.4471	0.4466	0.4560	0.4599	0.4468	0.4473
10^{-8}	0.4549	0.4559	0.4290	0.4294	0.4549	0.4559	0.4292	0.4295
10^{-9}	0.4546	0.4548	0.4698	0.4699	0.4546	0.4548	0.4698	0.4699
10^{-10}	0.4545	0.4545	0.4491	0.4491	0.4545	0.4545	0.4491	0.4491
10^{-11}	0.4545	0.4545	0.4541	0.4541	0.4545	0.4545	0.4541	0.4541
10^{-12}	0.4545	0.4545	0.4547	0.4547	0.4545	0.4545	0.4547	0.4547
HF	0.5675							
RI-MP2	0.4545							

(b) S nucleus of taurine

Table B.1: Largest principal component V_{zz} of the electric field gradient tensor in atomic units with different PNO truncation thresholds. Meaning of the column labels:
(1) Including all constraints and the derivative of ΔE_{PNO}.
(2) Including all constraints without the derivative of ΔE_{PNO}.
(3) Excluding the constraints for the PNOs and the semicanonical amplitudes.
(4) As in (3), but also excluding the localisation constraint.

	C_Q / MHz			
Settings	(1)	(2)	(3)	(4)
LoosePNO	−74.356	−74.562	−77.627	−77.243
NormalPNO	−74.542	−74.594	−78.716	−78.320
TightPNO	−74.587	−74.596	−73.421	−73.014
HF		−79.159		
RI-MP2		−74.585		
Experiment[196]		−73.04(8)		

(a) NQCC for the ^{35}Cl nucleus of chlorothiazide. The uncertainty of ±0.8 mb in the nuclear quadrupole moment translates into an error range of ±0.7 MHz for the calculated result.

	C_Q / MHz			
Settings	(1)	(2)	(3)	(4)
LoosePNO	1.512	1.523	−3.295	−3.312
NormalPNO	1.351	1.353	−2.632	−2.648
TightPNO	1.327	1.330	−2.553	−2.568
HF		1.911		
RI-MP2		1.297		
Experiment[197]		1.36(2)		

(b) NQCC for the ^{33}S nucleus of taurine. The uncertainty of ±0.4 mb in the nuclear quadrupole moment translates into an error range of ±7 kHz for the calculated result.

Table B.2: Nuclear quadrupole coupling constants (NQCCs) calculated with DLPNO-MP2 using the complete and approximate Lagrangians. Results using HF and RI-MP2, and experimentally determined values are shown for comparison. Meaning of the column labels:
(1) Including all constraints and the derivative of ΔE_PNO.
(2) Including all constraints without the derivative of ΔE_PNO.
(3) Excluding the constraints for the PNOs and the semicanonical amplitudes.
(4) As in (3), but also excluding the localisation constraint.

B.2 Localisation Hessian singularities

Table B.3 shows errors in the natural occupation numbers of the relaxed density for slightly distorted geometries. The data is plotted in Figure 3.9.

eigenvalue	root mean square		maximum	
	uncorrected	corrected	uncorrected	corrected
3.77×10^{-7}	6.40×10^{-2}	4.59×10^{-5}	5.83×10^{-1}	3.53×10^{-4}
1.72×10^{-5}	2.37×10^{-3}	4.59×10^{-5}	2.43×10^{-2}	3.55×10^{-4}
4.05×10^{-5}	6.77×10^{-5}	4.59×10^{-5}	5.16×10^{-4}	3.55×10^{-4}
2.54×10^{-4}	4.62×10^{-5}	4.61×10^{-5}	3.61×10^{-4}	3.61×10^{-4}
4.71×10^{-4}	5.06×10^{-5}	5.06×10^{-5}	3.65×10^{-4}	3.65×10^{-4}
7.03×10^{-4}	6.82×10^{-5}	6.82×10^{-5}	4.86×10^{-4}	4.86×10^{-4}

(a) benzene-ethyne dimer

eigenvalue	root mean square		maximum	
	uncorrected	corrected	uncorrected	corrected
1.29×10^{-5}	1.00×10^{-1}	3.48×10^{-4}	1.56	5.63×10^{-3}
2.52×10^{-5}	1.15×10^{-3}	8.01×10^{-4}	1.28×10^{-2}	1.12×10^{-2}
4.37×10^{-5}	9.38×10^{-3}	3.57×10^{-4}	1.49×10^{-1}	5.68×10^{-3}
2.05×10^{-4}	4.23×10^{-4}	3.76×10^{-4}	5.64×10^{-3}	5.64×10^{-3}
3.88×10^{-4}	3.61×10^{-4}	3.49×10^{-4}	5.77×10^{-3}	5.74×10^{-3}
1.85×10^{-3}	8.93×10^{-4}	8.91×10^{-4}	3.20×10^{-3}	3.21×10^{-3}

(b) KAMDOR

eigenvalue	root mean square		maximum	
	uncorrected	corrected	uncorrected	corrected
5.25×10^{-7}	1.73×10^{-2}	7.47×10^{-5}	2.26×10^{-1}	1.11×10^{-3}
4.02×10^{-6}	2.33×10^{-4}	9.52×10^{-5}	3.40×10^{-3}	1.14×10^{-3}
1.36×10^{-5}	2.63×10^{-4}	7.55×10^{-5}	4.41×10^{-3}	1.09×10^{-3}
3.63×10^{-5}	7.40×10^{-5}	7.40×10^{-5}	1.08×10^{-3}	1.08×10^{-3}
1.61×10^{-4}	7.27×10^{-5}	7.27×10^{-5}	1.08×10^{-3}	1.08×10^{-3}
3.27×10^{-4}	9.55×10^{-5}	9.55×10^{-5}	1.53×10^{-3}	1.53×10^{-3}

(c) $MgCp_2$

Table B.3: Deviations between natural occupation numbers calculated with the relaxed DLPNO-MP2 and RI-MP2 densities. The leftmost column shows the smallest eigenvalue (by absolute value) of the Foster-Boys orbital Hessian calculated for each structure. "Uncorrected" values were calculated using the unmodified Lagrangian, the "corrected" values after removing the eigenvector associated with the smallest eigenvalue.

B.3 Single-point geometric gradient calculations

B.3.1 Baker test set

Tables B.4 and B.5 show errors in the DLPNO-MP2 gradient for the Baker test set. The molecules are ordered by the number of atoms. A plot of the root mean square errors is provided in Figure 3.10.

Name	Atoms	RMS gradient error / $E_\mathrm{h}\,{a_0}^{-1}$		
		LoosePNO	NormalPNO	TightPNO
water	3	5.93×10^{-6}	1.61×10^{-7}	1.99×10^{-7}
acetylene	4	4.15×10^{-5}	1.59×10^{-5}	1.02×10^{-5}
ammonia	4	1.24×10^{-5}	2.06×10^{-6}	1.84×10^{-6}
hydroxysulphane	4	8.11×10^{-5}	2.28×10^{-5}	3.05×10^{-6}
allene	7	2.21×10^{-5}	1.14×10^{-5}	6.73×10^{-7}
methylamine	7	7.75×10^{-5}	2.61×10^{-5}	6.84×10^{-6}
ethane	8	7.60×10^{-5}	1.70×10^{-5}	9.33×10^{-6}
disilyl ether	9	3.52×10^{-5}	4.09×10^{-6}	3.06×10^{-6}
ethanol	9	1.03×10^{-4}	3.21×10^{-5}	1.15×10^{-5}
furan	9	1.12×10^{-4}	4.08×10^{-5}	8.80×10^{-6}
acetone	10	7.77×10^{-5}	4.03×10^{-5}	2.64×10^{-5}
benzene	12	9.44×10^{-5}	2.63×10^{-5}	7.58×10^{-6}
1,3-difluorobenzene	12	1.82×10^{-4}	5.66×10^{-5}	3.14×10^{-5}
1,3,5-trifluorobenzene	12	2.53×10^{-4}	1.16×10^{-4}	1.03×10^{-4}
benzaldehyde	14	1.26×10^{-4}	4.17×10^{-5}	1.50×10^{-5}
2-hydroxybicyclopentane	14	2.18×10^{-4}	9.87×10^{-5}	7.49×10^{-5}
ACHTAR10	16	9.46×10^{-5}	3.80×10^{-5}	1.73×10^{-5}
difuropyrazine	16	3.41×10^{-4}	1.45×10^{-4}	8.94×10^{-5}
mesityl oxide	17	1.43×10^{-4}	4.74×10^{-5}	1.52×10^{-5}
neopentane	17	1.20×10^{-4}	2.73×10^{-5}	1.46×10^{-5}
pterin	17	3.41×10^{-4}	1.19×10^{-4}	4.85×10^{-5}
1,5-difluoronaphthalene	18	3.38×10^{-4}	1.22×10^{-4}	5.04×10^{-5}
naphthalene	18	3.16×10^{-4}	9.09×10^{-5}	3.28×10^{-5}
1,3,5-trisilylacyclohexane	18	1.19×10^{-4}	2.25×10^{-5}	1.20×10^{-5}
ACANIL01	19	1.65×10^{-4}	6.51×10^{-5}	2.99×10^{-5}
histidine	20	2.07×10^{-4}	7.03×10^{-5}	3.10×10^{-5}
dimethylpentane	23	1.91×10^{-4}	5.08×10^{-5}	1.98×10^{-5}
caffeine	24	3.56×10^{-4}	1.36×10^{-4}	5.35×10^{-5}
benzidine	26	2.93×10^{-3}	1.12×10^{-3}	2.86×10^{-4}
menthone	29	2.26×10^{-4}	8.54×10^{-5}	3.00×10^{-5}

Table B.4: Root mean square (RMS) deviations of the DLPNO-MP2 nuclear gradient from RI-MP2 for molecules in the Baker test set.

Name	Atoms	Largest gradient error / $E_\mathrm{h}\,{a_0}^{-1}$		
		LoosePNO	NormalPNO	TightPNO
water	3	6.90×10^{-6}	2.28×10^{-7}	2.36×10^{-7}
acetylene	4	5.87×10^{-5}	2.24×10^{-5}	1.43×10^{-5}
ammonia	4	2.00×10^{-5}	2.12×10^{-6}	1.94×10^{-6}
hydroxysulphane	4	1.11×10^{-4}	3.29×10^{-5}	4.23×10^{-6}
allene	7	3.82×10^{-5}	2.05×10^{-5}	7.40×10^{-7}
methylamine	7	1.42×10^{-4}	5.17×10^{-5}	1.27×10^{-5}
ethane	8	1.49×10^{-4}	3.14×10^{-5}	1.85×10^{-5}
disilyl ether	9	7.05×10^{-5}	6.24×10^{-6}	4.46×10^{-6}
ethanol	9	1.95×10^{-4}	6.33×10^{-5}	2.35×10^{-5}
furan	9	2.14×10^{-4}	8.21×10^{-5}	1.51×10^{-5}
acetone	10	1.54×10^{-4}	7.57×10^{-5}	4.84×10^{-5}
benzene	12	1.30×10^{-4}	3.57×10^{-5}	1.03×10^{-5}
1,3-difluorobenzene	12	2.58×10^{-4}	9.00×10^{-5}	5.39×10^{-5}
1,3,5-trifluorobenzene	12	3.50×10^{-4}	1.67×10^{-4}	1.60×10^{-4}
benzaldehyde	14	2.53×10^{-4}	9.74×10^{-5}	3.37×10^{-5}
2-hydroxybicyclopentane	14	4.20×10^{-4}	2.06×10^{-4}	1.68×10^{-4}
ACHTAR10	16	2.02×10^{-4}	9.37×10^{-5}	4.49×10^{-5}
difuropyrazine	16	5.81×10^{-4}	3.07×10^{-4}	2.11×10^{-4}
mesityl oxide	17	3.33×10^{-4}	1.10×10^{-4}	3.05×10^{-5}
neopentane	17	2.37×10^{-4}	5.14×10^{-5}	2.82×10^{-5}
pterin	17	9.11×10^{-4}	3.13×10^{-4}	9.22×10^{-5}
1,5-difluoronaphthalene	18	5.30×10^{-4}	1.97×10^{-4}	7.90×10^{-5}
naphthalene	18	5.00×10^{-4}	1.44×10^{-4}	5.16×10^{-5}
1,3,5-trisilylacyclohexane	18	2.66×10^{-4}	4.66×10^{-5}	2.67×10^{-5}
ACANIL01	19	3.89×10^{-4}	1.64×10^{-4}	7.87×10^{-5}
histidine	20	4.15×10^{-4}	1.42×10^{-4}	6.31×10^{-5}
dimethylpentane	23	3.86×10^{-4}	1.14×10^{-4}	4.72×10^{-5}
caffeine	24	8.86×10^{-4}	3.18×10^{-4}	1.11×10^{-4}
benzidine	26	5.83×10^{-3}	2.29×10^{-3}	5.39×10^{-4}
menthone	29	4.80×10^{-4}	2.03×10^{-4}	6.54×10^{-5}

Table B.5: Largest deviations of the DLPNO-MP2 nuclear gradient from RI-MP2 for molecules in the Baker test set.

B.3.2 S66x8 test set

Tables B.6 to B.8 show the root mean square deviation between single-point gradients calculated with DLPNO-MP2 and RI-MP2 for the dimers in the S66x8 test set. The bottom row of each table contains the root mean square of root mean square deviations for each relative distance between the monomers. A graphical representation of the latter data is shown in Figure 3.11.

Distance scaling factor	0.90	0.95	1.00	1.05	1.10	1.25	1.50	2.00
Dimer	gradient RMSD / $E_\mathrm{h}\,{a_0}^{-1}$							
Water-Water	4.66×10^{-5}	4.37×10^{-5}	3.81×10^{-5}	3.45×10^{-5}	3.12×10^{-5}	2.41×10^{-5}	1.57×10^{-5}	9.75×10^{-6}
Water-MeOH	7.43×10^{-5}	7.25×10^{-5}	7.13×10^{-5}	6.76×10^{-5}	6.42×10^{-5}	7.17×10^{-5}	6.13×10^{-5}	6.35×10^{-5}
Water-MeNH2	7.20×10^{-5}	6.80×10^{-5}	6.41×10^{-5}	6.21×10^{-5}	6.05×10^{-5}	6.58×10^{-5}	5.17×10^{-5}	5.34×10^{-5}
Water-Peptide	1.07×10^{-4}	1.03×10^{-4}	1.01×10^{-4}	1.01×10^{-4}	1.00×10^{-4}	1.06×10^{-4}	9.49×10^{-5}	8.65×10^{-5}
MeOH-MeOH	9.30×10^{-5}	8.70×10^{-5}	8.58×10^{-5}	8.41×10^{-5}	8.27×10^{-5}	8.21×10^{-5}	7.29×10^{-5}	7.45×10^{-5}
MeOH-MeNH2	9.09×10^{-5}	9.32×10^{-5}	8.98×10^{-5}	8.71×10^{-5}	8.16×10^{-5}	7.82×10^{-5}	7.28×10^{-5}	6.72×10^{-5}
MeOH-Peptide	1.15×10^{-4}	1.11×10^{-4}	1.09×10^{-4}	1.06×10^{-4}	1.02×10^{-4}	9.92×10^{-5}	9.56×10^{-5}	9.32×10^{-5}
MeOH-Water	8.18×10^{-5}	7.80×10^{-5}	7.66×10^{-5}	7.51×10^{-5}	7.30×10^{-5}	6.87×10^{-5}	6.19×10^{-5}	5.71×10^{-5}
MeNH2-MeOH	7.97×10^{-5}	7.69×10^{-5}	7.76×10^{-5}	8.07×10^{-5}	7.91×10^{-5}	7.14×10^{-5}	7.01×10^{-5}	7.10×10^{-5}
MeNH2-MeNH2	8.81×10^{-5}	9.00×10^{-5}	8.80×10^{-5}	8.46×10^{-5}	8.19×10^{-5}	7.37×10^{-5}	6.60×10^{-5}	6.78×10^{-5}
MeNH2-Peptide	1.40×10^{-4}	1.35×10^{-4}	1.28×10^{-4}	1.26×10^{-4}	1.24×10^{-4}	1.22×10^{-4}	1.19×10^{-4}	1.17×10^{-4}
MeNH2-Water	8.02×10^{-5}	7.79×10^{-5}	7.80×10^{-5}	7.42×10^{-5}	7.19×10^{-5}	6.08×10^{-5}	7.13×10^{-5}	5.21×10^{-5}
Peptide-MeOH	1.40×10^{-4}	1.33×10^{-4}	1.29×10^{-4}	1.23×10^{-4}	1.20×10^{-4}	1.06×10^{-4}	9.83×10^{-5}	9.58×10^{-5}
Peptide- MeNH2	1.33×10^{-4}	1.25×10^{-4}	1.23×10^{-4}	1.22×10^{-4}	1.16×10^{-4}	1.06×10^{-4}	9.27×10^{-5}	8.74×10^{-5}
Peptide-Peptide	1.35×10^{-4}	1.35×10^{-4}	1.30×10^{-4}	1.28×10^{-4}	1.25×10^{-4}	1.18×10^{-4}	1.10×10^{-4}	1.02×10^{-4}
Peptide-Water	1.27×10^{-4}	1.26×10^{-4}	1.24×10^{-4}	1.28×10^{-4}	1.23×10^{-4}	1.14×10^{-4}	1.08×10^{-4}	1.03×10^{-4}
Uracil-Uracil (BP)	3.60×10^{-4}	3.65×10^{-4}	3.67×10^{-4}	3.69×10^{-4}	3.74×10^{-4}	3.66×10^{-4}	3.80×10^{-4}	3.85×10^{-4}
Water-Pyridine	9.24×10^{-5}	9.56×10^{-5}	9.46×10^{-5}	8.87×10^{-5}	9.33×10^{-5}	8.84×10^{-5}	8.95×10^{-5}	9.58×10^{-5}
MeOH-Pyridine	1.07×10^{-4}	1.08×10^{-4}	1.07×10^{-4}	1.02×10^{-4}	9.19×10^{-5}	8.94×10^{-5}	9.39×10^{-5}	9.66×10^{-5}

AcOH-AcOH	1.34×10^{-4}	2.25×10^{-4}	1.05×10^{-4}	1.03×10^{-4}	9.94×10^{-5}	1.05×10^{-4}	9.66×10^{-5}	8.58×10^{-5}
AcNH2-AcNH2	1.10×10^{-4}	1.05×10^{-4}	1.01×10^{-4}	9.66×10^{-5}	9.26×10^{-5}	9.13×10^{-5}	8.61×10^{-5}	8.44×10^{-5}
AcOH-Uracil	2.67×10^{-4}	2.69×10^{-4}	2.69×10^{-4}	2.73×10^{-4}	2.61×10^{-4}	2.63×10^{-4}	2.60×10^{-4}	2.75×10^{-4}
AcNH2-Uracil	2.73×10^{-4}	2.73×10^{-4}	2.62×10^{-4}	2.67×10^{-4}	2.66×10^{-4}	2.58×10^{-4}	2.63×10^{-4}	2.84×10^{-4}
Benzene-Benzene (π-π)	1.82×10^{-4}	1.73×10^{-4}	1.55×10^{-4}	1.42×10^{-4}	1.30×10^{-4}	1.02×10^{-4}	9.53×10^{-5}	9.41×10^{-5}
Pyridine-Pyridine (π-π)	1.88×10^{-4}	1.76×10^{-4}	1.72×10^{-4}	1.61×10^{-4}	1.57×10^{-4}	1.23×10^{-4}	1.01×10^{-4}	1.01×10^{-4}
Uracil-Uracil (π-π)	2.93×10^{-4}	2.87×10^{-4}	2.76×10^{-4}	2.65×10^{-4}	2.54×10^{-4}	2.25×10^{-4}	2.10×10^{-4}	2.06×10^{-4}
Benzene-Pyridine (π-π)	1.86×10^{-4}	1.78×10^{-4}	1.62×10^{-4}	1.53×10^{-4}	1.38×10^{-4}	1.08×10^{-4}	9.84×10^{-5}	9.74×10^{-5}
Benzene-Uracil (π-π)	3.73×10^{-4}	3.13×10^{-4}	2.96×10^{-4}	2.77×10^{-4}	2.62×10^{-4}	2.33×10^{-4}	2.06×10^{-4}	2.10×10^{-4}
Pyridine-Uracil (π-π)	2.64×10^{-4}	2.43×10^{-4}	2.22×10^{-4}	2.07×10^{-4}	1.96×10^{-4}	1.79×10^{-4}	1.72×10^{-4}	1.68×10^{-4}
Benzene-Ethene	1.32×10^{-4}	1.21×10^{-4}	1.27×10^{-4}	1.14×10^{-4}	1.01×10^{-4}	8.18×10^{-5}	7.89×10^{-5}	7.91×10^{-5}
Uracil-Ethene	2.23×10^{-4}	2.22×10^{-4}	2.18×10^{-4}	2.17×10^{-4}	2.12×10^{-4}	2.05×10^{-4}	1.96×10^{-4}	1.93×10^{-4}
Uracil-Ethyne	2.25×10^{-4}	2.17×10^{-4}	2.14×10^{-4}	2.11×10^{-4}	2.06×10^{-4}	1.94×10^{-4}	1.82×10^{-4}	1.78×10^{-4}
Pyridine-Ethene	1.37×10^{-4}	1.26×10^{-4}	1.19×10^{-4}	1.18×10^{-4}	1.14×10^{-4}	8.90×10^{-5}	8.47×10^{-5}	8.45×10^{-5}
Pentane-Pentane	1.93×10^{-4}	1.85×10^{-4}	1.73×10^{-4}	1.71×10^{-4}	1.66×10^{-4}	1.50×10^{-4}	1.29×10^{-4}	1.21×10^{-4}
Neopentane-Pentane	1.59×10^{-4}	1.52×10^{-4}	1.42×10^{-4}	1.34×10^{-4}	1.27×10^{-4}	1.20×10^{-4}	1.11×10^{-4}	1.07×10^{-4}
Neopentane-Neopentane	1.39×10^{-4}	1.40×10^{-4}	1.29×10^{-4}	1.21×10^{-4}	1.14×10^{-4}	1.05×10^{-4}	9.47×10^{-5}	9.16×10^{-5}
Cyclopentane-Neopentane	1.74×10^{-4}	1.69×10^{-4}	1.61×10^{-4}	1.56×10^{-4}	1.50×10^{-4}	1.39×10^{-4}	1.25×10^{-4}	1.19×10^{-4}
Cyclopentane-Cyclopentane	1.98×10^{-4}	1.90×10^{-4}	1.81×10^{-4}	1.79×10^{-4}	1.72×10^{-4}	1.61×10^{-4}	1.46×10^{-4}	1.41×10^{-4}
Benzene-Cyclopentane	2.00×10^{-4}	1.90×10^{-4}	1.76×10^{-4}	1.63×10^{-4}	1.62×10^{-4}	1.44×10^{-4}	1.27×10^{-4}	1.24×10^{-4}
Benzene-Neopentane	1.57×10^{-4}	1.46×10^{-4}	1.37×10^{-4}	1.32×10^{-4}	1.28×10^{-4}	1.09×10^{-4}	1.00×10^{-4}	9.98×10^{-5}
Uracil-Pentane	2.46×10^{-4}	2.38×10^{-4}	2.33×10^{-4}	2.29×10^{-4}	2.24×10^{-4}	2.10×10^{-4}	2.01×10^{-4}	1.95×10^{-4}
Uracil-Cyclopentane	2.84×10^{-4}	2.80×10^{-4}	2.68×10^{-4}	2.55×10^{-4}	2.49×10^{-4}	2.44×10^{-4}	2.26×10^{-4}	2.27×10^{-4}
Uracil-Neopentane	2.23×10^{-4}	2.21×10^{-4}	2.19×10^{-4}	2.15×10^{-4}	2.14×10^{-4}	2.08×10^{-4}	1.92×10^{-4}	1.85×10^{-4}
Ethene-Pentane	1.44×10^{-4}	1.36×10^{-4}	1.30×10^{-4}	1.28×10^{-4}	1.32×10^{-4}	1.18×10^{-4}	1.08×10^{-4}	1.04×10^{-4}
Ethyne-Pentane	1.54×10^{-4}	1.48×10^{-4}	1.46×10^{-4}	1.49×10^{-4}	1.46×10^{-4}	1.22×10^{-4}	1.11×10^{-4}	1.09×10^{-4}
Peptide-Pentane	1.90×10^{-4}	1.84×10^{-4}	1.77×10^{-4}	1.75×10^{-4}	1.68×10^{-4}	1.58×10^{-4}	1.35×10^{-4}	1.25×10^{-4}
Benzene-Benzene (TS)	1.53×10^{-4}	1.48×10^{-4}	1.40×10^{-4}	1.36×10^{-4}	1.35×10^{-4}	1.33×10^{-4}	1.26×10^{-4}	1.26×10^{-4}

Pyridine-Pyridine (TS)	1.23×10^{-4}	1.17×10^{-4}	1.15×10^{-4}	1.09×10^{-4}	1.04×10^{-4}	1.05×10^{-4}	1.05×10^{-4}	1.03×10^{-4}
Benzene-Pyridine (TS)	1.34×10^{-4}	1.28×10^{-4}	1.23×10^{-4}	1.18×10^{-4}	1.15×10^{-4}	1.13×10^{-4}	1.05×10^{-4}	1.03×10^{-4}
Benzene-Ethyne (CH-π)	1.40×10^{-4}	1.25×10^{-4}	1.18×10^{-4}	1.09×10^{-4}	9.96×10^{-5}	9.56×10^{-5}	8.22×10^{-5}	8.28×10^{-5}
Ethyne-Ethyne (TS)	9.06×10^{-5}	6.61×10^{-5}	5.36×10^{-5}	4.34×10^{-5}	3.67×10^{-5}	3.15×10^{-5}	2.28×10^{-5}	1.65×10^{-5}
Benzene-AcOH (OH-π)	1.39×10^{-4}	1.39×10^{-4}	1.27×10^{-4}	1.23×10^{-4}	1.23×10^{-4}	1.13×10^{-4}	1.05×10^{-4}	1.03×10^{-4}
Benzene-AcNH2 (NH-π)	1.71×10^{-4}	1.65×10^{-4}	1.61×10^{-4}	1.54×10^{-4}	1.53×10^{-4}	1.56×10^{-4}	1.50×10^{-4}	1.55×10^{-4}
Benzene-Water (OH-π)	1.55×10^{-4}	1.63×10^{-4}	1.14×10^{-4}	1.07×10^{-4}	1.02×10^{-4}	8.94×10^{-5}	8.59×10^{-5}	8.48×10^{-5}
Benzene-MeOH (OH-π)	1.33×10^{-4}	1.24×10^{-4}	1.20×10^{-4}	1.20×10^{-4}	1.14×10^{-4}	1.04×10^{-4}	9.15×10^{-5}	8.79×10^{-5}
Benzene-MeNH2 (NH-π)	1.29×10^{-4}	1.22×10^{-4}	1.14×10^{-4}	1.09×10^{-4}	1.04×10^{-4}	9.29×10^{-5}	8.68×10^{-5}	8.60×10^{-5}
Benzene-Peptide (NH-π)	1.70×10^{-4}	1.63×10^{-4}	1.53×10^{-4}	1.40×10^{-4}	1.35×10^{-4}	1.19×10^{-4}	1.03×10^{-4}	9.99×10^{-5}
Pyridine-Pyridine (CH-N)	9.36×10^{-5}	8.85×10^{-5}	8.86×10^{-5}	8.67×10^{-5}	7.84×10^{-5}	8.16×10^{-5}	8.19×10^{-5}	7.97×10^{-5}
Ethyne-Water (CH-O)	5.85×10^{-5}	4.34×10^{-5}	3.96×10^{-5}	3.67×10^{-5}	3.18×10^{-5}	2.20×10^{-5}	2.16×10^{-5}	1.67×10^{-5}
Ethyne-AcOH (OH-π)	1.12×10^{-4}	1.02×10^{-4}	9.38×10^{-5}	8.81×10^{-5}	8.83×10^{-5}	8.00×10^{-5}	7.28×10^{-5}	6.44×10^{-5}
Pentane-AcOH	1.53×10^{-4}	1.49×10^{-4}	1.46×10^{-4}	1.43×10^{-4}	1.41×10^{-4}	1.31×10^{-4}	1.19×10^{-4}	1.14×10^{-4}
Pentane-AcNH2	1.69×10^{-4}	1.65×10^{-4}	1.61×10^{-4}	1.56×10^{-4}	1.51×10^{-4}	1.36×10^{-4}	1.23×10^{-4}	1.19×10^{-4}
Benzene-AcOH	1.62×10^{-4}	1.49×10^{-4}	1.39×10^{-4}	1.33×10^{-4}	1.27×10^{-4}	1.17×10^{-4}	1.08×10^{-4}	1.07×10^{-4}
Peptide-Ethene	1.23×10^{-4}	1.17×10^{-4}	1.14×10^{-4}	1.09×10^{-4}	1.13×10^{-4}	1.03×10^{-4}	8.86×10^{-5}	8.65×10^{-5}
Pyridine-Ethyne	1.11×10^{-4}	1.07×10^{-4}	1.05×10^{-4}	1.03×10^{-4}	1.03×10^{-4}	1.04×10^{-4}	1.07×10^{-4}	1.10×10^{-4}
MeNH2-Pyridine	1.21×10^{-4}	1.14×10^{-4}	1.14×10^{-4}	1.12×10^{-4}	1.12×10^{-4}	1.04×10^{-4}	9.46×10^{-5}	9.22×10^{-5}
RMS(RMSD)	1.69×10^{-4}	1.64×10^{-4}	1.56×10^{-4}	1.51×10^{-4}	1.47×10^{-4}	1.38×10^{-4}	1.30×10^{-4}	1.30×10^{-4}

Table B.6: Root mean square deviation between the DLPNO-MP2 and RI-MP2 gradients for dimers in the S66x8 test set. LoosePNO thresholds were used for the DLPNO-MP2 calculations. The values are given in $E_\mathrm{h}\, {a_0}^{-1}$.

Distance scaling factor	0.90	0.95	1.00	1.05	1.10	1.25	1.50	2.00
Dimer	gradient RMSD / $E_\mathrm{h}\,{a_0}^{-1}$							
Water-Water	1.35×10^{-5}	1.15×10^{-5}	9.92×10^{-6}	1.08×10^{-5}	9.90×10^{-6}	5.90×10^{-6}	3.04×10^{-6}	2.00×10^{-6}
Water-MeOH	3.21×10^{-5}	3.22×10^{-5}	2.72×10^{-5}	2.71×10^{-5}	2.74×10^{-5}	3.63×10^{-5}	2.36×10^{-5}	2.25×10^{-5}
Water-MeNH2	2.81×10^{-5}	2.59×10^{-5}	2.54×10^{-5}	2.45×10^{-5}	2.40×10^{-5}	3.43×10^{-5}	2.19×10^{-5}	2.12×10^{-5}
Water-Peptide	4.41×10^{-5}	4.35×10^{-5}	4.24×10^{-5}	4.13×10^{-5}	4.03×10^{-5}	5.16×10^{-5}	4.11×10^{-5}	3.67×10^{-5}
MeOH-MeOH	3.73×10^{-5}	3.52×10^{-5}	3.39×10^{-5}	3.23×10^{-5}	3.17×10^{-5}	3.74×10^{-5}	2.82×10^{-5}	2.68×10^{-5}
MeOH-MeNH2	3.54×10^{-5}	3.37×10^{-5}	3.24×10^{-5}	3.24×10^{-5}	3.07×10^{-5}	3.17×10^{-5}	2.96×10^{-5}	2.65×10^{-5}
MeOH-Peptide	5.08×10^{-5}	5.01×10^{-5}	4.85×10^{-5}	4.77×10^{-5}	4.65×10^{-5}	4.76×10^{-5}	4.50×10^{-5}	4.24×10^{-5}
MeOH-Water	2.74×10^{-5}	2.86×10^{-5}	2.63×10^{-5}	2.69×10^{-5}	2.56×10^{-5}	2.44×10^{-5}	2.16×10^{-5}	2.09×10^{-5}
MeNH2-MeOH	3.21×10^{-5}	3.09×10^{-5}	3.01×10^{-5}	3.72×10^{-5}	3.80×10^{-5}	2.72×10^{-5}	2.62×10^{-5}	2.70×10^{-5}
MeNH2-MeNH2	3.39×10^{-5}	3.22×10^{-5}	3.23×10^{-5}	3.18×10^{-5}	3.13×10^{-5}	3.01×10^{-5}	2.66×10^{-5}	2.57×10^{-5}
MeNH2-Peptide	5.06×10^{-5}	4.96×10^{-5}	4.95×10^{-5}	4.73×10^{-5}	4.68×10^{-5}	4.66×10^{-5}	4.69×10^{-5}	4.32×10^{-5}
MeNH2-Water	2.80×10^{-5}	2.71×10^{-5}	2.63×10^{-5}	2.64×10^{-5}	2.49×10^{-5}	2.42×10^{-5}	3.41×10^{-5}	2.15×10^{-5}
Peptide-MeOH	6.03×10^{-5}	5.63×10^{-5}	5.46×10^{-5}	5.27×10^{-5}	5.39×10^{-5}	5.05×10^{-5}	4.88×10^{-5}	4.19×10^{-5}
Peptide- MeNH2	5.67×10^{-5}	5.37×10^{-5}	5.46×10^{-5}	5.32×10^{-5}	5.21×10^{-5}	4.99×10^{-5}	4.46×10^{-5}	3.82×10^{-5}
Peptide-Peptide	6.22×10^{-5}	6.05×10^{-5}	5.76×10^{-5}	5.53×10^{-5}	5.43×10^{-5}	5.21×10^{-5}	4.74×10^{-5}	4.37×10^{-5}
Peptide-Water	4.64×10^{-5}	4.35×10^{-5}	4.22×10^{-5}	4.09×10^{-5}	4.38×10^{-5}	4.06×10^{-5}	3.94×10^{-5}	3.55×10^{-5}
Uracil-Uracil (BP)	1.43×10^{-4}	1.44×10^{-4}	1.45×10^{-4}	1.43×10^{-4}	1.50×10^{-4}	1.46×10^{-4}	1.55×10^{-4}	1.50×10^{-4}
Water-Pyridine	3.75×10^{-5}	4.88×10^{-5}	4.09×10^{-5}	4.38×10^{-5}	3.95×10^{-5}	3.69×10^{-5}	3.43×10^{-5}	5.98×10^{-5}
MeOH-Pyridine	3.87×10^{-5}	3.99×10^{-5}	3.84×10^{-5}	3.78×10^{-5}	3.65×10^{-5}	3.08×10^{-5}	3.48×10^{-5}	5.67×10^{-5}
AcOH-AcOH	6.87×10^{-5}	7.92×10^{-5}	4.31×10^{-5}	4.31×10^{-5}	4.30×10^{-5}	5.55×10^{-5}	4.83×10^{-5}	4.31×10^{-5}
AcNH2-AcNH2	4.26×10^{-5}	4.10×10^{-5}	4.12×10^{-5}	3.96×10^{-5}	4.09×10^{-5}	3.43×10^{-5}	3.63×10^{-5}	4.00×10^{-5}
AcOH-Uracil	1.07×10^{-4}	1.32×10^{-4}	9.87×10^{-5}	1.02×10^{-4}	1.02×10^{-4}	9.95×10^{-5}	9.48×10^{-5}	1.05×10^{-4}
AcNH2-Uracil	9.87×10^{-5}	1.05×10^{-4}	9.59×10^{-5}	9.58×10^{-5}	9.33×10^{-5}	9.11×10^{-5}	9.54×10^{-5}	1.05×10^{-4}
Benzene-Benzene (pi-pi)	5.79×10^{-5}	4.94×10^{-5}	4.49×10^{-5}	4.13×10^{-5}	3.91×10^{-5}	2.97×10^{-5}	2.52×10^{-5}	2.45×10^{-5}

Pyridine-Pyridine (pi-pi)	7.23×10^{-5}	6.61×10^{-5}	5.63×10^{-5}	4.98×10^{-5}	5.61×10^{-5}	4.92×10^{-5}	3.02×10^{-5}	3.82×10^{-5}
Uracil-Uracil (pi-pi)	1.13×10^{-4}	1.09×10^{-4}	1.06×10^{-4}	1.05×10^{-4}	1.00×10^{-4}	8.49×10^{-5}	8.08×10^{-5}	8.33×10^{-5}
Benzene-Pyridine (pi-pi)	6.47×10^{-5}	6.48×10^{-5}	6.14×10^{-5}	6.05×10^{-5}	5.90×10^{-5}	4.37×10^{-5}	2.71×10^{-5}	3.22×10^{-5}
Benzene-Uracil (pi-pi)	1.39×10^{-4}	1.08×10^{-4}	1.03×10^{-4}	9.84×10^{-5}	9.87×10^{-5}	9.09×10^{-5}	7.89×10^{-5}	8.33×10^{-5}
Pyridine-Uracil (pi-pi)	9.56×10^{-5}	8.61×10^{-5}	8.05×10^{-5}	7.90×10^{-5}	7.87×10^{-5}	7.47×10^{-5}	7.60×10^{-5}	6.93×10^{-5}
Benzene-Ethene	3.47×10^{-5}	3.81×10^{-5}	4.21×10^{-5}	3.36×10^{-5}	2.88×10^{-5}	2.36×10^{-5}	2.03×10^{-5}	2.07×10^{-5}
Uracil-Ethene	8.77×10^{-5}	8.39×10^{-5}	8.59×10^{-5}	8.43×10^{-5}	8.36×10^{-5}	8.24×10^{-5}	7.97×10^{-5}	7.73×10^{-5}
Uracil-Ethyne	8.46×10^{-5}	8.32×10^{-5}	7.94×10^{-5}	7.96×10^{-5}	7.84×10^{-5}	8.45×10^{-5}	7.76×10^{-5}	7.36×10^{-5}
Pyridine-Ethene	4.01×10^{-5}	3.83×10^{-5}	3.60×10^{-5}	4.26×10^{-5}	4.15×10^{-5}	5.54×10^{-5}	3.06×10^{-5}	3.03×10^{-5}
Pentane-Pentane	8.03×10^{-5}	7.84×10^{-5}	7.83×10^{-5}	8.10×10^{-5}	7.96×10^{-5}	6.65×10^{-5}	5.70×10^{-5}	4.79×10^{-5}
Neopentane-Pentane	6.33×10^{-5}	6.13×10^{-5}	6.15×10^{-5}	5.94×10^{-5}	5.65×10^{-5}	5.31×10^{-5}	4.40×10^{-5}	3.94×10^{-5}
Neopentane-Neopentane	4.01×10^{-5}	3.85×10^{-5}	3.69×10^{-5}	3.55×10^{-5}	3.38×10^{-5}	3.23×10^{-5}	3.03×10^{-5}	2.98×10^{-5}
Cyclopentane-Neopentane	5.48×10^{-5}	5.45×10^{-5}	5.13×10^{-5}	4.95×10^{-5}	4.78×10^{-5}	4.39×10^{-5}	3.80×10^{-5}	3.57×10^{-5}
Cyclopentane-Cyclopentane	6.76×10^{-5}	6.55×10^{-5}	6.37×10^{-5}	6.22×10^{-5}	5.97×10^{-5}	5.31×10^{-5}	4.55×10^{-5}	4.04×10^{-5}
Benzene-Cyclopentane	6.30×10^{-5}	6.12×10^{-5}	5.65×10^{-5}	5.35×10^{-5}	4.97×10^{-5}	4.69×10^{-5}	3.71×10^{-5}	3.35×10^{-5}
Benzene-Neopentane	4.68×10^{-5}	4.76×10^{-5}	4.67×10^{-5}	4.15×10^{-5}	3.75×10^{-5}	3.50×10^{-5}	2.78×10^{-5}	2.77×10^{-5}
Uracil-Pentane	1.05×10^{-4}	1.01×10^{-4}	9.99×10^{-5}	1.00×10^{-4}	9.83×10^{-5}	8.85×10^{-5}	8.10×10^{-5}	7.69×10^{-5}
Uracil-Cyclopentane	1.06×10^{-4}	1.02×10^{-4}	9.79×10^{-5}	9.57×10^{-5}	9.47×10^{-5}	8.92×10^{-5}	7.93×10^{-5}	8.45×10^{-5}
Uracil-Neopentane	7.96×10^{-5}	7.64×10^{-5}	7.34×10^{-5}	7.35×10^{-5}	7.32×10^{-5}	7.06×10^{-5}	6.49×10^{-5}	6.36×10^{-5}
Ethene-Pentane	5.54×10^{-5}	5.54×10^{-5}	6.16×10^{-5}	6.00×10^{-5}	5.78×10^{-5}	5.17×10^{-5}	4.51×10^{-5}	4.01×10^{-5}
Ethyne-Pentane	5.89×10^{-5}	5.83×10^{-5}	5.53×10^{-5}	5.53×10^{-5}	5.74×10^{-5}	5.21×10^{-5}	4.39×10^{-5}	4.15×10^{-5}
Peptide-Pentane	7.64×10^{-5}	7.51×10^{-5}	7.45×10^{-5}	7.32×10^{-5}	7.09×10^{-5}	6.70×10^{-5}	5.43×10^{-5}	4.43×10^{-5}
Benzene-Benzene (TS)	4.17×10^{-5}	3.99×10^{-5}	3.72×10^{-5}	3.39×10^{-5}	3.14×10^{-5}	2.72×10^{-5}	2.52×10^{-5}	2.47×10^{-5}
Pyridine-Pyridine (TS)	3.95×10^{-5}	4.09×10^{-5}	4.42×10^{-5}	4.34×10^{-5}	4.12×10^{-5}	4.40×10^{-5}	4.08×10^{-5}	3.75×10^{-5}
Benzene-Pyridine (TS)	4.67×10^{-5}	4.63×10^{-5}	4.36×10^{-5}	4.12×10^{-5}	3.93×10^{-5}	3.55×10^{-5}	3.13×10^{-5}	3.16×10^{-5}
Benzene-Ethyne (CH-pi)	4.79×10^{-5}	3.45×10^{-5}	3.56×10^{-5}	3.01×10^{-5}	2.62×10^{-5}	2.42×10^{-5}	2.14×10^{-5}	2.21×10^{-5}
Ethyne-Ethyne (TS)	5.83×10^{-5}	2.62×10^{-5}	1.99×10^{-5}	1.35×10^{-5}	1.08×10^{-5}	1.38×10^{-5}	1.03×10^{-5}	4.43×10^{-6}
Benzene-AcOH (OH-pi)	4.52×10^{-5}	4.27×10^{-5}	4.02×10^{-5}	3.88×10^{-5}	3.68×10^{-5}	3.29×10^{-5}	3.08×10^{-5}	3.13×10^{-5}

Benzene-AcNH2 (NH-pi)	4.93×10^{-5}	5.00×10^{-5}	4.98×10^{-5}	4.76×10^{-5}	4.17×10^{-5}	4.44×10^{-5}	3.87×10^{-5}	3.46×10^{-5}
Benzene-Water (OH-pi)	6.47×10^{-5}	8.28×10^{-5}	6.49×10^{-5}	5.00×10^{-5}	4.11×10^{-5}	2.70×10^{-5}	2.25×10^{-5}	2.23×10^{-5}
Benzene-MeOH (OH-pi)	3.99×10^{-5}	4.06×10^{-5}	3.62×10^{-5}	3.44×10^{-5}	3.28×10^{-5}	3.48×10^{-5}	2.81×10^{-5}	2.61×10^{-5}
Benzene-MeNH2 (NH-pi)	4.32×10^{-5}	3.69×10^{-5}	3.31×10^{-5}	3.23×10^{-5}	3.29×10^{-5}	3.48×10^{-5}	2.61×10^{-5}	2.54×10^{-5}
Benzene-Peptide (NH-pi)	6.08×10^{-5}	5.63×10^{-5}	5.40×10^{-5}	5.67×10^{-5}	5.57×10^{-5}	4.81×10^{-5}	4.21×10^{-5}	3.88×10^{-5}
Pyridine-Pyridine (CH-N)	4.40×10^{-5}	4.20×10^{-5}	6.16×10^{-5}	6.33×10^{-5}	6.86×10^{-5}	6.55×10^{-5}	5.49×10^{-5}	3.82×10^{-5}
Ethyne-Water (CH-O)	1.61×10^{-5}	1.38×10^{-5}	1.17×10^{-5}	9.82×10^{-6}	1.07×10^{-5}	7.29×10^{-6}	5.71×10^{-6}	5.89×10^{-6}
Ethyne-AcOH (OH-pi)	5.39×10^{-5}	4.73×10^{-5}	3.91×10^{-5}	3.81×10^{-5}	4.27×10^{-5}	4.03×10^{-5}	3.76×10^{-5}	3.19×10^{-5}
Pentane-AcOH	6.34×10^{-5}	6.53×10^{-5}	6.37×10^{-5}	6.29×10^{-5}	6.30×10^{-5}	6.04×10^{-5}	5.02×10^{-5}	4.46×10^{-5}
Pentane-AcNH2	7.34×10^{-5}	7.25×10^{-5}	7.11×10^{-5}	6.71×10^{-5}	6.58×10^{-5}	6.19×10^{-5}	5.23×10^{-5}	4.61×10^{-5}
Benzene-AcOH	4.97×10^{-5}	4.35×10^{-5}	4.16×10^{-5}	3.89×10^{-5}	3.71×10^{-5}	3.77×10^{-5}	3.40×10^{-5}	3.43×10^{-5}
Peptide-Ethene	4.88×10^{-5}	5.18×10^{-5}	5.11×10^{-5}	4.91×10^{-5}	4.71×10^{-5}	4.67×10^{-5}	3.96×10^{-5}	3.79×10^{-5}
Pyridine-Ethyne	3.07×10^{-5}	2.97×10^{-5}	3.17×10^{-5}	2.91×10^{-5}	2.81×10^{-5}	2.66×10^{-5}	2.47×10^{-5}	5.76×10^{-5}
MeNH2-Pyridine	4.43×10^{-5}	4.78×10^{-5}	4.24×10^{-5}	3.94×10^{-5}	4.05×10^{-5}	3.44×10^{-5}	3.43×10^{-5}	3.40×10^{-5}
RMS(RMSD)	6.36×10^{-5}	6.22×10^{-5}	5.88×10^{-5}	5.76×10^{-5}	5.69×10^{-5}	5.41×10^{-5}	4.96×10^{-5}	4.93×10^{-5}

Table B.7: Root mean square deviation between the DLPNO-MP2 and RI-MP2 gradients for dimers in the S66x8 test set. NormalPNO thresholds were used for the DLPNO-MP2 calculations. The values are given in $E_\mathrm{h}\, {a_0}^{-1}$.

Distance scaling factor	0.90	0.95	1.00	1.05	1.10	1.25	1.50	2.00
Dimer	gradient RMSD / $E_\mathrm{h}\,{a_0}^{-1}$							
Water-Water	4.84×10^{-6}	4.62×10^{-6}	4.14×10^{-6}	5.22×10^{-6}	4.40×10^{-6}	2.60×10^{-6}	1.09×10^{-6}	1.03×10^{-6}
Water-MeOH	9.81×10^{-6}	9.45×10^{-6}	9.14×10^{-6}	9.27×10^{-6}	9.24×10^{-6}	1.82×10^{-5}	4.97×10^{-6}	5.02×10^{-6}
Water-MeNH2	8.63×10^{-6}	6.39×10^{-6}	6.01×10^{-6}	6.03×10^{-6}	5.91×10^{-6}	1.77×10^{-5}	4.47×10^{-6}	4.25×10^{-6}
Water-Peptide	1.70×10^{-5}	1.58×10^{-5}	1.52×10^{-5}	1.44×10^{-5}	1.40×10^{-5}	2.54×10^{-5}	1.34×10^{-5}	1.26×10^{-5}
MeOH-MeOH	1.11×10^{-5}	1.01×10^{-5}	1.05×10^{-5}	9.36×10^{-6}	9.80×10^{-6}	1.66×10^{-5}	5.68×10^{-6}	5.49×10^{-6}
MeOH-MeNH2	9.71×10^{-6}	9.48×10^{-6}	8.27×10^{-6}	8.35×10^{-6}	8.01×10^{-6}	8.14×10^{-6}	8.07×10^{-6}	5.13×10^{-6}
MeOH-Peptide	1.51×10^{-5}	1.49×10^{-5}	1.52×10^{-5}	1.47×10^{-5}	1.40×10^{-5}	1.37×10^{-5}	1.30×10^{-5}	1.18×10^{-5}
MeOH-Water	6.72×10^{-6}	1.03×10^{-5}	8.42×10^{-6}	8.19×10^{-6}	6.80×10^{-6}	5.25×10^{-6}	4.06×10^{-6}	3.62×10^{-6}
MeNH2-MeOH	8.66×10^{-6}	7.88×10^{-6}	7.69×10^{-6}	1.59×10^{-5}	1.56×10^{-5}	6.12×10^{-6}	5.42×10^{-6}	5.68×10^{-6}
MeNH2-MeNH2	9.13×10^{-6}	9.38×10^{-6}	1.04×10^{-5}	9.43×10^{-6}	8.63×10^{-6}	8.55×10^{-6}	6.62×10^{-6}	5.33×10^{-6}
MeNH2-Peptide	1.63×10^{-5}	1.63×10^{-5}	1.62×10^{-5}	1.73×10^{-5}	1.63×10^{-5}	1.68×10^{-5}	1.72×10^{-5}	1.15×10^{-5}
MeNH2-Water	7.56×10^{-6}	7.30×10^{-6}	6.98×10^{-6}	6.47×10^{-6}	6.34×10^{-6}	5.67×10^{-6}	1.74×10^{-5}	4.28×10^{-6}
Peptide-MeOH	1.97×10^{-5}	1.87×10^{-5}	1.80×10^{-5}	1.78×10^{-5}	2.05×10^{-5}	1.63×10^{-5}	1.73×10^{-5}	1.90×10^{-5}
Peptide- MeNH2	2.30×10^{-5}	2.21×10^{-5}	1.58×10^{-5}	1.86×10^{-5}	1.79×10^{-5}	1.83×10^{-5}	1.82×10^{-5}	1.32×10^{-5}
Peptide-Peptide	2.43×10^{-5}	2.35×10^{-5}	2.36×10^{-5}	2.29×10^{-5}	2.20×10^{-5}	1.67×10^{-5}	1.53×10^{-5}	1.85×10^{-5}
Peptide-Water	1.61×10^{-5}	1.65×10^{-5}	1.61×10^{-5}	1.50×10^{-5}	1.41×10^{-5}	1.37×10^{-5}	1.33×10^{-5}	1.24×10^{-5}
Uracil-Uracil (BP)	4.45×10^{-5}	4.86×10^{-5}	5.00×10^{-5}	4.76×10^{-5}	5.06×10^{-5}	5.20×10^{-5}	4.71×10^{-5}	4.59×10^{-5}
Water-Pyridine	2.20×10^{-5}	3.51×10^{-5}	2.31×10^{-5}	2.98×10^{-5}	2.39×10^{-5}	2.25×10^{-5}	2.29×10^{-5}	5.43×10^{-5}
MeOH-Pyridine	1.47×10^{-5}	1.59×10^{-5}	1.58×10^{-5}	1.58×10^{-5}	1.59×10^{-5}	1.27×10^{-5}	2.16×10^{-5}	4.94×10^{-5}
AcOH-AcOH	4.53×10^{-5}	4.26×10^{-5}	2.31×10^{-5}	2.35×10^{-5}	2.36×10^{-5}	3.37×10^{-5}	2.62×10^{-5}	2.13×10^{-5}
AcNH2-AcNH2	2.15×10^{-5}	2.13×10^{-5}	2.10×10^{-5}	2.19×10^{-5}	2.15×10^{-5}	1.99×10^{-5}	2.54×10^{-5}	2.89×10^{-5}
AcOH-Uracil	4.57×10^{-5}	4.48×10^{-5}	4.36×10^{-5}	4.47×10^{-5}	4.24×10^{-5}	4.15×10^{-5}	3.29×10^{-5}	3.55×10^{-5}
AcNH2-Uracil	3.51×10^{-5}	3.89×10^{-5}	3.44×10^{-5}	3.57×10^{-5}	3.63×10^{-5}	3.53×10^{-5}	3.18×10^{-5}	3.58×10^{-5}
Benzene-Benzene (pi-pi)	1.72×10^{-5}	1.70×10^{-5}	1.57×10^{-5}	1.45×10^{-5}	1.42×10^{-5}	1.18×10^{-5}	9.28×10^{-6}	7.94×10^{-6}

Pyridine-Pyridine (pi-pi)	3.49×10^{-5}	3.26×10^{-5}	2.71×10^{-5}	2.57×10^{-5}	3.30×10^{-5}	2.72×10^{-5}	1.29×10^{-5}	2.58×10^{-5}
Uracil-Uracil (pi-pi)	4.26×10^{-5}	3.99×10^{-5}	3.91×10^{-5}	3.70×10^{-5}	3.46×10^{-5}	2.75×10^{-5}	2.81×10^{-5}	3.25×10^{-5}
Benzene-Pyridine (pi-pi)	2.85×10^{-5}	3.31×10^{-5}	3.39×10^{-5}	3.92×10^{-5}	3.77×10^{-5}	1.92×10^{-5}	1.09×10^{-5}	1.91×10^{-5}
Benzene-Uracil (pi-pi)	3.24×10^{-5}	3.04×10^{-5}	2.97×10^{-5}	2.78×10^{-5}	2.65×10^{-5}	2.67×10^{-5}	2.50×10^{-5}	3.07×10^{-5}
Pyridine-Uracil (pi-pi)	3.10×10^{-5}	2.81×10^{-5}	3.02×10^{-5}	3.26×10^{-5}	3.25×10^{-5}	3.28×10^{-5}	3.76×10^{-5}	2.84×10^{-5}
Benzene-Ethene	1.13×10^{-5}	1.14×10^{-5}	9.98×10^{-6}	1.99×10^{-5}	1.38×10^{-5}	8.46×10^{-6}	7.23×10^{-6}	7.11×10^{-6}
Uracil-Ethene	2.87×10^{-5}	2.58×10^{-5}	2.78×10^{-5}	2.72×10^{-5}	2.68×10^{-5}	2.80×10^{-5}	2.77×10^{-5}	2.55×10^{-5}
Uracil-Ethyne	2.90×10^{-5}	2.79×10^{-5}	2.66×10^{-5}	2.91×10^{-5}	2.84×10^{-5}	3.43×10^{-5}	2.96×10^{-5}	2.69×10^{-5}
Pyridine-Ethene	1.72×10^{-5}	1.73×10^{-5}	1.66×10^{-5}	2.10×10^{-5}	2.04×10^{-5}	4.41×10^{-5}	2.03×10^{-5}	2.07×10^{-5}
Pentane-Pentane	2.96×10^{-5}	2.95×10^{-5}	2.74×10^{-5}	2.74×10^{-5}	2.56×10^{-5}	2.25×10^{-5}	1.79×10^{-5}	1.28×10^{-5}
Neopentane-Pentane	2.51×10^{-5}	2.35×10^{-5}	2.31×10^{-5}	2.31×10^{-5}	2.21×10^{-5}	1.90×10^{-5}	1.59×10^{-5}	1.32×10^{-5}
Neopentane-Neopentane	1.74×10^{-5}	1.69×10^{-5}	1.79×10^{-5}	1.61×10^{-5}	1.59×10^{-5}	1.53×10^{-5}	1.42×10^{-5}	1.43×10^{-5}
Cyclopentane-Neopentane	2.06×10^{-5}	1.93×10^{-5}	1.83×10^{-5}	1.80×10^{-5}	1.80×10^{-5}	1.74×10^{-5}	1.57×10^{-5}	1.50×10^{-5}
Cyclopentane-Cyclopentane	2.48×10^{-5}	2.34×10^{-5}	2.17×10^{-5}	2.08×10^{-5}	1.95×10^{-5}	1.76×10^{-5}	1.69×10^{-5}	1.49×10^{-5}
Benzene-Cyclopentane	2.21×10^{-5}	2.15×10^{-5}	2.10×10^{-5}	1.95×10^{-5}	1.80×10^{-5}	1.63×10^{-5}	1.41×10^{-5}	1.27×10^{-5}
Benzene-Neopentane	1.94×10^{-5}	1.88×10^{-5}	1.81×10^{-5}	1.67×10^{-5}	1.60×10^{-5}	1.35×10^{-5}	1.24×10^{-5}	1.21×10^{-5}
Uracil-Pentane	3.93×10^{-5}	3.67×10^{-5}	3.60×10^{-5}	3.59×10^{-5}	3.51×10^{-5}	3.00×10^{-5}	2.50×10^{-5}	2.24×10^{-5}
Uracil-Cyclopentane	3.79×10^{-5}	3.77×10^{-5}	3.73×10^{-5}	3.31×10^{-5}	3.32×10^{-5}	3.03×10^{-5}	2.60×10^{-5}	2.90×10^{-5}
Uracil-Neopentane	3.30×10^{-5}	3.10×10^{-5}	2.91×10^{-5}	2.86×10^{-5}	2.73×10^{-5}	2.75×10^{-5}	2.35×10^{-5}	2.32×10^{-5}
Ethene-Pentane	1.96×10^{-5}	1.94×10^{-5}	1.81×10^{-5}	1.69×10^{-5}	1.66×10^{-5}	1.67×10^{-5}	1.53×10^{-5}	1.05×10^{-5}
Ethyne-Pentane	1.85×10^{-5}	1.83×10^{-5}	1.80×10^{-5}	1.69×10^{-5}	1.64×10^{-5}	1.52×10^{-5}	1.31×10^{-5}	1.06×10^{-5}
Peptide-Pentane	2.70×10^{-5}	2.64×10^{-5}	2.46×10^{-5}	2.40×10^{-5}	2.39×10^{-5}	2.09×10^{-5}	1.77×10^{-5}	1.35×10^{-5}
Benzene-Benzene (TS)	1.82×10^{-5}	2.11×10^{-5}	1.51×10^{-5}	1.40×10^{-5}	1.41×10^{-5}	1.02×10^{-5}	8.99×10^{-6}	8.10×10^{-6}
Pyridine-Pyridine (TS)	1.87×10^{-5}	2.26×10^{-5}	2.41×10^{-5}	2.25×10^{-5}	2.19×10^{-5}	2.96×10^{-5}	3.07×10^{-5}	2.56×10^{-5}
Benzene-Pyridine (TS)	2.11×10^{-5}	1.95×10^{-5}	2.03×10^{-5}	2.02×10^{-5}	1.99×10^{-5}	2.11×10^{-5}	1.90×10^{-5}	1.92×10^{-5}
Benzene-Ethyne (CH-pi)	2.09×10^{-5}	1.37×10^{-5}	1.10×10^{-5}	1.11×10^{-5}	9.66×10^{-6}	1.09×10^{-5}	7.45×10^{-6}	7.45×10^{-6}
Ethyne-Ethyne (TS)	2.64×10^{-5}	1.20×10^{-5}	9.29×10^{-6}	3.95×10^{-6}	2.93×10^{-6}	6.14×10^{-6}	3.17×10^{-6}	1.58×10^{-6}
Benzene-AcOH (OH-pi)	2.27×10^{-5}	2.15×10^{-5}	2.15×10^{-5}	2.05×10^{-5}	1.93×10^{-5}	1.52×10^{-5}	1.48×10^{-5}	1.25×10^{-5}

Benzene-AcNH2 (NH-pi)	2.12×10^{-5}	2.09×10^{-5}	1.97×10^{-5}	1.85×10^{-5}	1.53×10^{-5}	1.75×10^{-5}	1.31×10^{-5}	1.20×10^{-5}
Benzene-Water (OH-pi)	1.14×10^{-5}	1.04×10^{-5}	1.08×10^{-5}	2.15×10^{-5}	1.60×10^{-5}	1.09×10^{-5}	7.36×10^{-6}	7.25×10^{-6}
Benzene-MeOH (OH-pi)	1.41×10^{-5}	1.98×10^{-5}	1.56×10^{-5}	1.64×10^{-5}	1.32×10^{-5}	1.05×10^{-5}	9.49×10^{-6}	7.49×10^{-6}
Benzene-MeNH2 (NH-pi)	1.45×10^{-5}	1.50×10^{-5}	1.28×10^{-5}	1.13×10^{-5}	1.07×10^{-5}	9.98×10^{-6}	8.83×10^{-6}	7.47×10^{-6}
Benzene-Peptide (NH-pi)	2.12×10^{-5}	2.04×10^{-5}	1.95×10^{-5}	2.85×10^{-5}	2.86×10^{-5}	2.74×10^{-5}	2.71×10^{-5}	2.16×10^{-5}
Pyridine-Pyridine (CH-N)	2.56×10^{-5}	2.60×10^{-5}	5.40×10^{-5}	5.56×10^{-5}	6.41×10^{-5}	5.95×10^{-5}	4.73×10^{-5}	2.58×10^{-5}
Ethyne-Water (CH-O)	5.56×10^{-6}	4.89×10^{-6}	4.85×10^{-6}	4.03×10^{-6}	3.89×10^{-6}	3.69×10^{-6}	1.71×10^{-6}	2.07×10^{-6}
Ethyne-AcOH (OH-pi)	3.42×10^{-5}	2.51×10^{-5}	1.83×10^{-5}	1.78×10^{-5}	2.16×10^{-5}	2.09×10^{-5}	1.91×10^{-5}	1.41×10^{-5}
Pentane-AcOH	2.27×10^{-5}	2.22×10^{-5}	2.21×10^{-5}	2.22×10^{-5}	2.47×10^{-5}	2.25×10^{-5}	1.68×10^{-5}	1.43×10^{-5}
Pentane-AcNH2	2.67×10^{-5}	2.55×10^{-5}	2.49×10^{-5}	2.38×10^{-5}	2.25×10^{-5}	2.02×10^{-5}	1.85×10^{-5}	1.56×10^{-5}
Benzene-AcOH	2.08×10^{-5}	1.59×10^{-5}	1.55×10^{-5}	1.48×10^{-5}	1.40×10^{-5}	1.89×10^{-5}	1.70×10^{-5}	1.72×10^{-5}
Peptide-Ethene	1.54×10^{-5}	1.51×10^{-5}	1.49×10^{-5}	1.46×10^{-5}	1.44×10^{-5}	1.53×10^{-5}	2.26×10^{-5}	2.16×10^{-5}
Pyridine-Ethyne	1.20×10^{-5}	1.19×10^{-5}	1.42×10^{-5}	1.28×10^{-5}	1.27×10^{-5}	1.26×10^{-5}	1.01×10^{-5}	5.20×10^{-5}
MeNH2-Pyridine	1.46×10^{-5}	1.91×10^{-5}	1.53×10^{-5}	1.57×10^{-5}	1.90×10^{-5}	1.29×10^{-5}	1.94×10^{-5}	2.07×10^{-5}
RMS(RMSD)	2.39×10^{-5}	2.34×10^{-5}	2.26×10^{-5}	2.30×10^{-5}	2.30×10^{-5}	2.26×10^{-5}	1.97×10^{-5}	2.12×10^{-5}

Table B.8: Root mean square deviation between the DLPNO-MP2 and RI-MP2 gradients for dimers in the S66x8 test set. TightPNO thresholds were used for the DLPNO-MP2 calculations. The values are given in $E_\mathrm{h}\, {a_0}^{-1}$.

B.4 Geometry optimisations

B.4.1 ROT34 test set

Rotational constants for the molecules in the ROT34 test set calculated using DLPNO-MP2 with different basis sets and threshold settings are provided in Tables B.10 and B.11. Table B.9 shows the RI-MP2 reference results calculated with different basis sets. The data was discussed in Section 3.3.5.1.

molecule	rotational constant / MHz								
	def2-SVP			def2-TZVP			def2-QZVPP		
	A	B	C	A	B	C	A	B	C
Ethynyl-cyclohexane	4261.887	1377.507	1116.501	4285.885	1394.25	1129.924	4300.878	1398.551	1133.374
Isoamyl-acetate	3289.969	728.968	704.523	3316.071	725.795	704.254	3317.489	726.249	704.786
Diisopropylketone	3042.761	1279.628	1240.819	3067.107	1292.071	1245.223	3076.974	1291.78	1252.23
Bicyclo[2.2.2]octadiene	2741.127	2653.365	2633.326	2758.982	2674.285	2648.406	2766.957	2682.678	2656.596
Triethylamine	2321.078	(2321.067)	(1339.714)	2332.938	(2332.897)	(1332.083)	2344.107	(2344.046)	(1334.248)
Vitamin C	1448.709	784.67	590.945	1453.416	773.483	584.151	1458.666	775.197	585.137
Serotonin	1150.542	662.728	450.862	1169.317	660.88	455.539	1174.999	660.67	456.644
Aspirin	1165.708	759.633	510.1	1165.132	765.611	512.987	1173.109	767.856	515.087
Cassyrane	859.749	751.579	513.309	861.073	756.512	514.287	864.282	757.885	515.587
Limonene	3052.667	718.331	679.97	3079.342	724.501	685.216	3090.155	726.101	687.328
Lupinine	1437.966	818.283	679.736	1434.087	821.896	681.106	1438.886	823.937	682.982
Proline derivative	1497.749	1075.201	721.55	1522.121	1068.709	721.408	1525.84	1073.698	723.866

Table B.9: Rotational constants for the RI-MP2 equilibrium geometries of the molecules in the ROT34 test set. The calculations were performed with the def2-SVP, def2-TZVP and def2-QZVPP basis sets.

molecule	rotational constant / MHz								
	LoosePNO			NormalPNO			TightPNO		
	A	B	C	A	B	C	A	B	C
Ethynyl-cyclohexane	4282.886	1393.053	1128.843	4284.938	1393.733	1129.485	4285.523	1394.121	1129.81
Isoamyl-acetate	3314.736	722.862	701.581	3315.614	724.562	703.126	3316.03	725.335	703.829
Diisopropylketone	3066.175	1290.141	1243.393	3067.024	1291.321	1244.533	3067.119	1291.786	1244.927
Bicyclo[2.2.2]octadiene	2756.8	2672.668	2647.188	2758.451	2673.991	2648.132	2758.76	2674.088	2648.32
Triethylamine	2330.941	(2330.915)	(1331.191)	2331.978	(2331.949)	(1331.565)	2332.602	(2332.558)	(1332.069)
Vitamin C	1454.181	770.881	582.505	1453.776	772.428	583.461	1453.662	772.971	583.823
Serotonin	1168.445	659.052	454.523	1168.89	660.197	455.126	1169.145	660.615	455.37
Aspirin	1161.533	764.876	511.969	1163.284	765.377	512.441	1164.318	765.526	512.783
Cassyrane	859.446	755.318	513.28	860.29	756.128	513.875	860.826	756.326	514.129
Limonene	3078.569	723.557	684.249	3079.328	724.185	684.778	3079.302	724.362	685.074
Lupinine	1431.906	820.243	679.44	1433.331	820.971	680.305	1433.896	821.493	680.805
Proline derivative	1519.413	1067.609	720.042	1521.37	1068.132	720.848	1522.039	1068.446	721.211

Table B.10: Rotational constants for the DLPNO-MP2 equilibrium geometries of the molecules in the ROT34 test set. The calculations were performed with the def2-TZVP basis set using different accuracy settings.

molecule	rotational constant / MHz					
	def2-SVP			def2-QZVPP		
	A	B	C	A	B	C
Ethynyl-cyclohexane	4261.759	1377.174	1116.218	4300.174	1398.169	1133.038
Isoamyl-acetate	3290.385	728.203	703.836	3319.207	725.299	703.816
Diisopropylketone	3042.564	1279.039	1240.296	3076.645	1291.057	1251.779
Bicyclo[2.2.2]octadiene	2740.785	2653.071	2633.371	2766.438	2682.412	2656.417
Triethylamine	2320.365	(2320.33)	(1339.076)	2343.427	(2343.337)	(1333.849)
Vitamin C	1449.1	783.841	590.388	1458.99	774.207	584.461
Serotonin	1150.367	662.202	450.594	1174.656	660.186	456.331
Aspirin	1164.949	759.297	509.849	1171.895	767.602	514.704
Cassyrane	858.907	751.383	512.996	863.797	757.57	515.285
Limonene	3052.531	718.141	679.616	3089.955	725.79	687.078
Lupinine	1437.47	817.705	679.308	1438.291	823.359	682.425
Proline derivative	1497.016	1074.891	721.11	1524.031	1073.594	723.337

Table B.11: Rotational constants for the DLPNO-MP2 equilibrium geometries of the molecules in the ROT34 test set. The calculations were performed using NormalPNO thresholds with the def2-SVP and def2-QZVPP basis sets. Results for the def2-TZVP set are provided in Table B.10.

B.4.2 Baker test set

Table B.12 contains the root mean square error of bond lengths for molecules in the Baker set. A graphical representation of the data is provided in Figure 3.13.

Name	Atoms	RMSD(r) / pm		
		LoosePNO	NormalPNO	TightPNO
water	3	0.0011	0.0005	0.0005
acetylene	4	0.0014	0.0017	0.0019
ammonia	4	0.0024	0.0009	0.0009
hydroxysulphane	4	0.0065	0.0018	0.0003
allene	7	0.0015	0.0008	0.0007
methylamine	7	0.0076	0.0031	0.0011
ethane	8	0.0063	0.0015	0.0006
disilyl ether	9	0.0097	0.0014	0.0010
ethanol	9	0.0102	0.0044	0.0017
furan	9	0.0105	0.0068	0.0012
acetone	10	0.0151	0.0078	0.0055
benzene	12	0.0085	0.0016	0.0014
1,3-difluorobenzene	12	0.0186	0.0062	0.0029
1,3,5-trifluorobenzene	12	0.0191	0.0064	0.0051
benzaldehyde	14	0.0157	0.0066	0.0022
2-hydroxybicyclopentane	14	0.0179	0.0062	0.0025
ACHTAR10	16	0.0181	0.0068	0.0032
difuropyrazine	16	0.0326	0.0101	0.0035
mesityl oxide	17	0.0291	0.0092	0.0038
neopentane	17	0.0222	0.0057	0.0028
pterin	17	0.0294	0.0113	0.0035
1,5-difluoronaphthalene	18	0.0341	0.0118	0.0042
naphthalene	18	0.0333	0.0109	0.0054
1,3,5-trisilylacyclohexane	18	0.0321	0.0049	0.0033
ACANIL01	19	0.0249	0.0097	0.0042
histidine	20	0.0335	0.0130	0.0113
dimethylpentane	23	0.0368	0.0082	0.0035
caffeine	24	0.0370	0.0153	0.0061
benzidine	26	0.0369	0.0143	0.0052
menthone	29	0.0437	0.0172	0.0068

Table B.12: Root mean square deviations of bond lengths between DLPNO-MP2 and RI-MP2. The RMSD was calculated over all covalent bonds in each molecule.

B.4.3 S66 test set

Table B.13 provides distances between the centres of mass of the monomers in the S66 set. The calculations were performed using DLPNO-MP2 with different threshold settings, and for comparison with RI-MP2. A graphical representation of errors in the distances is provided in Figure 3.15.

Dimer	Atoms	Distance / pm			
		RI-MP2	Loose	Normal	Tight
Water-Water	6	291.47	291.75	291.57	291.51
Water-MeOH	9	301.18	301.92	301.47	301.29
Water-MeNH2	10	298.78	299.55	299.01	298.91
Water-Peptide	15	381.25	382.03	381.60	381.41
MeOH-MeOH	12	335.49	336.47	336.17	335.76
MeOH-MeNH2	13	331.41	333.91	331.70	331.52
MeOH-Peptide	18	411.54	413.47	412.34	411.77
MeOH-Water	9	320.25	320.61	320.42	320.33
MeNH2-MeOH	13	351.08	352.78	351.70	351.29
MeNH2-MeNH2	14	344.47	346.27	345.17	344.78
MeNH2-Peptide	19	347.61	352.82	350.06	348.80
MeNH2-Water	10	298.92	299.60	299.15	299.04
Peptide-MeOH	18	381.97	386.32	383.42	382.40
Peptide- MeNH2	19	385.00	387.19	386.12	385.35
Peptide-Peptide	24	463.40	468.40	465.52	464.06
Peptide-Water	15	378.31	379.06	378.51	378.41
Uracil-Uracil (BP)	24	571.10	572.09	571.54	571.26
Water-Pyridine	14	425.85	426.54	426.10	425.95
MeOH-Pyridine	17	443.12	445.14	444.03	443.45
AcOH-AcOH	16	393.99	394.52	394.16	394.06
AcNH2-AcNH2	18	421.74	422.31	421.98	421.84
AcOH-Uracil	20	499.60	500.42	499.84	499.68
AcNH2-Uracil	21	506.16	507.07	506.66	506.28
Benzene-Benzene (pi-pi)	24	366.54	371.51	367.99	367.02
Pyridine-Pyridine (pi-pi)	22	352.78	357.50	353.97	353.19
Uracil-Uracil (pi-pi)	24	306.18	309.70	307.20	306.58
Benzene-Pyridine (pi-pi)	23	360.04	364.39	361.33	360.48
Benzene-Uracil (pi-pi)	24	328.41	332.67	329.49	328.82
Pyridine-Uracil (pi-pi)	23	324.38	328.28	325.57	324.81
Benzene-Ethene	18	335.60	341.24	336.82	335.95
Uracil-Ethene	18	325.54	329.99	326.70	325.92
Uracil-Ethyne	16	320.09	324.05	322.16	320.38
Pyridine-Ethene	17	330.94	335.23	332.03	331.26

Pentane-Pentane	34	383.35	390.81	386.85	383.73
Neopentane-Pentane	34	456.74	464.56	459.68	457.86
Neopentane-Neopentane	34	530.64	540.60	534.12	531.96
Cyclopentane-Neopentane	32	470.99	479.92	473.92	472.07
Cyclopentane-Cyclopentane	30	425.11	431.62	427.62	426.06
Benzene-Cyclopentane	27	388.68	393.53	390.35	389.27
Benzene-Neopentane	29	443.05	448.11	445.01	443.69
Uracil-Pentane	29	349.49	355.24	351.68	350.28
Uracil-Cyclopentane	27	370.36	375.31	372.32	371.00
Uracil-Neopentane	29	429.18	435.24	431.08	430.15
Ethene-Pentane	23	375.63	380.75	377.93	375.79
Ethyne-Pentane	21	362.03	368.47	363.89	362.63
Peptide-Pentane	29	359.78	365.01	361.48	360.46
Benzene-Benzene (TS)	24	479.36	482.94	480.63	480.02
Pyridine-Pyridine (TS)	22	478.85	482.47	479.96	479.27
Benzene-Pyridine (TS)	23	480.35	483.76	481.62	480.88
Benzene-Ethyne (CH-pi)	16	406.30	408.65	407.34	406.59
Ethyne-Ethyne (TS)	8	437.23	438.69	437.99	437.40
Benzene-AcOH (OH-pi)	20	405.75	408.70	406.81	406.17
Benzene-AcNH2 (NH-pi)	21	413.28	418.27	414.64	414.64
Benzene-Water (OH-pi)	15	322.38	324.04	322.95	322.62
Benzene-MeOH (OH-pi)	18	337.81	340.09	338.60	338.10
Benzene-MeNH2 (NH-pi)	19	353.26	355.91	354.11	353.66
Benzene-Peptide (NH-pi)	24	404.82	408.01	405.89	405.26
Pyridine-Pyridine (CH-N)	22	582.24	583.94	583.02	582.62
Ethyne-Water (CH-O)	7	390.81	391.27	390.99	390.85
Ethyne-AcOH (OH-pi)	12	391.88	392.88	392.31	392.05
Pentane-AcOH	25	371.41	376.63	373.61	372.48
Pentane-AcNH2	26	356.00	360.93	357.92	356.75
Benzene-AcOH	20	371.28	374.96	372.73	371.83
Peptide-Ethene	18	358.67	360.94	358.67	359.37
Pyridine-Ethyne	15	529.63	530.53	530.00	529.78
MeNH2-Pyridine	18	357.23	362.04	359.00	357.75

Table B.13: Distances between the centres of mass of the monomers in the S66 set. DLPNO-MP2 calculations were performed with different threshold settings (LoosePNO, NormalPNO, TightPNO), and the def2-TZVP set was used throughout. The original ordering of the systems from ref. [155] was preserved in this table.

Appendix C

Influence of the orbital localisation convergence on reaction energies

Results of local correlation calculations depend, to some extent, on the localisation criterion for the occupied orbitals. Even with the same mathematical criterion, the numerical procedure can influence the results, depending on the specific set of orbitals that it converges to.

Calculations with DLPNO-CCSD(T)[44] were performed for reaction energies in the ISOL24 set[242] (Table C.1), and for dimerisation energies in the S66 set (Table C.2) without counterpoise corrections. The def2-TZVP set was used in all calculations. In each case, the localised orbitals were determined with the Foster-Boys criterion: either using the default procedure with Jacobi sweeps, or with rational function optimisation as described in Section 3.2.4.

While most reaction energies in the ISOL24 set agree between the two localisation procedures, in a few cases (e.g. 1, 12, 18) there are significant deviations of up to $1\,\mathrm{kJ\,mol^{-1}}$. These are usually the consequence of the two procedures converging to different stationary points.

For the majority of examples in the S66 set, the dimerisation energies are sufficiently close for practical purposes. However, the respective dimerisation energies of systems 49 and 58 differ by ca. $4\,\mathrm{kJ\,mol^{-1}}$. In both cases, the Jacobi sweep procedure converges to

a saddle point for a pyridine monomer geometry, whereas the AHFB procedure correctly locates a local maximum.

Reaction	ΔE/kJ mol^{-1}		Reaction	ΔE/kJ mol^{-1}	
	default	AHFB		default	AHFB
1	292.91	293.77	13	131.55	131.41
2	163.48	163.48	14	14.75	14.75
3	38.45	38.45	15	18.34	18.35
4	291.74	291.74	16	85.96	85.96
5	138.46	138.46	17	41.88	40.89
6	92.08	91.99	18	110.87	110.15
7	74.63	74.63	19	73.11	73.11
8	79.78	79.78	20	20.61	20.57
9	93.69	93.69	21	48.79	48.78
10	22.16	22.15	22	4.32	4.17
11	159.62	159.54	23	109.11	108.88
12	0.63	1.46	24	63.13	63.13

Table C.1: Reaction energies in the ISOL24 set calculated with DLPNO-CCSD(T) using the def2-TZVP basis set. In each case, Foster-Boys orbitals were calculated either using the Jacobi sweep scheme (default) or using rational function optimisation (AHFB).

Dimer	ΔE/kJ mol^{-1}		Dimer	ΔE/kJ mol^{-1}	
	default	AHFB		default	AHFB
1	−22.38	−22.38	34	−13.78	−13.78
2	−24.27	−24.27	35	−9.14	−9.14
3	−29.48	−29.48	36	−5.93	−5.93
4	−32.63	−32.64	37	−8.46	−8.46
5	−25.23	−25.23	38	−10.39	−10.39
6	−32.52	−32.52	39	−16.50	−16.50
7	−33.96	−33.96	40	−13.11	−13.11
8	−22.82	−22.82	41	−21.10	−21.10
9	−13.07	−13.07	42	−18.18	−18.18
10	−18.03	−18.03	43	−16.08	−16.08
11	−22.33	−22.33	44	−7.19	−7.19
12	−31.34	−31.34	45	−6.65	−6.65
13	−26.38	−26.37	46	−17.15	−17.15
14	−32.34	−32.33	47	−13.75	−13.75
15	−34.82	−34.82	48	−16.06	−16.06
16	−23.19	−23.19	49	−11.03	−15.35
17	−65.75	−65.75	50	−13.26	−13.27
18	−27.79	−27.79	51	−5.93	−5.84
19	−30.69	−30.69	52	−20.56	−20.56
20	−73.74	−73.73	53	−18.25	−18.25
21	−62.83	−62.83	54	−16.24	−16.24
22	−75.37	−75.30	55	−19.35	−19.35
23	−74.71	−74.69	56	−14.91	−14.91
24	−15.90	−15.72	57	−23.81	−23.72
25	−20.40	−20.40	58	−12.03	−16.31
26	−44.99	−44.99	59	−13.61	−13.61
27	−18.46	−18.47	60	−18.05	−18.05
28	−28.42	−28.41	61	−11.58	−11.58
29	−32.29	−32.30	62	−14.16	−14.16
30	−7.07	−7.07	63	−17.03	−16.93
31	−15.01	−15.02	64	−11.97	−11.97
32	−15.98	−16.04	65	−16.58	−16.58
33	−9.10	−9.10	66	−16.91	−16.91

Table C.2: Dimerisation energies in the S66 set calculated with DLPNO-CCSD(T) using the def2-TZVP basis set. In each case, Foster-Boys orbitals were calculated either using the Jacobi sweep scheme (default) or using rational function optimisation (AHFB).

Bibliography

[1]T. Helgaker, J. Olsen, and P. Jørgensen, *Molecular Electronic-Structure Theory* (Wiley-Blackwell, 2013).

[2]I. Shavitt, and R. J. Bartlett, *Many-Body Methods in Chemistry and Physics* (Cambridge University Press, 2009).

[3]E. Solomonik, D. Matthews, J. R. Hammond, J. F. Stanton, and J. Demmel, "A massively parallel tensor contraction framework for coupled-cluster computations", J. Parallel Distrib. Comput. **74**, 3176–3190 (2014).

[4]J. A. Calvin, C. A. Lewis, and E. F. Valeev, "Scalable task-based algorithm for multiplication of block-rank-sparse matrices", in Proceedings of the 5th Workshop on Irregular Applications Architectures and Algorithms - IA3 '15 (2015).

[5]M. Katouda, A. Naruse, Y. Hirano, and T. Nakajima, "Massively parallel algorithm and implementation of RI-MP2 energy calculation for peta-scale many-core supercomputers", J. Comput. Chem. **37**, 2623–2633 (2016).

[6]S. Yoo, E. Aprà, X. C. Zeng, and S. S. Xantheas, "High-Level Ab Initio Electronic Structure Calculations of Water Clusters $(H_2O)_{16}$ and $(H_2O)_{17}$: A New Global Minimum for $(H_2O)_{16}$", J. Phys. Chem. Lett. **1**, 3122–3127 (2010).

[7]P. Pulay, "Localizability of dynamic electron correlation", Chem. Phys. Lett. **100**, 151–154 (1983).

[8]S. Saebø, and P. Pulay, "Local configuration interaction: An efficient approach for larger molecules", Chem. Phys. Lett. **113**, 13–18 (1985).

[9]P. Pulay, and S. Saebø, "Orbital-invariant formulation and second-order gradient evaluation in Møller-Plesset perturbation theory", Theor. Chim. Acta **69**, 357–368 (1986).

[10]S. Saebø, and P. Pulay, "Fourth-order Møller–Plessett perturbation theory in the local correlation treatment. I. Method", J. Chem. Phys. **86**, 914–922 (1987).

[11]S. Saebø, and P. Pulay, "The local correlation treatment. II. Implementation and tests", J. Chem. Phys. **88**, 1884–1890 (1988).

[12]I.-M. Høyvik, B. Jansik, and P. Jørgensen, "Trust Region Minimization of Orbital Localization Functions", J. Chem. Theory Comput. **8**, 3137–3146 (2012).

[13]I.-M. Høyvik, K. Kristensen, T. Kjærgaard, and P. Jørgensen, "A perspective on the localizability of Hartree–Fock orbitals", Theor. Chem. Acc. **133**, 1417 (2014).

[14]I.-M. Høyvik, and P. Jørgensen, "Characterization and Generation of Local Occupied and Virtual Hartree–Fock Orbitals", Chem. Rev. **116**, 3306–3327 (2016).

[15]M. Schütz, G. Hetzer, and H.-J. Werner, "Low-order scaling local electron correlation methods. I. Linear scaling local MP2", J. Chem. Phys. **111**, 5691–5705 (1999).

[16]C. Hampel, and H.-J. Werner, "Local treatment of electron correlation in coupled cluster theory", J. Chem. Phys. **104**, 6286–6297 (1996).

[17]M. Schütz, and H.-J. Werner, "Low-order scaling local electron correlation methods. IV. Linear scaling local coupled-cluster (LCCSD)", J. Chem. Phys. **114**, 661 (2001).

[18]M. Schütz, and H.-J. Werner, "Local perturbative triples correction (T) with linear cost scaling", Chem. Phys. Lett. **318**, 370–378 (2000).

[19]H.-J. Werner, F. R. Manby, and P. J. Knowles, "Fast linear scaling second-order Møller-Plesset perturbation theory (MP2) using local and density fitting approximations", J. Chem. Phys. **118**, 8149–8160 (2003).

[20]H.-J. Werner, and M. Schütz, "An efficient local coupled cluster method for accurate thermochemistry of large systems", J. Chem. Phys. **135**, 144116 (2011).

[21]O. Vahtras, J. Almlöf, and M. Feyereisen, "Integral approximations for LCAO-SCF calculations", Chem. Phys. Lett. **213**, 514–518 (1993).

[22]M. Feyereisen, G. Fitzgerald, and A. Komornicki, "Use of approximate integrals in ab initio theory. An application in MP2 energy calculations", Chem. Phys. Lett. **208**, 359–363 (1993).

[23]J. W. Boughton, and P. Pulay, "Comparison of the boys and Pipek-Mezey localizations in the local correlation approach and automatic virtual basis selection", J. Comput. Chem. **14**, 736–740 (1993).

[24]D. G. Liakos, M. Sparta, M. K. Kesharwani, J. M. L. Martin, and F. Neese, "Exploring the Accuracy Limits of Local Pair Natural Orbital Coupled-Cluster Theory", J. Chem. Theory Comput. **11**, 1525–1539 (2015).

[25]D. G. Liakos, and F. Neese, "Is It Possible To Obtain Coupled Cluster Quality Energies at near Density Functional Theory Cost? Domain-Based Local Pair Natural Orbital Coupled Cluster vs Modern Density Functional Theory", J. Chem. Theory Comput. **11**, 4054–4063 (2015).

[26]D. G. Liakos, Y. Guo, and F. Neese, "Comprehensive Benchmark Results for the Domain Based Local Pair Natural Orbital Coupled Cluster Method (DLPNO-CCSD(T)) for Closed- and Open-Shell Systems", J. Phys. Chem. A **124**, 90–100 (2019).

[27]C. Edmiston, and M. Krauss, "Pseudonatural Orbitals as a Basis for the Superposition of Configurations. I. $He_2{}^+$", J. Chem. Phys. **45**, 1833–1839 (1966).

[28]C. Edmiston, and M. Krauss, "Pseudonatural Orbitals as a Basis for the Superposition of Configurations. II. Energy Surface for Linear H_3", J. Chem. Phys. **49**, 192–205 (1968).

[29]W. Meyer, "Ionization energies of water from PNO-CI calculations", Int. J. Quantum Chem. **5**, 341–348 (1971).

[30]W. Meyer, "PNO–CI Studies of electron correlation effects. I. Configuration expansion by means of nonorthogonal orbitals, and application to the ground state and ionized states of methane", J. Chem. Phys. **58**, 1017–1035 (1973).

[31]R. Ahlrichs, H. Lischka, V. Staemmler, and W. Kutzelnigg, "PNO–CI (pair natural orbital configuration interaction) and CEPA–PNO (coupled electron pair approximation with pair natural orbitals) calculations of molecular systems. I. Outline of the method for closed-shell states", J. Chem. Phys. **62**, 1225–1234 (1975).

[32]R. Ahlrichs, and F. Driessler, "Direct determination of pair natural orbitals", Theor. Chim. Acta **36**, 275–287 (1975).

[33]F. Neese, F. Wennmohs, and A. Hansen, "Efficient and accurate local approximations to coupled-electron pair approaches: An attempt to revive the pair natural orbital method", J. Chem. Phys. **130**, 114108 (2009).

[34]F. Neese, A. Hansen, and D. G. Liakos, "Efficient and accurate approximations to the local coupled cluster singles doubles method using a truncated pair natural orbital basis", J. Chem. Phys. **131**, 064103 (2009).

[35]F. Neese, "The ORCA program system", WIREs Comput. Mol. Sci. **2**, 73–78 (2011).

[36]F. Neese, "Software update: the ORCA program system, version 4.0", WIREs Comput. Mol. Sci. **8**, e1327 (2017).

[37]C. Riplinger, and F. Neese, "An efficient and near linear scaling pair natural orbital based local coupled cluster method", J. Chem. Phys. **138**, 034106 (2013).

[38]C. Riplinger, B. Sandhoefer, A. Hansen, and F. Neese, "Natural triple excitations in local coupled cluster calculations with pair natural orbitals", J. Chem. Phys. **139**, 134101 (2013).

[39]J. Yang, Y. Kurashige, F. R. Manby, and G. K. L. Chan, "Tensor factorizations of local second-order Møller–Plesset theory", J. Chem. Phys. **134**, 044123 (2011).

[40]Y. Kurashige, J. Yang, G. K.-L. Chan, and F. R. Manby, "Optimization of orbital-specific virtuals in local Møller-Plesset perturbation theory", J. Chem. Phys. **136**, 124106 (2012).

[41]J. Yang, G. K.-L. Chan, F. R. Manby, M. Schütz, and H.-J. Werner, "The orbital-specific-virtual local coupled cluster singles and doubles method", J. Chem. Phys. **136**, 144105 (2012).

[42]M. Schütz, J. Yang, G. K.-L. Chan, F. R. Manby, and H.-J. Werner, "The orbital-specific virtual local triples correction: OSV-L(T)", J. Chem. Phys. **138**, 054109 (2013).

[43]P. Pinski, C. Riplinger, E. F. Valeev, and F. Neese, "Sparse maps—A systematic infrastructure for reduced-scaling electronic structure methods. I. An efficient and simple linear scaling local MP2 method that uses an intermediate basis of pair natural orbitals", J. Chem. Phys. **143**, 034108 (2015).

[44]C. Riplinger, P. Pinski, U. Becker, E. F. Valeev, and F. Neese, "Sparse maps—A systematic infrastructure for reduced-scaling electronic structure methods. II. Linear scaling domain based pair natural orbital coupled cluster theory", J. Chem. Phys. **144**, 024109 (2016).

[45]Y. Guo, C. Riplinger, U. Becker, D. G. Liakos, Y. Minenkov, L. Cavallo, and F. Neese, "Communication: An improved linear scaling perturbative triples correction for the domain based local pair-natural orbital based singles and doubles coupled cluster method [DLPNO-CCSD(T)]", J. Chem. Phys. **148**, 011101 (2018).

[46]M. Saitow, U. Becker, C. Riplinger, E. F. Valeev, and F. Neese, "A new near-linear scaling, efficient and accurate, open-shell domain-based local pair natural orbital coupled cluster singles and doubles theory", J. Chem. Phys. **146**, 164105 (2017).

[47]M. Sparta, M. Retegan, P. Pinski, C. Riplinger, U. Becker, and F. Neese, "Multilevel Approaches within the Local Pair Natural Orbital Framework", J. Chem. Theory Comput. **13**, 3198–3207 (2017).

[48]F. Pavošević, P. Pinski, C. Riplinger, F. Neese, and E. F. Valeev, "SparseMaps—A systematic infrastructure for reduced-scaling electronic structure methods. IV. Linear-scaling second-order explicitly correlated energy with pair natural orbitals", J. Chem. Phys. **144**, 144109 (2016).

[49]F. Pavošević, C. Peng, P. Pinski, C. Riplinger, F. Neese, and E. F. Valeev, "SparseMaps—A systematic infrastructure for reduced scaling electronic structure methods. V. Linear scaling explicitly correlated coupled-cluster method with pair natural orbitals", J. Chem. Phys. **146**, 174108 (2017).

[50]Y. Guo, K. Sivalingam, E. F. Valeev, and F. Neese, "SparseMaps—A systematic infrastructure for reduced-scaling electronic structure methods. III. Linear-scaling multireference domain-based pair natural orbital N-electron valence perturbation theory", J. Chem. Phys. **144**, 094111 (2016).

[51]J. Brabec, J. Lang, M. Saitow, J. Pittner, F. Neese, and O. Demel, "Domain-Based Local Pair Natural Orbital Version of Mukherjee's State-Specific Coupled Cluster Method", J. Chem. Theory Comput. **14**, 1370–1382 (2018).

[52]J. Lang, J. Brabec, M. Saitow, J. Pittner, F. Neese, and O. Demel, "Perturbative triples correction to domain-based local pair natural orbital variants of Mukherjee's state specific coupled cluster method", Phys. Chem. Chem. Phys. **21**, 5022–5038 (2019).

[53]W. B. Schneider, G. Bistoni, M. Sparta, M. Saitow, C. Riplinger, A. A. Auer, and F. Neese, "Decomposition of Intermolecular Interaction Energies within the Local Pair Natural Orbital Coupled Cluster Framework", J. Chem. Theory Comput. **12**, 4778–4792 (2016).

[54]A. K. Dutta, F. Neese, and R. Izsák, "Towards a pair natural orbital coupled cluster method for excited states", J. Chem. Phys. **145**, 034102 (2016).

[55]H.-J. Werner, G. Knizia, C. Krause, M. Schwilk, and M. Dornbach, "Scalable Electron Correlation Methods I.: PNO-LMP2 with Linear Scaling in the Molecular Size and Near-Inverse-Linear Scaling in the Number of Processors", J. Chem. Theory Comput. **11**, 484–507 (2015).

[56]M. Schwilk, Q. Ma, C. Köppl, and H.-J. Werner, "Scalable Electron Correlation Methods. 3. Efficient and Accurate Parallel Local Coupled Cluster with Pair Natural Orbitals (PNO-LCCSD)", J. Chem. Theory Comput. **13**, 3650–3675 (2017).

[57]Q. Ma, and H.-J. Werner, "Scalable Electron Correlation Methods. 5. Parallel Perturbative Triples Correction for Explicitly Correlated Local Coupled Cluster with Pair Natural Orbitals", J. Chem. Theory Comput. **14**, 198–215 (2017).

[58]Q. Ma, and H.-J. Werner, "Scalable Electron Correlation Methods. 2. Parallel PNO-LMP2-F12 with Near Linear Scaling in the Molecular Size", J. Chem. Theory Comput. **11**, 5291–5304 (2015).

[59]Q. Ma, M. Schwilk, C. Köppl, and H.-J. Werner, "Scalable Electron Correlation Methods. 4. Parallel Explicitly Correlated Local Coupled Cluster with Pair Natural Orbitals (PNO-LCCSD-F12)", J. Chem. Theory Comput. **13**, 4871–4896 (2017).

[60]F. Menezes, D. Kats, and H.-J. Werner, "Local complete active space second-order perturbation theory using pair natural orbitals (PNO-CASPT2)", J. Chem. Phys. **145**, 124115 (2016).

[61]C. Krause, and H.-J. Werner, "Scalable Electron Correlation Methods. 6. Local Spin-Restricted Open-Shell Second-Order Møller–Plesset Perturbation Theory Using Pair Natural Orbitals: PNO-RMP2", J. Chem. Theory Comput. **15**, 987–1005 (2018).

[62]G. Schmitz, B. Helmich, and C. Hättig, "A $O(N^3)$ scaling PNO–MP2 method using a hybrid OSV–PNO approach with an iterative direct generation of OSVs", Mol. Phys. **111**, 2463–2476 (2013).

[63]G. Schmitz, C. Hättig, and D. P. Tew, "Explicitly correlated PNO-MP2 and PNO-CCSD and their application to the S66 set and large molecular systems", Phys. Chem. Chem. Phys. **16**, 22167–22178 (2014).

[64]G. Schmitz, and C. Hättig, "Perturbative triples correction for local pair natural orbital based explicitly correlated CCSD(F12*) using Laplace transformation techniques", J. Chem. Phys. **145**, 234107 (2016).

[65]B. Helmich, and C. Hättig, "A pair natural orbital based implementation of ADC(2)-x: Perspectives and challenges for response methods for singly and doubly excited states in large molecules", Comput. Theor. Chem. **1040-1041**, 35–44 (2014).

[66]M. S. Frank, and C. Hättig, "A pair natural orbital based implementation of CCSD excitation energies within the framework of linear response theory", J. Chem. Phys. **148**, 134102 (2018).

[67]P. Y. Ayala, and G. E. Scuseria, "Linear scaling second-order Moller–Plesset theory in the atomic orbital basis for large molecular systems", J. Chem. Phys. **110**, 3660–3671 (1999).

[68]S. A. Maurer, D. S. Lambrecht, J. Kussmann, and C. Ochsenfeld, "Efficient distance-including integral screening in linear-scaling Møller-Plesset perturbation theory", J. Chem. Phys. **138**, 014101 (2013).

[69]S. A. Maurer, L. Clin, and C. Ochsenfeld, "Cholesky-decomposed density MP2 with density fitting: Accurate MP2 and double-hybrid DFT energies for large systems", J. Chem. Phys. **140**, 224112 (2014).

[70]G. E. Scuseria, and P. Y. Ayala, "Linear scaling coupled cluster and perturbation theories in the atomic orbital basis", J. Chem. Phys. **111**, 8330–8343 (1999).

[71]M. S. Lee, P. E. Maslen, and M. Head-Gordon, "Closely approximating second-order Møller–Plesset perturbation theory with a local triatomics in molecules model", J. Chem. Phys. **112**, 3592–3601 (2000).

[72]R. A. DiStasio, Y. Jung, and M. Head-Gordon, "A Resolution-Of-The-Identity Implementation of the Local Triatomics-In-Molecules Model for Second-Order Møller-Plesset Perturbation Theory with Application to Alanine Tetrapeptide Conformational Energies", J. Chem. Theory Comput. **1**, 862–876 (2005).

[73]J. E. Subotnik, A. Sodt, and M. Head-Gordon, "A near linear-scaling smooth local coupled cluster algorithm for electronic structure", J. Chem. Phys. **125**, 074116 (2006).

[74]S. Li, J. Ma, and Y. Jiang, "Linear scaling local correlation approach for solving the coupled cluster equations of large systems", J. Comput. Chem. **23**, 237–244 (2001).

[75]S. Li, J. Shen, W. Li, and Y. Jiang, "An efficient implementation of the "cluster-in-molecule" approach for local electron correlation calculations", J. Chem. Phys. **125**, 074109 (2006).

[76]Y. Guo, W. Li, and S. Li, "Improved Cluster-in-Molecule Local Correlation Approach for Electron Correlation Calculation of Large Systems", J. Phys. Chem. A **118**, 8996–9004 (2014).

[77]H. Stoll, "The correlation energy of crystalline silicon", Chem. Phys. Lett. **191**, 548–552 (1992).

[78]H. Stoll, B. Paulus, and P. Fulde, "On the accuracy of correlation-energy expansions in terms of local increments", J. Chem. Phys. **123**, 144108 (2005).

[79]J. Friedrich, M. Hanrath, and M. Dolg, "Fully automated implementation of the incremental scheme: Application to CCSD energies for hydrocarbons and transition metal compounds", J. Chem. Phys. **126**, 154110 (2007).

[80]M. Ziółkowski, B. Jansík, T. Kjærgaard, and P. Jørgensen, "Linear scaling coupled cluster method with correlation energy based error control", J. Chem. Phys. **133**, 014107 (2010).

[81]P. Baudin, P. Ettenhuber, S. Reine, K. Kristensen, and T. Kjærgaard, "Efficient linear-scaling second-order Møller-Plesset perturbation theory: The divide–expand–consolidate RI-MP2 model", J. Chem. Phys. **144**, 054102 (2016).

[82]T. Kjaergaard, P. Baudin, D. Bykov, K. Kristensen, and P. Jørgensen, "The divide-expand-consolidate coupled cluster scheme", WIREs Comput. Mol. Sci. **7**, e1319 (2017).

[83]Y. Guo, U. Becker, and F. Neese, "Comparison and combination of "direct" and fragment based local correlation methods: Cluster in molecules and domain based local pair natural orbital perturbation and coupled cluster theories", J. Chem. Phys. **148**, 124117 (2018).

[84]Z. Rolik, and M. Kállay, "A general-order local coupled-cluster method based on the cluster-in-molecule approach", J. Chem. Phys. **135**, 104111 (2011).

[85]Z. Rolik, L. Szegedy, I. Ladjánszki, B. Ladóczki, and M. Kállay, "An efficient linear-scaling CCSD(T) method based on local natural orbitals", J. Chem. Phys. **139**, 094105 (2013).

[86]P. R. Nagy, G. Samu, and M. Kállay, "An Integral-Direct Linear-Scaling Second-Order Møller–Plesset Approach", J. Chem. Theory Comput. **12**, 4897–4914 (2016).

[87]P. R. Nagy, G. Samu, and M. Kállay, "Optimization of the Linear-Scaling Local Natural Orbital CCSD(T) Method: Improved Algorithm and Benchmark Applications", J. Chem. Theory Comput. **14**, 4193–4215 (2018).

[88]J. Gauss, "Molecular Properties", in Modern Methods and Algorithms of Quantum Chemistry, Vol. 1, edited by J. Grotendorst, NIC Series (John von Neumann Institute for Computing, Forschungszentrum Jülich, Germany, 2000), pp. 509–560.

[89]A. El Azhary, G. Rauhut, P. Pulay, and H.-J. Werner, "Analytical energy gradients for local second-order Møller–Plesset perturbation theory", J. Chem. Phys. **108**, 5185–5193 (1998).

[90]M. Schütz, H.-J. Werner, R. Lindh, and F. R. Manby, "Analytical energy gradients for local second-order Møller–Plesset perturbation theory using density fitting approximations", J. Chem. Phys. **121**, 737–750 (2004).

[91]M. Dornbach, and H.-J. Werner, "Analytical energy gradients for local second-order Møller-Plesset perturbation theory using intrinsic bond orbitals", Mol. Phys. **117**, 1252–1263 (2018).

[92]K. Ledermüller, D. Kats, and M. Schütz, "Local CC2 response method based on the Laplace transform: Orbital-relaxed first-order properties for excited states", J. Chem. Phys. **139**, 084111 (2013).

[93]K. Ledermüller, and M. Schütz, "Local CC2 response method based on the Laplace transform: Analytic energy gradients for ground and excited states", J. Chem. Phys. **140**, 164113 (2014).

[94]M. Schütz, "Oscillator strengths, first-order properties, and nuclear gradients for local ADC(2)", J. Chem. Phys. **142**, 214103 (2015).

[95]G. Rauhut, and H.-J. Werner, "Analytical energy gradients for local coupled-cluster methods", Phys. Chem. Chem. Phys. **3**, 4853–4862 (2001).

[96]J. Gauss, and H.-J. Werner, "NMR chemical shift calculations within local correlation methods: the GIAO-LMP2 approach", Phys. Chem. Chem. Phys. **2**, 2083–2090 (2000).

[97]S. Loibl, and M. Schütz, "NMR shielding tensors for density fitted local second-order Møller-Plesset perturbation theory using gauge including atomic orbitals", J. Chem. Phys. **137**, 084107 (2012).

[98]S. Loibl, and M. Schütz, "Magnetizability and rotational g tensors for density fitted local second-order Møller-Plesset perturbation theory using gauge-including atomic orbitals", J. Chem. Phys. **141**, 024108 (2014).

[99]S. Schweizer, B. Doser, and C. Ochsenfeld, "An atomic orbital-based reformulation of energy gradients in second-order Møller–Plesset perturbation theory", J. Chem. Phys. **128**, 154101 (2008).

[100]S. Vogler, M. Ludwig, M. Maurer, and C. Ochsenfeld, "Low-scaling first-order properties within second-order Møller-Plesset perturbation theory using Cholesky decomposed density matrices", J. Chem. Phys. **147**, 024101 (2017).

[101]M. Maurer, and C. Ochsenfeld, "A linear- and sublinear-scaling method for calculating NMR shieldings in atomic orbital-based second-order Møller-Plesset perturbation theory", J. Chem. Phys. **138**, 174104 (2013).

[102]K. Kristensen, P. Jørgensen, B. Jansík, T. Kjærgaard, and S. Reine, "Molecular gradient for second-order Møller-Plesset perturbation theory using the divide-expand-consolidate (DEC) scheme", J. Chem. Phys. **137**, 114102 (2012).

[103]D. Bykov, K. Kristensen, and T. Kjærgaard, "The molecular gradient using the divide-expand-consolidate resolution of the identity second-order Møller-Plesset perturbation theory: The DEC-RI-MP2 gradient", J. Chem. Phys. **145**, 024106 (2016).

[104]Z. Ni, Y. Wang, W. Li, P. Pulay, and S. Li, "Analytical Energy Gradients for the Cluster-in-Molecule MP2 Method and Its Application to Geometry Optimizations of Large Systems", J. Chem. Theory Comput. **15**, 3623–3634 (2019).

[105]J. Friedrich, S. Coriani, T. Helgaker, and M. Dolg, "Implementation of the incremental scheme for one-electron first-order properties in coupled-cluster theory", J. Chem. Phys. **131**, 154102 (2009).

[106]J. Friedrich, H. R. McAlexander, A. Kumar, and T. D. Crawford, "Incremental evaluation of coupled cluster dipole polarizabilities", Phys. Chem. Chem. Phys. **17**, 14284–14296 (2015).

[107]D. Datta, S. Kossmann, and F. Neese, "Analytic energy derivatives for the calculation of the first-order molecular properties using the domain-based local pair-natural orbital coupled-cluster theory", J. Chem. Phys. **145**, 114101 (2016).

[108]M. Saitow, and F. Neese, "Accurate spin-densities based on the domain-based local pair-natural orbital coupled-cluster theory", J. Chem. Phys. **149**, 034104 (2018).

[109]H. R. McAlexander, and T. D. Crawford, "A Comparison of Three Approaches to the Reduced-Scaling Coupled Cluster Treatment of Non-Resonant Molecular Response Properties", J. Chem. Theory Comput. **12**, 209–222 (2015).

[110]P. Pinski, and F. Neese, "Communication: Exact analytical derivatives for the domain-based local pair natural orbital MP2 method (DLPNO-MP2)", J. Chem. Phys. **148**, 031101 (2018).

[111]P. Pinski, and F. Neese, "Analytical gradient for the domain-based local pair natural orbital second order Møller-Plesset perturbation theory method (DLPNO-MP2)", J. Chem. Phys. **150**, 164102 (2019).

[112]M. S. Frank, G. Schmitz, and C. Hättig, "The PNO–MP2 gradient and its application to molecular geometry optimisations", Mol. Phys. **115**, 343–356 (2016).

[113]R. Zhou, Q. Liang, and J. Yang, "Complete OSV-MP2 Analytical Gradient Theory for Molecular Structure and Dynamics Simulations", J. Chem. Theory Comput. **16**, 196–210 (2019).

[114]L. Goerigk, and S. Grimme, "Efficient and Accurate Double-Hybrid-Meta-GGA Density Functionals—Evaluation with the Extended GMTKN30 Database for General Main Group Thermochemistry, Kinetics, and Noncovalent Interactions", J. Chem. Theory Comput. **7**, 291–309 (2010); `https://www.chemie.uni-bonn.de/pctc/mulliken-center/software/GMTKN/gmtkn30`.

[115]J. Řezáč, and P. Hobza, "Benchmark Calculations of Interaction Energies in Noncovalent Complexes and Their Applications", Chem. Rev. **116**, 5038–5071 (2016).

[116]S. Grimme, "Improved second-order Møller–Plesset perturbation theory by separate scaling of parallel- and antiparallel-spin pair correlation energies", J. Chem. Phys. **118**, 9095–9102 (2003).

[117]Y. Jung, R. C. Lochan, A. D. Dutoi, and M. Head-Gordon, "Scaled opposite-spin second order Møller–Plesset correlation energy: An economical electronic structure method", J. Chem. Phys. **121**, 9793–9802 (2004).

[118]R. F. Fink, "Spin-component-scaled Møller–Plesset (SCS-MP) perturbation theory: A generalization of the MP approach with improved properties", J. Chem. Phys. **133**, 174113 (2010).

[119]S. Grimme, "Semiempirical hybrid density functional with perturbative second-order correlation", J. Chem. Phys. **124**, 034108 (2006).

[120]L. Goerigk, and S. Grimme, "Double-hybrid density functionals", WIREs Comput. Mol. Sci. **4**, 576–600 (2014).

[121]L. Goerigk, A. Hansen, C. Bauer, S. Ehrlich, A. Najibi, and S. Grimme, "A look at the density functional theory zoo with the advanced GMTKN55 database for general main group thermochemistry, kinetics and noncovalent interactions", Phys. Chem. Chem. Phys. **19**, 32184–32215 (2017).

[122]S. Grimme, and M. Steinmetz, "Effects of London dispersion correction in density functional theory on the structures of organic molecules in the gas phase", Phys. Chem. Chem. Phys. **15**, 16031 (2013).

[123]T. Risthaus, M. Steinmetz, and S. Grimme, "Implementation of nuclear gradients of range-separated hybrid density functionals and benchmarking on rotational constants for organic molecules", J. Comput. Chem. **35**, 1509–1516 (2014).

[124]S. Kozuch, and J. M. L. Martin, "Spin-component-scaled double hybrids: An extensive search for the best fifth-rung functionals blending DFT and perturbation theory", J. Comput. Chem. **34**, 2327–2344 (2013).

[125]D. Hait, and M. Head-Gordon, "How Accurate Is Density Functional Theory at Predicting Dipole Moments? An Assessment Using a New Database of 200 Benchmark Values", J. Chem. Theory Comput. **14**, 1969–1981 (2018).

[126]G. L. Stoychev, A. A. Auer, and F. Neese, "Efficient and Accurate Prediction of Nuclear Magnetic Resonance Shielding Tensors with Double-Hybrid Density Functional Theory", J. Chem. Theory Comput. **14**, 4756–4771 (2018).

[127]A. D. Boese, "Density Functional Theory and Hydrogen Bonds: Are We There Yet?", ChemPhysChem **16**, 978–985 (2015).

[128]A. Szabo, and N. S. Ostlund, *Modern Quantum Chemistry* (Dover Publications Inc., 1996).

[129]E. A. Hylleraas, "Über den Grundterm der Zweielektronenprobleme von H^-, He, Li^+, Be^{++} usw.", Z. Phys. **65**, 209–225 (1930).

[130]I. Mayer, *Simple Theorems, Proofs, and Derivations in Quantum Chemistry* (Springer US, 2003).

[131]P. Pulay, S. Saebø, and W. Meyer, "An efficient reformulation of the closed-shell self-consistent electron pair theory", J. Chem. Phys. **81**, 1901–1905 (1984).

[132]J. M. Foster, and S. F. Boys, "Canonical Configurational Interaction Procedure", Rev. Mod. Phys. **32**, 300–302 (1960).

[133]S. F. Boys, *Quantum Theory of Atoms, Molecules, and the Solid State*, edited by P.-O. Löwdin, (Academic Press, New York, 1966), pp. 253–262.

[134]J. Pipek, and P. G. Mezey, "A fast intrinsic localization procedure applicable for ab initio and semiempirical linear combination of atomic orbital wave functions", J. Chem. Phys. **90**, 4916–4926 (1989).

[135]C. Edmiston, and K. Ruedenberg, "Localized Atomic and Molecular Orbitals", Rev. Mod. Phys. **35**, 457–464 (1963).

[136]W. Kohn, "Analytic Properties of Bloch Waves and Wannier Functions", Phys. Rev. **115**, 809–821 (1959).

[137]S. Ismail-Beigi, and T. A. Arias, "Locality of the Density Matrix in Metals, Semiconductors, and Insulators", Phys. Rev. Lett. **82**, 2127–2130 (1999).

[138]H.-J. Werner, and K. Pflüger, "Chapter 4 On the Selection of Domains and Orbital Pairs in Local Correlation Treatments", in *Annual Reports in Computational Chemistry*, edited by D. C. Spellmeyer, (Elsevier, 2006), pp. 53–80.

[139]D. P. Tew, "Principal Domains in Local Correlation Theory", J. Chem. Theory Comput. **15**, 6597–6606 (2019).

[140]G. Hetzer, P. Pulay, and H.-J. Werner, "Multipole approximation of distant pair energies in local MP2 calculations", Chem. Phys. Lett. **290**, 143–149 (1998).

[141]H.-J. Werner, "Communication: Multipole approximations of distant pair energies in local correlation methods with pair natural orbitals", J. Chem. Phys. **145**, 201101 (2016).

[142]G. H. Golub, *Matrix Computations* (J. Hopkins Uni. Press, 2013).

[143]E. Schwegler, M. Challacombe, and M. Head-Gordon, "Linear scaling computation of the Fock matrix. II. Rigorous bounds on exchange integrals and incremental Fock build", J. Chem. Phys. **106**, 9708–9717 (1997).

[144]C. Ochsenfeld, C. A. White, and M. Head-Gordon, "Linear and sublinear scaling formation of Hartree–Fock-type exchange matrices", J. Chem. Phys. **109**, 1663–1669 (1998).

[145]F. Neese, F. Wennmohs, A. Hansen, and U. Becker, "Efficient, approximate and parallel Hartree–Fock and hybrid DFT calculations. A 'chain-of-spheres' algorithm for the Hartree–Fock exchange", Chem. Phys. **356**, 98–109 (2009).

[146]M. Häser, and R. Ahlrichs, "Improvements on the direct SCF method", J. Comput. Chem. **10**, 104–111 (1989).

[147]P. M. Gill, B. G. Johnson, and J. A. Pople, "A simple yet powerful upper bound for Coulomb integrals", Chem. Phys. Lett. **217**, 65–68 (1994).

[148]D. S. Lambrecht, and C. Ochsenfeld, "Multipole-based integral estimates for the rigorous description of distance dependence in two-electron integrals", J. Chem. Phys. **123**, 184101 (2005).

[149]S. A. Maurer, D. S. Lambrecht, D. Flaig, and C. Ochsenfeld, "Distance-dependent Schwarz-based integral estimates for two-electron integrals: Reliable tightness vs. rigorous upper bounds", J. Chem. Phys. **136**, 144107 (2012).

[150]G. Bistoni, C. Riplinger, Y. Minenkov, L. Cavallo, A. A. Auer, and F. Neese, "Treating Subvalence Correlation Effects in Domain Based Pair Natural Orbital Coupled Cluster Calculations: An Out-of-the-Box Approach", J. Chem. Theory Comput. **13**, 3220–3227 (2017).

[151]P. Pulay, "Convergence acceleration of iterative sequences. the case of scf iteration", Chem. Phys. Lett. **73**, 393–398 (1980).

[152]J. Friedrich, and J. Hänchen, "Incremental CCSD(T)(F12*)|MP2: A Black Box Method To Obtain Highly Accurate Reaction Energies", J. Chem. Theory Comput. **9**, 5381–5394 (2013).

[153]U. R. Fogueri, S. Kozuch, A. Karton, and J. M. Martin, "The Melatonin Conformer Space: Benchmark and Assessment of Wave Function and DFT Methods for a Paradigmatic Biological and Pharmacological Molecule", J. Phys. Chem. A **117**, 2269–2277 (2013).

[154]S. Kozuch, S. M. Bachrach, and J. M. Martin, "Conformational Equilibria in Butane-1,4-diol: A Benchmark of a Prototypical System with Strong Intramolecular H-bonds", J. Phys. Chem. A **118**, 293–303 (2013).

[155]J. Řezáč, K. E. Riley, and P. Hobza, "S66: A Well-balanced Database of Benchmark Interaction Energies Relevant to Biomolecular Structures", J. Chem. Theory Comput. **7**, 2427–2438 (2011).

[156]Y. Guo, W. Li, and S. Li, "An efficient linear scaling procedure for constructing localized orbitals of large molecules based on the one-particle density matrix", J. Chem. Phys. **135**, 134107 (2011).

[157]S. Koßmann, "Efficient Novel Approaches for the Calculation of Molecular Response Properties: Second-Order Many-Body Perturbation and Double-Hybrid Density Functional Theory", PhD thesis (Rheinische Friedrich-Wilhelms-Universität Bonn, 2012).

[158]A. Hansen, D. G. Liakos, and F. Neese, "Efficient and accurate local single reference correlation methods for high-spin open-shell molecules using pair natural orbitals", J. Chem. Phys. **135**, 214102 (2011).

[159]N. C. Handy, and H. F. Schaefer, "On the evaluation of analytic energy derivatives for correlated wave functions", J. Chem. Phys. **81**, 5031–5033 (1984).

[160]L. Adamowicz, W. D. Laidig, and R. J. Bartlett, "Analytical gradients for the coupled-cluster method", Int. J. Quantum Chem. **26**, 245–254 (1984).

[161]G. Fitzgerald, R. J. Harrison, and R. J. Bartlett, "Analytic energy gradients for general coupled-cluster methods and fourth-order many-body perturbation theory", J. Chem. Phys. **85**, 5143–5150 (1986).

[162]A. C. Scheiner, G. E. Scuseria, J. E. Rice, T. J. Lee, and H. F. Schaefer, "Analytic evaluation of energy gradients for the single and double excitation coupled cluster (CCSD) wave function: Theory and application", J. Chem. Phys. **87**, 5361–5373 (1987).

[163]J. Rice, and R. Amos, "On the efficient evaluation of analytic energy gradients", Chem. Phys. Lett. **122**, 585–590 (1985).

[164]P. Jørgensen, and T. Helgaker, "Møller–Plesset energy derivatives", J. Chem. Phys. **89**, 1560–1570 (1988).

[165]T. Helgaker, P. Jørgensen, and N. C. Handy, "A numerically stable procedure for calculating Møller-Plesset energy derivatives, derived using the theory of Lagrangians", Theor. Chim. Acta **76**, 227–245 (1989).

[166]T. U. Helgaker, and J. Almlöf, "A second-quantization approach to the analytical evaluation of response properties for perturbation-dependent basis sets", Int. J. Quantum Chem. **26**, 275–291 (1984).

[167]R. M. Stevens, R. M. Pitzer, and W. N. Lipscomb, "Perturbed Hartree—Fock Calculations. I. Magnetic Susceptibility and Shielding in the LiH Molecule", J. Chem. Phys. **38**, 550–560 (1963).

[168]J. Gerratt, and I. M. Mills, "Force Constants and Dipole-Moment Derivatives of Molecules from Perturbed Hartree–Fock Calculations. I", J. Chem. Phys. **49**, 1719–1729 (1968).

[169]J. A. Pople, R. Krishnan, H. B. Schlegel, and J. S. Binkley, "Derivative Studies in Hartree-Fock and Møller-Plesset Theories", Int. J. Quantum Chem. **16**, 225–241 (1979).

[170]N. Handy, R. Amos, J. Gaw, J. Rice, and E. Simandiras, "The elimination of singularities in derivative calculations", Chem. Phys. Lett. **120**, 151–158 (1985).

[171]W. England, "Continuous degeneracy and energy-localization of molecular orbitals", Int. J. Quantum Chem. **5**, 683–697 (1971).

[172]P. Scheurer, and W. H. E. Schwarz, "Externally localized molecular orbitals: A numerical investigation of localization degeneracy", Int. J. Quantum Chem. **76**, 420–427 (2000).

[173]P. Scheurer, and W. H. E. Schwarz, "Continuous degeneracy of sets of localized orbitals", Int. J. Quantum Chem. **76**, 428–433 (2000).

[174]K. Toyota, M. Ehara, and H. Nakatsuji, "Elimination of singularities in molecular orbital derivatives: minimum orbital-deformation (MOD) method", Chem. Phys. Lett. **356**, 1–6 (2002).

[175]K. Toyota, M. Ishida, M. Ehara, M. J. Frisch, and H. Nakatsuji, "Singularity-free analytical energy gradients for the SAC/SAC-CI method: coupled perturbed minimum orbital-deformation (CPMOD) approach", Chem. Phys. Lett. **367**, 730–736 (2003).

[176]J. R. Shewchuk, *An Introduction to the Conjugate Gradient Method Without the Agonizing Pain*, Carnegie Mellon University, Pittburgh, (1994) `https://www.cs.cmu.edu/~quake-papers/painless-conjugate-gradient.pdf`.

[177]E. R. Davidson, "The iterative calculation of a few of the lowest eigenvalues and corresponding eigenvectors of large real-symmetric matrices", J. Comput. Phys. **17**, 87–94 (1975).

[178]M. Crouzeix, B. Philippe, and M. Sadkane, "The Davidson Method", SIAM J. Sci. Comput. **15**, 62–76 (1994).

[179]S. Kossmann, and F. Neese, "Efficient Structure Optimization with Second-Order Many-Body Perturbation Theory: The RIJCOSX-MP2 Method", J. Chem. Theory Comput. **6**, 2325–2338 (2010).

[180]L. E. McMurchie, and E. R. Davidson, "One- and two-electron integrals over cartesian gaussian functions", J. Comput. Phys. **26**, 218–231 (1978).

[181]F. Neese, T. Schwabe, and S. Grimme, "Analytic derivatives for perturbatively corrected "double hybrid" density functionals: Theory, implementation, and applications", J. Chem. Phys. **126**, 124115 (2007).

[182]R. Barr, and H. Basch, "Improved convergence in orbital localization methods", Chem. Phys. Lett. **32**, 537–540 (1975).

[183]R. C. Haddon, and G. R. Williams, "Calculation of localised molecular orbitals with the Foster—Boys criterion", Chem. Phys. Lett. **42**, 453–455 (1976).

[184]J. M. Leonard, and W. L. Luken, "Quadratically convergent calculation of localized molecular orbitals", Theor. Chim. Acta **62**, 107–132 (1982).

[185]J. E. Subotnik, Y. Shao, W. Liang, and M. Head-Gordon, "An efficient method for calculating maxima of homogeneous functions of orthogonal matrices: Applications to localized occupied orbitals", J. Chem. Phys. **121**, 9220–9229 (2004).

[186]J. E. Subotnik, A. Sodt, and M. Head-Gordon, "Localized orbital theory and ammonia triborane", Phys. Chem. Chem. Phys. **9**, 5522 (2007).

[187]Q. Sun, "Co-iterative augmented Hessian method for orbital optimization", arxiv:1610.08423 [physics.chem-ph] (2016).

[188]A. Banerjee, N. Adams, J. Simons, and R. Shepard, "Search for stationary points on surfaces", J. Phys. Chem. **89**, 52–57 (1985).

[189]F. Aquilante, T. B. Pedersen, A. S. de Merás, and H. Koch, "Fast noniterative orbital localization for large molecules", J. Chem. Phys. **125**, 174101 (2006).

[190]A. H. Al-Mohy, and N. J. Higham, "A New Scaling and Squaring Algorithm for the Matrix Exponential", SIAM J. Matrix Anal. Appl. **31**, 970–989 (2010).

[191]R. Shepard, S. R. Brozell, and G. Gidofalvi, "The Representation and Parametrization of Orthogonal Matrices", J. Phys. Chem. A **119**, 7924–7939 (2015).

[192]J. Almlöf, K. Faegri, and K. Korsell, "Principles for a Direct SCF Approach to LCAO-MO Ab-Initio Calculations", J. Comput. Chem. **3**, 385–399 (1982).

[193]L. Cheng, S. Stopkowicz, J. F. Stanton, and J. Gauss, "The route to high accuracy in ab initio calculations of Cu quadrupole-coupling constants", J. Chem. Phys. **137**, 224302 (2012).

[194]S. Stopkowicz, and J. Gauss, "Revised values for the nuclear quadrupole moments of ^{33}S and ^{35}S", Phys. Rev. A **90**, 022507 (2014).

[195]R. Björnsson, and M. Bühl, "Electric field gradients of transition metal complexes from density functional theory: assessment of functionals, geometries and basis sets", Dalton Trans. **39**, 5319 (2010).

[196]F. A. Perras, and D. L. Bryce, "Direct Investigation of Covalently Bound Chlorine in Organic Compounds by Solid-State ^{35}Cl NMR Spectroscopy and Exact Spectral Line-Shape Simulations", Angew. Chem. Int. Ed. **51**, 4227–4230 (2012).

[197]L. A. O'Dell, and C. I. Ratcliffe, "Crystal Structure Based Design of Signal Enhancement Schemes for Solid-State NMR of Insensitive Half-Integer Quadrupolar Nuclei", J. Phys. Chem. A **115**, 747–752 (2011).

[198]C. R. Groom, I. J. Bruno, M. P. Lightfoot, and S. C. Ward, "The Cambridge Structural Database", Acta Crystallogr. B Struct. Sci. Cryst. Eng. Mater. **72**, 171–179 (2016).

[199]A. Johnston, J. Bardin, B. F. Johnston, P. Fernandes, A. R. Kennedy, S. L. Price, and A. J. Florence, "Experimental and Predicted Crystal Energy Landscapes of Chlorothiazide", Cryst. Growth Des. **11**, 405–413 (2011).

[200]A. D. Becke, "Density-functional exchange-energy approximation with correct asymptotic behavior", Phys. Rev. A **38**, 3098–3100 (1988).

[201]J. P. Perdew, "Density-functional approximation for the correlation energy of the inhomogeneous electron gas", Phys. Rev. B **33**, 8822–8824 (1986).

[202]S. Grimme, J. Antony, S. Ehrlich, and H. Krieg, "A consistent and accurate ab initio parametrization of density functional dispersion correction (DFT-D) for the 94 elements H-Pu", J. Chem. Phys. **132**, 154104 (2010).

[203]S. Grimme, S. Ehrlich, and L. Goerigk, "Effect of the damping function in dispersion corrected density functional theory", J. Comput. Chem. **32**, 1456–1465 (2011).

[204]C. E. Briant, and D. W. Jones, "Neutron refinement of the crystal structure of partially exchanged taurine, $(ND_3^+)_{0.65}(NH_3^+)_{0.35}(CH_2)_2SO_3^-$", J. Chem. Crystallogr. **27**, 481–483 (1997).

[205]K. A. Peterson, and T. H. Dunning, "Accurate correlation consistent basis sets for molecular core–valence correlation effects: The second row atoms Al–Ar, and the first row atoms B–Ne revisited", J. Chem. Phys. **117**, 10548–10560 (2002).

[206]T. H. Dunning, "Gaussian basis sets for use in correlated molecular calculations. I. The atoms boron through neon and hydrogen", J. Chem. Phys. **90**, 1007–1023 (1989).

[207]C. Hättig, "Optimization of auxiliary basis sets for RI-MP2 and RI-CC2 calculations: Core–valence and quintuple-ζ basis sets for H to Ar and QZVPP basis sets for Li to Kr", Phys. Chem. Chem. Phys. **7**, 59–66 (2005).

[208]F. Weigend, A. Köhn, and C. Hättig, "Efficient use of the correlation consistent basis sets in resolution of the identity MP2 calculations", J. Chem. Phys. **116**, 3175–3183 (2002).

[209]D. Sundholm, and J. Olsen, "Finite element multiconfiguration Hartree–Fock determination of the nuclear quadrupole moments of chlorine, potassium, and calcium isotopes", J. Chem. Phys. **98**, 7152–7158 (1993).

[210]N. Stone, "Table of nuclear electric quadrupole moments", At. Data Nucl. Data Tables **111-112**, 1–28 (2016).

[211]A. Kumar, and T. D. Crawford, "Frozen Virtual Natural Orbitals for Coupled-Cluster Linear-Response Theory", J. Phys. Chem. A **121**, 708–716 (2017).

[212]T. Korona, K. Pflüger, and H.-J. Werner, "The effect of local approximations in coupled-cluster wave functions on dipole moments and static dipole polarisabilities", Phys. Chem. Chem. Phys. **6**, 2059–2065 (2004).

[213]S. Grimme, J. G. Brandenburg, C. Bannwarth, and A. Hansen, "Consistent structures and interactions by density functional theory with small atomic orbital basis sets", J. Chem. Phys. **143**, 054107 (2015).

[214]R. Sure, and S. Grimme, "Corrected small basis set Hartree-Fock method for large systems", J. Comput. Chem. **34**, 1672–1685 (2013).

[215]J. Baker, "Techniques for geometry optimization: A comparison of cartesian and natural internal coordinates", J. Comput. Chem. **14**, 1085–1100 (1993).

[216]A. Karton, A. Tarnopolsky, J.-F. Lamère, G. C. Schatz, and J. M. L. Martin, "Highly Accurate First-Principles Benchmark Data Sets for the Parametrization and Validation of Density Functional and Other Approximate Methods. Derivation of a Robust, Generally Applicable, Double-Hybrid Functional for Thermochemistry and Thermochemical Kinetics", J. Phys. Chem. A **112**, 12868–12886 (2008).

[217]S. Kozuch, D. Gruzman, and J. M. L. Martin, "DSD-BLYP: A General Purpose Double Hybrid Density Functional Including Spin Component Scaling and Dispersion Correction", J. Phys. Chem. C **114**, 20801–20808 (2010).

[218]S. Kozuch, and J. M. L. Martin, "DSD-PBEP86: in search of the best double-hybrid DFT with spin-component scaled MP2 and dispersion corrections", Phys. Chem. Chem. Phys. **13**, 20104 (2011).

[219]S. Saebø, W. Tong, and P. Pulay, "Efficient elimination of basis set superposition errors by the local correlation method: Accurate ab initio studies of the water dimer", J. Chem. Phys. **98**, 2170–2175 (1993).

[220]M. Schütz, G. Rauhut, and H.-J. Werner, "Local Treatment of Electron Correlation in Molecular Clusters: Structures and Stabilities of $(H_2O)_n$, $n = 2 - 4$", J. Phys. Chem. A **102**, 5997–6003 (1998).

[221]G. Rauhut, A. El Azhary, F. Eckert, U. Schumann, and H.-J. Werner, "Impact of local approximations on MP2 vibrational frequencies", Spectrochim. Acta, Part A **55**, 647–658 (1999).

[222]S. Boys, and F. Bernardi, "The calculation of small molecular interactions by the differences of separate total energies. Some procedures with reduced errors", Mol. Phys. **19**, 553–566 (1970).

[223]A. Halkier, W. Klopper, T. Helgaker, P. Jørgensen, and P. R. Taylor, "Basis set convergence of the interaction energy of hydrogen-bonded complexes", J. Chem. Phys. **111**, 9157–9167 (1999).

[224]L. A. Burns, M. S. Marshall, and C. D. Sherrill, "Comparing Counterpoise-Corrected, Uncorrected, and Averaged Binding Energies for Benchmarking Noncovalent Interactions", J. Chem. Theory Comput. **10**, 49–57 (2013).

[225]M. K. Kesharwani, A. Karton, N. Sylvetsky, and J. M. L. Martin, "The S66 Non-Covalent Interactions Benchmark Reconsidered Using Explicitly Correlated Methods Near the Basis Set Limit", Aust. J. Chem. **71**, 238 (2018).

[226]D. G. Liakos, R. Izsák, E. F. Valeev, and F. Neese, "What is the most efficient way to reach the canonical MP2 basis set limit?", Mol. Phys. **111**, 2653–2662 (2013).

[227]K. A. Peterson, T. B. Adler, and H.-J. Werner, "Systematically convergent basis sets for explicitly correlated wavefunctions: The atoms H, He, B–Ne, and Al–Ar", J. Chem. Phys. **128**, 084102 (2008).

[228]K. E. Yousaf, and K. A. Peterson, "Optimized auxiliary basis sets for explicitly correlated methods", J. Chem. Phys. **129**, 184108 (2008).

[229]B. Brauer, M. K. Kesharwani, S. Kozuch, and J. M. L. Martin, "The S66x8 benchmark for noncovalent interactions revisited: explicitly correlated ab initio methods and density functional theory", Phys. Chem. Chem. Phys. **18**, 20905–20925 (2016).

[230]N. O. B. Lüttschwager, T. N. Wassermann, R. A. Mata, and M. A. Suhm, "The Last Globally Stable Extended Alkane", Angew. Chem. Int. Ed. **52**, 463–466 (2012).

[231]J. N. Byrd, R. J. Bartlett, and J. A. Montgomery, "At What Chain Length Do Unbranched Alkanes Prefer Folded Conformations?", J. Phys. Chem. A **118**, 1706–1712 (2014).

[232]D. G. Liakos, and F. Neese, "Domain Based Pair Natural Orbital Coupled Cluster Studies on Linear and Folded Alkane Chains", J. Chem. Theory Comput. **11**, 2137–2143 (2015).

[233]J. Černý, M. Pitoňák, K. E. Riley, and P. Hobza, "Complete Basis Set Extrapolation and Hybrid Schemes for Geometry Gradients of Noncovalent Complexes", J. Chem. Theory Comput. **7**, 3924–3934 (2011).

[234]R. A. Kendall, T. H. Dunning, and R. J. Harrison, "Electron affinities of the first-row atoms revisited. Systematic basis sets and wave functions", J. Chem. Phys. **96**, 6796–6806 (1992).

[235]S. Grimme, C. Bannwarth, and P. Shushkov, "A Robust and Accurate Tight-Binding Quantum Chemical Method for Structures, Vibrational Frequencies, and Noncovalent Interactions of Large Molecular Systems Parametrized for All spd-Block Elements (Z = 1–86)", J. Chem. Theory Comput. **13**, 1989–2009 (2017).

[236]R. Sure, and S. Grimme, "Comprehensive Benchmark of Association (Free) Energies of Realistic Host–Guest Complexes", J. Chem. Theory Comput. **11**, 3785–3801 (2015).

[237]F. Pavošević, F. Neese, and E. F. Valeev, "Geminal-spanning orbitals make explicitly correlated reduced-scaling coupled-cluster methods robust, yet simple", J. Chem. Phys. **141**, 054106 (2014).

[238]W. Győrffy, G. Knizia, and H.-J. Werner, "Analytical energy gradients for explicitly correlated wave functions. I. Explicitly correlated second-order Møller-Plesset perturbation theory", J. Chem. Phys. **147**, 214101 (2017).

[239]N. J. Russ, and T. D. Crawford, "Potential energy surface discontinuities in local correlation methods", J. Chem. Phys. **121**, 691–696 (2004).

[240]R. A. Mata, and H.-J. Werner, "Calculation of smooth potential energy surfaces using local electron correlation methods", J. Chem. Phys. **125**, 184110 (2006).

[241]J. E. Subotnik, and M. Head-Gordon, "A local correlation model that yields intrinsically smooth potential-energy surfaces", J. Chem. Phys. **123**, 064108 (2005).

[242]R. Huenerbein, B. Schirmer, J. Moellmann, and S. Grimme, "Effects of London dispersion on the isomerization reactions of large organic molecules: a density functional benchmark study", Phys. Chem. Chem. Phys. **12**, 6940 (2010).